The Catalytic Dehydrogenation of Conventional Chemicals using Unconventional Methods

by

Quan Do

A dissertation submitted to the Department of Chemical and Biomolecular Engineering

in partial fulfillment of the requirements for the degree of

Doctor of Philosophy

In Chemical Engineering

Chair of Committee: Dr. Lars Grabow

Committee Member: Dr. Michael Harold

Committee Member: Dr. Praveen Bollini

Committee Member: Dr. Paul Ruchhoeft

Committee Member: Dr. Kaiwalya Sabnis

University of Houston

December 2019

Acknowledgements

Admittedly, there are too many people to thank within a confined space of two pages. First and foremost, however, I must thank those who are personally closest to me. There are always nightmare stories about graduate school experiences; it was never that bad for me, but I truly appreciate those who have supported me emotionally and mentally along the way. Those who are dearest and nearest to me have walked this journey with me, cheering at my highs and standing as a rock at my lows. For that, I am most grateful.

In the Grabow Group, I have had an excellent experience with almost everyone who has stepped foot in our group. I am proud to say that I entered our group with my fellow graduate students as colleagues and now exit the group as friends. Academically, I am grateful for Drs. Hieu Doan, Byeongjin Baek, and Sashank Kasiraju for initially showing me the ropes in computational modeling. Dr. Yuying Song was instrumental in my understanding of microkinetic modeling, Dr. Shengguang Wang taught me the basics of kinetic Monte Carlo and trendlines, and Dr. Juan Manuel Arce Ramos provided me useful scripts to develop figures. In the present group, I am grateful for (soon-to-be Dr.) Hari Thirumalai for general catalysis discussions, Xiao Li for her assistance in kinetic Monte Carlo, and Karun Kumar Rao for working alongside me in machine learning and regression model development. I have also had the wonderful opportunity to mentor undergraduate students. Charlie Chirino was my first mentee, and we developed our understanding of DFT together. I inherited Lucas Von Ruff from the departing Dr. Hieu Doan, and he sparked my own personal interest in different catalytic applications because of his incessant interest. Cindy Mai began with two summers as a high school student through ACS Project Seed, and I learned through her how to teach my own research. James

Sutjianto was my fourth mentee, and I appreciated how he fully integrated into our group and attended everything that I set up. Lastly, Khoa Pham, my final undergraduate student, was one of the best coders I have ever met and performed the underlying DFT calculations in Chapter 6, as well as the exploratory machine learning calculations in that chapter.

Within the chemical engineering department at the University of Houston, I must thank Drs. Michael Harold and Praveen Bollini for serving on my various defense committees and providing valuable feedback for research directions and improvement. An invaluable and underappreciated person within the department who I greatly appreciated was Nicolette Solano, who was such a lifesaver for both the littlest and the biggest of things. Yolanda Thomas was also always there to make sure my PhD always sailed smoothly. In the electrical engineering department, I thank Dr. Paul Ruchhoeft for serving on both my master's and PhD committees.

I had the fantastic opportunity to spend six months at SABIC on an internship through the NSF. In particular, Travis Conant, Kaiwalya Sabnis (who served on my defense committee), and Kevin Bazazzadeh not only were excellent mentors for me, but they reinforced my desire to be just like them in my career.

Lastly, none of this would have been possible without the best advisor possible. Lars has been a godsend to me both personally and academically. He has allowed me to pursue my passions in and outside of research, I have had the opportunity to take on leadership and mentorship opportunities, and I was given the chance to take six months off to intern at SABIC. There are so many horror stories about graduate students and their advisors; I only have positive things to say. While I look forward to the future, I remain sad that it is time to go. I am honored to have been a part of his group for five years.

Abstract

Catalytic dehydrogenation, or the selective removal of hydrogen from hydrocarbons, is an economically-driven process. In general, all dehydrogenation processes share the same two difficulties. First, non-oxidative dehydrogenation is difficult. C-H bonds are strong and the dehydrogenation process is endothermic, indicating both the kinetic and thermodynamic challenges of these reactions. Second, even if the kinetic and thermodynamic obstacles are overcome, only the partial dehydrogenation of the reactant molecule is usually desired. The complete removal of hydrogen from a hydrocarbon reactant is unwanted because it leads to the formation of catalyst-deactivating coke. Therefore, the key to unlocking selective dehydrogenation is finding an effective catalyst that rises above the activity challenges of the reaction, yet remains selective to the desired product.

Recently, a class of catalysts known as single-atom alloys has attracted attention. These single-atom alloys consist of a highly active, isolated promoter atom that sits within the surface of a less-active host metal. A reactant would dissociate on the promoter atom and the resulting intermediates would diffuse away to the host metal, where it binds weaker and can desorb or undergo further chemistry. In our theory-driven work, we begin by examining the efficacy of these single-atom alloys. First, we find that they outperform the best literature monometallic catalyst in breaking the strong triple bond of N_2, which is the rate-determining step of the Haber-Bosch process. We also determine that isolated palladium atoms in gold surfaces can actively and selectively dissociate methane for further upgrade in both non-oxidative and oxidative mechanisms. We then perform stability tests

for all combinations of metals to determine which combinations are stable as single-atom alloys.

Finally, we introduce a new paradigm that couples multi-faceted density functional theory and kinetic Monte Carlo to rationally design and optimize the size, shape, and promoter metals of a catalyst nanoparticle. As a case study, we examine the dehydrogenation of methanol to formaldehyde on silver and determine that small, cubic nanoparticles decorated with zinc or palladium promoters would optimize the reaction. Our paradigm can be extended to any catalytic reaction on metal surfaces and offers a bridge between computational and experimental catalysis.

Table of Contents

List of Tables

List of Figures

Chapter 1. Introduction

1.1. Catalytic Dehydrogenation

The general objective of any industrial process is quite basic: to turn a reactant into a higher-value product. While these billion-dollar ventures are highly complicated mazes of unit operations, the key step of many industrial plants involves the removal of the simplest atom, hydrogen. The primary example of an industrial reaction that involves the removal of hydrogen is catalytic dehydrogenation, where hydrogen molecules are removed from a hydrocarbon, often to convert single bonds into double bond, or paraffins into olefins, and can be generalized as

$$C_xH_yO_z \rightarrow C_xH_{y-2}O_z + H_2. \quad (1)$$

From organic chemistry, the π bonds in the olefinic products are more available for further reactions, including hydration, halogenation, oxidation, alkylation, olefin metathesis, epoxidation, and polymerization.

To provide a case study, a classic example of a dehydrogenation reaction is the dehydrogenation of propane to propylene in the reaction

$$C_3H_8 \rightarrow C_3H_6 + H_2. \quad (2)$$

Historically, propylene has been produced primarily through hydrocracking and steam cracking. As the United States continues to move away from crude oil and towards lighter shale gas, however, propylene supply began to dwindle because fluidized catalytic cracking throughput decreased and smaller feedstocks were used in steam crackers. Since propylene remained in high demand because of its status as a precursor to polypropylene, the second-most produced polymer after polyethylene, an on-demand reaction to form propylene was needed. As such, the propane dehydrogenation (PDH) reaction has seen a dramatic rise in

the 21st century, and more than 2 million metric tons/year of new PDH capacity came online between 2010-2015.[1] The rise of the PDH reaction has partially led to a greater push in understanding the behaviors seen in catalytic dehydrogenation reactions.

The hydrogen atoms of the reactants, such as propane, can be removed either non-oxidatively, seen in Equation 1, or oxidatively. In the oxidative mechanism, oxygen is co-fed with the hydrocarbon reactant and abstracts hydrogen to form water, and can be generalized in the reaction

$$C_xH_yO_z + \frac{1}{2}O_2 \rightarrow C_xH_{y-2}O_z + H_2O. \quad (3)$$

For instance, the oxidative dehydrogenation (ODH) of propane follows the reaction

$$C_3H_8 + \frac{1}{2}O_2 \rightarrow C_3H_6 + H_2O. \quad (4)$$

In all cases of dehydrogenation, the non-oxidative route results in an endothermic reaction, while the oxidative route leads to an exothermic reaction due to the formation of water rather than dihydrogen, which has an enthalpy of formation of zero. In many cases then, including PDH, the oxidative pathway for the dehydrogenation of hydrocarbons is the more-studied pathway of the two, primarily because the oxidative route is much more favorable at lower temperatures than the non-oxidative one.[2] This can be seen in the different routes of the PDH reaction. For a given catalyst, such as Mo-Ni/Al_2O_3 catalysts, the oxidative dehydrogenation is preferred at temperatures lower than ~550°C, whereas the non-oxidative dehydrogenation reaction is preferred at temperatures above 550°C.[3] The presence of oxygen in the feedstream leads to a higher conversions at lower temperatures, and since chemical plants would prefer to run at lower temperatures and higher conversions, the oxidative dehydrogenation route presently tends to dominate in industry.[2]

There are considerable drawbacks for the oxidative dehydrogenation route, however, causing the difficult non-oxidative route to remain well-researched as a pipe dream for many industrial reactions. While higher oxygen partial pressures lead to higher conversions of reactant to product, selectivity tends to suffer, as more CO and CO_2 are produced.[3–6] The drop in selectivity to desired products precludes many oxidative processes from being industrialized, including the oxidative coupling of methane, which will be further discussed in Chapter 3.1. Furthermore, many oxidative processes require pure oxygen to improve selectivity; for instance, in the oxidative dehydrogenation of ethane to ethylene, the replacement of air (21% oxygen) with pure oxygen causes a selectivity jump of over 30 percentage points for various mixed metal oxides and membrane reactors.[7] Not only would the use of excess air lead to greater capital and energy costs, but the necessary purification of oxygen feedstreams is an expensive venture. Lastly, while the primary objective of any industrial process is to maximize the output of the desired product, the oxidative dehydrogenation process contains water as a co-product, whereas the non-oxidative dehydrogenation process contains H_2 as the co-product. H_2 is a highly valuable gas and can be burned for energy or fuel, used as a feedstock in other operations, or sold to other chemical producers. The implementation of any oxidative process would then minimize the return of the valuable H_2 byproduct.

While there are advantages to removing oxygen from the reactant feedstream, there are also many pitfalls that come along with non-oxidative dehydrogenation. As mentioned above, higher temperatures are needed to perform the reaction. This is largely due to the strong C-H and O-H bonds in the hydrocarbon reactants.[8] A catalyst for the non-oxidative reaction would need to directly break the C-H and O-H bonds, whereas oxygen or other

reactant species can assist in the bond scission in the oxidative scheme; more studies are discussed for oxygen-assisted dehydrogenation in Chapter 3. The higher temperatures needed to non-oxidatively dehydrogenate paraffins and light hydrocarbons lead to high energy costs, corrosion issues for the reactor, and sintering of the catalyst particles. Furthermore, at such high temperatures, the deep dehydrogenation, or the complete removal of hydrogen from the reactant species, is often favored, leading to the formation of coke species;[4] the tendency of reactants to undergo deep dehydrogenation is further discussed in Chapter 3.3. Thus, while oxidative dehydrogenation schemes have an issue with lower selectivities, non-oxidative dehydrogenation reactions are victimized by poor conversion values.

In catalytic dehydrogenation reactions, further problems can also arise after the paraffin or hydrocarbon have been dehydrogenated. The desired olefinic products are much more reactive than their precursors and can undergo hydrogenolysis, cracking, or isomerization, which greatly affect the product composition and selectivities by introducing new byproducts.[6] Therefore, in catalytic dehydrogenation, an optimal catalyst or reaction would optimize both conversion and selectivity while avoiding the complex byproduct formations that may result from the presence of highly reactive olefinic products.

1.2. Innovative Catalyst Surface Strategies

A single reaction on a heterogeneous catalyst, in its totality, is a highly complex system with myriad combinations of phenomena that come together to turn reactants into products. Due to its incredible complexity, it is necessary to identify trends and properties

that would yield high catalytic activity. These trends are in many cases captured by simpler property descriptors, thus allowing for the simplification of a difficult problem to a simple trendline. These trendlines, heavily examined by the group of Nørskov,[9–18] suggest that catalytic activity may be proportionally or inversely related to certain descriptors. For instance, one of the first studies involving descriptors, known as the Brønsted-Evans-Polanyi (BEP) relation, states that there is a linear relationship between the activation energy and the reaction energy of an elementary reaction step.[19,20] The BEP relation marries the concepts of kinetics (activation energy) and thermodynamics (reaction energy) by suggesting that favorable thermodynamics would yield favorable kinetics as well. The BEP relations were first quantitatively examined for the Haber-Bosch process,[18,21] where ammonia is formed from its constituent nitrogen and hydrogen gases; more background on the Haber-Bosch process is discussed in Chapter 2.1. The researchers indeed find that the activation energy and reaction energy are linearly related for the rate-limiting step, which is the dissociation of the N_2 triple bond. Furthermore, the authors find that the binding energy of a single N adatom can be used as a descriptor in predicting catalytic activity; a stronger, more negative binding energy for a single N adatom on a catalyst surface yields a lower activation energy barrier. Similarly, dehydrogenation reactions can be treated using descriptors and scaling relations as well. Wang and coworkers examined over 200 dehydrogenation mechanisms of small molecules on close-packed catalyst surfaces and found that the respective reaction energies and activation energies for the individual dehydrogenation reactions are linearly related.[16] In addition, when considering the dehydrogenation of H_2O, NH_3, and CH_4, the researchers found that the adsorption energy of the dehydrogenation reaction intermediates also linearly corresponded to the activation

energy, as shown in Figure 1. As the intermediates bound to the surface stronger, ie. with a lower binding energy, the transition state energy was also found to be lower.

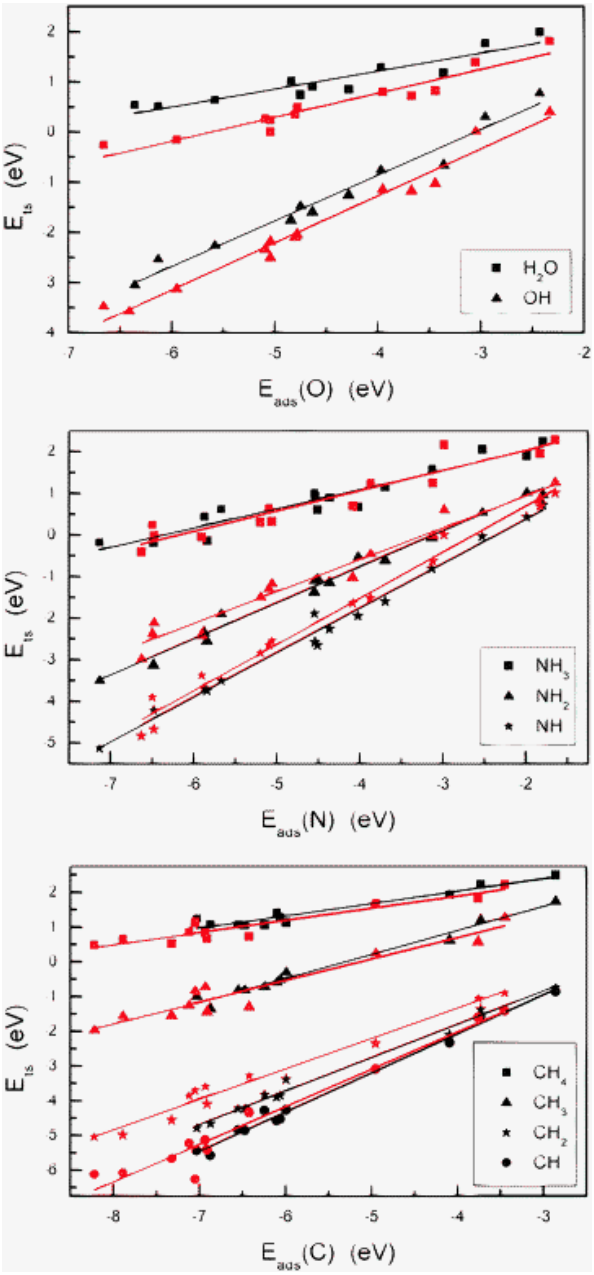

Figure 1. The transition state energies of dehydrogenation reactions plotted vs. the binding energies of reaction intermediates, from Wang et al.[16] The linear relationships suggest that as adsorption becomes stronger, the activation energy decreases.

From the linear scaling relations, it may seemingly follow that in order to improve the kinetics of a catalytic reaction, a catalyst surface that binds the intermediates very

strongly should be selected. Contrary to expectations, however, a catalyst surface that binds intermediates too strongly would also hinder the reaction from obtaining its maximum yield. In the 1910s, Sabatier suggested that the best catalysts should not bind reactants too weakly, as the catalyst would fail to activate the reactant, nor should they bind reactants too strongly, as the product would be unable to desorb from the catalyst surface.[22] Thus, there is an optimal, intermediate binding strength for adsorbates on catalyst surfaces; this concept is known as Sabatier's principle and is depicted in Figure 2.

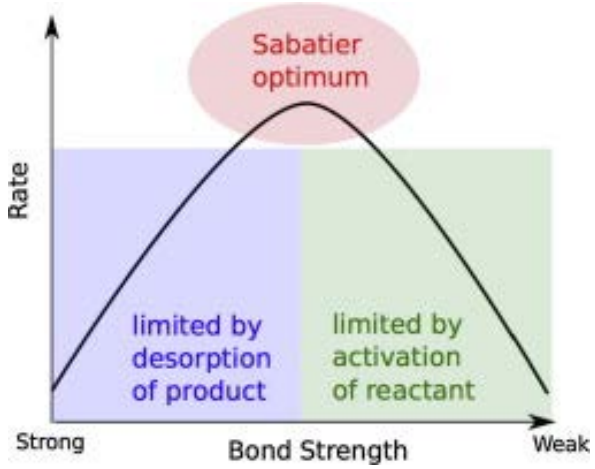

Figure 2. An illustration of Sabatier's principle, from Nørskov and coworkers.[14] There is an optimal, intermediate binding strength for any given reaction and intermediate.

While it is a qualitative concept, Sabatier's principle has been demonstrated in many quantitative works by plotting reaction rates against intermediate binding energies,[23–25] such as in the Haber-Bosch reaction[14] discussed above; the role of Sabatier's principle in guiding a large research direction in this dissertation will be discussed in Chapter 2.1. By creating similar plots, or activity volcanos, for dehydrogenation reactions, the optimal binding strength for an intermediate, or any other descriptor, can be determined.

Without considering any financial implications, a single-metal catalyst that sits atop the activity volcano for a given reaction would be ideal. This is rarely the case, however, that a monometallic surface would reach the Sabatier maximum. An alternative rational approach to approach the peak of Sabatier's activity volcano is by alloying two monometallic catalysts. A combination of a metal that binds an intermediate too weakly with one that binds the intermediate too strongly would potentially yield an alloyed bimetal that is closer to the optimum binding energy. This has been demonstrated in cases such as Co-Mo catalysts for the Haber-Bosch reaction,[14,21,26] Ni-Fe catalysts for methanation,[27] and Pt-Bi catalysts for the hydrogen evolution reaction.[28,29]

The activity volcano shown in Figure 2 plots the reaction rate against a single descriptor, the binding strength of an adsorbate on the catalyst surface. The single descriptor can be replaced by any other descriptor as long as the two descriptors can form a scaling relation between the two; for example, since the binding strength of an adsorbed species linearly corresponds to the transition state energy of the reaction, the x-axis of Figure 2 can be replaced with a transition state energy scale. The limitations of using a bimetallic alloy catalyst can be shown, however, when a multidimensional activity volcano is drawn, such as when the reaction rate is depicted as a function of two or more descriptors.

In Figure 3 below, taken from the work by Nørskov and coworkers,[30] an activity volcano is depicted for the electroreduction of CO_2 to CO. In this volcano, there are two descriptors: the adsorption energy of the CO intermediate and the adsorption energy of the COOH intermediate. The electrocatalytic activity is logarithmically represented by the colors given in the color bar on the right-hand side of the figure and is calculated using microkinetic modeling; microkinetic modeling is explained, performed, and analyzed in

Chapters 2 and 5 in this dissertation. The transition metals are represented by circles, while naturally-occurring, non-industrial enzymes are represented by the green triangles. A trendline is drawn to represent the expected activity of a metal, non-enzyme catalyst. Overall, from the activity volcano, the most active catalysts for the reaction are the two enzyme catalysts. Au and Cu are the best catalysts for the transition metals, but their activities are two orders of magnitude lower than that of the enzymatic catalysts. The strategy of alloying two monometallic catalysts would not work either; a bimetallic alloy of any two transition metals would remain on the trendline, and the trendline does not cross the peak of the activity volcano. Therefore, for this reaction and various other reactions, the traditional strategy of alloying to form conventional bimetallic alloys would not optimize the possible activity. Other design strategies are needed to develop a catalyst that would obtain the highest activity possible.

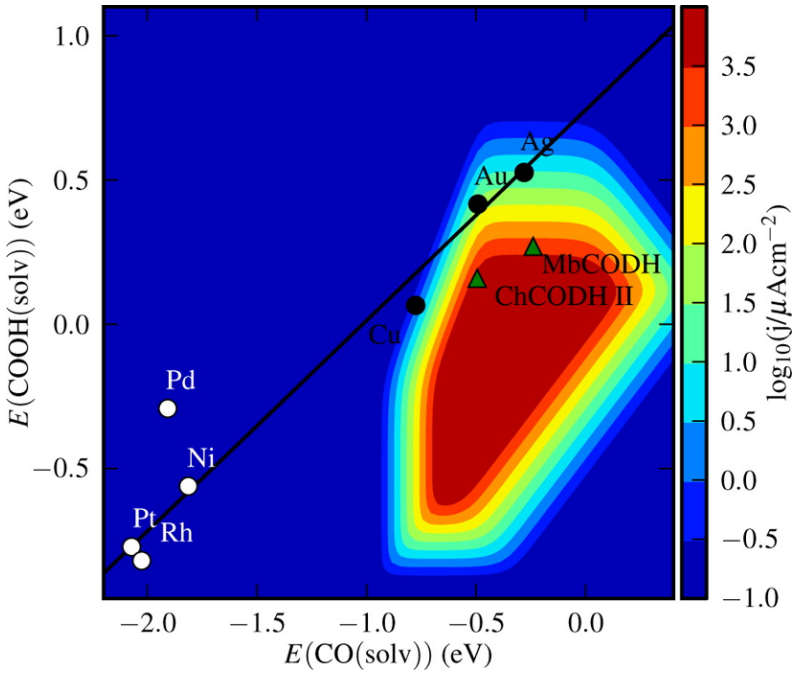

Figure 3. The activity volcano for the electroreduction of CO_2 to CO. The trendline for the metal catalysts never passes through the peak of the activity volcano, indicating that traditional catalyst design strategies would not optimize the reaction rate.

Since catalysis occurs on the active sites of a catalyst surface, new design strategies that circumvent the scaling relations and break the trendlines must start there. In Figure 4, from Vojvodic and Nørskov,[13] a schematic is depicted suggesting that a catalyst surface can break the scaling relations by adding a structural or electronic effect, shown on the x-axis of an idealized parameter space, or by adding an intrinsic or extrinsic effect, shown on the y-axis of the same space. In the work of this dissertation, we examined some of these design strategies to circumvent the scaling relations that are seen in dehydrogenation catalysts. In particular, we heavily examine doping and promoters, discussed in Chapters 1, 2, 3, 6, and 7; co-adsorption, discussed primarily in Chapter 3; and surface faceting and nanostructuring, examined in Chapters 4 and 5.

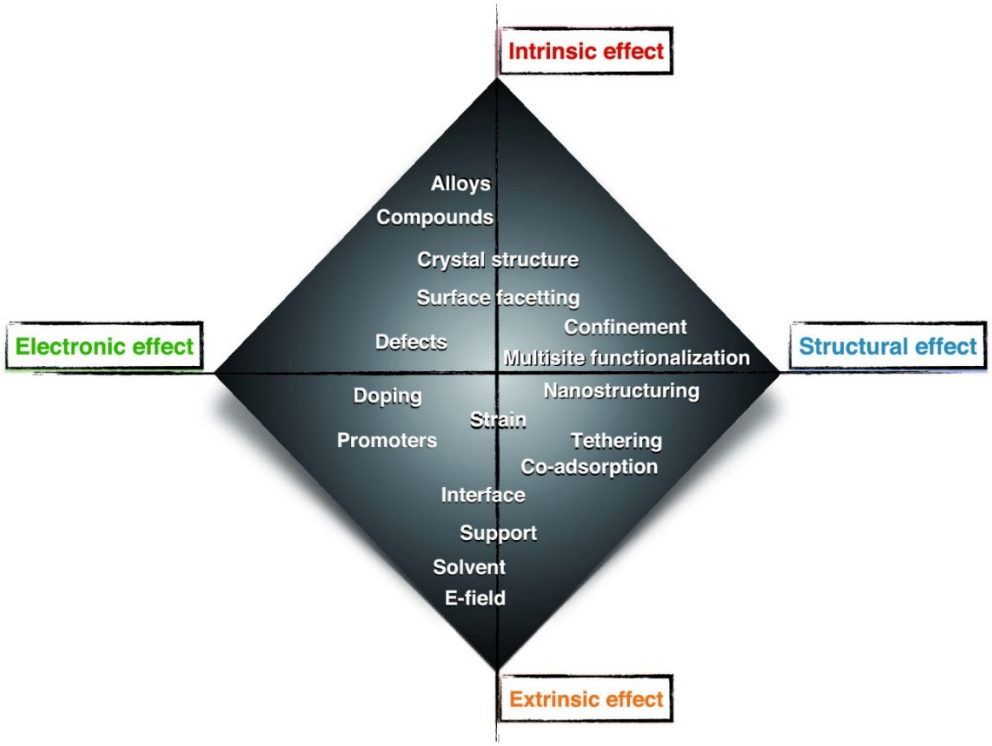

Figure 4. An idealized parameter space suggesting different strategies to alter active sites in order circumvent scaling relations. Taken from Vojvodic and Nørskov.[13]

1.3. Single Atom Alloys

A primary reason that bimetallic catalyst surfaces largely fail to circumvent the scaling relations is the homogeneity of the "well-mixed" catalyst surface.[12] In general, the adsorption energies on a bimetallic catalyst are just interpolations of the adsorption energies on its constituent monometallic surfaces,[12] and adsorbates experience the ligand effect, which affects binding energies through electronic interactions.[31,32] Homogeneously mixed bimetallic surfaces, however, tend to fail to truly use the ensemble effect, where two different active sites physically exist and work in geometric synergy to kinetically affect the reaction.[12,31,32] An alloyed catalyst surface that is non-uniform might take greater advantage of the ensemble effect and break the aforementioned scaling relations instead.

In the early 1990s, Nørskov and coworkers found through scanning tunneling microscopy that when Au is deposited on Ni(110), an Au monolayer covers the surface of the Ni surface, partially because Au is immiscible in Ni bulk.[33] This concept of forming monolayers was adapted by many researchers to weaken binding energies, such as Pt monolayers on Ru(0001) to decrease the adsorption energy of carbon monoxide,[34] Ni overlayers on Pt(111) for hydrogen,[35] and V overlayers on Pd(111) and Rh(111) for CO.[36] These surfaces containing an overlayer of one metal on top of another metal were coined "near surface alloys" (NSAs) by Greeley and Mavrikakis,[37,38] who found that these surfaces contain a distinct property; in H_2 activation, these catalysts bind H_2 weakly, yet dissociate the H-H bond readily at lower temperatures. This directly contradicts the scaling relations that suggest that stronger binding energies yield lower activation energies, which indicates that NSAs are a potential strategy to circumvent the established trendlines.

A considerable issue that NSAs face is that they are difficult to synthesize, as the monolayer amounts of added dopant tends to mix with the bulk host metal.[39] From density functional theory calculations on Pt NSAs, under vacuum conditions, the only systems that are stable are Ag/Pt(111) and Au/Pt(111) NSAs, where Ag and Au are monolayers on top of the Pt core.[40] Otherwise, the alloyed metal prefers to reside in the subsurface. Under acidic, alkaline, and oxygen reduction reaction (ORR) conditions, only Pt/Rh and Pt/Pd NSAs are stable, with Pt as the overlayer.[40] Therefore, while NSAs and core-shell particles are a promising subset of catalysts that could circumvent the scaling relations, they are limited by their lack of stability and difficulty in synthesis.

The extreme limit of the ensemble effect is reached by reducing the active site to its smallest size possible, a single atom. Single-atom catalysis has grown rapidly over the past decade and has become a major research topic due to improved catalytic conversions and selectivities.[41–44] In this dissertation, I will focus primarily on a class of single-atom catalysts known as single-atom alloys (SAAs), which consist of a single, isolated dopant atom that is dispersed in the surface layer of another metal. Generally, the single dopant atom, or the "promoter" atom, is a metal that is highly reactive for the target reaction and binds the reaction intermediates strongly, while the bulk metal, or the "host" metal, is a metal that is much less reactive for the target reaction and binds the reaction intermediates weakly. On these SAA surfaces, the reactant molecule dissociates on the promoter site. The subsequently formed reaction intermediates bind in sites that are shared by both the promoter atom and the adjacent host metal atoms. Eventually, the intermediates are entropically driven to diffuse or "spill over" to sites that consist of only weakly-binding host atoms, where it is easier for the reaction intermediates to desorb from the surface.[45]

Figure 5 below, taken from Sykes and coworkers,[45] depicts how these SAAs escape the BEP relations by combining low activation energy barriers on the reactive promoter atom with weak binding on the host metal sites. Figure 5 also includes a model cartoon that indicates how these SAAs would dissociate a reactant.[45]

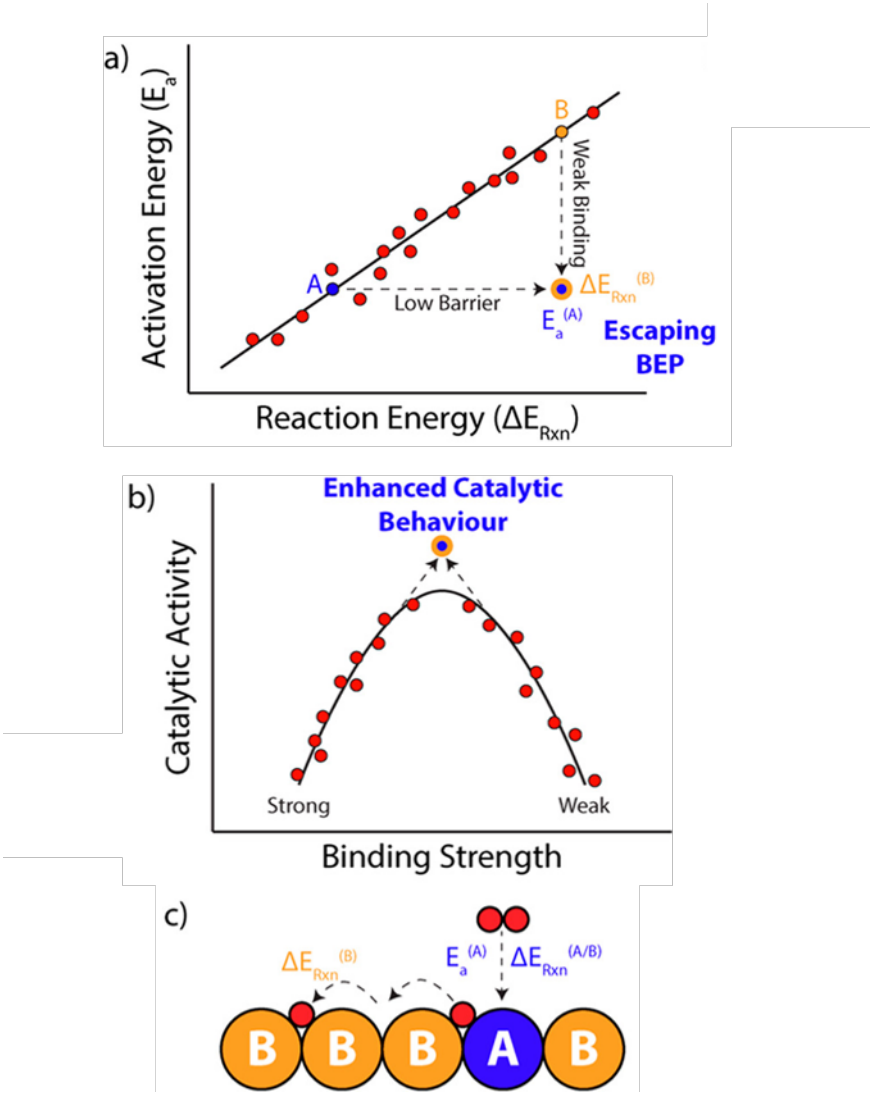

Figure 5. (a) A diagram indicating that the SAAs break linear trends by combining low barriers with weak binding. **(b)** The SAAs extend beyond the traditional optima of activity volcanos. **(c)** SAAs dissociate reactants and spill them over.

A key aspect of SAA surfaces is that adsorbates can diffuse away from the strong-binding promoter site and onto weaker-binding host sites, where they can desorb or undergo further reactions. A considerable issue of this key aspect, however, is that the spillover from the strong-binding site to the weak-binding one is energetically difficult. The entropic driving force for this phenomena, derived in the Supporting Information in a work by Sykes and coworkers, is derived in Chapter 1.4.

These SAA surfaces, heavily championed by the groups of Sykes and Flytzani-Stephanopoulos, have been investigated for many other reactions, including hydrogenation,[46–50] dehydrogenation,[51,52] oxidation,[53,54] and reduction [55,56] reactions. They also prove to be economically promising catalysts because they minimize the amount of precious metal used in the catalyst.[57] In this dissertation, in Chapter 2, I begin by probing the efficacy of SAA surfaces in the Haber-Bosch reaction, which is a reaction that has not yet been exclusively studied on SAA catalysts. In Chapter 3, I examine the $Au_3Pd(111)$ surface, which contains a surface geometry that is reminiscent of SAA catalysts, for dehydrogenating methane both non-oxidatively and oxidatively. In Chapter 6, I delve into the stability of these SAA surfaces and provide a table that indicates that there are many different SAA surfaces that are stable. Finally, in Chapter 7, I combine my examination of methanol dehydrogenation on Ag nanoparticles in Chapters 4 and 5 with SAA surface strategies and find marked improvement on bond scission activity on two particular surfaces. In the chapters listed above, more background exposition is given in their respective introductions for specific cases of SAA catalysts.

1.4. Spillover of Adsorbates on Single-Atom Alloys

A key aspect of SAA surfaces is that adsorbates can diffuse away from the strong-binding promoter site and onto weaker-binding host sites, where they can desorb or undergo further reactions. A considerable issue of this key aspect, however, is that the spillover from the strong-binding site to the weak-binding one is energetically difficult. In the Supporting Information of a work by Sykes and coworkers, it is argued that the diffusion from the promoter to the host site is entropically driven.[45] In Figure 6 below, taken from the SI of Sykes et al., the energetic values of $-E_1$ and $-E_2$ are defined as the binding energies of the adsorbate onto the host and promoter sites, respectively.

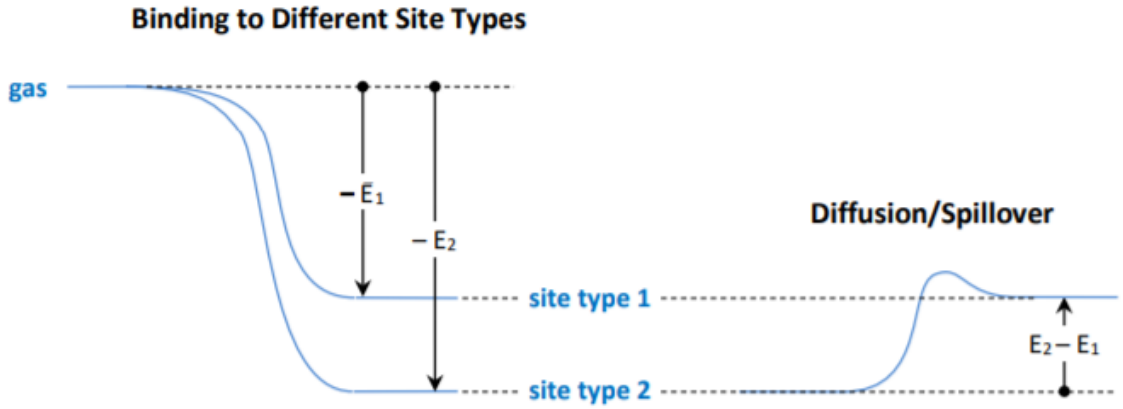

Figure 6. A diagram indicating energetic values for the adsorption of any given adsorbate on the host and promoter sites of a single-atom alloy.

To determine the free energy driving forces of the spillover to weaker-binding sites, a grand canonical ensemble is assumed, where chemical potentials are represented by the symbol μ. The total energetics of a given site are defined as

$$\varepsilon_i = i * -E_i, \quad i = 0,1, \dots, m_i, \tag{5}$$

where ε_i is the energy of a given microstate, m_i is the total number of sites of type i, and E_i is the adsorption energy, which is negative in Equation 5 to indicate that it is exothermic.

The degeneracy (ω) of each energy level is then derived. Since there are two distinguishable sites, there are mC_i ways to generate a microstate with a given ε_i, or

$$\omega_i = \binom{m_1}{i} = \frac{m_1!}{(m_1-i)!\cdot i!}. \quad (6)$$

Therefore, the partition function (Ξ_i) of the adsorbates on a site type i is

$$\Xi_i = \sum_{i=0}^{m_1} \omega_i \cdot \exp\left(-\frac{\varepsilon_i-\mu\cdot i}{k_B T}\right) = \sum_{i=0}^{m_1}\binom{m_1}{i} \cdot \exp\left(\frac{i\cdot(E_i+\mu)}{k_B T}\right), \quad (7)$$

where k_B is the Boltzmann constant and T is temperature. From the binomial theorem, which states that

$$(1+x)^n = \sum_{k=0}^{n}\binom{n}{k}\cdot x^k, \quad (8)$$

the partition function can then be rewritten as

$$\Xi_i = (1+\exp\left(\frac{E_i+\mu}{k_B T}\right))^{m_i}. \quad (9)$$

Thus, the grand potential Φ_G of an adsorbate on site type j = 1,2 can be defined as

$$\Phi_{G,j} = -k_B T \ln \Xi_j, \quad (10)$$

or

$$\Phi_{G,j} = -k_B T m_j \ln(1+\exp\left(\frac{E_j+\mu}{k_B T}\right)), \quad j = 1,2. \quad (11)$$

From Equation 11, it can be seen that the grand potential Φ_G is proportional to the number of sites, m_j. If the host sites are given as j = 1 and promoter sites are j = 2, m_1 is much greater than m_2 by the definition of single-atom alloys, which causes the equilibrium to shift towards the host sites. While E_2 is greater than E_1 due to the stronger-binding on the promoter site, the difference is assumed to be small, especially when considering the difference between the multiplicities of the two site types.

1.5. Density Functional Theory

Density functional theory, or DFT, has been firmly entrenched as a powerful research tool over the past 25 years.[58] Since 1990, the number of research publications per year based on "density functional" or "DFT" has exponentially increased, as shown in Figure 7.[58]

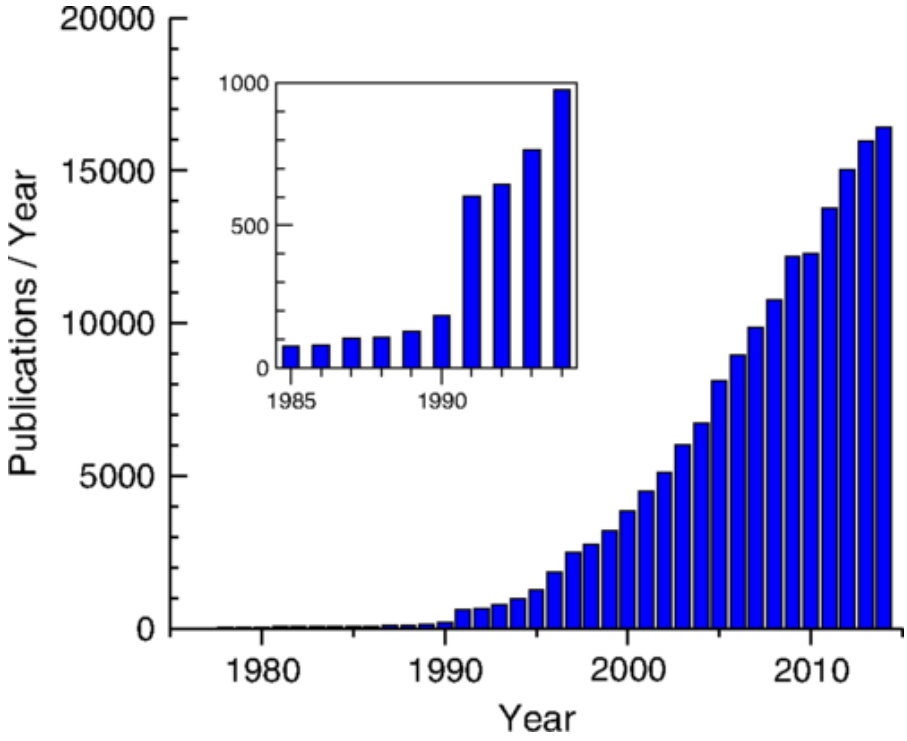

Figure 7. The exponential growth of publications per year based on DFT.[58]

Density functional theory is widely used now throughout the catalysis field because it allows for the calculation of the total energy of a system, which then yields the system's structure and various other properties, all without any experimental input.[58] While detailed explanations can readily be found in reviews[58,59] and textbooks,[60,61] this section will provide a brief summary of the steps taken in DFT calculations.

A seemingly simple equation that provides information on the total energy of a system is the time-independent, nonrelativistic Schrödinger equation,

$$H\psi = E\psi, \tag{12}$$

where H is the Hamiltonian operator, Ψ is the product of individual electron wavefunctions and the set of solutions of the Hamiltonian, and E is the ground-state energy of the system. To solve a system with N electrons, the Hamiltonian operator in the Schrödinger equation must be expanded, yielding the more complete, time-independent Schrödinger equation without considering electron spin,

$$\left[-\frac{\hbar^2}{2m}\sum_{i=1}^{N}\nabla_i^2 + \sum_{i=1}^{N}V(\boldsymbol{r}_i) + \sum_{i=1}^{N}\sum_{j<1}U(\boldsymbol{r}_i,\boldsymbol{r}_j)\right]\psi(\boldsymbol{r}_1,\dots,\boldsymbol{r}_N) = E\psi(\boldsymbol{r}_1,\dots,\boldsymbol{r}_N), \tag{13}$$

where, within the Hamiltonian operator, the first term is the kinetic energy of each electron, the second term is the interaction energy between each electron and the atomic nuclei, and the third term is the interaction energy between two different electrons.[60] Furthermore, the wavefunction Ψ is a function of the spatial coordinates $\boldsymbol{r}$ of each of the electrons. Just a cursory examination of the equation leads to immediate issues though. A single O_2 molecule contains 16 electrons, and since there are three spatial dimensions per electron, the wavefunction is then dependent on 48 dimensions. A 3x3x4 slab of silver atoms contains 1,692 electrons, or 5,076 spatial dimensions. Even worse, the wavefunction of an individual electron cannot be determined without simultaneously considering the other electrons in the system due to the final term of the Hamiltonian operator, which defines electron-electron interactions.[60] This difficult issue, then, makes the Schrödinger equation a many-body problem.[60]

The wavefunction contains extraneous information though, because electrons are indistinguishable, and the only measurable quantity is the density of electrons at a particular position in space,

$$n(\boldsymbol{r}) = 2\sum_i \psi_i^*(\boldsymbol{r})\psi(\boldsymbol{r}), \tag{14}$$

where $n(\boldsymbol{r})$ is the density of electrons and the term inside the summation is the probability that the electrons are at a particular set of coordinates, and the asterisk denotes a complex conjugate.[60] This quantity is useful for solving the Schrödinger equation because it reduces the number of coordinates from 3N to just three.

Various researchers attempted to build models based on this function, such as the Thomas-Fermi-Dirac model in the late 1920s,[62–64] and the Hartree-Fock-Slater model in 1951[65], but these models failed for various reasons, including slight absolute errors in energy.[59] However, in 1964, the groundwork for density functional theory was established in a paper by Hohenberg and Kohn,[66] the latter of whom went on to win a Nobel Prize for his contributions to the understanding of the electronic properties of materials. Their paper established two major theorems. The first theorem stated that the ground-state energy of the Schrödinger equation is a functional of the electron density and can be expressed as $E[n(\boldsymbol{r})]$, simplifying the Schrödinger equation to just three coordinates.[60,66] The second theorem is just as important, stating that the electron density that minimizes the total energy of the functional is the correct electron density for the Schrödinger equation.[59,60,66]

One year later, Kohn and Sham developed the equations that are the basis for DFT.[67] In their work, they described the energy functional as

$$E[\{\psi_i\}] = E_{known}[\{\psi_i\}] + E_{xc}[\{\psi_i\}], \tag{15}$$

where E_{known} is the collection of contributions from the electron kinetic energies, the electron-nucleus interactions, the electron-electron interactions, and the nucleus-nucleus interactions, and E_{XC} is the exchange-correlation functional, which contains all other quantum mechanical effects.[60,67] From their work, the one-electron Kohn-Sham (KS) equation, which is similar to the time-independent Schrödinger equation, is

$$\left[-\frac{\hbar^2}{2m}\nabla^2 + V(\boldsymbol{r}) + V_H(\boldsymbol{r}) + V_{XC}(\boldsymbol{r})\right]\psi_i(\boldsymbol{r}) = \varepsilon_i\psi_i(\boldsymbol{r}). \quad (16)$$

In the KS equation, the first potential, $V(\boldsymbol{r})$, is the known part of Equation 16 and is the same as the second term in the Hamiltonian operator of Equation 12.[60,67] The second potential, $V_H(\boldsymbol{r})$, is known as the Hartree potential, describes the Coulombic repulsion between the considered electron and the total electron density, and is defined as

$$V_H(\boldsymbol{r}) = e^2 \int \frac{n(\boldsymbol{r}')}{|\boldsymbol{r}-\boldsymbol{r}'|} d^3r'. \quad (17)$$

The third potential, $V_{XC}(\boldsymbol{r})$, describes the exchange and correlation contributions, and is defined as

$$V_{XC}(\boldsymbol{r}) = \frac{\delta E_{XC}(\boldsymbol{r})}{\delta n(\boldsymbol{r})}. \quad (18)$$

The KS equations are now circular and considered to be self-consistent, and can be solved using the following algorithm from Sholl and Steckel[60]:

1. Define the trial electron density, $n(\boldsymbol{r})$.
2. Using the trial electron density, solve the KS equations for the single-particle wavefunction, $\Psi_i(\boldsymbol{r})$.
3. Using the wavefunction from Step 2, solve for the Kohn-Sham electron density $n_{ks}(\boldsymbol{r})$ using Equation 16.

4. Compare $n(\boldsymbol{r})$ and $n_{ks}(\boldsymbol{r})$, and if the electron densities are the same within a predefined tolerance, then the density is equal to the ground-state electron density, which can be used to calculate the total energy. If they are not the same, another iteration is necessary.

The only remaining challenge was then to determine what the exchange-correlation functional was. Since the publication of the KS equations, many theorists have developed their own functionals, and John Perdew, who is responsible for many functionals, classified and illustrated the hierarchy of functionals using "Jacob's Ladder," as depicted in Figure 8.[68]

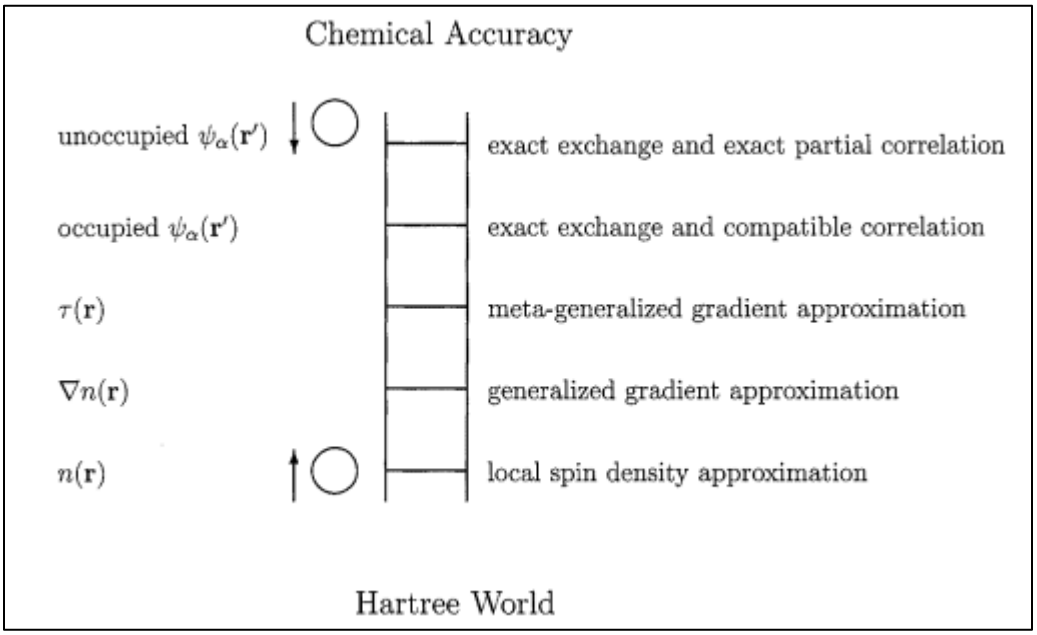

Figure 8. Perdew's "Jacob's Ladder," where higher rungs on the ladder are more accurate, but may have more constraints and be more computationally expensive.[68]

In this dissertation, multiple exchange-correlation functionals are used. In Chapter 3, the exchange-correlation functional PW91, developed by Perdew and Wang, is used.[69,70] PW91 is a generalized gradient approximation (GGA), meaning that it is not biased

towards the description of intermolecular interactions,[71] and it uses information about both the local electron density and its gradient,[60] as defined below:

$$V_{XC}^{GGA}(\boldsymbol{r}) = V_{XC}[n(\boldsymbol{r}), \nabla n(\boldsymbol{r})]. \quad (19)$$

The PW91 functional is a widely used functional because is usually more accurate than the Local Density Approximation (LDA) functionals with regards to total energies, atomization energies, energy barriers, and structural energy differences without being too computationally expensive.[72]

In Chapters 4, 6, and 7, the exchange-correlation functional PBE, developed by Perdew, Burke, and Ernzenhof, is used.[72] The PBE functional is similar to the PW91 functional, with improvements in the accurate description of the linear response of the electron gas, correct behavior under uniform scaling, and smoother potentials, and it has a simpler form and derivation, allowing for easier implementation and future improvement.[72] In Chapter 2, the revised Perdew, Burke, and Ernzenhof (RPBE) functional is used.[73] The RPBE functional improves upon the chemisorption energetics of atoms and small molecules on transition state metals.[73] When performing DFT calculations and comparing with literature results, it is necessary to ensure that the functionals used remain consistent throughout the work.

In conjunction with the PBE functional, in Chapters 4 and 7, the Bayesian error estimation functional with van der Waals correlation (BEEF-vdW) is used.[74] A drawback of the PBE functionals is their inability to capture the effects of dispersion forces, so systems including zeolite surfaces or even transition metal surfaces with local interactions suffer when calculated using PBE.[75] The BEEF-vdW functional provides a reliable description of van der Waals forces, accurately predicts chemisorption energies, and gives

an error estimation ensemble, making BEEF-vdW a powerful and reliable functional for different catalyst surfaces.[74]

In this dissertation, despite using different functionals, surfaces, reactants, products, and intermediates, all projects related to first-principles DFT follow the same general method to describe and quantify reactions on catalysts surfaces. First, after selecting the target surface, the lattice constants of the metal are optimized by varying the spacing between bulk metal atoms until a global minimum energy is obtained. The lattice constants that correspond to that global minimum energy are then compared to literature experimental lattice constants to ensure that the there is a match between theoretical and experimental results. Once the correct lattice constants have been obtained, a surface is created, with vacuum spacing made available in the *z*-direction to separate the surfaces in the periodically repeating unit cells.

To model the physisorption and chemisorption of adsorbates, first, precursor molecules must be optimized and their energies must be obtained in the gas-phase. The obtained gas-phase energies of these molecules are then the reference energies for any adsorption energy calculations. Then, all possible reactants, intermediates, and desired and undesired products are placed on all possible binding sites on the catalyst surface. The adsorption or binding energies of any given adsorbate can then be calculated by referencing the clean surface energy and the reference molecule energy in a generalized equation,

$$B.E. = E_{sys} - E_{surf} - E_{ref}, \tag{20}$$

where *B.E.* is the binding energy, E_{sys} is the energy of the entire system of adsorbate and surface, E_{surf} is the surface energy, and E_{ref} is the energy of the reference molecule. For

instance, in a study where methane is dehydrogenated, the binding energy of methyl (CH_3) can be calculated as follows:

$$B.E.(CH_3) = E_{surf+CH_3} - E_{surf} - E_{CH_4} + \frac{1}{2}E_{H_2}. \quad (21)$$

In the above equation, the binding energy of methyl is calculated by taking the energy of the system, subtracting the energy of the metal surface as well as the reference energy of gas-phase methane, and adding the reference energy of gas-phase hydrogen. Methane and hydrogen are used as the reference gases because methyl is composed of the sum of those two gases. To determine if a given binding site is globally stable for an adsorbate, frequency calculations are then performed on the adsorbates. If an imaginary vibrational mode is present in the frequencies, then the global minimum in energy has not yet been reached and further adsorption calculations must be performed.

After the most favorable binding positions for the adsorbates are ascertained, images for an initial state and a final state of a reaction must be prepared. For instance, in the first step of the dehydrogenation of methane, which follows the reaction

$$CH_4* \rightarrow CH_3* + H*, \quad (22)$$

the most stable binding positions of physisorbed CH_4 and chemisorbed CH_3* and H* must be determined. The initial state (IS) image should already be available from the optimized geometries of CH_4* physisorbed on the catalyst surface, but the final state (FS) must be generated by co-adsorbing CH_3* and H*, preferably in their most stable binding sites and positioned to minimize any translational movement between the IS and FS. Once these images have been relaxed, the activation energy barrier of the reaction is calculated by using the climbing image nudged elastic band (CI-NEB) method.[76,77] The activation energy barrier is confirmed to be a true saddle point by performing a frequency calculation on the

transition state (TS). If one imaginary vibrational mode is present and that vibrational mode corresponds with the appropriate bond breaking or forming, then the transition state is confirmed to be a true saddle point. If not, a new CI-NEB calculation must be performed with either a new pathway, interpolated images, or tighter convergences, and if this still does not yield a true TS, the dimer method must be performed.[78]

Finally, using the Atomic Simulation Environment's (ASE) Thermochemistry module, various thermodynamic values of the IS, TS, and FS can be determined using calculated vibrational modes. This allows the effects of temperature to be encapsulated in free energies. These values can then be input into various kinetic models, such as in Chapters 2, 5, and 7, and rates on the surfaces can be discerned.

Chapter 2. Exploring the Efficacy of Single-Atom Alloys for the Haber-Bosch Process

In this chapter, the efficacy of single-atom alloys is tested, and we show how single-atom alloys can follow microscopic trendlines that break macroscopic trendlines when combined together. The DFT work in this chapter was performed in conjunction with Cindy Mai, who was then a high school student who earned a summer research position through the ACS Project Seed and was my mentee, as well as Manuel Rojas, an undergraduate student who was mentored by our postdoctoral researcher, Shengguang Wang. One of the earliest examples of single-atom alloys was explored by Sykes and coworkers.[50] In their seminal work, they found that isolated Pd sites in Cu are excellent for H_2 dissociation in ultra-high vacuum (UHV) conditions. Generally, the Cu(111) surface is inert towards the dissociation of H_2 due to high activation barriers.[79] Meanwhile, on the Pd(111) surface, although H_2 dissociation is not activated due to a near-zero barrier, the resultant H adatoms bind to the Pd surface too strongly and are less available for further catalysis.[50] Sykes and colleagues found that the Pd/Cu(111) SAA has a hydrogen dissociation barrier of 0.02 eV, or nearly barrierless, while binding H adatoms to the surface at a binding energy that is closer to that of the H binding energy on Cu(111);[50] the combination of facile H_2 dissociation and weak intermediate binding circumvents the established scaling relations. The researchers depict and compare the hydrogen binding energies and activation energy barriers of the Pd(111), Cu(111), and Pd/Cu(111) surfaces in Figure 9 below.

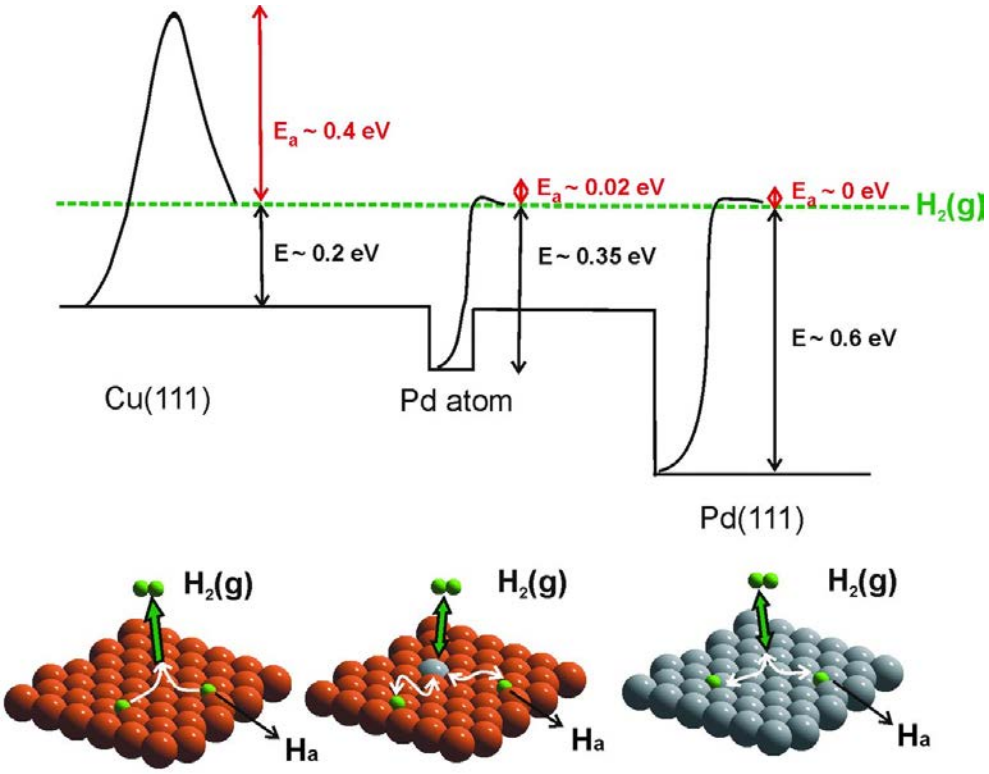

Figure 9. From Sykes and coworkers,[50] the activation energy barriers and the binding energies of H adatoms on Cu(111), Pd/Cu(111), and Pd(111), from left to right.

While there are many more examples of bond dissociations that are improved on SAA surfaces and will be discussed in the future chapters, the dissociation of H_2 is the simplest case study. In this chapter, we hope to ascertain if the SAAs can perform similarly in the dissociation of another homonuclear diatomic molecule, N_2. Of the homonuclear diatomic molecules, probing N_2 would provide the clearest contrast between the activity of a pure surface and the SAAs, since N_2 has a triple bond, the strongest bond of the homonuclear diatomic molecules. The splitting of N_2 is the rate-determining step of the Haber-Bosch process, which is a highly important reaction that currently consumes over 2% of the world's energy.[80,81] Recently, Nørskov and coworkers have explored new types of surfaces for the Haber-Bosch process.[82,83] In their work, they focus on the cobalt/molybdenum system, where cobalt is the host metal and molybdenum is the

promoter metal. They determine that a surface dimer of molybdenum in a cobalt host would optimize the reaction, but acknowledge that the Mo/Co(0001) SAA would also be effective in splitting the N_2 molecule. In this chapter, we explore different combinations of SAAs, rather than just focus on one specific combination of metals. We also introduce a microkinetic model that allows for the quantification of a rate on our surfaces. Although there are a few drawbacks of using a microkinetic model for quantifying kinetic rates on a SAA, we show that some SAAs are able to improve upon the activity on ruthenium, which is experimentally the most active monometallic catalyst for the Haber-Bosch process.

2.1. Introduction

The Haber-Bosch process, which produces ammonia from its constituent elements, has been considered one of the greatest inventions in history due to its role in fertilizer-based food production and the population explosion in the 20th century.[80,81] The important reaction, $N_2 + 3\ H_2 \rightarrow 2\ NH_3$, is industrially performed over Fe-based catalysts at high pressures (200-300 bar) and temperatures (400-500°C).[84,85] Two grand energetic and catalytic challenges exist within the Haber-Bosch process. First, the activation of the N_2 triple bond is difficult and has been shown to be the rate limiting step both experimentally[86] and theoretically.[21,87] Second, the overall process is exothermic at low temperatures, causing the reaction intermediates N*, NH*, and NH_2* to bind too strongly,[18] particularly on Ru-based catalysts. Ru-based catalysts are known to be the most active catalysts for the reaction,[88] yet are too expensive to be used industrially. Due to these two challenges, the current industrial means of performing the Haber-Bosch process requires a high temperature to reduce the reaction intermediates' binding strength, as well as a high

pressure to recoup the exothermicity that was lost when the temperature was increased.[18] Thus, it has been proposed that an optimal catalyst for the reaction would be one that both has a lower barrier for the N_2 scission and can bind the reaction intermediates weakly.[18]

Linear scaling relations have been well-established for many different catalytic reactions, which allows for an enhanced understanding of trends in catalysis. These scaling relations, such as the Brønsted-Evans-Polanyi relations,[9] indicate that metal catalysts that have lower activation energy barriers for a given reaction typically bind the reaction's intermediates strongly. Bimetallic alloys can be used to alter the reactivity of its constituent metals, but these too are governed by the established linear scaling relations.[89,90] To circumvent these scaling relations, a recent class of catalysts known as single-atom alloys have been pioneered.[45] A single-atom alloy (SAA) is comprised of a single, highly-reactive metal atom that is doped and sits within the surface of a less-reactive metal. In general, a reactant molecule would adsorb and dissociate on the single promoter atom with a low activation energy barrier. The resultant adsorbates would disperse from the promoter atom to the host atoms, where it would bind weakly, allowing for desorption or further chemistry. For instance, one of the earliest applications of SAAs in catalysis was H_2 activation on Pd/Cu(111), where Pd is the promoter atom and Cu is the host metal.[91,92] H_2 is able to dissociate on the single Pd atom and activate at lower temperatures on Pt/Cu(111) than on Cu(111), yet the H adatoms bind weakly since it is not fully surrounded by Pd atoms, limiting the ensemble effect and allowing for dispersion away from the active site. Thus, SAAs are promising options for breaking the linear scaling relations.

In this work, we aim to predict a SAA catalyst that optimizes the Haber-Bosch process. First, we examine the N_2 activation behavior of eight different metals in Figure

10, with the data adopted and re-purposed from Nørskov and coworkers.[14] From the volcano plot and by the understanding of Sabatier's principle,[22] Re, Mo, and Fe bind nitrogen too strongly and therefore are limited by the desorption of the ammonia product, but should activate N_2 quite readily. Meanwhile, Rh, Co, Ni, and Pt bind the nitrogen adatom weakly, but have low N_2 activation energy barriers. Ru sits at the top of the volcano, verifying that it is the best single-metal catalyst for N_2 activation.[88]

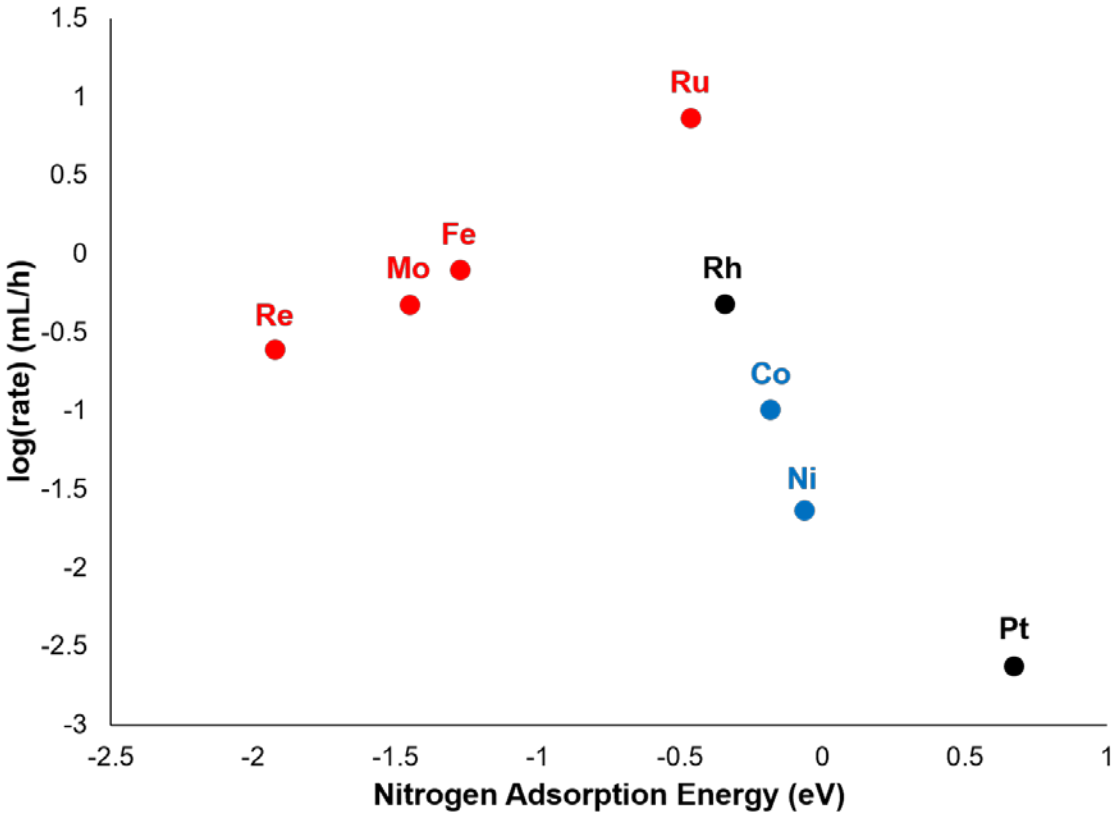

Figure 10. The volcano plot for the Haber-Bosch process. The metals colored red are considered as potential promoter atoms, the ones colored blue are host metals, and the ones in black are not considered in this study due to prohibitive costs.

Since we wish to have a promoter atom that is highly active, we consider Re, Mo, Fe, and Ru, or the elements that are colored red in Figure 10. Likewise, the host metal should bind the intermediate adsorbates weakly, so Co and Ni are considered, or the

elements that are colored blue in Figure 1. We eliminated Rh and Pt, colored black in Figure 10, from consideration as host metals because of their cost; if the price of Ru is prohibitive for use in the Haber-Bosch process, so should the price of Rh and Pt. While Re, Mo, and Ru are expensive metals as well, they will be used as single-atom promoters and comprise only 1% of the metal content, therefore potentially remaining cost-effective.[57] Thus, eight total SAA combinations were tested in this work to determine their efficacy for the Haber-Bosch process: Re, Mo, Fe, and Ru doped onto the Co(0001) surface; and Re, Mo, Fe, and Ru doped onto the Ni(111) surface.

2.2. Density Functional Theory Methods

The periodic density functional theory (DFT) calculations were performed using the Vienna ab initio Simulation Package (VASP)[93–96] in the Atomic Simulation Environment.[97] The exchange-correlation effects were described by the revised Perdew-Burke-Ernzenhof (RPBE) functional[73] using an energy cutoff of 400 eV. The core and valence electrons were represented with the projected augmented wave (PAW) method.[98,99] Gaussian smearing was used with Fermi temperatures of k_bT = 0.1 eV, and the electronic energies were subsequently extrapolated to 0 K. All geometries were optimized until the forces were less than the convergence criterion of 0.05 eV/Å.

Using an 11×11×11 *k*-point set, the optimized bulk lattice constants for Co were a = 2.514 Å and c/a = 1.623, which agree with experimental values of a = 2.514 Å and c/a = 1.633.[100] Likewise, the bulk lattice constant for Ni was calculated to be 3.553 Å, which matches with the experimental lattice constant value of 3.524 Å.[101] All surfaces were modeled as four-layered slabs with periodic (3×3) unit cells, and the bottom two layers

were fixed to their bulk positions, while the top two layers were fully relaxed. For the single-atom alloys, the center surface atom of the unit cell of Co(0001) or Ni(111) was replaced by the respective dopant atom and geometrically optimized, and their representations can be seen in Figures 11 and 12. All surface models contained a vacuum distance of 20 Å between the slabs in the normal direction. The Brillouin zone for all models were sampled by a (4×4×1) Monkhorst-Pack *k*-point set.[102]

The adsorption energies are calculated with reference to the respective clean surfaces and the gas-phase energy of N_2. The activation energy barriers were calculated using the climbing image nudged elastic band (CI-NEB) method[76] and the transition states were confirmed to be true saddle points using a vibrational analysis in the harmonic oscillator approximation, which showed one imaginary frequency along the reaction pathway.

2.3. Microkinetic Modeling Methods for the Haber-Bosch Process

The steady-state microkinetic model used to examine the Haber-Bosch process on the various SAA catalysts was implemented using CatMAP.[103] Two separate sites were defined in the microkinetic model: the host site (h) and the promoter site (p). In our model, the splitting of N_2 occurs on the promoter site. The resultant nitrogen adatoms then diffuse from the promoter site to the host sites, where it becomes hydrogenated to form ammonia. Thus, the elementary steps examined in the model are given below, where the parentheses indicate the location of the adsorbate or site.

N_2 Activation on Promoter Site

$$N_{2\,(g)} + 2*_{(p)} \leftrightarrow 2N*_{(p)} \tag{23}$$

N Diffusion to Host Site

$$N^*_{(p)} \leftrightarrow N^*_{(h)} \quad (24)$$

Hydrogenation of N to Ammonia on Host Site

$$H_{2\,(g)} + *_{(h)} \leftrightarrow 2H^*_{(h)} \quad (25)$$

$$N^*_{(h)} + H^*_{(h)} \leftrightarrow NH^*_{(h)} + *_{(h)} \quad (26)$$

$$NH^*_{(h)} + H^*_{(h)} \leftrightarrow NH_2{}^*_{(h)} + *_{(h)} \quad (27)$$

$$NH_2{}^*_{(h)} + H^*_{(h)} \leftrightarrow NH_{3\,(g)} + 2*_{(h)} \quad (28)$$

In our microkinetic model, we adopted a ratio of 99:1 for the host:promoter sites and assumed that any steps for molecular adsorption and desorption were non-activated.

The binding and transition state energies used in the N_2 activation and N adatom diffusion steps were collected from the DFT calculations in this work. Since the hydrogenation of nitrogen to form ammonia occurs on the large ensembles of host metals, it is assumed that those binding and transition state energies are equivalent to those of pure metals, and therefore, those energies are adopted from literature.[104] The frequencies of the species in the first two steps were calculated on the promoter sites, but they were found to be similar to those of the pure metals from literature, so the literature values were adopted instead to ensure consistency.[104] Entropy corrections were applied in the model using the Shomate equation for the gas-phase molecules and the harmonic approximation for the adsorbates. Frequencies were calculated on the pure surfaces and adopted for the SAA surfaces.

2.4. Results

2.4.1. Adsorption of N/N_2

The adsorption of N_2 was examined on all eight SAA surfaces, as well as on pure Co(0001) and Ni(111). From the adsorption trends seen in Figure 10 and our design of the SAAs, we expect that N_2 should bind stronger to the promoter atoms on our SAAs than on the host metals. Figures 11 and 12 compare the binding energies of N_2 on the promoter site with the binding energy of N_2 on a host atom directly adjacent to that promoter site, as well as on the respective, pure host metal surface for Co(0001) and Ni(111), respectively. The N_2 molecules geometrically relax to adsorb perpendicularly on the top sites of the metal atoms. While N_2 does bind stronger to the promoter sites than the host metals for the Mo-, Re-, and Ru-promoted Co(0001) and Ni(111) surfaces, surprisingly, it slightly prefers the host metal sites adjacent to the promoter atoms on the Fe-promoted Co(0001) and Ni(111) surfaces. This is notable particularly because nitrogen binds stronger to the pure, close-packed Fe(110) surface than the pure surfaces of Co(0001) and Ni(111).[18] In all cases, N_2 binds stronger to the preferential binding site on all SAAs than on the pure surfaces, including on the Fe-promoted Co(0001) and Ni(111) surfaces; N_2 binds stronger to the host sites on those surfaces than on their pure metal precursors.

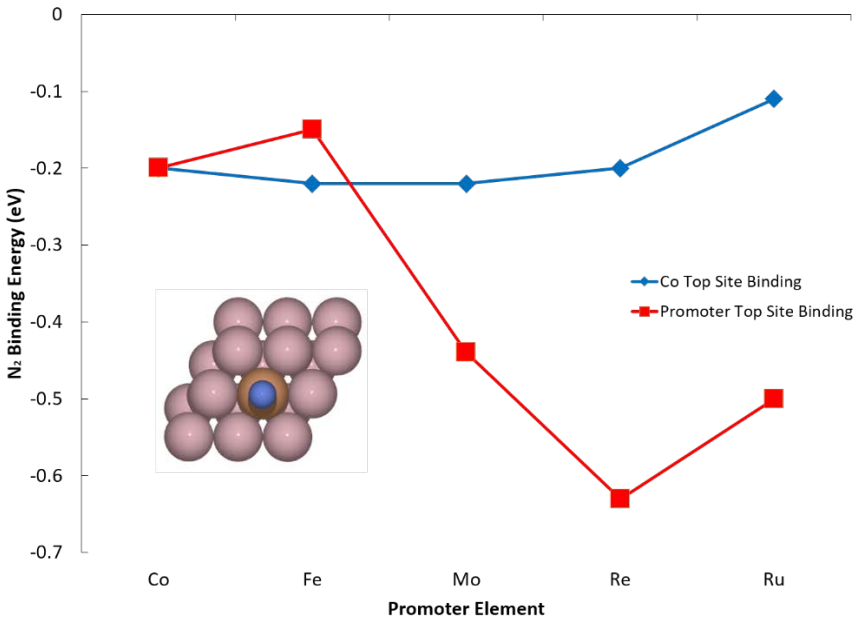

Figure 11. The binding energies of N_2 on the different sites of the Co(0001) and the Fe-, Mo-, Re-, and Ru-promoted Co(0001) surfaces. **(inset)** The binding location of N_2 on the top site of the Fe promoter on Co(0001).

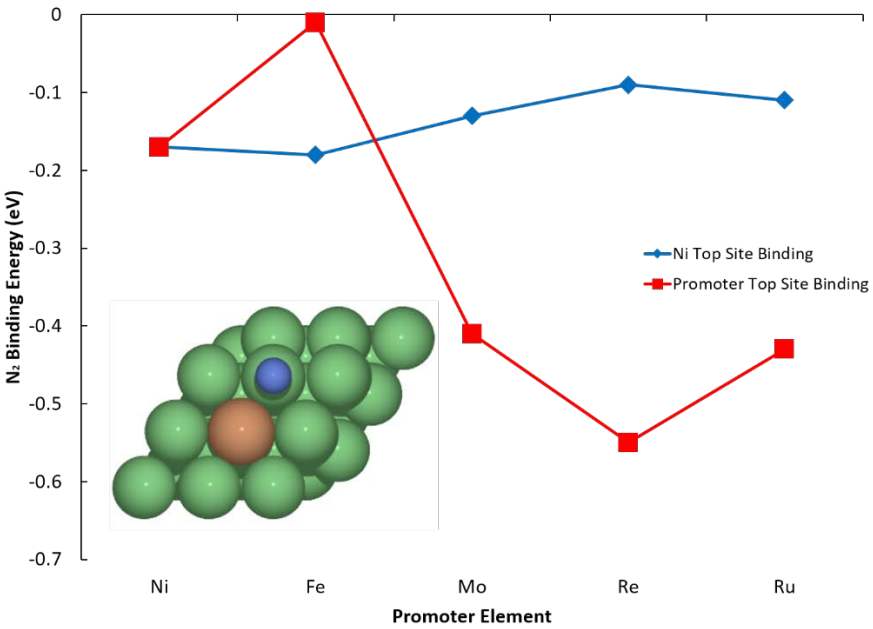

Figure 12. The binding energies of N_2 on the different sites of the Ni(1111) and the Fe-, Mo-, Re-, and Ru-promoted Ni(111) surfaces. **(inset)** The binding location of N_2 on the top site of the host metal on the Fe-promoted Ni(111) surface.

A few trends can be seen in Figures 11 and 12. First, the binding energies of N_2 on the host sites of the SAA surfaces are nearly equal to the binding energies of N_2 on the respective pure metal surfaces. This indicates that the host sites of the SAAs can adequately predict the behavior of the pure host metal, which will become relevant in the microkinetic modeling studies. In addition, for both the Co(0001) and Ni(111) SAAs, when considering only the binding of N_2 to the promoter site, the binding strength follows the trend of Re > Ru > Mo > host metal > Fe. Meanwhile, from the volcano plot showing the activities of the pure metal surfaces, nitrogen binding strength follows a trend of Re > Mo > Fe > Ru > host metal. In particular, N_2 binds much stronger than expected on Ru and much weaker on Fe. A *d*-band analysis shows that the Ru/Co(0001) and Ru/Ni(111) systems have sharper peaks near the Fermi level than the host metal, potentially indicating that the promoter site is much more reactive than its precursor, according to the *d*-band theory.[105] It is also important to note that the covalent radius of Ru (1.46 Å) is much larger than that of Co (1.26 Å) and Fe (1.32 Å),[106] possibly introducing strain effects on the surface and strengthening any adsorbate bonding.

The adsorption of a single N adatom can also be inspected. The N adatom relaxes to the three-fold sites on the metal surfaces. In Figures 13 and 14, the binding energies of the single N adatom are shown for the SAAs and the pure Co(0001) and Ni(111) surfaces, respectively. If nitrogen is bound to the “promoter” three-fold site, then it contacts one promoter atom and two host atoms, whereas if it is bound to a “host” three-fold site, then it contacts three host atoms. In all cases on the Co(0001) surfaces, N binds stronger to the promoter site than the host sites, even including the Fe-promoted Co(0001) SAA surface, where N_2 binds stronger on the Co host than on the Fe promoter site. On the other hand,

on the Ni(111) surfaces, N binds stronger to the promoter site than the host sites for all sites but the Fe-promoted Ni(111) surface. On the Fe/Ni(111), the N adatom binds stronger to the host site than the Fe promoter site, following the trend set by the adsorption of N_2 on Fe/Ni(111).

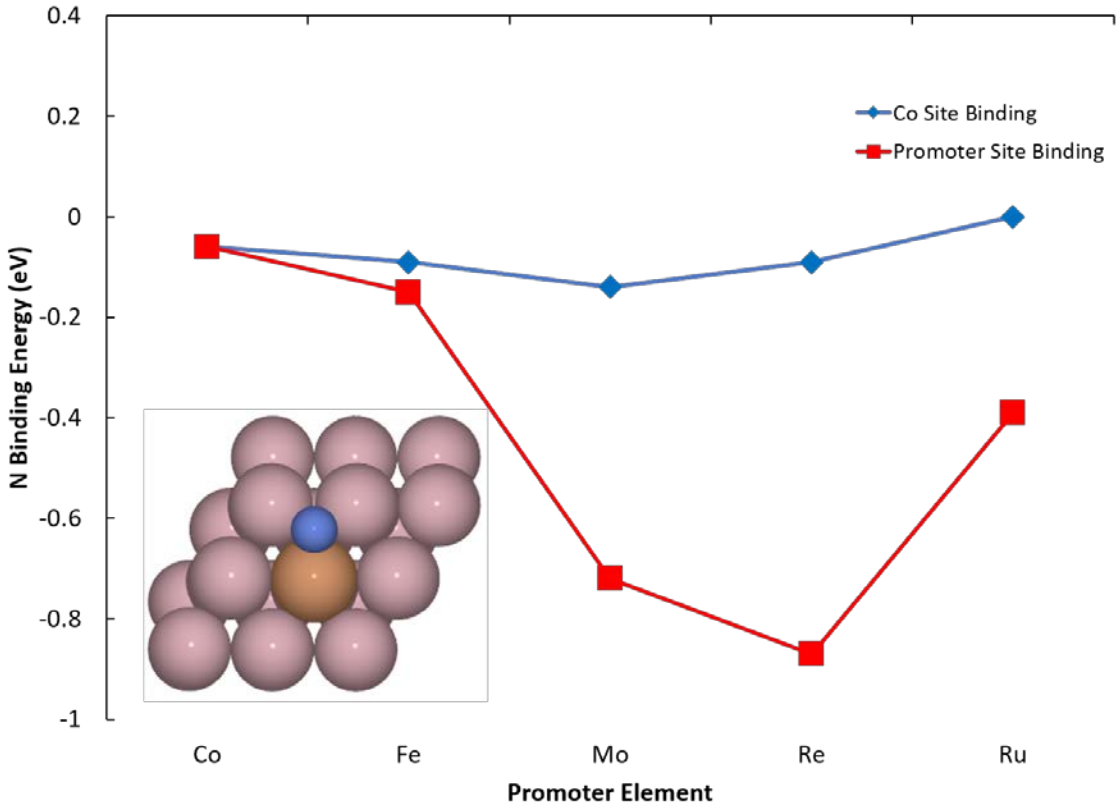

Figure 13. The binding energies of N on the different sites of the Co(0001) and the Fe-, Mo-, Re-, and Ru-promoted Co(0001) surfaces. **(inset)** The binding location of N on the promoter site of the Fe/Co(0001) surface.

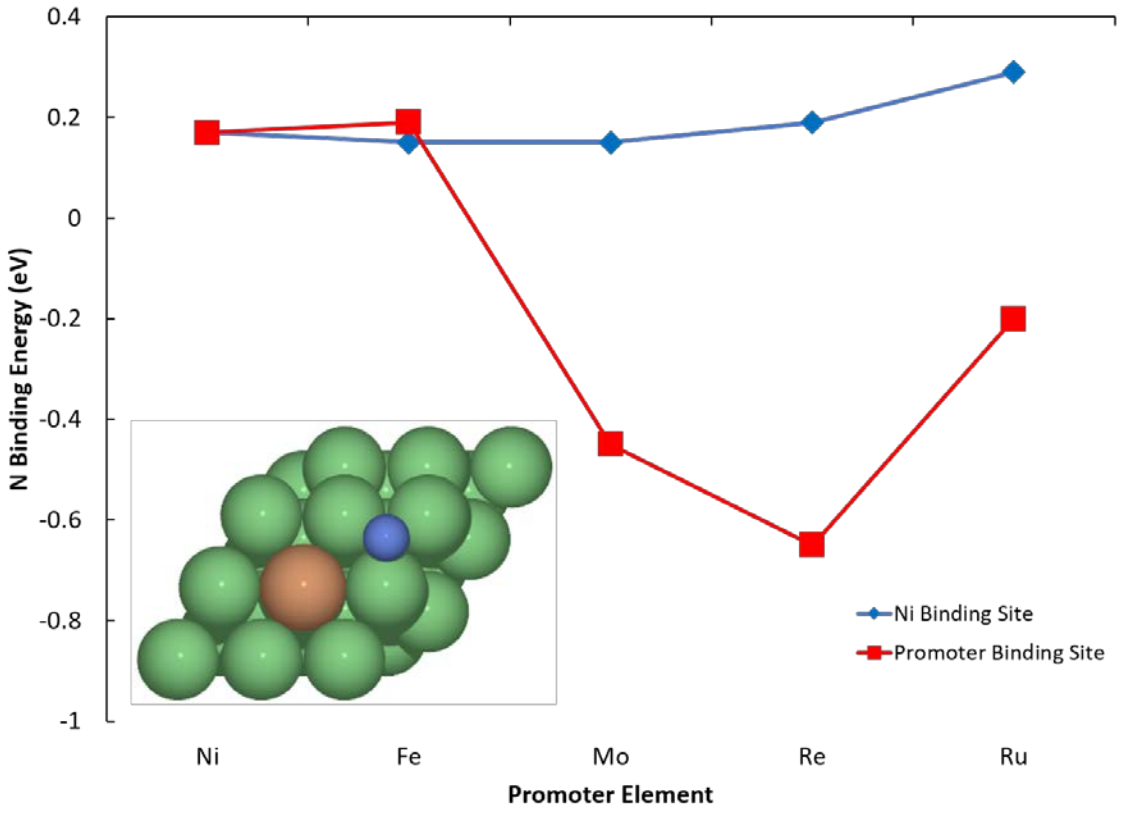

Figure 14. The binding energies of N on the different sites of the Ni(111) and Fe-, Mo-, Re-, and Ru-promoted Co(111) surfaces. **(inset)** The binding location of N on the host site of the Fe/Co(0001) surface.

Similar to the adsorption of N_2, there are a few trends that can be examined in Figures 13 and 14 for the binding of N adatoms. For all SAA surfaces, the N adatom adsorbs on the host sites with comparable binding energies to the pure host metals, indicating that these host sites can sufficiently approximate the activity of the pure host metal, similarly to the adsorption of N_2. On the Co(0001) SAAs, the binding strength trend for N adatoms is Re > Mo > Ru > Fe > Co, compared to Re > Ru > Mo > Co > Fe for the binding of N_2 on Co(0001). The improved binding strengths of Mo and Fe are promising, as they indicate that the reaction would be more exothermic on these surfaces, and from the transition state scaling laws, this should decrease the activation energy barriers. On the Ni(111) SAAs, the

binding strength trend for N adatoms is Re > Mo > Ru > Ni > Fe, compared to Re > Mo > Ru > Ni > Fe for the binding of N_2. As mentioned previously, the binding of N on the Fe promoter site is weaker than both the Ni site of the SAA and the pure Ni(111) surface, which is also seen in the N_2 binding on the same SAA. In addition, all binding energies of N adatoms are considerably weaker on the Ni(111) SAAs than on the corresponding Co(0001) SAAs; for instance, the binding energies of N adatoms are weaker on both the promoter and host sites of the Mo/Ni(111) SAAs than on the promoter and host sites of the Mo/Co(0001) SAA. Indeed, from the activity volcano plot in Figure 10, nitrogen should bind stronger to Co than Ni.[107] On all surfaces, the N adatom bound strongest to the hcp sites.

2.4.2. Activation of N_2

After N_2 binds to the SAA surfaces, the strong N-N triple bond breaks and the constituent nitrogen atoms bind to three-fold sites. Figure 15 below compares the activation energy barriers of the minimum energy pathways (MEPs) of N_2 dissociation on each of the SAAs, as well as its barrier on Ru(0001), calculated by Logadottir and Nørskov.[108] Figure 15 also includes images showing the initial state (IS), transition state (TS), and final state (FS) of the dissociation of N_2 on the Mo/Co(0001) SAA.

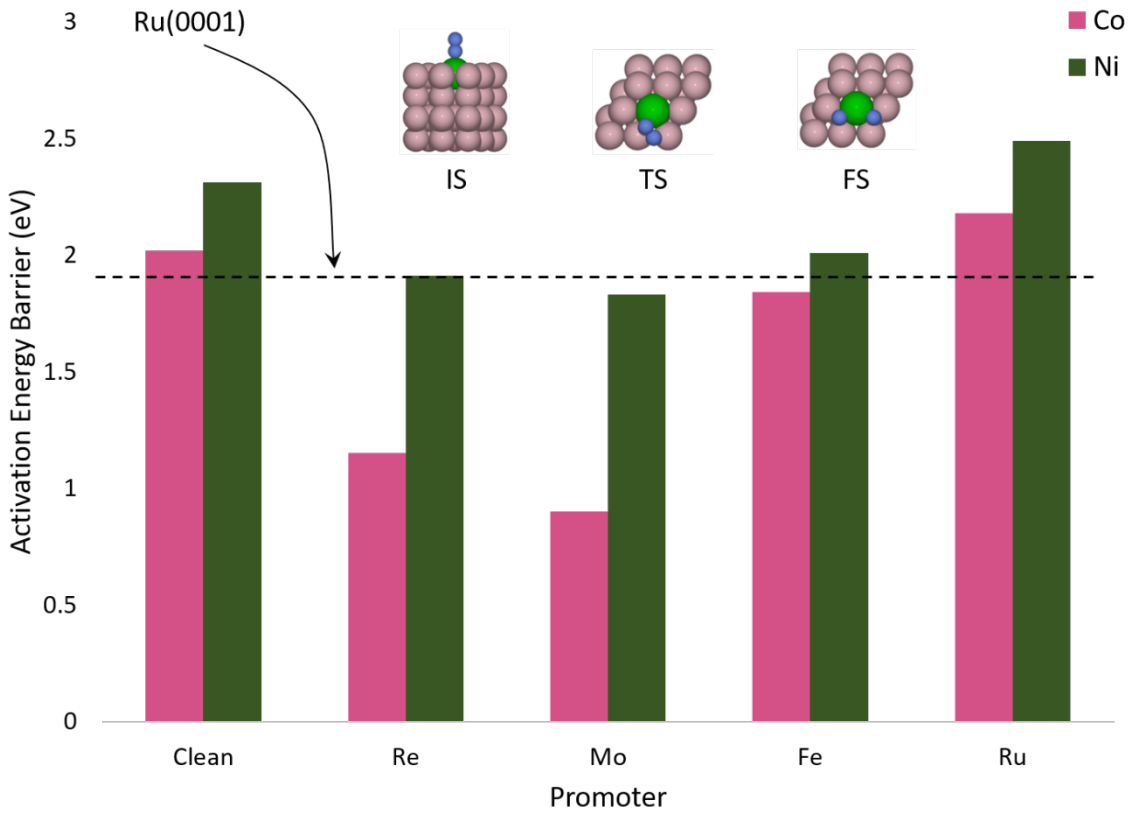

Figure 15. The comparison of the activation energy barriers for the dissociation of N_2 over pure Ru(0001)[108] and the promoter sites of the studied SAAs, as well as images depicting the IS, TS, and FS of the reaction on the Mo/Co(0001) SAA.

The most promising SAA is the Mo/Co(0001) SAA, with an activation energy barrier of only 0.90 eV, compared to a calculated barrier of 1.9 eV on the Ru(0001) terrace from the work of Logadottir and Nørskov.[108] The Co-Mo system has previously been suggested as the ideal bimetallic system for the Haber-Bosch process. In 2000, Jacobsen found that Co_3Mo_3N catalysts outperformed the commercial iron catalysts for the process,[109] and shortly thereafter, Kojima and Aiki were able to come to the same conclusions.[110–112] The Nørskov group predicted that the Co-Mo system would yield the optimal results for a bimetallic alloy,[14,26,82] and a recent study from Albrecht et al. found that the cobalt molybdenum nitrides remain stable during the Haber-Bosch reaction.[113] The

other Mo-promoted SAA, Mo/Ni(111), also slightly improved upon the Ru(0001) standard with an activation energy barrier of 1.83 eV. The Ni-Mo system has also been studied for the Haber-Bosch process in the nitride form,[109,114,115] but researchers have found its activity to be lower than that of the Co-Mo system, similarly to what is seen in Figure 15.

The other two SAA catalysts that improve upon the activation energy barrier of Ru(0001) are Re/Co(0001) and Fe/Co(0001), with barriers of 1.15 eV and 1.84 eV, respectively. Like the Co-Mo and Ni-Mo systems, the Co-Re system has also been studied in its nitride form,[116,117] but its activity is lower than that of the Co-Mo nitride.[113] Interestingly, it was determined that the addition of cobalt to rhenium catalysts was effective for improving the activity, but the addition of nickel to rhenium was not,[117] which corresponds to our activation barriers in Figure 15. The Co-Fe system has also been found to improve upon ammonia synthesis over pure Fe as bimetallic alloys,[118–120] and has been found to produce more ammonia than its Ni-Fe counterpart.[121] The Co-Fe and Ni-Fe systems are the only systems that

The only SAA combinations that perform poorer than their pure metal counterparts are the Ru/Co(0001) and Ru/Ni(111) SAAs. From the x-axis interpolation of the volcano plot in Figure 10, the Co-Ru and Ni-Ru bimetallic systems should give the worst activities of the studied alloys.[14,26] Furthermore, it has been shown in kinetic equations that one of the key electronic energy parameters that dictate the activity of a catalyst for the Haber-Bosch equation is the reaction energy (ΔE_{rxn}) of N_2 dissociation to two N adatoms on the surface.[14,82] A ΔE_{rxn} that is more negative would yield greater activity. As noted in Chapter 2.4.1, the binding energy of N adatoms on the Ru/Co(0001) and Ru/Ni(111) SAAs are weakened and are lower than that of N_2 adsorption on the respective surfaces. As a result,

the ΔE_{rxn} values are more positive, at -0.28 eV and 0.03 eV for the Ru/Co(0001) and Ru/Ni(111) systems, respectively.

To examine if there is a trendline for the dissociation of N_2 at the promoter site, the activation energy barriers (E_A) are plotted against the dissociation energy (E_D) in Figure 16 below. In this plot, the dissociation energy refers to the energy of the reaction $N_2^* \rightarrow 2N^*$, where N_2^* indicates that the dinitrogen molecule is already adsorbed onto the promoter site of the SAA. In the case of Fe-promoted Co(0001) and Ni(111), the binding energy of N_2 at the promoter site is used, even though the molecule binds stronger on the host site.

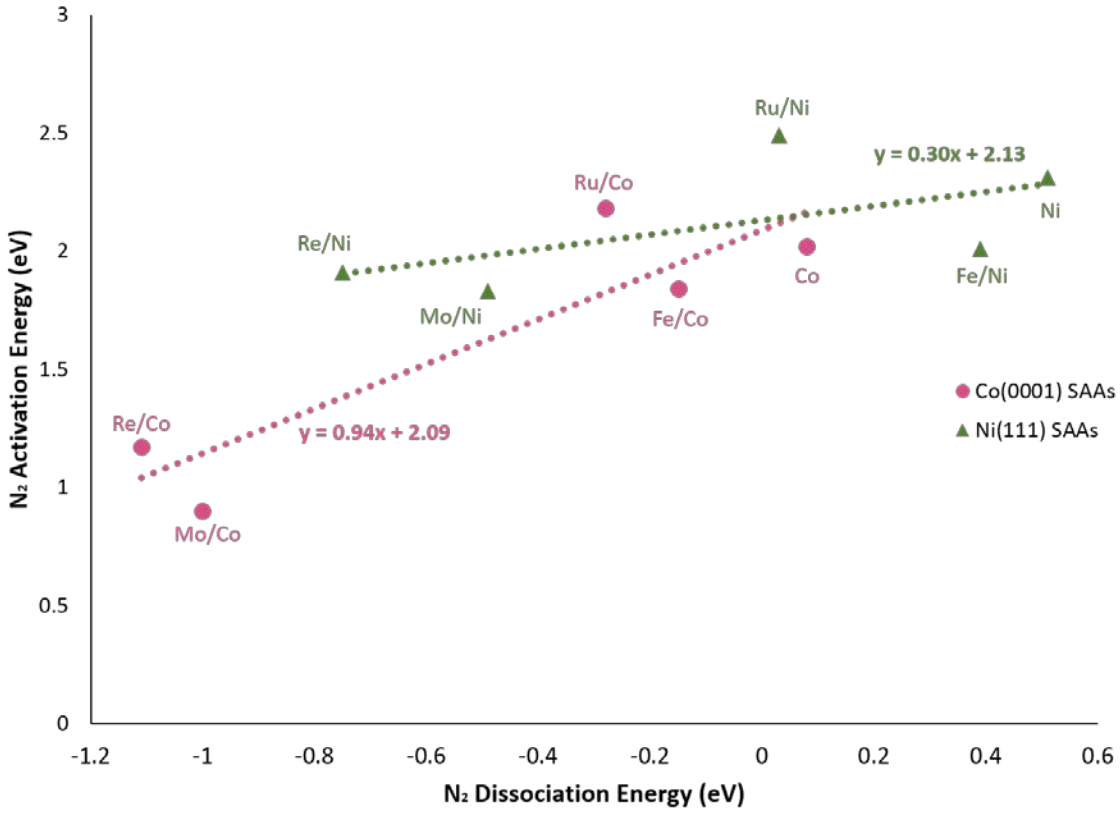

Figure 16. The trendlines comparing the dissociation energy of N_2 with the activation energy barriers on the Co(0001) and Ni(111) SAAs.

In Figure 16, the Co(0001) SAA surfaces, including pure Co(0001), are marked by circular, purple markers, while the Ni(111) SAA surfaces, including pure Ni(111), are

marked by triangular, green markers. Two trendlines are shown, one for the Co(0001) surfaces and one for the Ni(111) surfaces. The Co(0001) SAA surfaces share a trendline with the relation $E_A = 0.94E_D + 2.09$, while the Ni(111) surfaces share a trendline of $E_A = 0.30E_D + 2.13$. If all data points are considered together and only one trendline is created, the mutual trendline shows a relationship of $E_A = 0.70E_D + 2.06$. Of the three trendlines, the Co(0001) SAA trendline is closest to the literature trendline of $E_A = 0.90E_D + 2.07$, established by Jacobsen and coworkers.[122] Regardless, these microscopic trendlines show that lower N_2 dissociation energies yield lower N_2 activation energies.

2.4.3. Dispersion of N Adatoms

The key step that single atom alloys utilize to circumvent the established scaling relations is the dispersion of the intermediates from the strong-binding promoter site to the weak-binding host site. After the N_2 molecule dissociates into its constituent N adatoms, the N adatoms spill over from the promoter site to the host sites. Although this diffusion step is uphill in energy and therefore unfavorable, the diffusion still occurs due to the shift of thermodynamic equilibrium to states with greater site multiplicity (see Chapter 1.4), as well as displacement push from any N_2 that would adsorb onto the promoter site.[45] Regardless, in this section, we examine the diffusion of N adatoms from the promoter hcp site, the strongest binding promoter sites on the surface, to a host fcc site that is bordered by three host metal atoms. The diffusion of N adatoms is also examined on the pure metal surfaces. The diffusion barriers, or the activation energy barriers that the N adatom must overcome to diffuse from the promoter hcp site to the host fcc site, are shown below in Figure 17.

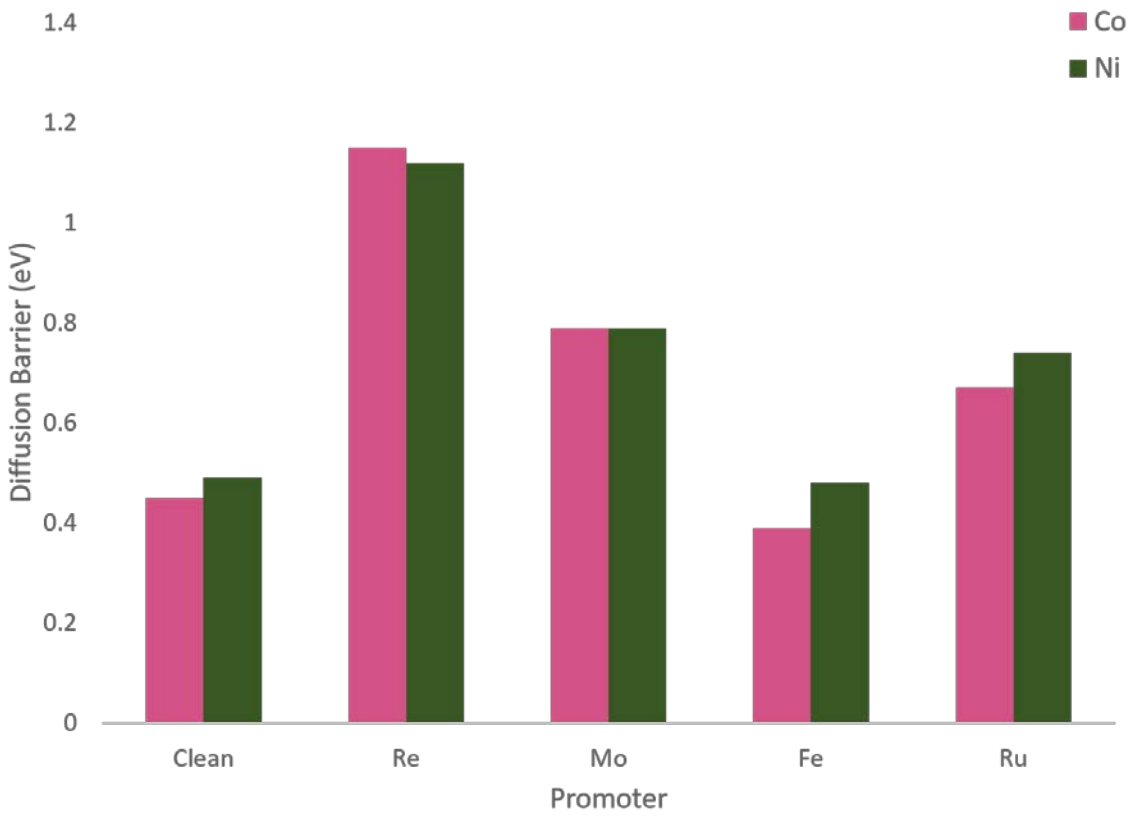

Figure 17. The diffusion barriers for an N adatom to diffuse from a promoter hcp site to a host fcc site.

In most cases, the N diffusion barriers are lower than the N_2 dissociation barriers on the respective surfaces. The lone exception is on the Re/Co(0001) SAA; while the Re/Co(0001) has the second-lowest activation energy barrier for N_2 activation at 1.15 eV, it has the highest diffusion barrier, with an identical value of 1.15 eV. Although the thermodynamic equilibrium effect must be taken into consideration, the energetic limitations of diffusing the N adatom away from the Re promoter of the Co(0001) and Ni(111) surfaces may be debilitating. If the N adatom cannot diffuse away, it would simply act as a poison for the promoter site, unless any molecular N_2 can adsorb onto the promoter site and displace the N adatom. Figure 18 below is a model that depicts which sites the N adatom would diffuse to and from on the Co(0001) SAAs.

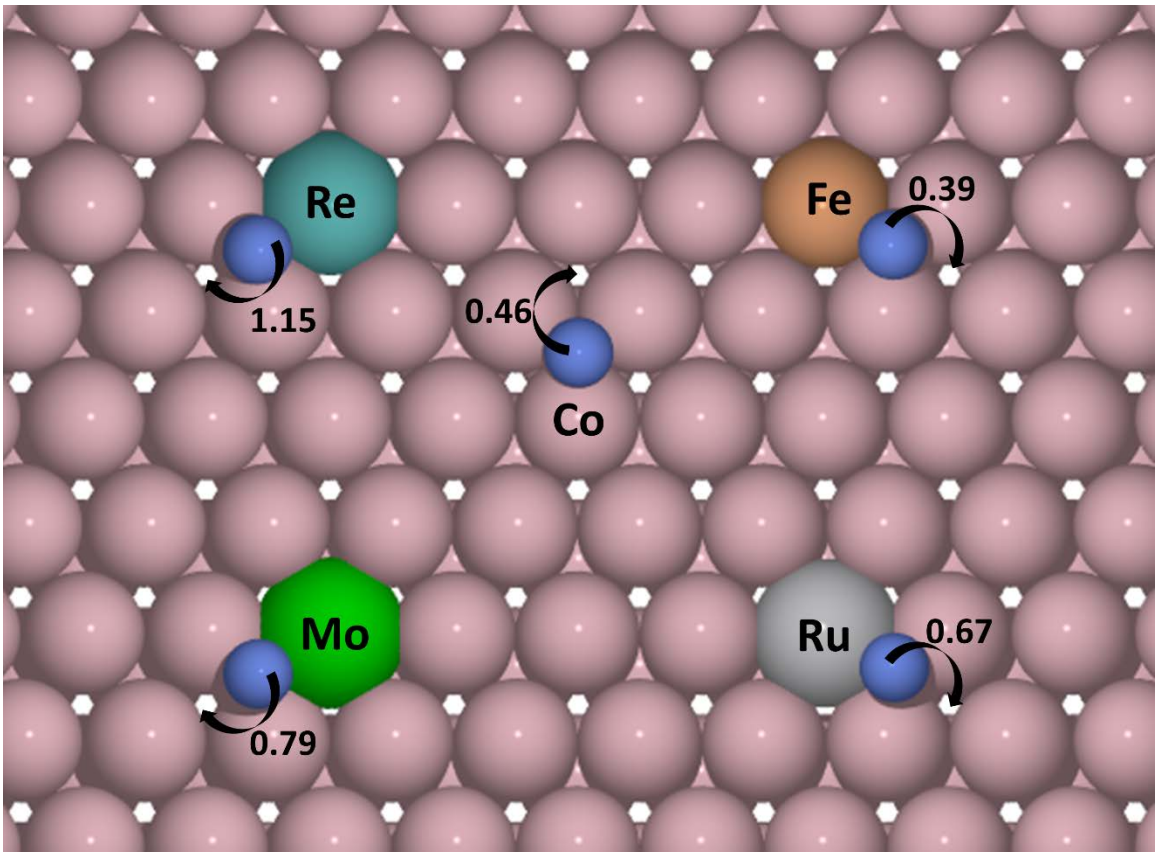

Figure 18. The diffusion barriers for N adatoms on model Co(0001) surfaces.

Similarly to how a microscopic trendline can be formed between the N_2 dissociation energy and the N_2 dissociation activation energy barriers, microscopic trendlines can be drawn between the binding energies of N adatoms on the promoter sites (E_N) and the N diffusion barriers away from the promoter site (E_{diff}). The trendlines for this relation are shown below in Figure 19.

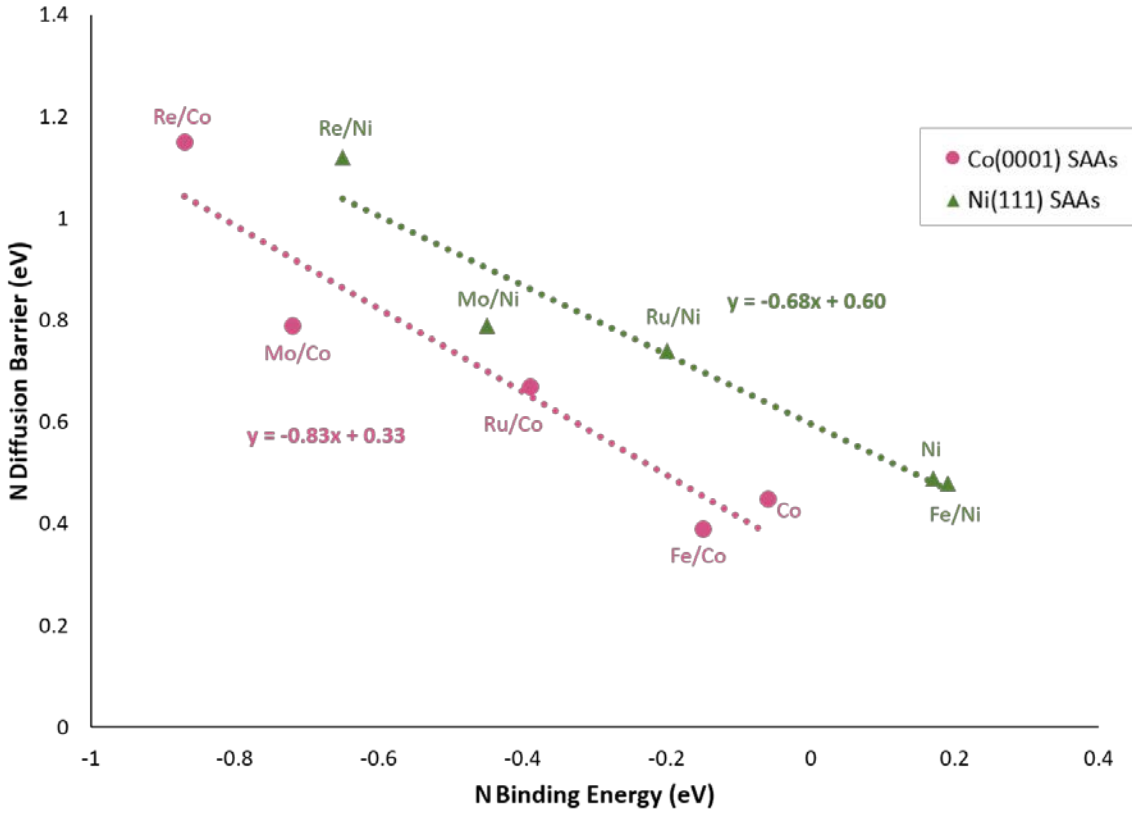

Figure 19. The trendlines comparing the diffusion barriers of N adatoms with the N binding energies on the Co(0001) and Ni(111) SAAs.

As in Figure 16, the data in Figure 19 can be divided into the diffusion barriers on the Co(0001) and Ni(111) SAA surfaces. The Co(0001) surfaces, including pure Co(0001), are marked by circular, purple markers, while the Ni(111) SAA surfaces, including pure Ni(111), are marked by triangular, green markers. The Co(0001) SAA surfaces share a trendline with the relation $E_N = -0.83E_{diss} + 0.33$, while the Ni(111) surfaces share a trendline of $E_N = -0.68E_{diss} + 0.60$. If all data points are considered together and only one trendline is created, the mutual trendline between all points shows a relationship of $E_N = -0.63E_{diss} + 0.51$. The negative slopes for all relations indicate that if N binds to a site stronger, it is more difficult for it to diffuse away.

2.4.4. Circumventing Scaling Relations

With the energetics of the adsorption of N_2 onto the promoter site, dissociation of N_2 on the promoter site, adsorption of N on the promoter site, and dispersion of N from the promoter site to the host sites fully determined, the entirety of the reaction can be drawn and compared for each SAA surface. Inspired by the "butterfly" plots from the work of Sykes et al.,[123] Figure 20 below presents a split potential energy diagram. Starting in the middle at Point 1 and going towards the left, the energetics of the entire reaction are given for the Mo/Co(0001) SAA surface, which yielded the lowest barrier for the rate-determining step, the activation of N_2. Meanwhile, starting at the middle and going to the right, the energetics are given for the entire reaction on the pure Co(0001) surface, including a one-step diffusion from an energetically favorable hcp site to a less-favorable fcc site. This diffusion step on the Co(0001) surface is performed to remain analogous with the Mo/Co(0001) surface, where a nitrogen adatom spills over from the promoter site to the host site. In the final diffusion step on Mo/Co(0001), it is assumed that the N adatom diffuses far away enough such that it no longer feels any electronic effect from the Mo promoter site and has the same adsorption energy of N on a pure Co(0001) surface. This assumption can be drawn especially because the binding energies of N on the host sites of all SAAs are similar to the binding energies of N on the pure host metals, from Figures 13 and 14. This assumption also allows the conclusion to be drawn that once the N_2 molecule has been activated on the promoter site, it can diffuse to a surface that is identical to the weak-binding host metal.

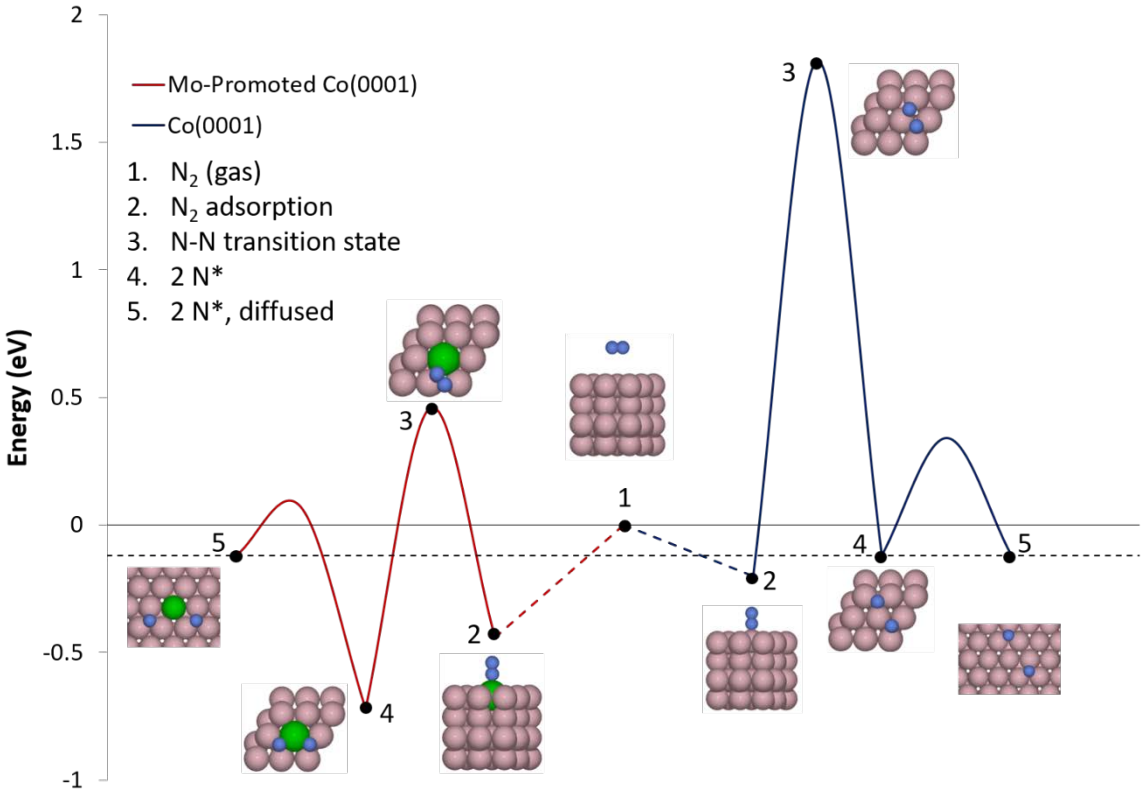

Figure 20. A "butterfly" potential energy diagram comparing the energetics of the overall reaction on Mo/Co(0001) to the left and pure Co(0001) to the right.

In Figure 20, it is shown that the transition state energy (E_{TS}), or the energy difference between the reference energy at Point 1 and the highest energy state at Point 3, is drastically reduced on the Mo/Co(0001) SAA catalyst (0.46 eV) in comparison with the pure Co(0001) catalyst (1.82 eV). The dashed line that goes through both Points 5 indicates that once the N adatom has diffused away from the promoter site of the SAA, it experiences a similar, weak binding to that of the N adatom on the pure host metal. Furthermore, the potential energy diagram for the SAA has a smaller energy difference between the highest and lowest energy states at 1.18 eV compared to an energy difference of 2.02 eV for the pure Co(0001) surfaces. A lower energy difference between the highest and lowest energy

states typically corresponds to more reaction turnovers, according to the energetic span model.[124]

Although Figures 16 and 19 in the sections on N_2 dissociation and N diffusion show data points following a trendline behavior, these trendlines work in conjunction to break established scaling relations. From Figure 20 on the Co/Mo(0001) catalyst, after the N adatom disperses from the promoter site to the host metal site, the final binding energy of the N adatom is seen to be weak. Despite this, the overall reaction transition state energy remains low, which is counter-intuitive to the Brønsted-Evans-Polanyi relationship, which suggests that surfaces that have weaker binding adsorbates would have higher transition state energies. The ability of the studied SAAs to circumvent the BEP relations can be seen by comparing the final state energies (ΔE) and the transition state energies (E_{TS}) with the literature scaling relation of $E_{TS} = 0.90\Delta E + 2.07$ for close-packed surfaces, established by Jacobsen et al.,[122] in Figure 21.

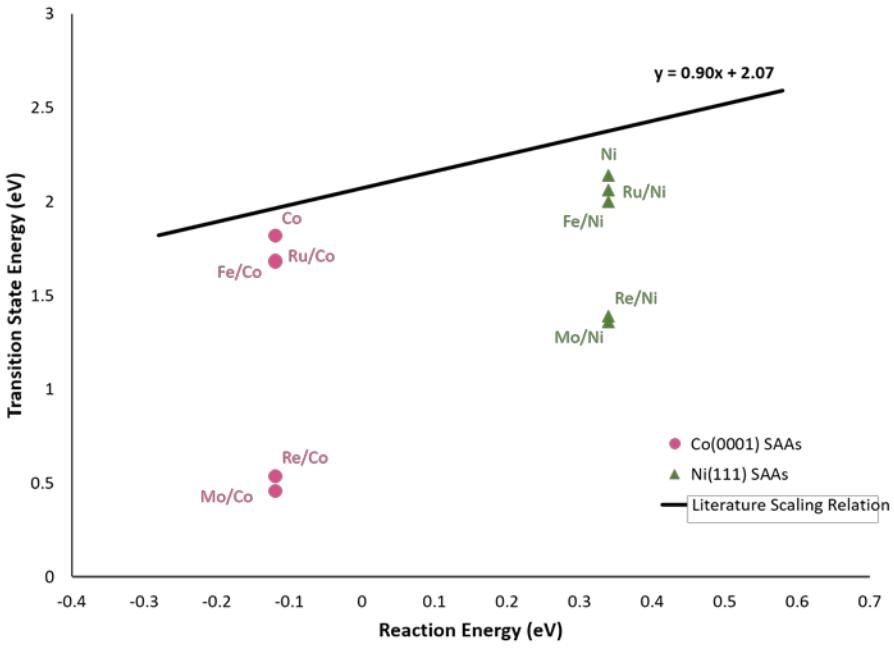

Figure 21. The comparison of examined surfaces with the literature scaling relation.[122]

From Figure 21 above, all Co- and Ni-based SAAs have the same respective reaction energies because it is assumed that the N adatoms diffuse far away from the promoter, where it binds with the same energy as on a pure Co or Ni host. In the figure, the established scaling relations are confirmed for pure, close-packed surfaces due to the proximity of the pure Co(0001) and Ni(111) data points to the line. Meanwhile, it is also confirmed that many of these SAA surfaces indeed circumvent the established BEP relations by yielding a lower transition state energy despite having higher than expected reaction energies. In particular, the Mo- and Re-promoted Co(0001) and Ni(111) SAA surfaces show the greatest deviation from the linear trend. If it were to follow the linear trend, the Mo-promoted Co(0001) SAA, which deviates from the trend the most, would require a ΔE of -1.79 eV to reach the E_{TS} of 0.46 eV, whereas the SAA requires a more reasonable ΔE of -0.28 eV. This study indicates then that SAAs are promising catalyst surfaces to circumvent the established scaling relations and improve the activity of the Haber-Bosch process.

2.4.5. Microkinetic Modeling Results

By examining the N_2 dissociation barriers and the differences between the highest and lowest energy states of the reaction, we can begin to predict which SAA catalysts are most active for the Haber-Bosch reaction. The Mo/Co(0001) SAA is the most promising one due to its lowest N_2 dissociation barrier of 0.90 eV and an energy difference between the highest and lowest energy states of 1.18 eV. A kinetic model, however, is still needed to fully predict the outcomes of each of the SAA surfaces. Following the methods presented

in Chapter 2.3, the results of the microkinetic model for temperatures between 500-800 K and a pressure of 300 bar are shown in Figure 22.

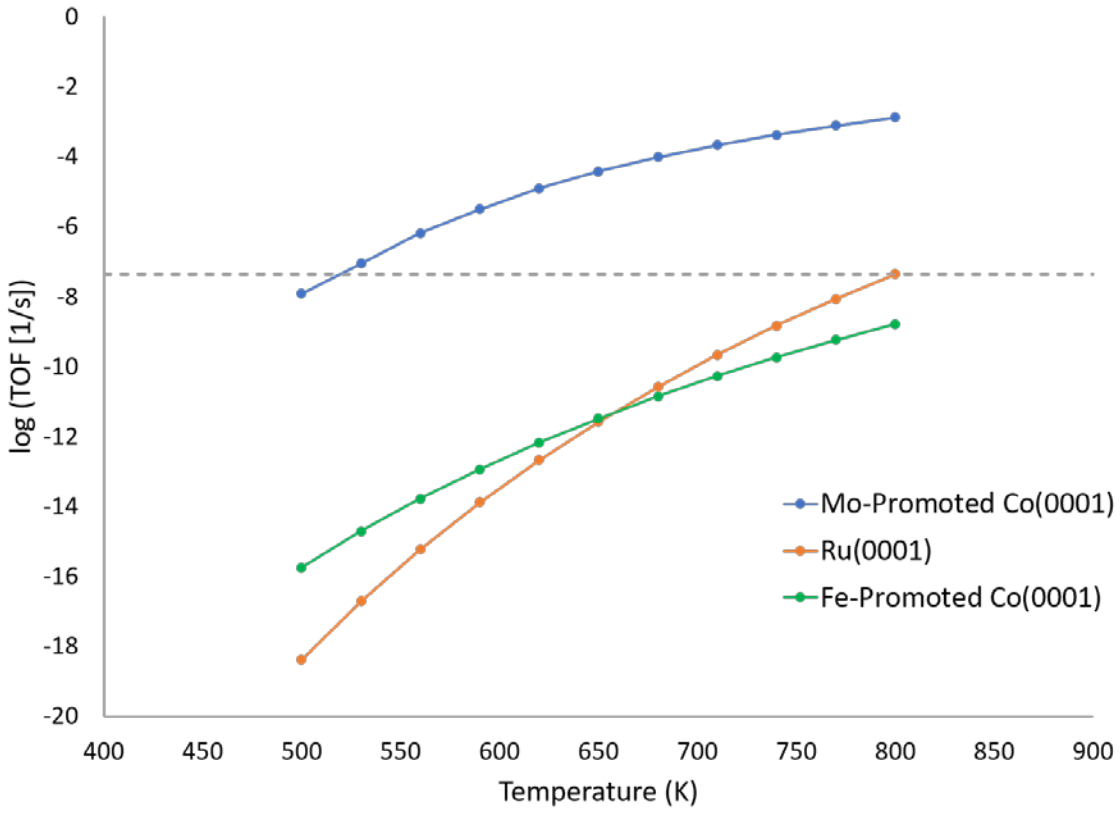

Figure 22. The results of the microkinetic model between 500-800 K at 300 bar for the Haber-Bosch reaction on Mo/Co(0001), Fe/Co(0001), and Ru(0001).

In Figure 22, the Mo/Co(0001) and Fe/Co(0001) SAAs are compared to Ru(0001), where all energies are adopted from the work by Logadottir and Nørskov.[108] From the results in Figure 22, the Mo/Co(0001) SAA catalyst shows a turnover frequency that is four orders of magnitude greater than on Ru(0001) at 800 K, which is the upper bounds of the temperatures used for the reaction industrially. Meanwhile, the Fe/Co(0001) SAA performs better than the Ru(0001) surface at lower temperatures, but at the upper temperature bounds of this study, the Ru(0001) surface performs at an order of magnitude better. The primary reason for the difference in the curves of the SAA catalysts and the

pure metal catalyst is that diffusion is considered on the SAA catalysts while on the pure catalysts, it is not. This is because there is a clear distinction between promoter and host sites on the SAA catalyst, whereas all sites on the pure surface are indistinguishable.

A drawback of the microkinetic modelling method for the description of SAA catalysts is its inability to distinguish spatial features.[125–127] In the microkinetic model, it is assumed that the promoter atoms take up 1% of the available sites and that any diffusion must occur between the promoter site and a host site, but there is no way to indicate that a promoter site must be surrounded by six host sites, that adsorbates may interact with each other laterally, or that diffusion is allowed between different host sites without explicitly defining every single site that exists. Therefore, it is expected that these microkinetic models underestimate the amount of diffusion that occurs on the surface of the SAA catalysts, but they still provide a reasonable prediction of the overall activity of the SAA catalyst surface.

An important consideration when designing SAA catalysts is the energetic stability of the SAA surface; this consideration is heavily investigated in Chapter 6 of this dissertation. While we initially assumed that the SAA catalysts are stable in the configuration where one single promoter atom sits isolated in the catalyst surface, energetically, it is possible that the promoter atom could diffuse into the subsurface and bulk, diffuse within the surface to form dimers and larger islands, or even fail to penetrate the surface and sit as an adatom. In the study in this work, we compared the energies of the SAA surfaces with surfaces where the promoter atom and the atom directly below it in the first subsurface are switched. Since the number of each atomic species remains the same, the DFT energies of the two surfaces can be directly compared. A differential chart

showing the difference between the energies of the SAA surfaces and their respective subsurface configurations is presented in Figure 23 below.

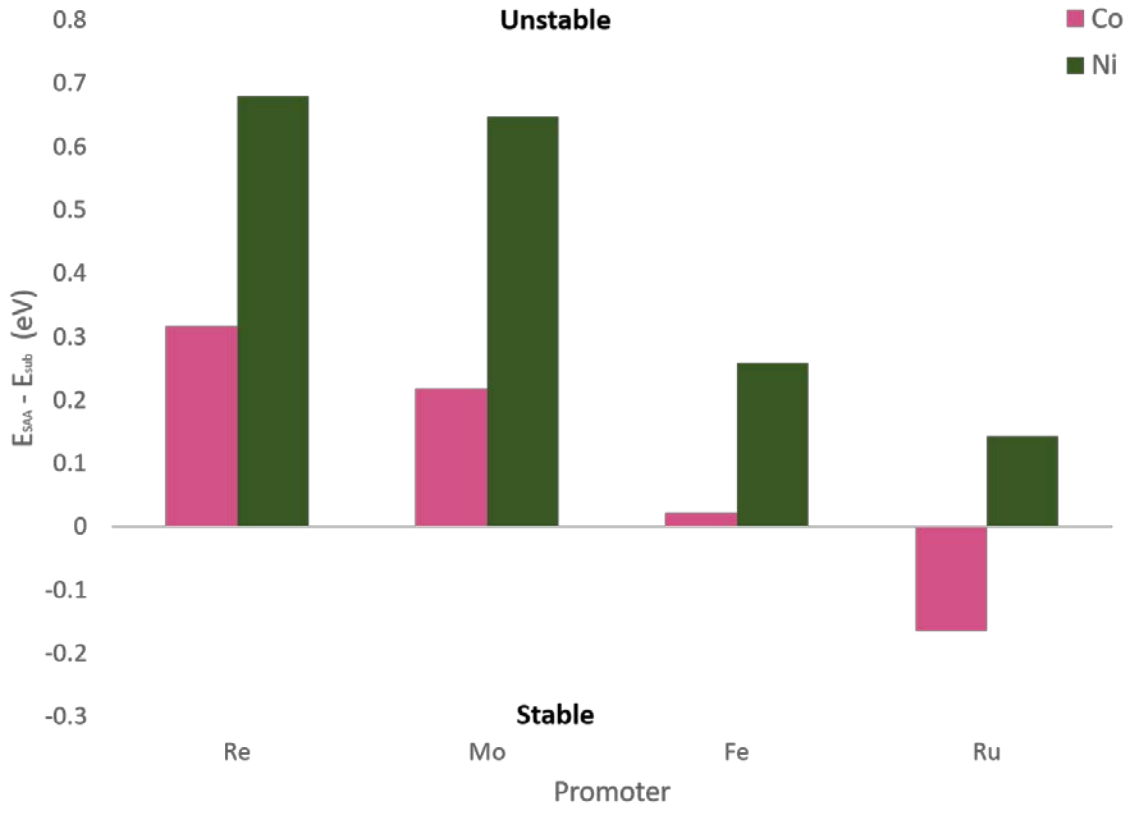

Figure 23. The energetic differences between the DFT energies of the SAA surfaces and a subsurface counterpart surface for the eight bimetallic systems.

In Figure 23 above, a negative value indicates that the SAA surface is more stable than its subsurface counterpart. Figure 23 shows that only Ru/Co(0001) is more stable as a SAA, but from the energetics of the reaction and microkinetic modeling, that combination of metals does not optimize the reaction. The energies of the Fe/Co(0001) SAA and subsurface configuration are nearly indistinguishable, so the Fe/Co(0001) SAA may be a potential stable configuration, as there would be some diffusion barrier needed for the Fe promoter to diffuse to the subsurface. From the microkinetic modeling results shown in Figure 22, although the Fe/Co(0001) catalyst does not perform as well as the laboratory

standard Ru(0001), it may hold more potential due to its lower costs. The promising Mo/Co(0001) SAA catalyst is likely hindered by the poor stability of the SAA catalyst itself. In some cases, such as those explored by Greeley and Mavrikakis for their near-surface alloys[37] and CO on various SAAs,[128] the partial pressure of reactant gases could tune the stability of the SAA through adsorbate-induced surface segregation. If the adsorbate binds strongly enough with the promoter metal of the SAA, it could potentially "pull" the promoter metal out of the bulk and onto the surface. The binding energy of N_2 on the subsurface configuration of the Mo/Co(0001) alloy is -0.27 eV, whereas the binding energy of N_2 on the Mo/Co(0001) SAA is -0.44 eV, indicating that N_2 does bind stronger to the Mo promoter site. Further studies are needed to determine if this energy difference is sufficient for N_2-induced surface segregation to occur on the Mo/Co(0001) catalyst, which has been suggested to be a promising catalyst for the reaction in the literature.[14,26,82,113]

2.5. Conclusion

We investigated the efficacy of single-atom alloys (SAAs) for the Haber-Bosch process. By examining the volcano plot of single-metal catalyst surfaces for ammonia synthesis, we selected four strong-binding metals (Fe, Mo, Re, and Ru) and two weak-binding metals (Co and Ni) to form eight SAAs. Through first-principles density functional theory (DFT) calculations, we examined the surfaces of all eight SAAs on close-packed surfaces and compared their activities to their respective pure-metal precursors, Co(0001) and Ni(111). From adsorption studies, in most cases, the promoter metal binds nitrogen strongly, whereas the host metal binds nitrogen weakly and similarly to their pure-metal

precursors. N_2 dissociates over the promoter metals on the SAAs, and in the examination of the dissociation barrier, the Mo-, Re-, and Fe-promoted Co(0001) SAAs and the Mo-promoted Ni(111) SAA outperform the literature reports on the close-packed Ru(0001) surface, which is widely accepted to be the best pure-metal surface for the Haber-Bosch reaction. Once the N_2 molecule has dissociated over the promoter metal, the resultant N adatoms bind to the sites surrounding the promoter atom before dispersing or spilling over to the surrounding host metal sites. On the host metal sites, the N adatoms bind weaker, allowing for easier hydrogenation to occur and for ammonia to form. The weak binding of the N adatom on the host sites also pushes the reaction energy to be more positive, and coupled with the lowered activation energy barriers and transition state energies, these SAAs circumvent established linear scaling relations. The SAAs are then further studied in a microkinetic model, and at 800 K and 300 bar, the Mo-promoted Co(0001) SAA outperforms Ru(0001) by four orders of magnitude. Another promising SAA catalyst, Fe/Co(0001), is outperformed by Ru(0001) by one order of magnitude at those conditions, but remains promising due to its lower costs and greater energetic stability. In this work, we have found that isolated promoter metal species in SAA catalysts are promising active sites for the Haber-Bosch process and circumvent the established scaling relations for the reaction.

Chapter 3. The Synergy of Dilute Pd and Surface Oxygen Species for Methane Upgrading on $Au_3Pd(111)$

In Chapter 2, we confirmed the effectiveness of single-atom alloys (SAAs) for the dissociation of the strong triple bond of nitrogen. In this chapter, which was published in *Energy Technology* in 2019, we explored the efficacy of isolated palladium atoms for the dehydrogenation reactions. Our target molecule in this work was methane, the smallest yet most difficult to work with. Methane (CH_4) is the simplest hydrocarbon and is readily available. CH_4 constitutes approximately 75% of natural gas by volume, and according to the BP Statistical Review of World Energy in 2015, there is an estimated 187.1 x 10^{12} m^3 of natural gas reserves.[129] Furthermore, this number does not include any reservoirs that have yet to be discovered or are too costly to mine; for instance, natural gas hydrates in the crystalline form are currently too complex to recover, but have been considered as a potential energy source,[130,131] and there are an estimated 1.5 x 10^{16} m^3 in reserve.[130] In addition, the evolution of the extraction of natural gas from shale rock formations has allowed access to huge quantities of natural gas from previously impermeable and impractical sources.[132] Finally, other sources of methane include fossil fuel production and combustion, which is responsible for at least 33% of human methane emissions;[133] biogas from anaerobic digestion of crops;[133,134] and the decomposition of biodegradable solid waste from landfills.[133]

While methane is a readily available resource, the direct transformation of methane into useful chemicals is limited. Presently, less than 10% of natural gas is used as a chemical feedstock.[135] One of the biggest reasons natural gas is often flared rather than converted is because the mass and energy density (0.7-0.9 kg/m^3 and 30-40 MJ/m^3,

respectively) of natural gas are approximately three orders of magnitude lower than that of oil (0.7-0.9 kg/dm^3 and 30-40 MJ/m^3, respectively), which makes transportation more expensive.[135] Profitable conversion of natural gas into useful chemicals would justify the high transportation costs, but presently, only methane conversion to synthesis gas, hydrogen cyanide, acetylene, and chlorinated methane has been realized industrially.[135]

The lack of profitability from direct natural gas conversion is due to the difficulty in activating methane. The four C-H bonds are very stable at 440 kJ/mol, and because of the molecule's symmetry, the bonds are only very weakly polarized. Methane resists nucleophilic reactions because the electron donation into the C-H σ* orbital is difficult and sterically hindered, and removing electrons from the C-H σ bond by electrophilic reactions is also challenging.[135] Acid-base catalysis generally cannot occur because methane has low proton affinity and is a very weak acid (pK_a = 40).[135] Thus, the easiest method to activate the C-H bond is through the homolytic bond cleavage to a methyl radical and a hydrogen atom radical.[135] However, if the inert methane can be activated, then its target species will be even easier to activate; for instance, the C-H bond of the methyl radical is easier to activate than the C-H bond of methane, leading to the methylene radical.[135] This is an issue because the activation of one C-H bond in methane would likely lead to a series of C-H bond activations until just carbon, or coke, remains.

These challenges in the activation of methane limit the possibilities of methane conversion. Presently, there are only two industrial methods of converting methane. The first and most prominent method is the production of synthesis gas.[135] Synthesis gas, or syngas, is a major industrial intermediate for the production of methanol and ammonia and consists of H_2, CO, and CO_2. Syngas is catalytically and industrially produced from

methane via steam reforming, dry reforming, and autothermal reforming. Syngas technology has been studied for decades and many reviews[136–138] and books[139,140] are available for more detail. The only other industrial use of methane in direct conversion is the formation of hydrogen cyanide through the BMA process or the Andrussow process.

The successful activation and upgrade of methane in an active and selective manner is so highly sought-after that it is considered a "holy grail" of catalysis. In this chapter, we use the surface geometries of SAAs to impact the surface chemistry and lead to the active and selective dehydrogenation of methane in non-oxidative and oxidative pathways. The results of this work are represented in Figure 24 below, which suggests that the $Au_3Pd(111)$ can upgrade methane with activity, unlike pure Au, and with selectivity, unlike pure Pd.

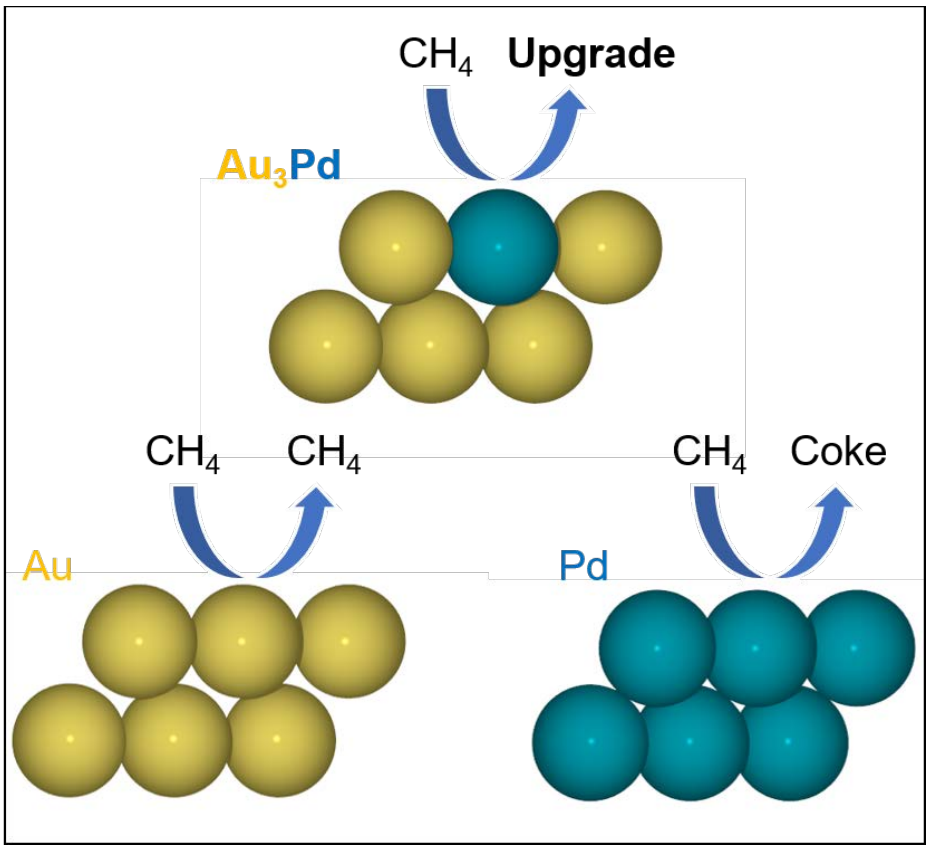

Figure 24. Au_3Pd allows for the active and selective upgrade of methane.

3.1. Introduction

Since methane is an abundant and low-cost resource, its conversion to higher-value chemicals is highly desirable. Immense efforts have been poured into methane conversion research, and while these have led to great advances in understanding, methane upgrade chemistry remains limited. Less than ten percent of natural gas is used as a chemical feedstock, and presently, only the conversion of methane to synthesis gas, hydrogen cyanide, acetylene, and chlorinated methane have been realized industrially.[135] The lack of profitability from direct methane conversion is due to the difficulty in selectively activating the molecule's C-H bonds. The four C-H bonds are stable at 439 kJ mol^{-1},[8] and because of the molecule's symmetry, the bonds do not offer any obvious point of attack. Consequently, the rate-determining step for almost all heterogeneously-catalyzed methane activation schemes is commonly assumed to be the first C-H bond dissociation step.[141]

One strategy to facilitate the catalytic activation of methane is to introduce a dopant into the heterogeneous catalyst to produce an electronic effect.[13,142] For instance, single-atom alloys (SAAs) are a relatively new class of catalysts, where a single active promoter atom sits within the surface of a less-reactive host metal;[41,45,143] these SAAs have been studied for a variety of reactions, including hydrogenation,[46–49,144] dehydrogenation,[51,52] oxidation,[53,54] and reduction[55,56] reactions. In the majority of these reactions facilitated by SAAs, the reactant interacts with or is activated by the promoter atom, and the subsequent reaction intermediate moves or "spills over"[91,92] to the less-reactive host atom, where it can desorb or undergo further chemistry.

An alloy combination of highly-reactive (stronger binding) and less-reactive (weaker binding) metals that has garnered recent interest for methane activation is the gold-

palladium (Au-Pd) alloy. The Au-Pd alloy combination is catalytically promising because Au tends to isolate Pd atoms, providing an ensemble effect that inhibits the formation of certain byproducts,[145–147] similar to the effect shown by the SAA catalysts. Within the family of methane conversion processes, Au-Pd alloys have been studied for methane combustion;[148] methane oxidation to methanol;[149,150] and the partial oxidation of methane to syngas.[151]

Inspired by the recent work on Au-Pd catalysts, we seek to investigate the role of various surface oxygen species for methane activation on $Au_3Pd(111)$, a surface that has isolated Pd surface atoms fully surrounded by Au atoms, reminiscent of the surface geometry seen in SAAs. Literature on oxidative processes on the Au-Pd SAA system is scarce, partially because ensembles of Pd are required to lower the dissociation barrier of O_2.[152,153] Pure Au catalysts, however, are known to be excellent oxidation catalysts,[154–157] and recently Cargnello and coworkers found that Au-Pd SAA catalysts can be used for the selective oxidation of 2-propanol to acetone via a hydroperoxyl intermediate.[158] We hypothesize that the oxidation activity of the Au host, combined with the hydrogen abstraction ability of a single platinum-group metal promoter,[51,52,159] would result in a catalytic system that would ease the activation of methane. To this end, we have studied methane activation pathways on $Au_3Pd(111)$ using density functional theory and compared against Au(111) and Pd(111) model surfaces as reference systems. We find that $Au_3Pd(111)$ offers strategic advantages over Au(111) and Pd(111) due to a surface geometry that mimics SAAs in both non-oxidative and oxidative reaction pathways.

3.2. Methods

The periodic density functional theory (DFT) calculations were performed using the Vienna ab initio Simulation Package (VASP)[94,95,160,161] in combination with the Atomic Simulation Environment (ASE).[162] The core and valence electrons were represented using the projector augmented wave (PAW) method[98] using an energy cutoff of 400 eV. The exchange and correlation were described by the Perdew-Wang (PW91) functional.[163] Gaussian smearing[164] was used with a Fermi temperature of $k_bT = 0.1$ eV, and the electronic energies were subsequently extrapolated to $k_bT = 0$ eV. All geometries were optimized until the residual forces on each atom were converged below 0.02 eV/Å.

The optimized lattice constant for Au_3Pd was a = 4.117 Å, which is in good agreement with the experimentally determined value of 4.083 Å.[165] The lattice constants of bulk Au and Pd were calculated to be 4.177 Å and 3.958 Å, respectively. The Au(111), Pd(111), and Au_3Pd(111) surfaces were modeled in (2×2) periodic unit cells containing four atomic layers each, where the top two layers were allowed to fully relax, while the bottom two layers were fixed at their bulk positions. The subsequent slabs were separated in the *z*-direction by a vacuum space of 14 Å. All unit cells were sampled with a 6×6×1 Monkhorst-Pack *k*-point set[166] after testing was performed to confirm its convergence. Spin-polarization was considered in all calculations.

The binding and reaction energies were calculated in reference to the clean surfaces and to gas-phase CH_4, H_2, and O_2. All gas-phase molecules were centered in 20×20×20 $Å^3$ boxes and calculated with the same settings as those used in the slab calculations, with the exceptions of a tighter force convergence criterion of 0.01 eV/Å, Γ-point sampling, and a dipole correction along all three Cartesian directions. Due to the known calculation

difficulties in describing oxygen's triplet state, the gas-phase energy of O_2 was obtained from the formation of water, where the enthalpy of formation of water was -2.506 eV.[167,168]

The transition states were found using the climbing image nudged elastic band (NEB) method[77] and fully optimized to a force conversion criterion of 0.05 eV/Å. These transition states were confirmed to be true saddle points in the potential energy surface by a frequency analysis, performed by the harmonic oscillator approximation with a Cartesian displacement of 0.01 Å, which showed a single imaginary frequency along the reaction pathway. The *d*-band centers were calculated and analyzed according to the *d*-band model of Hammer and Nørskov,[105,169] and partial charges were estimated from a Bader's analysis.[170]

A series of methane activation pathways, summarized in Scheme 1, were studied on the Au(111), Pd(111), and Au_3Pd(111) surfaces. Each surface was modified with a different pre-adsorbed oxygen species, or motif. These motifs – atomic oxygen (O*), molecular oxygen (O_2*), hydroxyl (OH*), and hydroperoxyl (OOH*) – can mediate the methane activation pathways, as described in Equations 29-33:

$$CH_4\,(g) + 2^* \rightarrow CH_3^* + H^*, \quad (29)$$

$$CH_4\,(g) + O^* + ^* \rightarrow CH_3^* + OH^*, \quad (30)$$

$$CH_4\,(g) + O_2^* + ^* \rightarrow CH_3^* + OOH^*, \quad (31)$$

$$CH_4\,(g) + OH^* + ^* \rightarrow CH_3^* + H_2O^*, \text{ and} \quad (32)$$

$$CH_4\,(g) + OOH^* + ^* \rightarrow CH_3^* + H_2O_2^*. \quad (33)$$

We can generalize all of the studied reactions in the equation $CH_4\,(g) + ^* + O_xH_y^* \rightarrow CH_3^* + O_xH_{y+1}^*$, where O_xH_y represents the pre-adsorbed motifs. On the clean surfaces, where

methane dissociation is not mediated by a pre-adsorbed motif, the values of *x* and *y* are zero.

3.3. Results and Discussion

The activation of methane in the presence of pre-adsorbed O* or OH* species on both Au(111) and Pd(111) has been well-studied.[16,171–173] To the best of our knowledge, however, similar studies on gold-palladium alloys have not been reported yet. Prior to presenting our results on the three surfaces, we introduce the potential energy diagram of the O_2-assisted CH_4 activation mechanism on $Au_3Pd(111)$ in Figure 25 as an example. In this mechanism, we begin with the reference state (RS) at 0 eV, where molecular oxygen (O_2) is pre-adsorbed onto the clean $Au_3Pd(111)$ on the top site of the Pd atom. In the following step, which we will refer to as the initial state (IS), methane is introduced and physisorbs weakly at -0.06 eV onto an Au top site. In this step, the energy of the system is given as a co-adsorption energy, i.e. infinite separation is not considered. The co-adsorption energy was chosen because we assume that the adsorbates must be close enough in order for the oxygen species to facilitate in the C-H bond cleavage of methane. In the subsequent methane activation step, the hydrogen atom is transferred from methane to the O_2*. The transition state energy (E_{TS}) of this particular system is 1.34 eV and is calculated with respect to the RS. The corresponding activation energy barrier (E_a) is therefore 1.40 eV. In the final state (FS), also calculated as a co-adsorption energy, a hydroperoxyl (OOH*) is bound to the Pd top site while the methyl (CH_3*) is bound to an Au top site. The final state energy (E_{FS}) is described as the difference in energy between the FS and the RS, and it is calculated to be 0.58 eV in this mechanism.

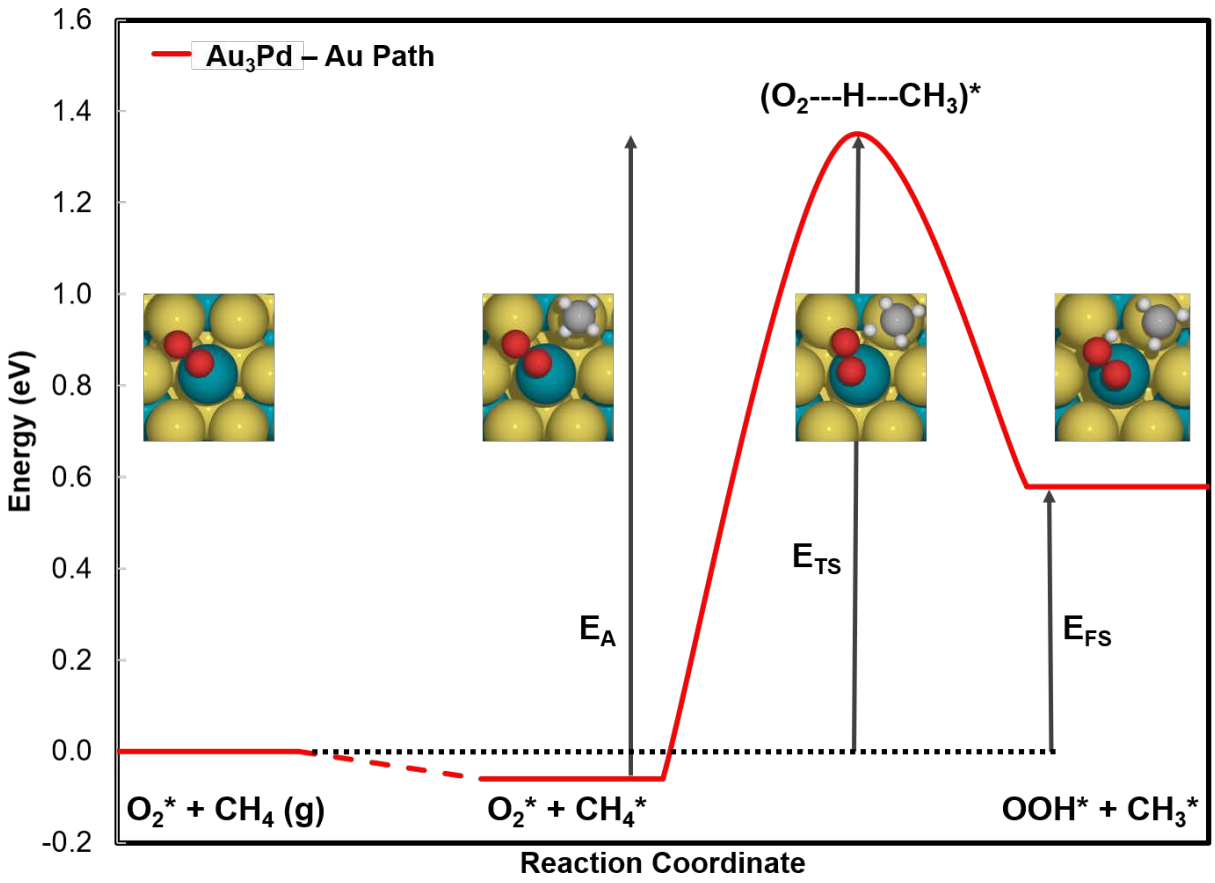

Figure 25. The potential energy diagram of the O_2-assisted methane activation mechanism in the Au pathway over $Au_3Pd(111)$.

It is also imperative to distinguish between the two possible pathways on the $Au_3Pd(111)$ surface. In one pathway, termed the "Au pathway," the methyl group resides on the Au top site in the FS. The example given in Figure 25 depicts the Au pathway for the O_2-assisted mechanism; in this example, the CH_3* sits on the Au top site and the OOH* sits on the Pd top site in the FS. On the other hand, in the "Pd pathway," the methyl group resides on the Pd top site in the FS. This is an important distinction because CH_3* binds weaker to the Au top site than the Pd top site; the weaker binding on the Au top site reduces the likelihood of complete dehydrogenation to coke, increases the probability of CH_3•

radical desorption, and therefore provides selectivity benefits for the potential upgrade of methane to useful chemicals.

Before we continue the discussion of the oxygen-assisted mechanism, we examine the direct dissociation of methane on the three clean surfaces in the absence of any pre-adsorbed species, as illustrated in Figure 26. The direct dissociation of methane on the three surfaces exhibits Brønsted-Evans-Polanyi type behavior, where an increase in E_{FS} results in an increase in E_{TS}. As expected, the activation of methane over Pd(111) is most favored, both kinetically and thermodynamically. This is consistent with Pd being a good methane combustion catalyst,[174,175] but the unselective activation of C-H bonds is undesirable in the upgrade of methane to partial oxidation products.[176] In contrast, Au(111) shows poor C-H bond scission ability but could be promising for partial oxidation reactions.[177] Meanwhile, the non-oxidative activation and upgrade of methane on $Au_3Pd(111)$ may be promising. On $Au_3Pd(111)$, the Pd pathway is kinetically and thermodynamically preferred; the reaction following the Pd pathway behaves similarly to the reaction on Pd(111), while the Au pathway resembles the reaction on Au(111). Although the activation of methane via the Pd pathway on $Au_3Pd(111)$ has a higher barrier and reaction energy than on Pd(111) due to the less favorable binding of the FS species on $Au_3Pd(111)$, the subsequent dissociation of CH_3* to CH_2* and H* on $Au_3Pd(111)$ has a substantial energy barrier of 1.40 eV. This energy barrier is greater than the barrier of 1.17 eV for CH_4 activation on the $Au_3Pd(111)$ surface, indicating that the dissociation of methane on $Au_3Pd(111)$ might not be carried out to completion, but rather, the dissociation steps could terminate at the CH_3* bound at the Pd top site. To make this comparison, the barrier for CH_3* to desorb as a radical was calculated to be 1.51 eV without taking into account the substantial entropy

gain upon desorption of a CH_3 radical. Using tabulated values the entropy of a free gas phase CH_3 radical at 500 K is 1.12 eV.[178] In contrast, the dissociation of CH_3* into CH_2* and H* involves only surface bound species for which the entropy change is expected to be small.Thus, CH_3 radical formation is likely to occur at elevated temperatures and $Au_3Pd(111)$ may be a promising surface for the further investigation of non-oxidative methane activation and other non-oxidative dehydrogenation reactions.

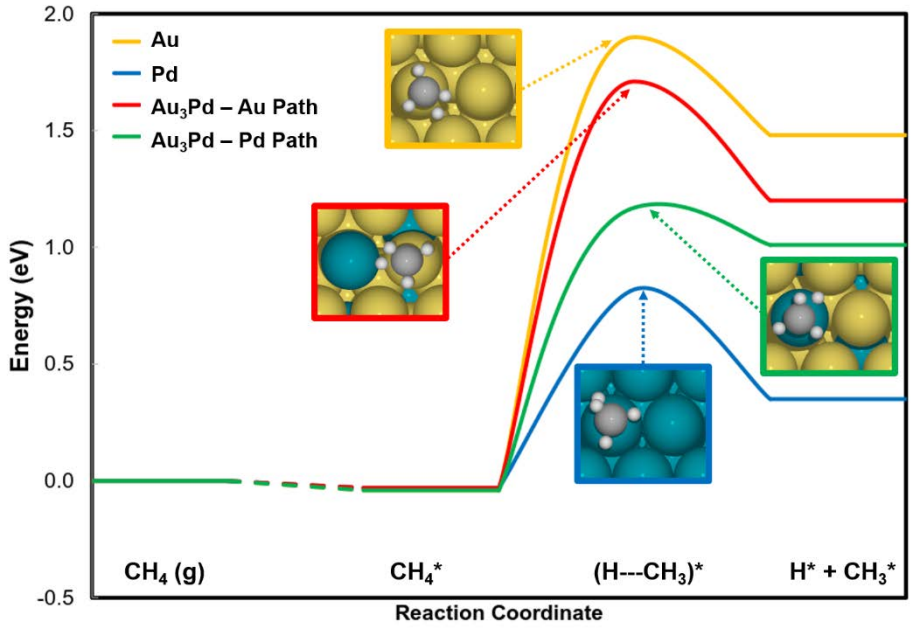

Figure 26. The potential energy diagram comparing the direct dissociation of methane on Au(111), Pd(111), and the two pathways of $Au_3Pd(111)$. The labels on the bottom of the plot indicate the compounds involved in the steps directly above.

The potential energy diagrams for the O-assisted, O_2-assisted, OH-assisted, and OOH-assisted methane activation mechanisms in all four pathways are depicted in Figure 27. In these diagrams, the distinction between the Au pathway and the Pd pathway on the $Au_3Pd(111)$ surface is most obvious in the O_2-, OH-, and OOH-assisted mechanisms. For the two pathways of $Au_3Pd(111)$, the reference states are the same; the pre-adsorbed motifs

are adsorbed in their most favorable binding positions, which are on top of the Pd surface atom for O_2*, OH*, and OOH*, and adjacent to the Pd surface atom in the fcc site for O*. In the initial states of the Pd pathway, however, the O_2*, OH*, and OOH* must move away from the Pd site in order to allow the methane molecule to physisorb onto the Pd site, resulting in an endothermic energy change. In the O-assisted mechanism, since O* does not impede the physisorption of methane onto the Pd site, the O* does not have to move away from its reference state position. Therefore, there is no endothermic energy change associated with the first steps of the O-assisted mechanism on the Pd pathway of $Au_3Pd(111)$.

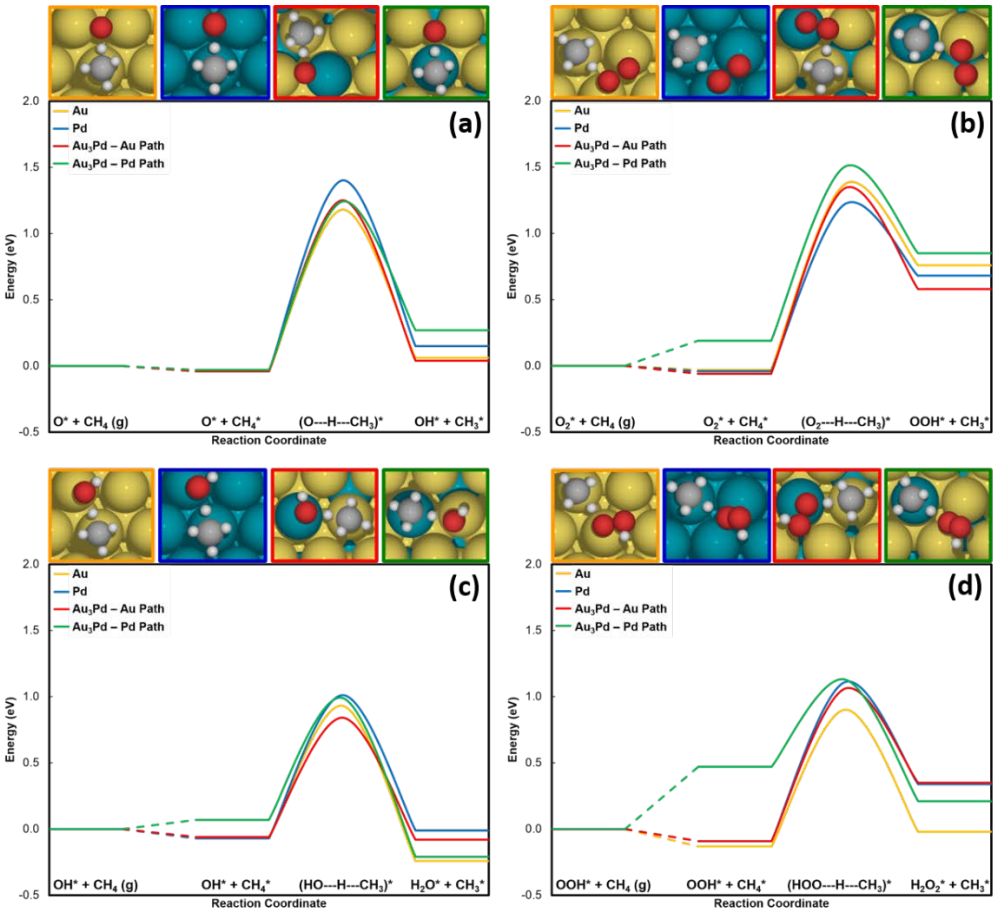

Figure 27. Potential energy diagrams for CH_4 activation via the **(a)** O-assisted mechanism; **(b)** O_2-assisted mechanism; **(c)** OH-assisted mechanism; and **(d)** OOH-assisted mechanism on Au(111), Pd(111) and $Au_3Pd(111)$.

The energetics of the O-assisted mechanism, illustrated in Figure 27a, shows that methane activation via this mechanism is more favorable on Au(111) than Pd(111), directly contrary to the results of the unassisted, direct dissociation mechanism. These results agree with prior reports on monometallic systems.[171–173,177,179] These reports found that O* promoted the cleavage of the C-H bond on noble metals, such as Au, and exerts the opposite effect on more reactive metals, including Pd. Indeed, in our results, on Au(111), the O-assisted mechanism gives a lower E_{TS} (1.18 eV) in comparison to the direct dissociation mechanism's E_{TS} (1.90 eV), promoting the C-H bond dissociation, whereas on Pd(111), the O-assisted mechanism gives a higher E_{TS} (1.38 eV) than the direct dissociation mechanism's E_{TS} (0.82 eV), inhibiting the dissociation. Meanwhile, the O-assisted mechanism via the Pd pathway and the Au pathway on $Au_3Pd(111)$ have similar values of E_{TS} (1.24 eV vs. 1.25 eV). The reaction is nearly thermoneutral through the Au pathway (E_{FS} = 0.04 eV) while it is more endothermic through the Pd pathway (E_{FS} = 0.27 eV). This indicates that the reaction is thermodynamically favored when it proceeds through the Au pathway, which is advantageous since the resulting CH_3* product resides on the Au top site, allowing for greater selectivity in methane upgrade reactions. Like their Au(111) and Pd(111) counterparts, the O-assisted mechanism following the Au pathway (E_{TS} = 1.25 eV) promotes the activation of methane over the direct dissociation mechanism (E_{TS} = 1.71 eV), while in the Pd pathway, the presence of O* in the O-assisted mechanism (E_{TS} = 1.24 eV) slightly inhibits the direct dissociation mechanism (1.17 eV).

The O_2-assisted mechanism, depicted in Figure 27b, begins with molecular oxygen bound on the Au top site of Au(111) and the Pd top site of Pd(111) and $Au_3Pd(111)$ in the respective reference states. Between the reference and initial states of the Pd pathway on

$Au_3Pd(111)$, the O_2* must diffuse from the Pd top site to the Au top site so that methane can physisorb to the Pd site, resulting in an endothermic methane adsorption step of 0.19 eV. Consequently, the Pd pathway on $Au_3Pd(111)$ yields the highest E_{TS} value (1.50 eV) for the O_2-assisted mechanism, and the Au pathway dominates on $Au_3Pd(111)$ due to its superior kinetics and thermodynamics. On the other hand, Pd(111) exhibits the lowest E_{TS} (1.22 eV) for this mechanism, which is in contrast with the O-assisted mechanism, where the mechanism was favored for Au(111) over Pd(111). Similarly to the O-assisted mechanism though, the presence of O_2* lowers the E_{TS} on Au(111) and the Au pathway of $Au_3Pd(111)$ while raising the E_{TS} on Pd(111) and the Pd pathway of $Au_3Pd(111)$, in comparison to the direct dissociation mechanism. In all cases, the final state comprises of a methyl and a hydroperoxyl located on surface top sites.

The OH-assisted mechanism, illustrated in Figure 27c, commences with OH* bound to the bridge sites on Au(111) and Pd(111) and the bridge site spanning the Pd and Au atoms on $Au_3Pd(111)$. In the Pd pathway of $Au_3Pd(111)$, the OH* must diffuse away from its original location adjacent to the Pd atom to a bridge site spanning two Au atoms to allow methane to physisorb to the Pd top site, resulting in an endothermic step of 0.07 eV. In the OH-assisted mechanism on monometallic systems, Au(111) is favored over Pd(111), reminiscent of the O-assisted mechanism. Furthermore, the OH-assisted mechanism promotes methane activation over the direct dissociation mechanism on Au(111), while inhibiting methane activation on Pd(111). These results on the monometallic surfaces follow the trends found by others.[172] On the $Au_3Pd(111)$ surface, the OH-assisted mechanism is kinetically favored in the Au pathway, where the E_{TS} (0.84 eV) is not only lower than its Pd pathway counterpart, but also outperforms the E_{TS} of the

monometallic Au(111) surface. In contrast, although the Pd pathway yields a higher E_{TS}, it yields a lower E_{FS} because the H_2O* product has no site preference on $Au_3Pd(111)$, and therefore the E_{FS} is largely dependent on the binding energy of CH_3*, which prefers the Pd top site.

Lastly, the OOH-assisted mechanism, shown in Figure 27d, initiates with OOH* bound to the top sites on the monometallic systems and the Pd top site of the $Au_3Pd(111)$ surface. In the Pd pathway of $Au_3Pd(111)$, OOH* diffuses to an hcp site surrounded by solely Au atoms, resulting in a large endothermic step of 0.47 eV and consequently the largest E_{TS} value of 1.13 eV. Conversely, the overall mechanism on Au(111) is slightly exothermic and yields the lowest E_{TS} value of 0.90 eV, indicating that Au(111) would be the preferred surface for OOH-assisted methane activation. Previous studies have also shown that the OOH* motif on Au is beneficial for other reactions, including the catalytic oxidation of CO.[157]

The four motifs can be divided into whether they have one or two oxygen atoms. As previously discussed, the motifs containing only one oxygen atom, O* and OH*, have been previously examined to elucidate their roles in the promotional activation of C-H bonds.[171–173,176,179] Meanwhile, to the best of our knowledge, no theoretical work has yet been reported on the promotional activation of C-H bonds using the motifs with two oxygen atoms, O_2* and OOH*. To determine whether a motif containing one or two oxygen atoms is preferred, the dissociative activation of O_2* to 2 O* is studied on all three surfaces, and their energy values are given in Table 1. As expected, on the monometallic surfaces, O_2 activation is highly preferred on Pd(111) over Au(111) due to a lower activation energy barrier and its reaction exothermicity. These results are corroborated by

previous works that show that the dissociative chemisorption of O_2 is facile on Pd(111) but is a highly activated process on Au(111).[180–183] Meanwhile, the activation of O_2 occurs over the Pd site of $Au_3Pd(111)$, with activation and reaction energies between those of the monometallic surfaces.

Table 1. The activation and reaction energies of O_2 dissociation on the three different surfaces.

Surface	**E_{TS} (eV)**	**E_{FS} (eV)**
Au(111)	1.68	0.56
Pd(111)	0.78	-1.16
$Au_3Pd(111)$	1.29	0.20

Assuming that O_2 plays a role in the methane activation mechanisms on all three surfaces, the dissociation of O_2* competes with the O_2-assisted activation of methane. On Pd(111), the activation energy of the exothermic O_2 dissociation (E_{TS} = 0.78 eV) is lower than that of the endothermic O_2-assisted activation of methane (E_{TS} = 1.22 eV), indicating that the splitting of O_2* to 2 O* will occur first. Therefore, the activation of methane on Pd(111) in the presence of O_2 most likely proceeds via the direct or the O-assisted mechanism, depending on the O* coverage.[175] Once the O* has been hydrogenated through the abstraction of H from methane, OH* could remain on the surface, and the OH-assisted mechanism becomes accessible. In contrast, on Au(111), the dissociation of O_2 (E_{TS} = 1.68 eV) is less favorable than the O_2-assisted activation of methane (E_{TS} = 1.37 eV), indicating that on Au(111), the oxidative dissociation of methane is most likely initiated via the O_2-assisted mechanism and continue through the OOH-assisted mechanism. On $Au_3Pd(111)$, O_2 dissociates over the Pd site (E_{TS} = 1.29 eV and E_{FS} = 0.20 eV) and is more

thermodynamically favorable than the O_2-assisted methane activation in the Au pathway (E_{TS} = 1.34 eV and E_{FS} = 0.58 eV), although it is kinetically competitive. Consequently, on $Au_3Pd(111)$, the oxidative dissociation of methane is expected to proceed through the O-assisted mechanism. The potential energy diagram of the most competitive oxidative dissociation mechanisms of methane to methyl and OH* or OOH* on the three different surfaces is shown in Figure 28. In addition, the unassisted, direct dissociation on Pd(111) and the O_2-assisted mechanism on $Au_3Pd(111)$ are included for comparison.

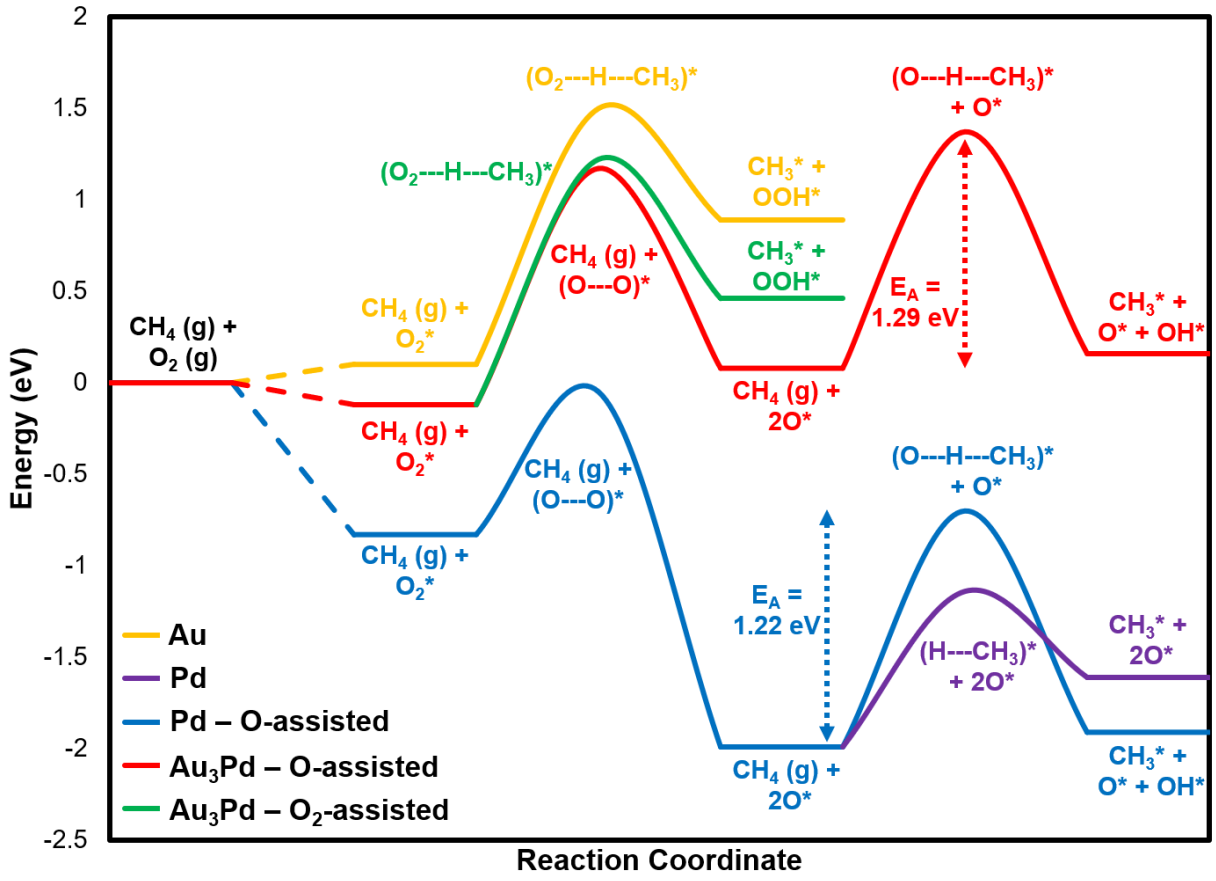

Figure 28. The potential energy diagram of the oxidative dissociation of methane pathways on Au(111), Pd(111), and $Au_3Pd(111)$, as well as the non-oxidative dissociation pathway on Pd(111).

The use of Au(111) for methane activation would be desirable because it binds CH_3* weakly and therefore offers selectivity advantages towards upgraded products. Furthermore, in the oxidative activation of methane, the presence of any oxygen-based motif greatly lowers energy barrier that needs to be overcome. The inherent issue with the oxidative activation of methane, however, is that it there is poor interaction between oxygen and the Au(111) surface, as evidenced by the weak binding energies and previous literature.[180–182,184,185] This is solved via the addition of the single Pd surface site, seen in the $Au_3Pd(111)$ surface. The binding energies of all oxygen species are stronger on the Pd site of the alloy than on pure Au(111), indicating that the presence of Pd allows for the adsorption and splitting of O_2. Additionally, in all of the mechanisms, the Au pathway is preferred over the Pd pathway, which benefits the selectivity to partial oxidation products because it leaves the CH_3* weakly bound to the Au top sites. As a result, the key role of monomeric Pd surface atoms in the $Au_3Pd(111)$ system is to bring oxygen to the noble Au surface while preventing the undesired, complete dehydrogenation of methane.

When comparing the oxidative and non-oxidative dissociation mechanisms of methane, the Au(111) surface still prefers the O_2-assisted mechanism over the non-oxidative dissociation of methane due to the inherent inability of Au to cleave C-H bonds. On the Pd(111) surface the direct or O-assisted mechanism is most plausible depending on the O* coverage resulting from facile dissociative O_2 adsorption. On $Au_3Pd(111)$, however, the preference is not so straightforward. The direct dissociation of methane on $Au_3Pd(111)$ via the Pd pathway is kinetically favored (E_{TS} = 1.17 eV) over the splitting of O_2 on the same surface (E_{TS} = 1.29 eV), but the non-oxidative mechanism is much more endothermic (ΔE = 1.01 eV) than the initial O_2-splitting step of the oxidative one (ΔE = 0.20 eV).

Regardless of which mechanism occurs, the presence of dilute amounts of Pd in an Au host is still highly desirable because the complete dehydrogenation of methane is unfavorable in both mechanisms; in the oxidative dissociation, since the mechanism follows the Au pathway, the resulting methyl group resides on the Au sites where it is less likely to further dissociate, whereas in the non-oxidative dissociation, the mechanism follows the Pd pathway, where the subsequent dehydrogenations of CH_x have higher activation energy barriers than the first dehydrogenation of CH_4 to CH_3.

It is seemingly contradictory that Au(111), a surface that poorly dissociates the C-H bond of methane in the non-oxidative mechanism, generally acts superiorly to the other surfaces when the pre-adsorbed motifs are present. Meanwhile, on Pd(111), where the non-oxidative dissociation of methane is facile, the presence of oxygen moieties tends to hinder the catalytic dissociation of methane. The lower activation energy barriers exhibited by Au(111) when the O*, OH*, and OOH* pre-adsorbed motifs are available is due to the greater exothermic benefit on noble metals when the adsorbate is reduced.[173] Since the adsorbates are weakly bound on the noble surface, they act as strong Brønsted bases, allowing for the easier abstraction of H from methane. This is prominently seen in the OH- and OOH-assisted mechanisms on Au(111), where the hydrogenation of the adsorbate results in the desorption of the product from the noble surface, leading to exothermic reaction energies. Thus, the binding strength of the pre-adsorbed motif is inversely related to the motif's ability to catalyze the C-H bond scission; an endothermic adsorbate binding energy generally yields a more exothermic reaction energy. This relationship has been found for various other non-metal adsorbates, including B, C, N, P, S, and Se.[172] This is also seen in the Au and Pd pathways of $Au_3Pd(111)$. The trends seen in the reactions via

the Au pathway mirror that of Au(111), while those seen on the Pd pathway show similar effects to those on Pd(111).

To understand the role of the oxygen moieties on the three surface, in Figure 29, the activation energy (E_{TS}) is plotted against the change in energy when the surface or an adsorbate abstracts a hydrogen atom on Au(111), Pd(111), and both pathways of $Au_3Pd(111)$. The change in energy when an adsorbate adds a hydrogen atom will be referred to as $\Delta E_{X+H\rightarrow XH}$ and is calculated as $\Delta E_{X+H\rightarrow XH} = E_{XH} - E_X - E_H$, where E_{XH} is the binding energy of the hydrided adsorbate, E_X is the binding energy of the pre-adsorbed motif, and E_H is the energy of a hydrogen atom calculated relative to the energies of gas-phase water and oxygen, as calculated by Nørskov and coworkers.[186] On the clean surfaces, where there are no pre-adsorbed motifs, E_X is zero. Abild-Pedersen and coworkers have shown that $\Delta E_{X+H\rightarrow XH}$ holds an inverse relationship to E_X when the adsorbate is a single adatom.[172] Figure 29 shows that E_A and $\Delta E_{X+H\rightarrow XH}$ are linearly related with two outliers, represented by circle markers, with one each on Pd(111) and the Pd pathway of $Au_3Pd(111)$. These two outliers are the unassisted, direct dissociation of methane on those two surfaces. Those two points are outliers because they do not have a “radical-like” transition state, which is defined by Nørskov and coworkers as a transition state where the methyl is not chemisorbed onto the surface.[10] These two transition states are also the only two transition states where the atomic distance between the centers of the carbon atom and the nearest surface metal atom is less than 2.20 Å. Although the direct dissociations of methane on Au(111) and the Au pathway of $Au_3Pd(111)$ result in a final state where the methyls are bound to the Au(111) and the Au site on $Au_3Pd(111)$, the interaction of the methyl groups with the surface are so weak such that the transition state retained radical

behavior; Nørskov and coworkers also found that Au(111) was indeed a metal surface on which a radical-like TS was observed.[10] As a result, the illustrated trendline, defined by the equation $E_{TS} = 0.56\Delta E_{X+H\rightarrow XH} + 0.95$ with a mean absolute error (MAE) of 0.25, ignores the two outlier points and only considers the mechanisms where a radical-like TS is observed. Thus, following the linear relation, to decrease the intrinsically high activation energy barriers of dissociating methane, the surface requires a great exothermic change when a hydrogen atom is added. As we have seen, this may also involve pre-adsorbed motifs, where a weakly-bound adsorbate would take in a hydrogen atom with the greatest exothermic gain. This, again, is the greatest advantage of the inclusion of dilute Pd within the Au host; the Pd promoter draws adsorbates that would have otherwise bound too unfavorably to pure Au(111) without binding the adsorbates too strongly such that the system behaves like pure Pd(111).

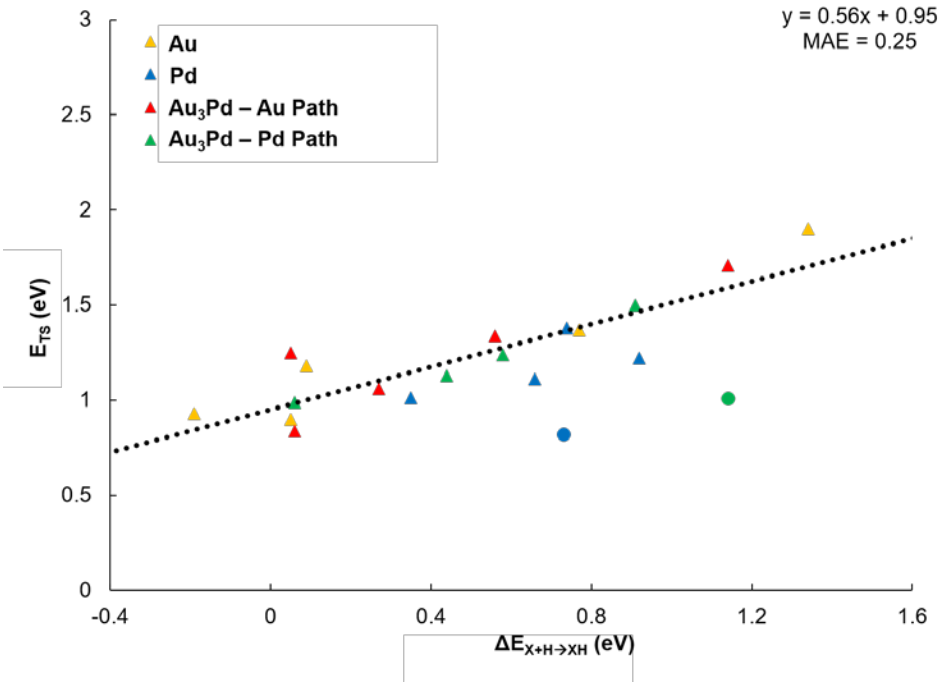

Figure 29. The linear scaling relation between the transition state energy (E_{TS}) of all studied mechanisms and the change in energy when a hydrogen atom is added to a pre-adsorbed motif ($\Delta E_{X+H\rightarrow XH}$). The two circle markers are outliers.

3.4. Conclusions

On the unreconstructed $Au_3Pd(111)$ surface Pd atoms are fully surrounded by Au atoms and can therefore mimic certain features of a single-atom alloy comprised of a Pd promoter and an Au host. We compared the mechanisms of the non-oxidative and oxidative activation of methane on $Au_3Pd(111)$ with its monometallic counterparts, Au(111) and Pd(111). In the first step of the non-oxidative dissociation of methane, $Au_3Pd(111)$ exhibits initial activity similar to that of Pd(111), a surface that is non-selective to methane upgrade because it cleaves the C-H bonds of methane too easily and favors complete combustion or dehydrogenation of methane to coke. After the first dehydrogenation step of methane to methyl, however, $Au_3Pd(111)$ more resembles Au(111), where the subsequent dehydrogenation steps are more difficult than the first. Thus, $Au_3Pd(111)$ inherits both the high activity of Pd(111) and the high selectivity of Au(111) in the non-oxidative activation of methane. We also examined the role of four pre-adsorbed oxygenate motifs – O*, O_2*, OH*, and OOH* – in the oxidative activation of methane. We found that while the adsorbates do greatly improve the C-H bond scission activity on Au(111), they bind poorly to the noble metal's surface and therefore would not be present on the Au(111) surface in the first place. The inclusion of dilute amounts of monomeric Pd in the surface draws adsorbates to the weakly-binding Au, allowing the adsorbates to then facilitate the activation of methane. As an added bonus, since the adsorbates occupy the binding sites adjacent to the Pd atom, the resulting methyl product must bind to an Au site, where it is more favorable to undergo further chemistry. Lastly, we found that the binding strength of a pre-adsorbed motif is inversely related to its ability to facilitate the activation of methane, and we drew a linear scaling relation between the transition state energy of a methane

activation mechanism and the respective energy change when a surface or adsorbate abstracts a hydrogen atom from methane. These findings indicate that alloys containing dilute amounts of Pd in Au may be promising for methane activation and other catalytic dehydrogenation and selective oxidation reactions. Surprisingly, the role of the reactive metal is not necessarily to lower the C-H bond scission energy directly, but rather to bring oxygen moieties to the surface. Thus, the use of singly isolated reactive metals to increase the coverage of O_xH_y species as hydrogen abstraction sites is a promising strategy for methane upgrading and catalytic dehydrogenation or selective oxidation reactions.

Chapter 4. The Non-Oxidative Dehydrogenation of Methanol on the (100), (111), and (211) Facets of Ag

In Chapter 2, we confirmed the efficacy of single-atom alloys in breaking the strong triple bonds of N_2 molecules. In Chapter 3, we published an article that established that single atoms can actively and selectively activate methane for further upgrade. In Chapters 4, 5, and 7, we explore new strategies to improve upon the non-oxidative dehydrogenation of methanol to formaldehyde. In Chapter 4, specifically we explore the reactivity of different surface facets of silver crystals for the reaction. This lays the first-principles, density functional theory groundwork for the future rational design of Ag nanoparticles for this reaction.

4.1. Introduction

Formaldehyde is a critical and commercially relevant chemical building block. Based on data estimates from the United States Bureau of Labor Statistics, the American Chemical Council estimated that formaldehyde and its chemical derivatives accounted for 483 billion dollars in sales in 2014, or almost 3% of the United States gross domestic product in that year.[187] These important chemical derivatives include various resins, plastics, and butanediol. Presently, a wide variety of industrial applications depend on the production of formaldehyde, including the construction, automotive, aviation, pharmaceutical, and cosmetic industries.[188]

Historically, formaldehyde has been produced industrially via the catalytic upgrade of methanol. Originally, silver gauze or crystals were used as dehydrogenation catalysts for the endothermic reaction $CH_3OH \rightarrow CH_2O + H_2$, which would be performed at

temperatures from 600-720°C and a pressure of 1 MPa.[189] In many industrial cases, a co-feed of air over the same catalysts and reaction conditions would promote the secondary, exothermic oxidation reaction $CH_3OH + ½O_2 \rightarrow CH_2O + H_2O$. More recently, Johnson Matthey has implemented the FORMOX™ technology, which replaced the silver-based catalysts with MoO_3-Fe_2O_3 catalysts.[190] The FORMOX™ process, which runs under an excess of air, only promotes the selective oxidation reaction, but the process is run at 300-400°C, with quantitative methanol conversion and selectivities above 90%. All of these reactions are run at high space velocities or low residence times to avoid the decomposition of formaldehyde.

While the FORMOX™ process operates at a lower temperature, which is beneficial for lower energy expenditures and the mitigation of corrosion, the non-oxidative dehydrogenation reaction is still highly desirable. As with other dehydrogenation reactions, the use of a great excess of air leads to higher capital and energy costs. Furthermore, the oxidation reaction's waste gas containing trace amounts of formaldehyde is incombustible and therefore must be specially purified, whereas the non-oxidative dehydrogenation reaction's byproduct hydrogen with trace formaldehyde can be burned as fuel.[191] In addition, the mixture of the feedstreams of methanol and air and the product stream of water is flammable at certain ratios, raising up potential safety issues.[192] Finally, the low-temperature FORMOX™ oxide catalysts require excess air, which drives up utility costs; are more expensive than the traditional Ag catalysts; and cannot be regenerated on-site, unlike the Ag catalysts. Thus, there remains a heavy industrial push to continue studies on Ag catalysts, particularly on understanding the optimal catalyst nanoparticles for different operating conditions.[192] In the review work by Millar and Collins, the authors lament that

"academic literature has focused on fundamental studies of catalyst mechanisms on silver catalyst but only rarely addressed problems which are industrially important such as … design of improved catalysts which are industrially viable [and] impact of catalyst poisoning and how to mitigate these effects."[192]

Our desire is to drive the rational design of industrial catalysts using a theoretical basis. Before we can even tackle the construction of a nanoparticle, we must first understand the catalytic reaction on an atomic scale. In this chapter, through first-principle approaches, we examine the non-oxidative methanol dehydrogenation on the (100), (111), and (211) facets of Ag crystals. We calculate all of the energetics of the elementary reactions that are relevant to the reaction to build an understanding that can be used in the spatial design of a catalyst in Chapter 5.

4.2. Density Functional Theory Methods

The periodic density functional theory (DFT) calculations were performed using the Vienna ab initio Simulation Package (VASP)[93–96] in the Atomic Simulation Environment.[97] The exchange-correlation effects were described by the Bayesian error estimation functional with van der Waals correction (BEEF-vdW)[74] using an energy cutoff of 400 eV. The core and valence electrons were represented with the projected augmented wave (PAW) method.[98,99] Gaussian smearing was used with Fermi temperatures of k_bT = 0.1 eV, and the electronic energies were subsequently extrapolated to 0 K. All geometries were optimized until the forces were less than the convergence criterion of 0.02 eV/Å.

Using an 11×11×11 *k*-point set, the optimized bulk lattice constant for Ag was a = 4.222 Å, which is within 3% error with the experimental value of a = 4.086.[193] All surfaces

were modeled as four-layered slabs with periodic (3×3) unit cells, and the bottom two layers were fixed to their bulk positions, while the top two layers were fully relaxed. Three surface facets were cut: Ag(100), Ag(111), and Ag(211). While the Ag(100) and Ag(111) facets are conventional surface cuts, the Ag(211) "facet" is the step site formed by the intersection of the Ag(100) and Ag(111) facets. The top and side views of the Ag(211) step are shown in Figure 30 below. In particular, the middle column in these two views constitute the step site. All surface models contained a vacuum distance of 20 Å between the slabs in the normal direction. The Brillouin zones for all surface models were sampled with a (4×4×1) Monkhorst-Pack *k*-point set.[102]

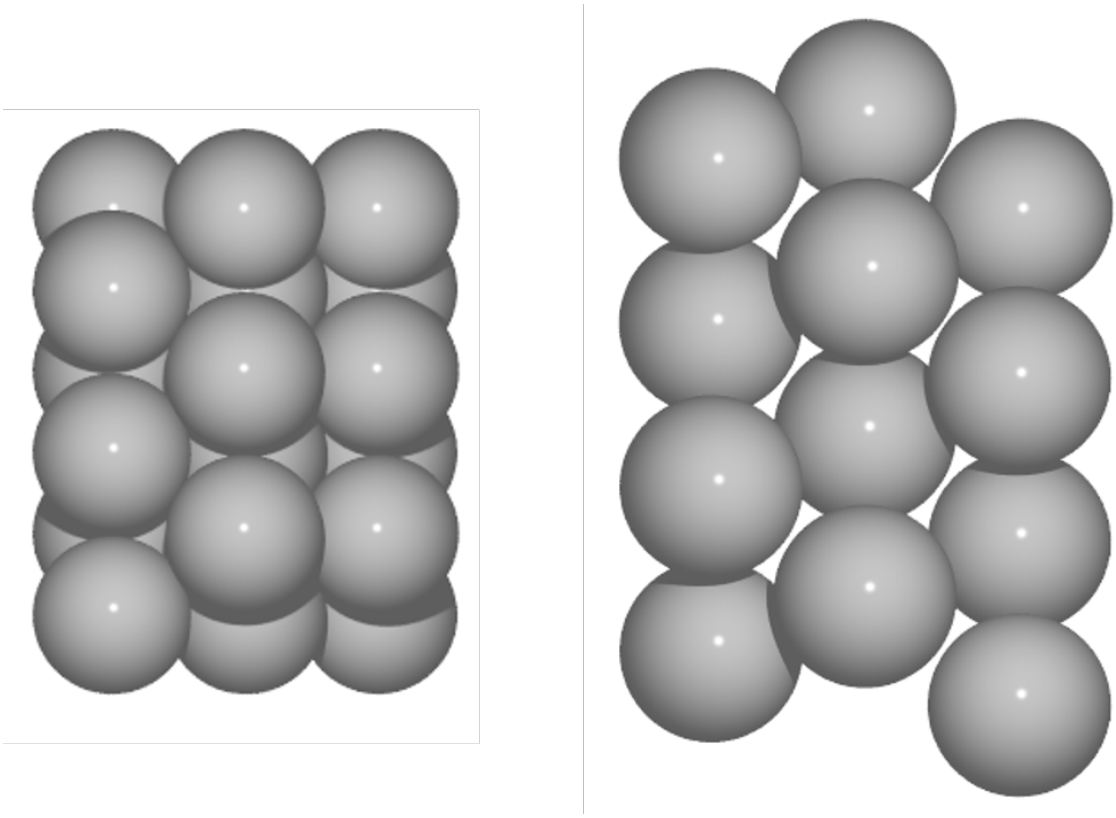

Figure 30. (left) The top view of Ag(211). **(right)** The side view of Ag(211).

There are multiple pathways that the non-oxidative dehydrogenation of methanol can follow on a surface. The pathways considered in this study are presented in the flowchart in Figure 31 below, where a symbol with one (*) indicates monodentate binding while a symbol with two (**) indicates bidentate binding onto the surface.

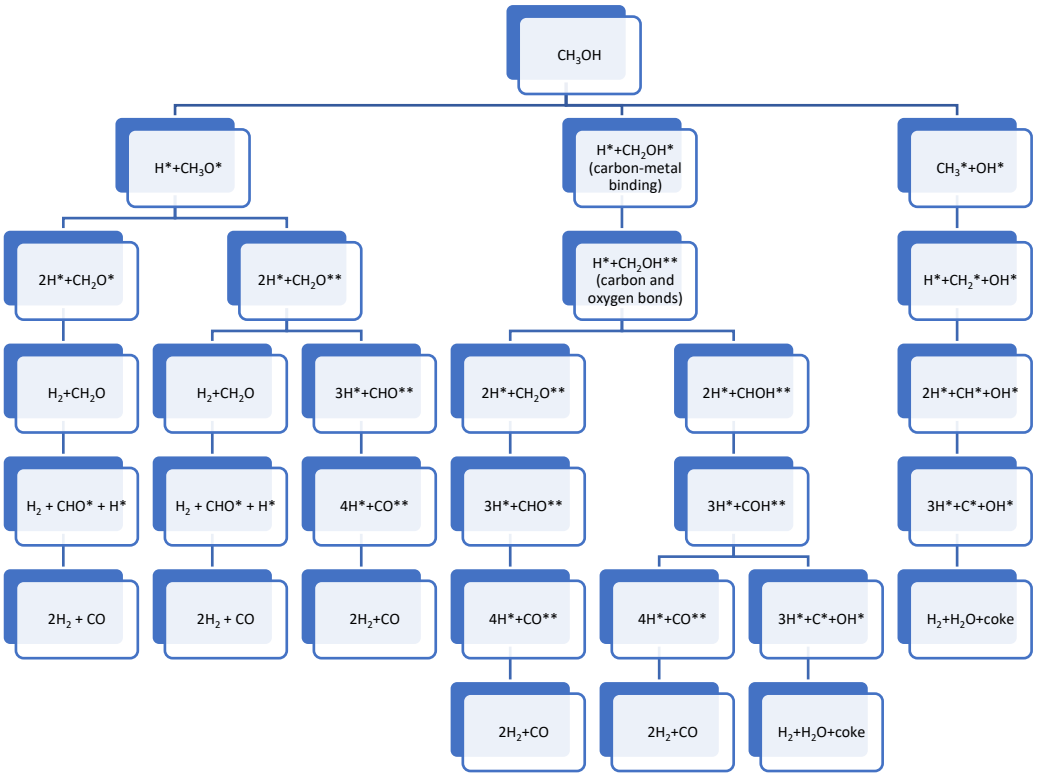

Figure 31. A flowchart of possible and considered methanol dehydrogenation pathways on a metal surface.

In particular, the left-most branch of the flowchart in Figure 31 was most considered because the O-H bond is expected to break much easier than the C-H or C-O bonds. In this chapter, the following set of primary elementary dissociation reactions are examined:

Step 1: $CH_3OH^* + * \leftrightarrow CH_3O^* + H^*$, (33)

Step 2: $CH_3O^* + * \leftrightarrow CH_2O^* + H^*$, (34)

Step 3: $CH_2O^* + * \leftrightarrow CHO^* + H^*$, and (35)

Step 4: $CHO^* + * \leftrightarrow CO^* + H^*$. (36)

In addition, while multiple byproduct formation pathways were considered and calculated, only one is reported in this chapter, where the C-H bond of methanol is broken rather than the O-H bond:

Step 5: $CH_3OH^* + * \leftrightarrow CH_2OH^* + H^*$. (37)

Since there would be multiple H adatoms available on the surface, the recombination of hydrogen on the surface is given as

Step 6: $2H^* \leftrightarrow H_2^* + *$. (38)

Finally, the adsorption and desorption of physisorbed species is considered:

Step 7: $CH_3OH\ (g) + * \leftrightarrow CH_3OH^*$, (39)

Step 8: $CH_2O\ (g) + * \leftrightarrow CH_2O^*$, (40)

Step 9: $CO\ (g) + * \leftrightarrow CO^*$, and (41)

Step 10: $H_2\ (g) + * \leftrightarrow H_2^*$. (42)

The above reactions will be referred to by their Step number in this chapter.

The binding energies are calculated with reference to the respective clean surfaces and the gas-phase energies of methanol and hydrogen. The activation energy barriers were calculated using the climbing image nudged elastic band (CI-NEB) method[76] and the transition states were confirmed to be true saddle points using a vibrational analysis in the harmonic oscillator approximation, which showed one imaginary frequency along the reaction pathway. The free energies are calculated using the ASE Thermochemistry Module.[97]

4.3. Results

4.3.1. Adsorption of Intermediates for the Dehydrogenation of Methanol

First, the binding energies of all intermediates for the primary pathway of the deep, non-oxidative dehydrogenation of methanol to CO were calculated. These binding energies, calculated with respect to gas-phase methanol and hydrogen, are provided below in Table 2.

Table 2. The binding energies (eV) of all methanol dehydrogenation intermediates, calculated with respect to gas-phase methanol and hydrogen.

Adsorbate	Ag(100)	Ag(111)	Ag(211)
CH_3OH* (methanol)	-0.24	-0.21	-0.34
CH_3O* (methoxy)	0.10	0.38	0.30
CH_2O* (formaldehyde)	0.87	0.88	0.80
CHO* (formyl)	1.68	1.81	1.68
CO* (carbon monoxide)	1.19	1.25	1.14
H_2* (dihydrogen)	-0.05	-0.05	-0.06
H* (hydrogen)	0.47	0.42	0.40

There are four closed-shell species that are expected to weakly bind onto all three Ag surfaces: methanol, formaldehyde, carbon dioxide, and dihydrogen. All four of these species physisorb onto the surface with similar binding energies, although the oxygenate closed-shell species do bind slightly stronger on the Ag(211) step. On the Ag(211) step, the oxygen atom of methanol and formaldehyde interact more strongly with the step, leading to a slightly stronger physisorption onto the step site. Regardless, when probing all possible adsorption sites for these four species, the binding energies remained relatively the same, and diffusion barriers for the physisorbed species were calculated to be near zero, indicating that there is no true preferential binding site for the physisorbed species.

For the chemisorbed species, in the dry dehydrogenation, methoxy and hydrogen are the most important ones. From the literature on dry dehydrogenation, the rate-determining step of the dry dehydrogenation of methanol is the initial hydrogen bond scission.[194,195] If Step 1 from $CH_3OH^* + * \rightarrow CH_3O^* + H^*$ is indeed the rate-determining step, then the activation energy for that step must be lowered to achieve higher activities.

4.3.2. Activation Energy Barriers for the Dehydrogenation of Methanol on Ag Facets

The activation energy barriers were calculated for each of the reactions listed in Chapter 4.2. Table 3 shows the activation energy barriers and reaction energies for Steps 1-6 on the three facets.

Table 3. The activation energy barriers and reaction energies of Steps 1-6, in eV.

	Ag(100)		**Ag(111)**		**Ag(211)**	
	E_A	**ΔE**	**E_A**	**ΔE**	**E_A**	**ΔE**
Step 1	**1.40**	0.81	1.51	1.01	1.84	1.04
Step 2	1.19	1.24	1.32	0.92	1.29	0.90
Step 3	1.56	1.28	**1.67**	1.35	1.55	1.28
Step 4	0.28	-0.02	0.56	-0.14	0.58	-0.14
Step 5	2.25	1.90	2.32	1.87	2.26	1.80
Step 6	0.60	-0.99	0.80	-0.89	0.87	-0.86

Almost all of the elementary dehydrogenation steps (Steps 1-5) are endothermic, following the general expectancy for dehydrogenation reactions. The lone outlier is Step 4 on all facets, where the unstable formyl intermediate decomposes into the stably physisorbed CO adsorbate and a hydrogen adatom. Since hydrogen adatoms bind weakly to all three facets, the recombination of the adatoms to form H_2 is very exothermic, but the recombination is not unactivated. On all three facets, the dehydrogenation of methanol to methoxy (Step 1) is more difficult than the dehydrogenation of methoxy to formaldehyde (Step 2), yet easier than the dehydrogenation of formaldehyde to formyl (Step 3). On all three facets, the formation of methoxy (Step 1) is much easier than the formation of CH_2OH. From the bolded barriers in Table 3, Ag(100) is suggested to be the most active facet because it contains the lowest barrier for Step 1, while Ag(111) is the most selective facet because it contains the highest barrier for step 3. Many of these steps in Table 3, and Steps 2 and 4 in particular, show that a trendline cannot be drawn for a metal between

different surface facets, as a lower reaction energy in those steps do not necessarily yield a lower activation energy barrier. Nørskov and coworkers[196] have suggested that different trendlines must be drawn for close-packed and stepped surfaces,[197] and this strategy could also be used to break scaling relations.[196]

To visually compare the reaction energies and the activation energies, the full dehydrogenation scheme (Steps 1-4) as well as the adsorption of methanol (Step 7) and desorptions of formaldehyde and CO (Steps 8 and 9) are drawn in the potential energy diagram depicted below in Figure 32. In this diagram, all adsorbed species are considered to be infinitely separated such that the binding energy of a state is equivalent to the sum of the binding energies of the adsorbates contained in that state. For instance, the binding energy of the (methoxy*+hydrogen*) state is equal to the sum of the binding energies of methoxy* and hydrogen*. The dehydrogenation of methanol to CH_2OH is not shown in Figure 32 to improve readability.

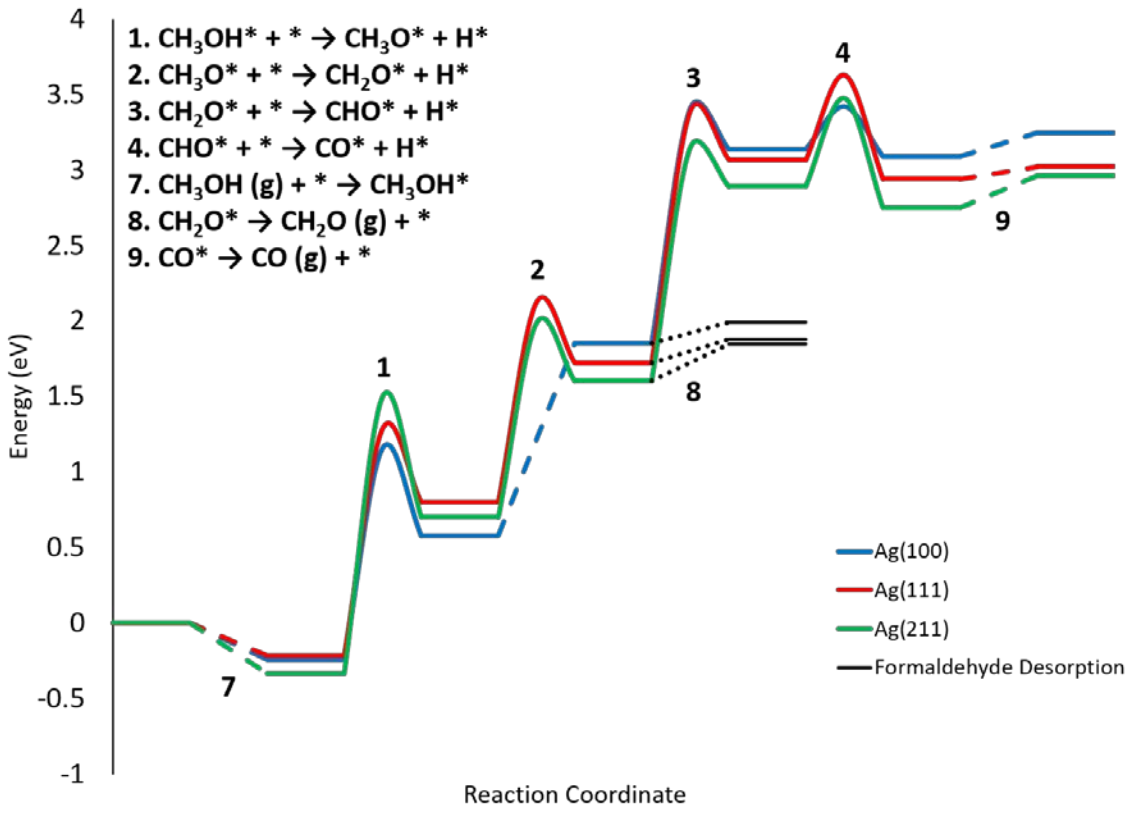

Figure 32. The potential energy diagram for the deep dehydrogenation of methanol over Ag(100), Ag(111), and Ag(211), without any hydrogen desorption.

In Figure 32 above, the numbers above and below each step indicate the step numbers given in Chapter 4.2. The deep dehydrogenation of methanol to carbon monoxide over Ag(100), Ag(111), and Ag(211) is colored in blue, red, and green, respectively. The dotted black lines at Step 8 indicate the desired route, where the physisorbed formaldehyde desorbs to form gas-phase formaldehyde, ceasing the deep dehydrogenation to CO. The dashed colored lines at Steps 7 and 9 indicate the adsorption and desorption of methanol and CO, respectively.

In Figure 32, the hydrogen atoms that break off the methanol molecule are assumed to adsorb onto the surface without any recombinative desorption. The hydrogen adsorption therefore drives up the endothermicity of the reaction and causes the dashed line at Step 2

for Ag(100). In that step on that surface, the sum of the binding energies of the product of that elementary step is greater than the transition state energy of that step. Instead, if the hydrogen atoms are assumed to recombine and desorb without any barrier such that the hydrogen product species in each elementary reaction is ½H_2 (g) rather than H*, then the potential energy diagram would be updated as the below Figure 33.

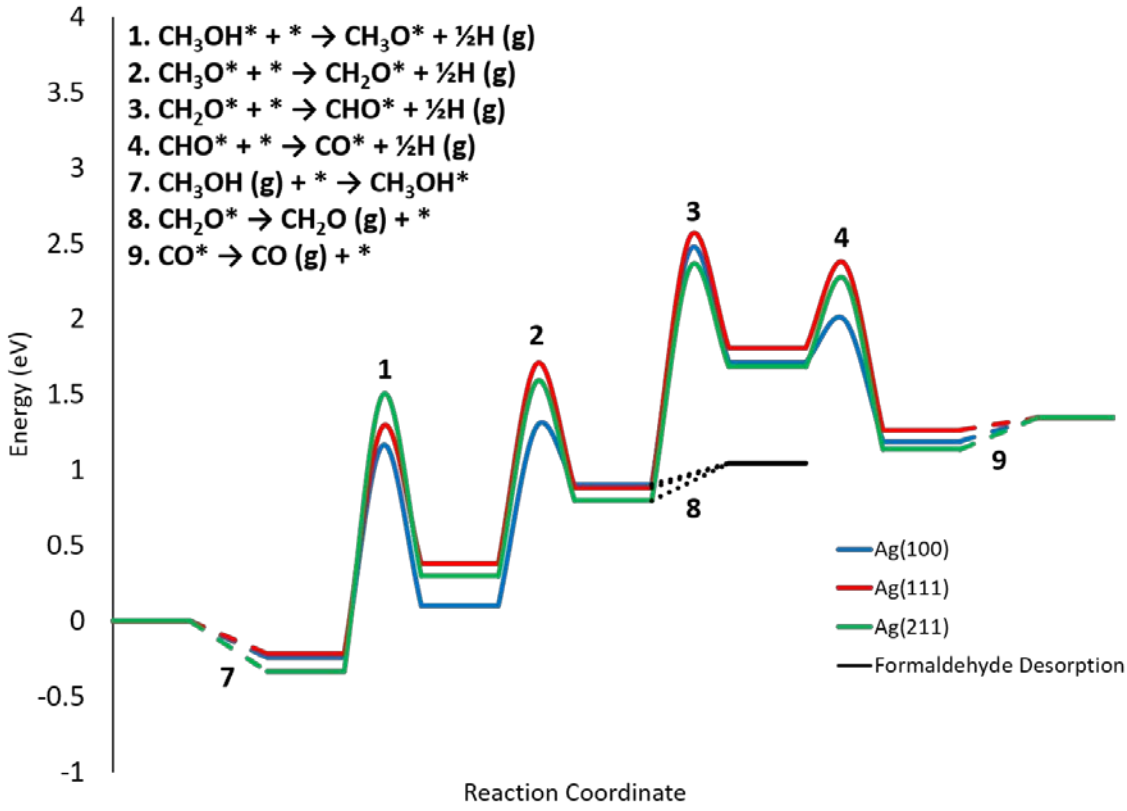

Figure 33. The potential energy diagram for the deep dehydrogenation of methanol over Ag(100), Ag(111), and Ag(211), assuming that hydrogen adatoms recombine and desorb as H_2 without a barrier.

In Figure 33, by removing the effects of hydrogen from the potential energy diagram, the transition state energy of the dissociation of methoxy to formaldehyde on Ag(100) can now be depicted. Since four H* atoms are now allowed to desorb into the gas phase at approximately 0.4 eV for each H*, approximately 1.6 eV of energy is gained on

each respective surface. In Figure 33, it also becomes clear that the first two steps of the dehydrogenation of methanol to formaldehyde is favored on the Ag(100) surface. The undesired dehydrogenation of physisorbed formaldehyde to formyl remains unfavorable in comparison to the desorption of the physisorbed formaldehyde to the gas phase on all three facets.

4.3.3. Methanol Dehydrogenation on Ag Facets in Microkinetic Modeling

To understand how the differences in energetics plays a role at higher temperatures and pressures, a microkinetic model was implemented.[103] Steps 1-10 in Chapter 4.2 were included in the microkinetic model, and the model was run for temperatures from 600-1000 K and pressures of 1-9 bar. The inlet gas concentrations were varied, but the highest activity was obtained when the feed was pure methanol. The frequencies used in the model were obtained through vibrational frequency calculations on the adsorbates and the transition states of the dehydrogenation steps. Entropy corrections were applied in the model using the Shomate equation for the gas-phase molecules and the harmonic approximation for the adsorbates and transition states.[97] Figure 34, 35, and 36 below show the production rates, in units of s^{-1}, of the three main products on Ag(100), Ag(111), and Ag(211), respectively.

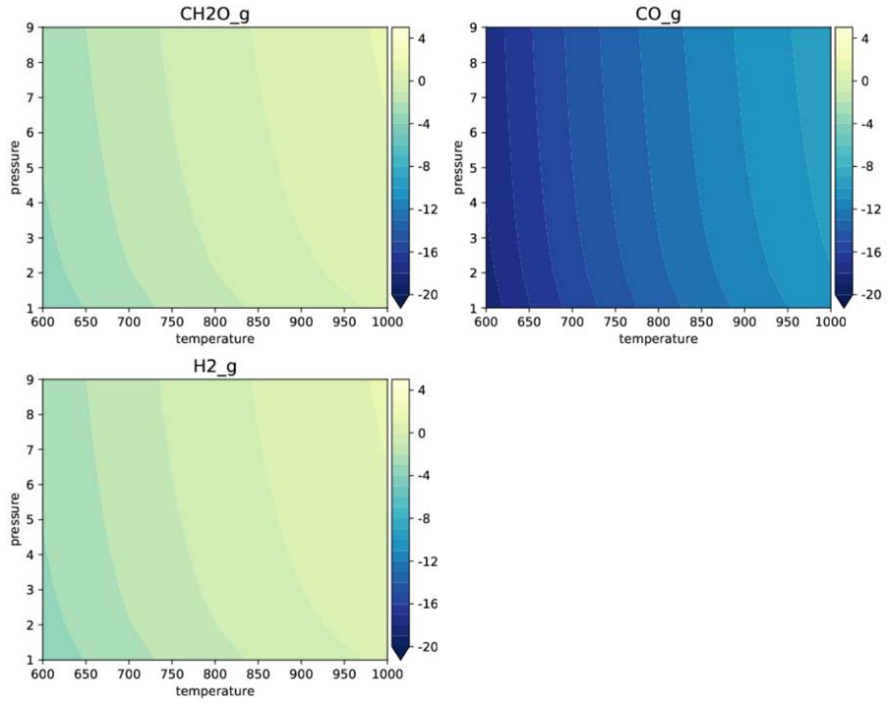

Figure 34. The production rates (s^{-1}) of formaldehyde, carbon monoxide, and hydrogen gas on Ag(100).

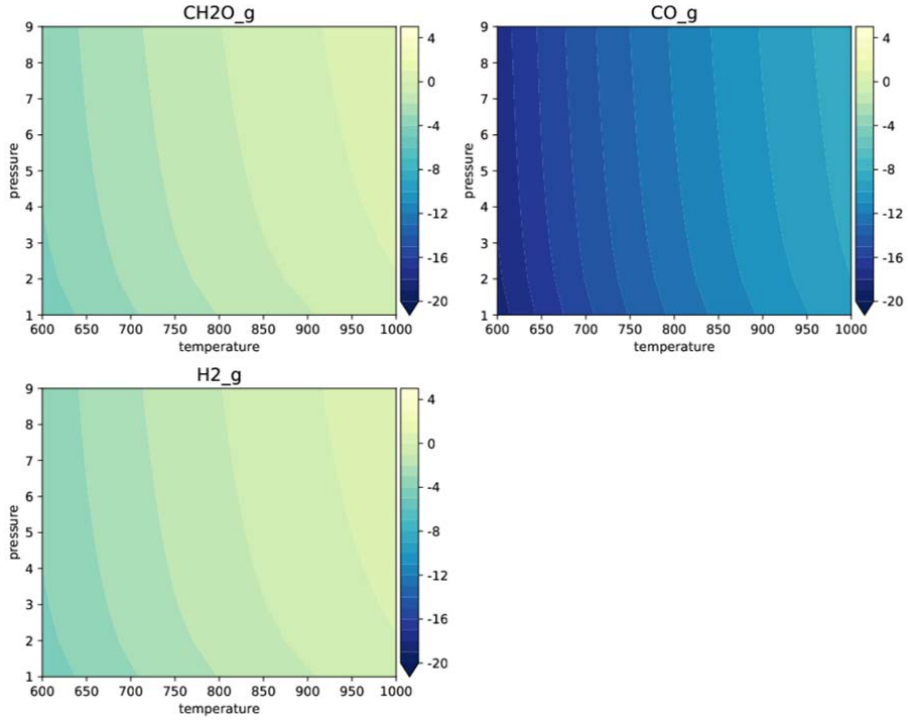

Figure 35. The production rates (s^{-1}) of formaldehyde, carbon monoxide, and hydrogen gas on Ag(111).

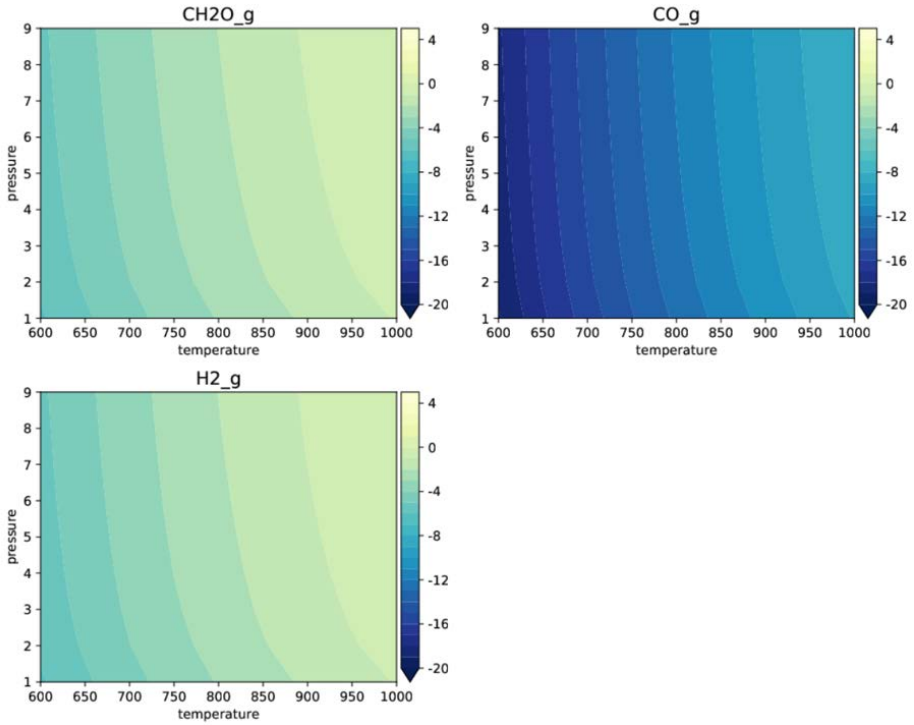

Figure 36. The production rates (s^{-1}) of formaldehyde, carbon monoxide, and hydrogen gas on Ag(211).

From Figures 34, 35, and 36, with increasing temperatures and pressures, more formaldehyde is formed, alongside more undesired CO. From the color map and contours of the three figures, the production rates of formaldehyde for the three surfaces go in the order of $r_{(100)} > r_{(111)} > r_{(211)}$. This can be seen below in Table 4, where the production rates of formaldehyde and CO at the typical process conditions of 1 bar and 800, 850, and 900 K are presented.

Table 4. The turnover frequencies in s^{-1} of formaldehyde and CO at 1 bar and varying temperatures.

	Ag(100)		Ag(111)		Ag(211)	
Temperature	**CH_2O**	**CO**	**CH_2O**	**CO**	**CH_2O**	**CO**
800 K	4.9e-2	3.3e-14	1.0e-2	1.6e-13	1.2e-3	1.6e-13
850 K	1.3e-1	2.7e-13	3.1e-2	1.7e-12	4.4e-3	2.1e-12
900 K	3.2e-1	1.8e-12	8.2e-2	1.4e-11	1.4e-2	2.1e-11

Table 4 confirms that for formaldehyde production, $r_{(100)} > r_{(111)} > r_{(211)}$. This also confirms an experimental study by Kourouklis and Nix who found that Ag(100) was the most reactive surface of the ones studied in this work.[198] In their work, they also examined the coverage of methanol and other intermediates on their Ag surfaces and found none at temperatures up to 600 K; they did not study higher temperatures. The coverage of methanol on Ag(100) at the temperatures and pressures of this study is shown below in Figure 37.

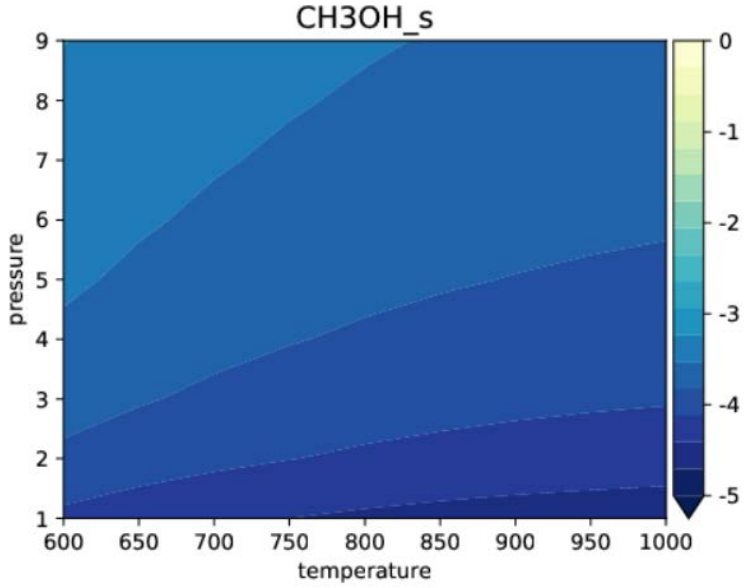

Figure 37. The coverage of methanol on Ag(100) on a logarithmic scale.

The coverages shown in Figure 37 are displayed on a logarithmic scale, so at 600 K and 1 bar, which are the upper bounds of the conditions in the work by Kourouklis and Nix,[198] the coverage of methanol on the Ag(100) surface has an order of magnitude of 10^{-4}. The other intermediates have zero coverage as well, and the surfaces of the other Ag facets are empty too.

Finally, the degree of rate control, developed by Campbell et al., can also be gleamed from the microkinetic model.[199–201] The degree of rate control for any species *i* is given as

$$X_i = \left(\frac{\partial(\ln r)}{\partial\left(\frac{-G_i}{RT}\right)}\right)_{G_{j\neq i}}. \quad (43)$$

In the above equation, r is the production rate of the product of interest, G_i is the Gibbs free energy of species i, G_j is the Gibbs free energy of species j, R is the gas constant, and T is the temperature. A positive degree of rate control indicates that the production rate will increase if the energy of the species is decreased or made more stable, whereas a negative degree of rate control indicates that the production rate would decrease if the species was made less stable. This then allows for the determination of the rate-determining step, which would be unclear by simply analyzing the energetics; while Step 1 has the highest activation energy barrier in the methanol-to-formaldehyde process, Step 2 has the highest apparent activation energy and energetic span.[124] From the microkinetic models, the degree of rate control is +1 for the transition state of Step 1, indicating that the first dehydrogenation step is the rate-determining step in the process. Thus, any future work performed to improve the activity of Ag catalysts for the non-oxidative dehydrogenation of methanol to formaldehyde would need to focus on improving the first dehydrogenation step.

4.4. Conclusion

In this chapter, the non-oxidative dehydrogenation of methanol to formaldehyde was investigated on the (100), (111), and (211) facets of a Ag crystal using first-principles density functional theory calculations. The deep dehydrogenation of methanol to carbon dioxide and other undesired, secondary elementary steps were also explored. From the adsorption studies of the intermediates and the calculated kinetics and thermodynamics in the comparative potential energy diagrams, the energetics suggest that Ag(100) is the most promising surface for the methanol-to-formaldehyde reaction. The undesired deep dehydrogenation reaction was also found to be highly unfavorable. The energetics were input into a microkinetic model, which confirmed that Ag(100) is the most active facet of the three studied facets, followed by Ag(111) and then Ag(211). Interestingly, the coverages of all intermediates and adsorbates were near zero on all surfaces at all temperatures and pressures. Finally, a study of the degree of rate control indicated that the rate-determining step for the non-oxidative dehydrogenation of methanol to formaldehyde is the first hydrogen abstraction step to form methoxy. This would suggest that any future studies to improve this specific reaction should target the first hydrogen bond scission.

Chapter 5. The Terrace Model in Kinetic Monte Carlo Simulations for the Development of an Optimal Catalyst for Methanol Dehydrogenation

In Chapter 4, we elucidated the kinetics and thermodynamics of the methanol dehydrogenation reaction on the Ag(100), Ag(111), and Ag(211) surface facets using first-principles density functional theory. From these calculations, we can begin to build a spatially optimized catalyst nanoparticle for the reaction and industrial operating conditions. We have developed a design paradigm that uses these calculations that predicts an optimal nanoparticle size, shape, and promoter metal for any given reaction; this design paradigm is summarized in Figure 38 below.

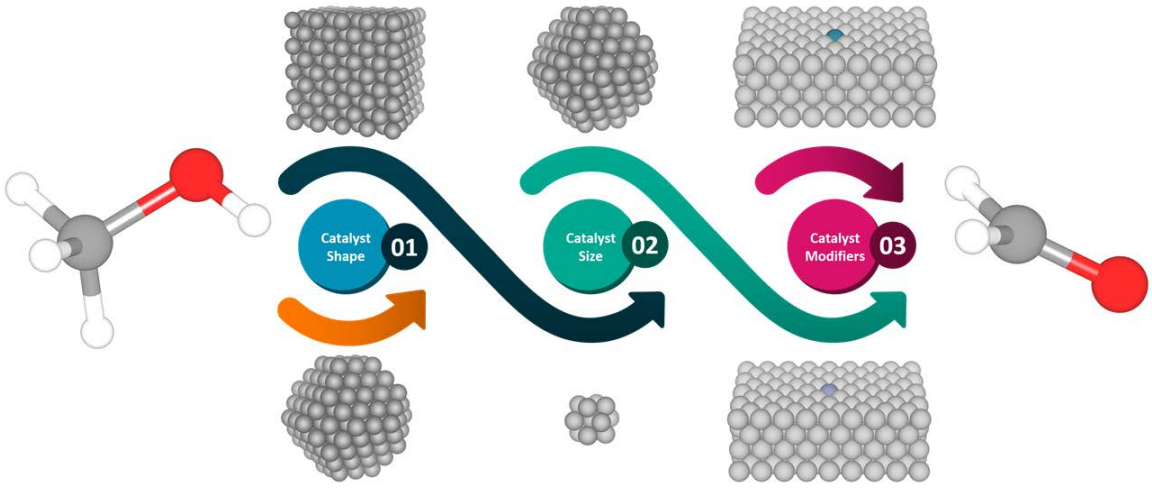

Figure 38. A design paradigm that uses first-principles density functional theory calculations and inputs them into a "terrace model" of a kinetic Monte Carlo simulation to optimize a catalyst nanoparticle size, shape, and promotion.

In our research strategy, we use our first-principles DFT calculations on our pure metal surfaces and input them into a “terrace model” in a kinetic Monte Carlo (KMC) simulation. The KMC simulation allows for the optimization of the nanoparticle shape and size. Then, we can perform further DFT calculations on surfaces that are modified by single-atom promoters in the single-atom alloy surface geometry. The DFT values on the SAAs are then input into new KMC simulations, where we can confirm the effectiveness of the promoter metal and if the catalyst nanoparticle shape and size remains optimal for the reaction conditions.

In this chapter, we use the energetics obtained in Chapter 4 to perform the first two steps, the optimization of size and shape, of our Ag catalyst nanoparticles. A terrace model is created in our KMC simulations and we determine an ideal Ag catalyst nanoparticle for methanol dehydrogenation.

5.1. Introduction

First-principles DFT calculations offer valuable insight into the energetics of a reaction, but kinetic models are needed to translate energetic data into an understanding of reaction rates, production rates, rate control, and turnover frequencies. In Chapter 4, we used microkinetic models (MKM) to estimate the reactivity of the (100), (111), and (211) surface facets of Ag. MKM models have been used heavily for describing heterogeneous catalyst surfaces, and relevantly for this work, the study of methanol dehydrogenation over Pt(111),[195,202–204] Rh(111)[205], and Ni(100)[206] as well as the partial oxidation of methanol over silver surfaces,[207–209] Pd surfaces,[210] Ir(111),[211] Pt_3Sn(111),[212] and MoO_3(010).[213] The

MKM models, however, do have one considerable drawback that prevent its use in our predictive work for the design of an optimal catalyst size and shape.

Although MKM models are computationally efficient, one of the reasons they are efficient is because they take a mean-field approximation with regards to spatial correlations in the surface adlayer.[214] The mean-field approximations cause two different estimations to study. First, diffusion barriers are typically found to be lower than expected in MKM models because the models implicitly consider diffusion to be fast in order to yield perfect mixing for mean-field approximations.[215] In the terrace model later presented in Chapter 5.2, a kinetic model must be able to accurately describe the diffusion of adsorbed intermediates such as methoxy or H adatoms not only across one surface, but between surfaces facets as well. Furthermore, if single-atom alloy surfaces are to be considered, such as in the third step of the design paradigm presented in Figure 38 and in Chapter 7 of this dissertation, the diffusion of an adsorbate away from a promoter atom must be well-represented. The breakdown of the mean-field approximation due to underestimated diffusion barriers has been shown to lead to an overestimation of turnover frequencies of two orders of magnitude in MKM models.

The mean-field approximation that is used in MKM models also leads to difficulty in accurately describing lateral interactions between adsorbates. Lateral interactions occur when two adsorbates are present near each other and are energetically affected by each other. Although we expect that lateral interactions will play a minimal effect on this reaction due to low surface coverages seen in the MKM models in Chapter 4 and literature experiments,[198] if we intend to extend our catalyst design paradigm to other catalytic

reactions and surfaces, we must be able to account for lateral interactions in our kinetic models.

The lattice-based kinetic Monte Carlo (KMC) simulations, first attributed to Bortz et al.,[216] has similar origins to the MKM models. Both MKM and KMC originate and utilize the Markov master equation, which describes the time evolution of a catalytic system.[214] Where they differ, however, is the treatment of the Markov master equation. MKM models apply a system-size expansion and mean-field approximations, which considers the behavior of the Markov master equation at large lattice sizes. MKM models, then, can use ordinary differential equations to describe surface coverages.[217] On the other hand, KMC simulations individually treat events with stochastic realizations that follow the Markov master equation.[125,127,218] Thus, all diffusion events and lateral interactions are explicitly treated by KMC. While computationally expensive, this gives a more accurate description of any catalyst surface, which is desired for our terrace model. For further insight and explanations of the algorithmic details of KMC, the work by Chatterjee and Vlachos is highly recommended.[125]

First-principles KMC simulations have been performed in a variety of systems. Relevantly to the work in this study, KMC simulations have been performed for the non-oxidative dehydrogenation of methanol on Cu(100)[219] and Pd(211),[220] the partial oxidation of methanol on Cu(110),[221,222] and both the non-oxidative and oxidative mechanisms on ZnCu(111).[223] In this chapter, we examine the non-oxidative dehydrogenation on three surface facets of Ag catalysts, both individually and altogether in one terrace model.

5.2. Density Functional Theory and Kinetic Monte Carlo Methods

The periodic density functional theory (DFT) calculations were performed using the Vienna ab initio Simulation Package (VASP)[93–96] in the Atomic Simulation Environment.[97] The exchange-correlation effects were described by the Bayesian error estimation functional with van der Waals correction (BEEF-vdW)[74] using an energy cutoff of 400 eV. The core and valence electrons were represented with the projected augmented wave (PAW) method.[98,99] Gaussian smearing was used with Fermi temperatures of k_bT = 0.1 eV, and the electronic energies were subsequently extrapolated to 0 K. All geometries were optimized until the forces were less than the convergence criterion of 0.02 eV/Å.

Using an 11×11×11 *k*-point set, the optimized bulk lattice constant for Ag was a = 4.222 Å, which is within 3% error with the experimental value of a = 4.086.[193] All surfaces were modeled as four-layered slabs with periodic (3×3) unit cells, and the bottom two layers were fixed to their bulk positions, while the top two layers were fully relaxed. Three surface facets were cut: Ag(100), Ag(111), and Ag(211). While the Ag(100) and Ag(111) facets are conventional surface cuts, the Ag(211) "facet" is the step site formed by the intersection of the Ag(100) and Ag(111) facets. All surface models contained a vacuum distance of 20 Å between the slabs in the normal direction. The Brillouin zone for all models were sampled by a (4×4×1) Monkhorst-Pack *k*-point set.[102]

In this chapter, the following set of primary elementary dissociation reactions are examined:

Step 1: $CH_3OH^* + * \leftrightarrow CH_3O^* + H^*$, (44)

Step 2: $CH_3O^* + * \leftrightarrow CH_2O^* + H^*$, (45)

Step 3: $CH_2O^* + * \leftrightarrow CHO^* + H^*$, and (46)

Step 4: $CHO^* + * \leftrightarrow CO^* + H^*$. (47)

In addition, while multiple byproduct formation pathways were considered and calculated, only one is reported in this chapter, where the C-H bond of methanol is broken rather than the O-H bond:

Step 5: $CH_3OH^* + * \leftrightarrow CH_2OH^* + H^*$. (48)

Since there would be multiple H adatoms available on the surface, the recombination of hydrogen on the surface is given as

Step 6: $2H^* \leftrightarrow H_2^* + *$. (49)

Finally, the adsorption and desorption of physisorbed species is considered:

Step 7: $CH_3OH\ (g) + * \leftrightarrow CH_3OH^*$, (50)

Step 8: $CH_2O\ (g) + * \leftrightarrow CH_2O^*$, (51)

Step 9: $CO\ (g) + * \leftrightarrow CO^*$, and (52)

Step 10: $H_2\ (g) + * \leftrightarrow H_2^*$. (53)

The above reactions will be referred to by their Step number in this chapter.

The binding energies are calculated with reference to the respective clean surfaces and the gas-phase energies of methanol and hydrogen. The activation energy barriers were calculated using the climbing image nudged elastic band (CI-NEB) method[76] and the transition states were confirmed to be true saddle points using a vibrational analysis in the harmonic oscillator approximation, which showed one imaginary frequency along the reaction pathway. The free energies are calculated using the ASE Thermochemistry Module.[97]

To execute our kinetic Monte Carlo (KMC) simulations, we used the Zacros package developed by Stamatakis.[126,224] Within graph theoretical kinetic Monte Carlo,[126]

the catalyst surface is represented in three different zones with periodic boundary conditions, as depicted in Figure 39 below. The first zone, depicted in blue, represents the lattice of the Ag(100) surface. In the (100) zone, the atoms are set in a rectangular matrix, where each atom is 4-fold coordinated. The second zone, depicted in red, represents the lattice of the Ag(211) surface. In the (111) zone, the atoms are set in a hexagonal matrix, where each atom is 6-fold coordinated. The terrace lengths of each of the first two zones can by varied by the number of atoms. The terrace length of the (100) zone will be denoted by x and the terrace length of the (111) zone will be denoted by y, in the form of $[x \times y]$. For example, a lattice that is $[7 \times 9]$ will have a (100) terrace length of 7 atoms and a (111) terrace length of 9 atoms. The (100) and (111) terraces are separated by one column of Ag(211) step sites. The heights of the terraces and the step column are set at 8 atoms and kept equal throughout these simulations. By creating this terrace model, we expect to determine the optimal lengths for the (100) and (111) terraces. These values would then allow for the rational design of an optimal nanoparticle size and shape.

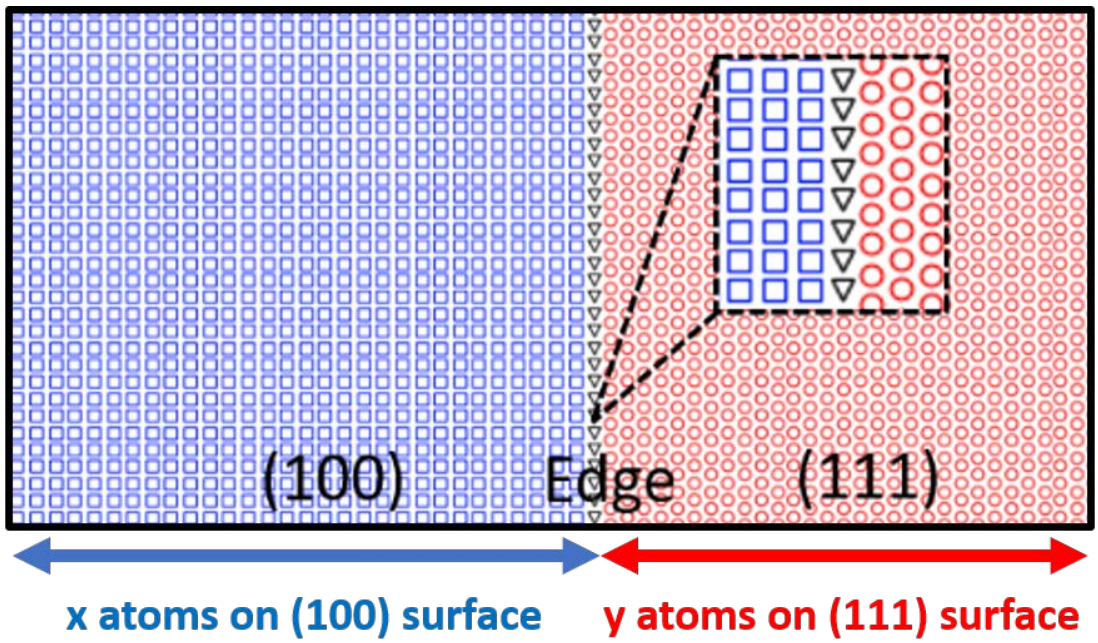

Figure 39. The terrace model implemented in the KMC simulations.

In addition to Steps 1-10 above, the diffusion of adsorbates may play a considerable role in the kinetics of the overall reaction. In this model, we do not consider the diffusion of the physisorbed species (methanol, formaldehyde, CO, and H_2) because they can readily adsorb and desorb, nor do we consider formyl or CH_2OH diffusion. Thus, the two diffusion steps in this model are

$$\textbf{Step 11: } CH_3O_a^* \leftrightarrow CH_3O_b^*, \tag{54}$$

and

$$\textbf{Step 12: } H_a^* \leftrightarrow H_b^*, \tag{55}$$

where *a* and *b* are two different sites on the same surface facet. Diffusion between the different surface facets should be considered as well, but due to the difficulty in modeling a surface to calculate these values in DFT, the diffusion barrier for methoxy and the

hydrogen adatom is assumed to be equivalent to the highest same-surface diffusion barrier of the three surface facets.

The kinetics of all the reactions (Steps 1-12) must be input into the KMC simulation. The input parameters included in this study are a pre-exponential and an activation energy. There are two ways to describe the kinetics of the reactions in this chapter. For surface-mediated reactions, such as the dehydrogenation reactions (Steps 1-6) and the diffusion reactions (Steps 11-12), the reaction kinetics follows the Arrhenius expression. From transition state theory, the rate of a reaction can be defined as

$$k_{rxn} = \frac{k_B T}{h} \exp(-\frac{\Delta G^{\ddagger}}{k_B T}), \tag{56}$$

where k_{rxn} is the rate of the reaction, k_B is the Boltzmann constant, T is the temperature in Kelvin, h is Planck's constant, and $\Delta G^{\ddagger}$ is the difference in Gibbs free energies of the transition state and the initial state, or the Gibbs activation energy. The pre-exponential term is then

$$A_{rxn} = \frac{k_B T}{h}, \tag{57}$$

where A_{rxn} is the pre-exponential term that is used in the input file. Meanwhile, the exponential term from Equation 56 can be rewritten as

$$\exp(-\frac{\Delta G^{\ddagger}}{k_B T}) = \frac{Q^{\ddagger}}{Q_{reactant}} \exp(-\frac{\Delta E^{\ddagger}}{k_B T}), \tag{58}$$

where $Q^{\ddagger}$ and $Q_{reactant}$ are the quasi-partition functions of transition states and reactants, respectively, and $\Delta E^{\ddagger}$ is the zero-point corrected activation energy.[127] Furthermore, in a surface-mediated reaction, the ratio of vibrational partition functions is approximately unity.[127] Therefore, the reaction rate can be re-written as

$$k_{rxn} = \frac{k_B T}{h} \exp(-\frac{\Delta E^{\ddagger}}{k_B T}), \tag{59}$$

and the activation energy needed for Zacros is the $\Delta E^{\ddagger}$ value.

The adsorption and desorption of molecules (Steps 7-10) must be treated differently. Although there is no activation energy for these processes, a pre-exponential for the adsorption must be given, as well as a pre-exponential ratio of the forward and reverse reactions to dictate the kinetics of the desorption of the molecule. In the non-activated adsorption of a species onto the surface, the adsorption rate constant is estimated from collision theory. Since the exponential term is unity due to a zero activation energy, the pre-exponential for the adsorption of a species is equal to

$$A_{ads} = \frac{p * A_{SA}}{\sqrt{2\pi m k_B T}}, \tag{60}$$

where A_{ads} is the adsorption pre-exponential, p is the pressure, A_{SA} is the surface area, and m is the mass of the species.[127] Through partition functions, the pre-exponential ratio is equal to

$$ratio = \exp(\frac{\Delta S}{k_B}), \tag{61}$$

where ΔS is the change in entropy when the species is adsorbed onto the surface. The change in entropy, then, is equal to the entropy of the adsorbate minus the gas-phase entropy. The gas-phase entropy of methanol, formaldehyde, CO, and H_2 are calculated using the Shomate Equation, and the entropy of the adsorbate is estimated using the relation of Campbell.[225]

Lastly, an important feature of KMC is the ability to consider spatial features, including lateral interactions between different adsorbates. To extract the interaction energy between two species, the pairwise interactions between the adsorbates in Figure 40 are considered.

CH_3OH-CH_3OH	CH_3O-CH_3O	CH_2O-CH_2O	CHO-CHO	CO-CO	H_2-H_2	H-H
CH_3OH-CH_3O	CH_3O-CH_2O	CH_2O-CHO	CHO-CO	CO-H_2	H_2-H	
CH_3OH-CH_2O	CH_3O-CHO	CH_2O-CO	CHO-H_2	CO-H		
CH_3OH-CHO	CH_3O-CO	CH_2O-H_2	CHO-H			
CH_3OH-CO	CH_3O-H_2	CH_2O-H				
CH_3OH-H_2	CH_3O-H					
CH_3OH-H						

Figure 40. All combinations of pairwise interactions considered for lateral interactions.

To perform this calculation, each pair of adsorbates was placed in their most-favorable binding position and positioned so that they were approximately one Ag atomic distance away. The adsorbates were allowed to relax and geometrically optimize, and the final energy was obtained. The surface energy and the individual binding energies of the constituent adsorbates from the final energy to yield the interaction energy. An interaction energy that was negative indicated that the pair became more stable when they were in close proximity, whereas a positive interaction energy indicated that the pair became less stable in close proximity. These calculations were performed on the Ag(100) and Ag(111) surfaces, and the interaction energies were input as “clusters” into Zacros. When clusters of adsorbates came together, the interaction energies would be considered. Due to the sheer number of values considered for the interaction energies, the interaction energies will be listed in the Appendix.

5.3. Results

5.3.1. Calculation of Free Energies

The free energies of all gas-phase molecules at standard pressure and adsorbates were calculated through the ASE Thermochemistry module in the ideal gas and harmonic limits, respectively.[97] The temperature considered for the calculations of the free energies was 700°C, or the industrial reaction temperature. The binding energies of the adsorbates were calculated and are tabulated in Table 5 below. In Table 5, the surface energies of Ag(100), Ag(111), and Ag(211) were assumed to be unaffected by any temperature change.

In Table 5 below, the binding energies of methanol, methoxy, dihydrogen, and hydrogen considerably weakened, while formaldehyde, formyl, and carbon monoxide bound considerably stronger in comparison to the DFT energies in Chapter 4.3.1. Likewise, the free energies of the transition states were also calculated. Then, in Table 6, the DFT activation energy barriers are compared to the free energy barriers for the reactions involving hydrogen, or Steps 1-6.

Table 5. The binding free energies (eV) of all methanol dehydrogenation intermediates, calculated with respect to the free energies of gas-phase methanol and hydrogen.

Adsorbate	Ag(100)	Ag(111)	Ag(211)
CH_3OH* **(methanol)**	0.89	0.87	0.88
CH_3O* **(methoxy)**	0.84	1.24	1.13
CH_2O* **(formaldehyde)**	0.08	0.51	0.65
CHO* **(formyl)**	0.80	0.82	0.73
CO* **(carbon monoxide)**	-0.68	-0.89	-0.74
H_2* **(dihydrogen)**	0.92	0.30	0.48
H* **(hydrogen)**	0.99	0.99	0.95

Table 6. The DFT activation energy barriers (E_A) and the Helmholtz free energy barriers (E_{A_F}) of Steps 1-6, in eV.

	Ag(100)		**Ag(111)**		**Ag(211)**	
	E_A	**E_{A_F}**	**E_A**	**E_{A_F}**	**E_A**	**E_{A_F}**
Step 1	1.40	1.72	1.51	1.85	1.84	1.96
Step 2	1.19	1.05	1.32	0.94	1.29	1.01
Step 3	1.56	2.09	1.67	1.77	1.55	1.59
Step 4	0.28	0.24	0.56	0.43	0.58	0.51
Step 5	2.25	2.35	2.32	2.38	2.26	2.40
Step 6	0.60	0.65	0.80	0.69	0.87	0.68

In Table 6 above, Steps 1, 3, and 5 see an increase in the activation energy barriers at higher temperatures, while Steps 2 and 4 see lower activation energy barriers at higher temperatures. This is due to entropy. In Steps 1, 3, and 5, a physisorbed molecule must chemisorb and dissociate into two bound states, which is unfavorable entropically at high temperatures. On the other hand, in Steps 2 and 4, a bound state becomes an unbound physisorbed adsorbate, which causes a gain in entropy. A free energy diagram that assumes that all hydrogen adatoms immediately recombine and desorb is presented in Figure 41 below.

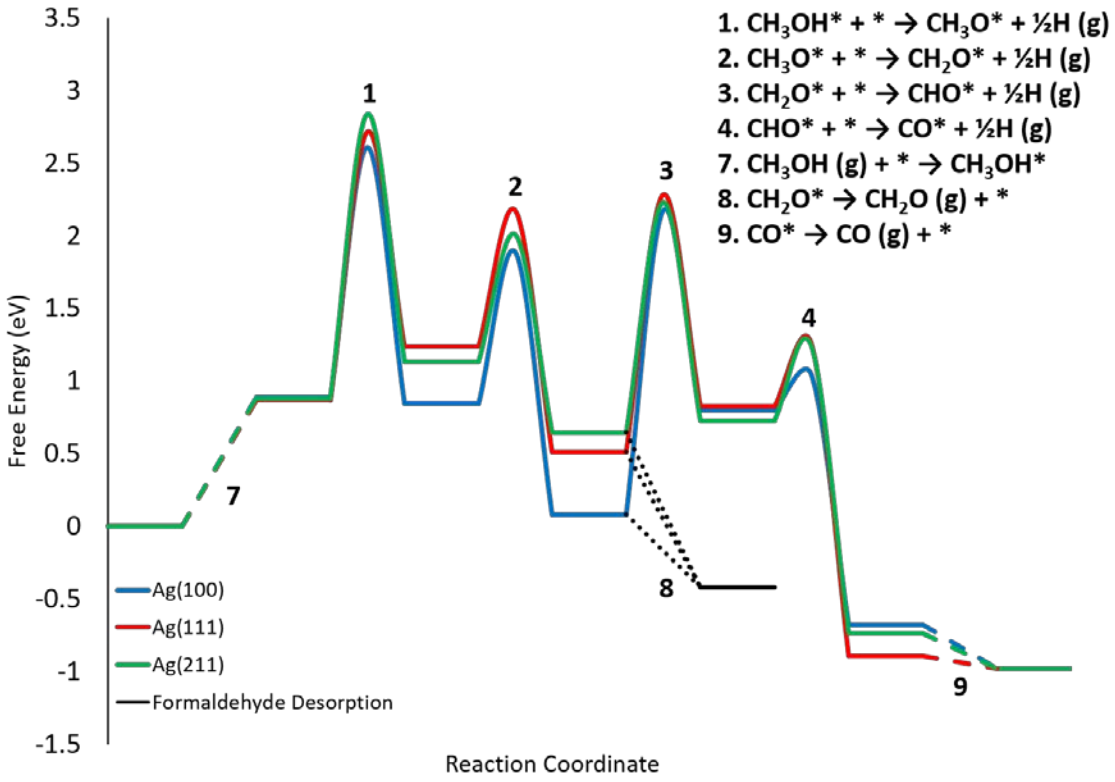

Figure 41. The free energy diagram for the deep dehydrogenation of methanol to CO, assuming that all hydrogen products recombine and desorb without barrier.

In Figure 41, the entire reaction from methanol to adsorbed CO, as well as the desired reaction to form formaldehyde, becomes exergonic at 700°C. If the adsorption of hydrogen remains considered such that the hydrogen adatoms do not recombine and desorb as H_2, the reaction becomes highly endergonic. The Ag(100) seems to remain the preferred surface for the reaction, with the lowest barriers in Steps 1 and 2, as well as a prohibitive activation energy barrier in the undesired Step 3. In this figure, the desorption of formaldehyde is much more favorable, as it physisorbs unfavorably to all three surfaces. To compare with a potential energy diagram using only DFT energies, see Figure 33 in Chapter 4.3.2.

5.3.2. Ag(100) and Ag(111) in Kinetic Monte Carlo

First, the rates of adsorption and desorption are calculated following the methods given in Chapter 5.2. The rates are dependent on the surface areas of the different facets. For the Ag(100) and Ag(111) surfaces, the rates were calculated with the assumption that the terraces were five atoms high and 20 atoms wide, or 100 atoms total. Based on the calculated lattice constant of a = 4.222 Å, the surface area of the Ag(100) terrace was 1783 Å^2, while the surface area of the Ag(111) terrace was 1544 Å^2. The pre-exponentials and pre-exponential ratios of the four major adsorbates on Ag(100) and Ag(111) at 700°C are given below in Table 7.

Table 7. The pre-exponential A (in s^{-1}) and prefactor ratio r (unitless) for the adsorption of the four major adsorbates on Ag(100) and Ag(111).

	Ag(100)		**Ag(111)**	
Adsorbate	***A***	***r***	***A***	***r***
CH_3OH	2.66e10	2.85e-7	2.30e10	2.85e-7
CH_2O	2.75e10	1.88e-6	2.38e10	1.88e-6
CO	2.84e10	8.05e-6	2.46e10	8.05e-6
H_2	1.06e11	9.44e-5	9.18e10	9.44e-5

For the Ag(211) step, in the terrace model, only a single column of these edge sites exist. Therefore, the rate of adsorption of the molecules on the Ag(211) step sites was assumed to be equal to 1/20th of the values for the Ag(100) site. For all sites, the pre-exponential ratio remains consistent because it is dependent on the gas-phase entropy of the adsorbate calculated through the Shomate equation, as well as an assumed adsorbate entropy following Campbell's relation.[225]

The binding energies and interaction energies are input into the simulations as clusters for all three facets. The interaction energies between the Ag(211) step and the terrace sites are omitted due to the difficulty in describing the interaction between an adsorbate on the step site and an adsorbate on either the Ag(100) or Ag(111) terrace. The adsorption/desorption pre-exponential and pre-exponential ratios, as well as the reaction pre-exponentials and zero-point corrected activation energies, are input into the mechanism, which includes Steps 1-12 from Chapter 5.2 on all three facets.

First, the calculations were run on just the Ag(100) and Ag(111) terraces separately. After the first trial calculations, it was apparent that three mechanisms dominated the computational time for the model. The first was the immediate adsorption and desorption of methanol. Due to entropic effects and the lack of interaction of methanol with the surface of Ag, the desorption of methanol was favored over the adsorption of methanol, so any methanol adsorbed onto the surfaces immediately desorbed back into the gas-phase. In addition, the rates of adsorption and desorption are orders of magnitude higher than the rate of dissociating physisorbed methanol into methoxy. Therefore, the heavy majority of the computational time was used in calculating simply the adsorption/desorption behavior of methanol. To remedy this, it was assumed that the adsorption of methanol was automatically dissociative with a barrier equivalent to the barrier for dehydrogenating physisorbed methanol to methoxy. In addition, to further encourage the adsorption of methanol, the pressure was increased to 10 bar, despite industrial reactions occurring at atmospheric pressure. While this does not necessarily reflect real adsorption of methanol, it drastically reduced the computational expense needed to see any surface mechanisms.

After the adsorption of methanol was fixed, the second and third mechanisms that dominated computational time were the surface diffusions of hydrogen adatoms and chemisorbed methoxy. The diffusion barriers for the two adsorbates are so low that the surface mechanisms were dominated by adsorbate hopping. Furthermore, since the coverages of hydrogen were low and two hydrogen adatoms sitting in adjacent sites are needed to desorb as H_2, it became very difficult unlikely for the hydrogen adatoms to randomly "find" each other. Likewise, since the diffusion of methoxy had a much higher rate than the dissociation of methoxy into formaldehyde, minimal dissociation was seen. To decrease the dominance of diffusion events and lower computational expense for meaningful events to occur, the diffusion barriers for both adsorbates were artificially increased. First, both the methoxy and hydrogen adatom diffusion barriers were first increased to 0.75 eV, then to 1.00 eV. The resulting turnover frequencies are presented in Table 8 below.

Table 8. The turnover frequencies, in s^{-1}, of Ag(100) and Ag(111) when the diffusion barriers of methoxy and H are artificially increased.

Diffusion Barrier of CH_3O* and H* (eV)	**Turnover Frequency on Ag(100)**	**Turnover Frequency on Ag(111)**
0.75	1.50±0.05	0.69±0.01
1.00	2.03±0.02	0.78±0.01

On both surfaces, the increase in diffusion barrier led to a higher production rate of formaldehyde, although this was more pronounced on the Ag(100) surface. To improve computational efficiency, the diffusion barriers were selected to be 1.00 eV in the rest of this chapter. For comparison, in the microkinetic modeling (MKM) results in Chapter 4.3,

the turnover frequencies on the same surfaces at 1000 K and 9 bar were 13.6 and 4.0 s^{-1}, respectively. Discrepancies between the two kinetic models may be due to factors such as forced dissociative adsorption in the KMC model, the ability to diffuse between sites in the KMC model, and the inability of the MKM to consider discrete adsorbate-adsorbate interactions. It is believed that the largest source of discrepancy comes from the diffusion of adsorbates, which is absent on the MKM model. While the absolute error between the two kinetic models are quite large, it remains promising that the turnover frequencies follow the same trend where the Ag(100) surface is expected to promote the formation of formaldehyde over Ag(111).

Kinetic Monte Carlo can be useful for the determination of coke formation and deactivation.[226–228] Often, modelers would run their reactions at long times to determine when selectivity or rates change. The Ag(100) and Ag(111) surfaces were simulated to 2e6 seconds, or more than 23 days, but there was no change whatsoever to the production rates of any of the products. An examination of the coverages indicated that there was no buildup of surface coverage whatsoever in KMC, which corresponds with what MKM and experimental literature reported[198] as well. If there is no coverage on the surface, then no coking can occur, and the only catalyst deactivation mechanisms that can occur include particulate deactivation, such as sintering and aggregation, but these studies are outside the realm of this work.

5.3.3. Examining Size in the Terrace Model in Kinetic Monte Carlo

The terrace model was generated, as discussed in Chapter 5.2. First, to optimize the nanoparticle size, the lengths of the (100) and (111) terraces of Figure 39 were varied, yet

kept the same between the terraces such that $x = y$. The height of the terraces was always kept constant at 8 atoms. These calculations gave an estimate of the optimal size for a nanoparticle. The turnover frequencies per site are plotted against the terrace sizes below in Figure 42.

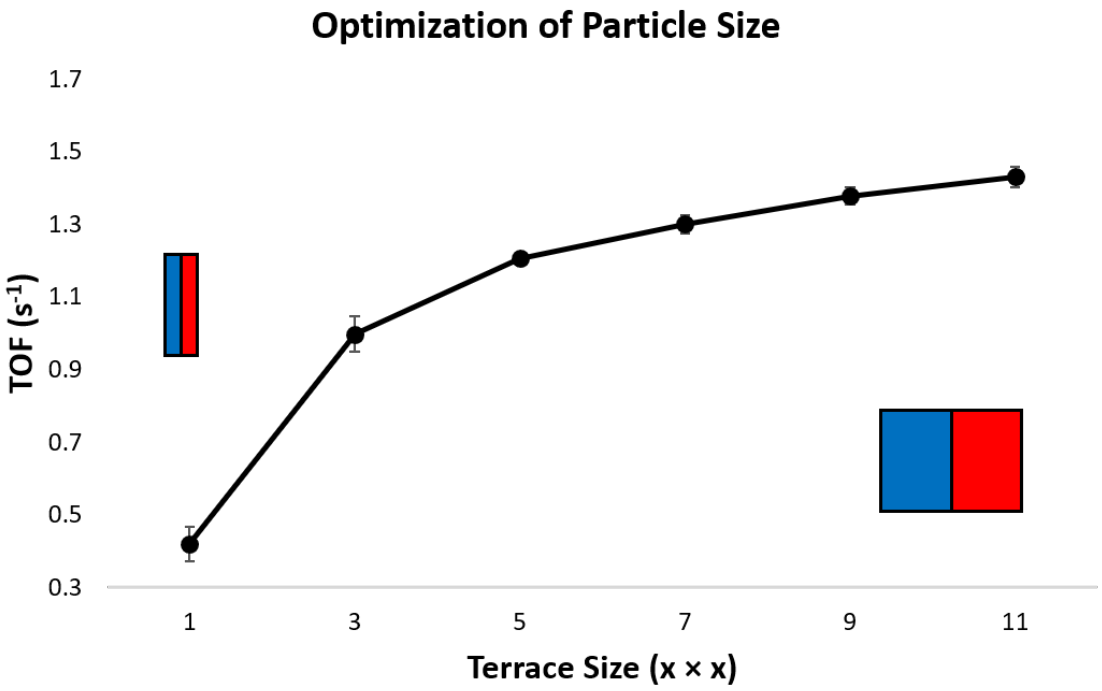

Figure 42. The turnover frequencies per site for different terrace sizes in KMC.

Figure 42 suggests that under the condition that the terrace lengths are the same, the turnover frequency would logarithmically increase as the terrace lengths increase as well. Since the Ag(100) facet dominates and the ratio of Ag(100) sites to total sites increases as the terrace lengths increase, it would then follow that larger Ag nanoparticles are more useful for the dehydrogenation of methanol to formaldehyde.

5.3.4. Examining Shape in the Terrace Model of Kinetic Monte Carlo

Similarly to Chapter 5.3.3, the terrace model was generated, but in these models, the lengths of the Ag(100) and Ag(111) were not the same. By altering the terrace sizes of the Ag(100) and Ag(111) facets and determining which combinations of sizes leads to the highest turnover frequencies, the optimal nanoparticle shapes can be predicted. Figure 43 below plots the turnover frequencies against a changing ratio of terrace sizes and relatively depicts the terrace lengths.

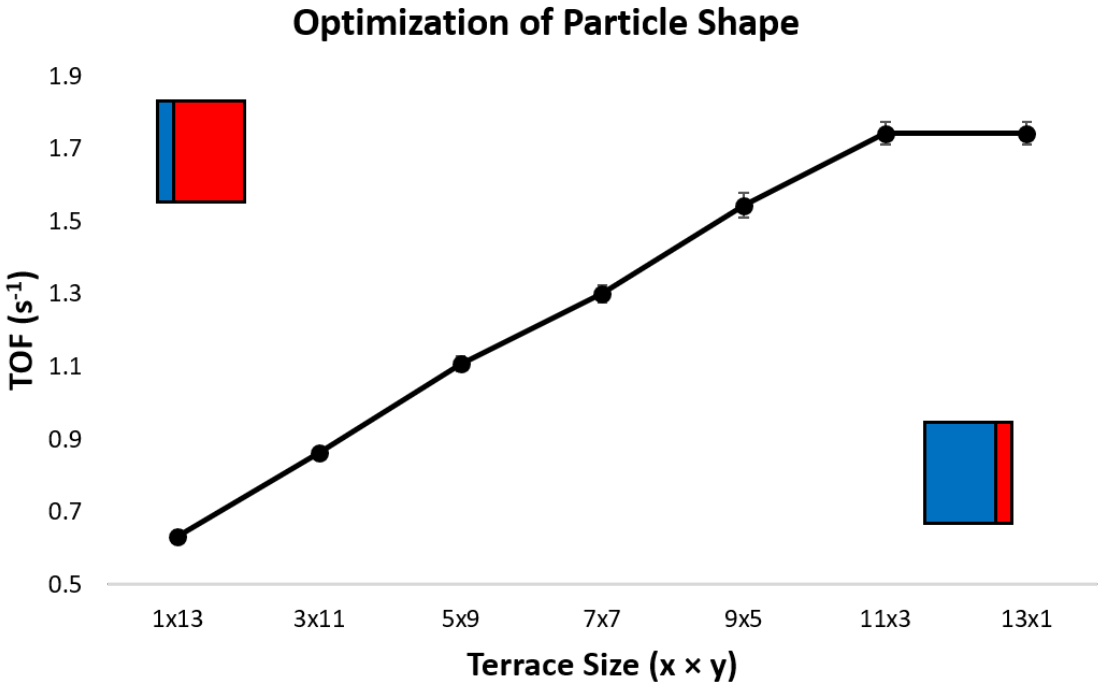

Figure 43. Turnover frequencies of the terrace model when the terrace lengths of the Ag(100) and Ag(111) surfaces are altered.

In Figure 43, the optimal terrace sizes are reached at [11×3] and [13×1] atoms, indicating that higher turnovers result from having more Ag(100) exposure. This would agree with all DFT and MKM calculations up to this point. A nanoparticle that contains a majority of Ag(100) facets, such as the one below in Figure 44, would be cubic in shape.

It is important to note, however, that the dehydrogenation of methoxy to formaldehyde is easier at higher temperatures on the Ag(111) surface than on the Ag(100) surface; if more diffusion were permitted, it is possible that some Ag(111) terraces would improve the production rates of methanol more than a plain cubic structure.

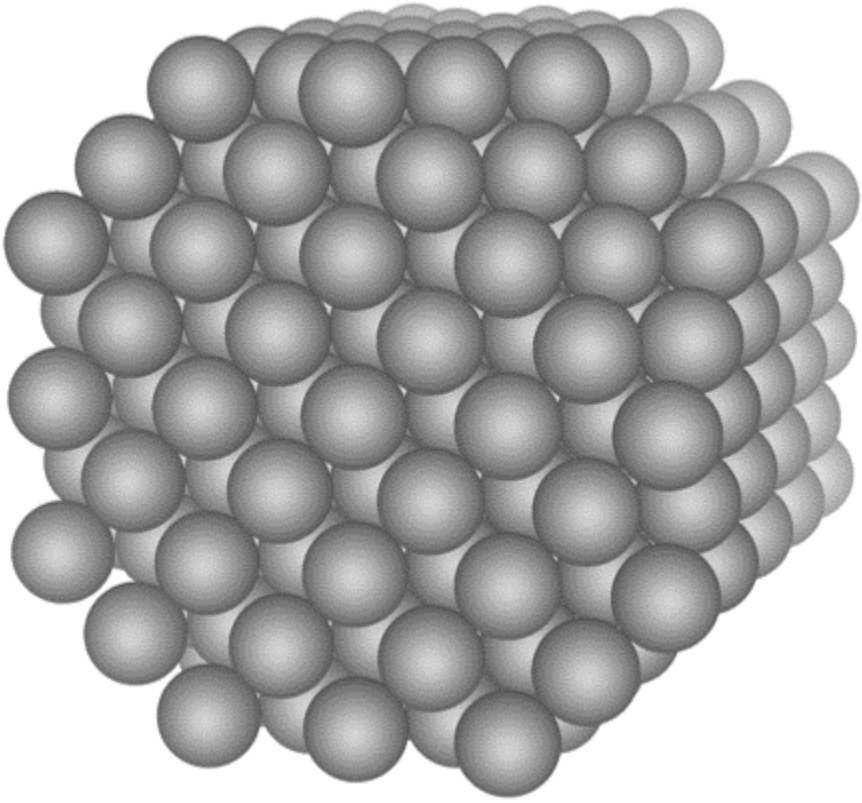

Figure 44. A cube-like Ag nanoparticle would optimize the dehydrogenation of methanol to formaldehyde.

5.4. Conclusion

The energetics of first-principles density functional theory for the dehydrogenation of methanol to formaldehyde were input into a kinetic Monte Carlo (KMC) simulation. In KMC, the reactions were examined on the Ag(100) and Ag(111) surfaces, where it was found that the Ag(100) yielded much higher turnover numbers. A periodic terrace model was then constructed that contained a Ag(100) terrace, a Ag(111) terrace, and a Ag(211)

step that divided the two terraces. The terrace lengths could be altered, which allowed for the examination of different sizes and shapes of nanoparticles. First, by keeping the terrace lengths of Ag(100) and Ag(111) equal to each other and then lengthening and shortening them together, an optimal size for Ag nanoparticles was determined. Then, but altering the terrace lengths of Ag(100) and Ag(111) such that they no longer equaled each other, an optimal shape for Ag nanoparticles was found. The KMC studies in this chapter suggest that small, cube-like nanoparticles would yield the greatest activity for the non-oxidative dehydrogenation of methanol. More importantly, this case study suggests that this process of coupling DFT calculations with a terrace model in KMC can allow for the rational design of catalyst nanoparticles for any catalytic reaction on a metal surface. We hope that this work could begin to bridge the theoretical and experimental realms of heterogeneous catalysis.

Chapter 6. The Stability of Single-Atom Alloy Surfaces

In Chapters 4 and 5, through first-principles DFT calculations coupled with KMC simulations, we have begun to unlock a design paradigm for the rational development of a pure catalyst nanoparticle for methanol dehydrogenation. Our design paradigm of examining different surface facets and tying them together in a terrace model of a KMC simulation can be extended to any catalytic reaction on a metal surface.

Many industrial catalysts also include promoters to improve the activity or selectivity of their catalysts. We have studied promoters in the form of single-atom alloy surfaces. In Chapter 2, we first explored SAAs for the activation of N_2 in the Haber-Bosch process. Next, in Chapter 3, we studied isolated Pd sites in surface geometries akin to SAAs for the abstraction of hydrogen from methane in both non-oxidative and oxidative mechanisms. As an addition to our design paradigm developed in Chapters 4 and 5, we consider adding promoters as SAAs to our model nanoparticles. A considerable issue that was first encountered in Chapter 2, however, was that the SAA surface was not stable; although the Mo-promoted Co(0001) surface was the most active for N_2 dissociation, the surface was more stable when the Mo promoter diffused into the subsurface and bulk, which potentially made it prohibitive as a catalyst promoter. In addition to the diffusion into the bulk, a promoter could diffuse within the surface and find another promoter to aggregate with and form islands, or a promoter could fail to enter the host surface altogether, which would leave the promoter sitting on the host metal as an adatom. In this chapter, we seek to determine which combinations of metals are stable as SAAs. Our table of SAA stability in this chapter will hopefully guide research directions into isolated metal promoters and augment our design paradigm introduced in Chapters 4 and 5. In this work,

the regression and machine learning studies were performed by Karun Kumar Rao, while the majority of the underlying DFT calculations were performed by Khoa Pham, an undergraduate mentee.

6.1. Introduction

Over the past few decades, many catalytic reactions have been tied to linear scaling relationships. These linear scaling relationships often reduce the complexity of catalytic reactions to a few descriptors, such as the binding energy of an adatom or adsorbate that can describe the reactivity of single metal and homogeneous bimetal alloy catalysts quite well.[15,229] In many cases, however, these linear trends must be "broken" through modifications in order to fully optimize the catalytic activity of the metal.[57,144] For instance, a well-established trend in literature is drawn between the binding strength of an intermediate and the transition state energy on single metals and bulk alloys; this is known as the Brønsted-Evans-Polanyi relationship.[229–233] This relationship is an inverse relationship; as the binding strength increases (i.e., the binding is more exothermic), the transition state energy decreases. While it may seem advantageous to select a surface that binds intermediates stronger, therefore decreasing the transition state energy and improving reaction kinetics, this would result in adsorbates that are too strongly bound to the surface, which subjects the surface to severe desorption limitations. Thus, it is highly desirable to find a surface that breaks these linear trends and decreases the transition state energy, while not binding the intermediates too strongly.

Simple alloying would not break these linear scaling relationships. Bimetallic alloys allow for the alteration of the binding energies on its constituent single metals,[12,28,37,234] but the homogeneity of these alloys leads to ensemble and ligand effects

that cause these alloys to behave similarly to single metals.[31,235,236] As a result, there have been many highly innovative strategies proposed by various authors that avoid the formation of homogeneous bimetallic alloys and break these linear trends.[37,38,82,237–246] A popular strategy is to decrease the ensemble effect in metal alloys by reducing the amount of one of the metals to its lowest possible quantity: one single atom. These alloys are known as single-atom alloys (SAAs). In general, single-atom alloys consist of one highly-reactive promoter atom that sits within the surface of a less-reactive host metal.[144] Reactants are activated on the promoter atom with greater activity than the host metal, but intermediates bind less weakly and often disperse or spill over [92] onto the weaker-binding host metal. Thus, these SAAs break linear trends because of a lower transition state energy due to the effects of the promoter atom, yet have intermediates that bind less strongly due to the effects of the host metal.[45]

An early example of the use of SAAs in catalysis is in H_2 activation on both the Pd/Cu(111) and Pd/Au(111) surfaces,[144] where Cu(111) and Au(111) are the respective host metal surfaces and Pd is the promoter atom in both cases. The activation of H_2 requires a high temperature on the pure Cu(111) and Au(111) surfaces, but the presence of the single Pd atom allows for a lower temperature H_2 activation pathway. The H adatoms can then readily diffuse from the Pd atom to the host metal, where it binds weaker and is available for hydrogenation mechanisms. The success of the SAAs for this simple mechanism has led to the exploration of these catalyst surfaces for many other reactions, including hydrogenation,[46–49] dehydrogenation,[51,52] oxidation,[53,54] and reduction [55,56] reactions.

The ascendancy and efficacy of the utilization of SAAs for the above reactions have motivated the discovery of new SAAs for other catalytic reactions; however, the synthesis

of stable SAAs is non-trivial. Even if a certain SAA can be synthesized, dynamic restructuring of surface atoms may occur at the elevated temperatures necessary to drive a catalytic reaction and compromise the unique SAA geometry. Moreover, the presence of adsorbates may also drive the segregation of surface atoms. The understanding of how metal impurities segregate on surfaces was first explored decades ago. Beginning in the late 1970s, various empirical models [247–249] built off the work of Miedema [250] to predict surface segregation, which is the phenomenon where the atomic composition of the surface of an alloy is different from that in the bulk. In the late 1990s, Nørskov and coworkers created databases of surface segregation energies for single metal atom impurities within another metal host using Green's function, first-principles calculations based on density functional theory.[251–253] In these more recent works, the authors calculate surface segregation energies for 24 × 24 combinations of alloys, where a negative surface segregation energy indicates that an impurity within the host would segregate to the surface, whereas a positive surface segregation energy indicates that the impurity would dissolve into the bulk. In addition, they examine the curvature or the 2nd derivative of the surface energies as a function of the concentration of impurity metal within the surface of the host metal. A positive curvature signifies that phase separation and island formation is thermodynamically favorable, while a negative curvature suggests that some level of mixing is expected. These works greatly pushed forward the understanding of surface segregation, but were limited by the understanding of species isolation in the surface, the inability to consider strain effects near the metal impurity likely due to heavy computational demand, the small number of surface structures considered, and the

relatively low-level theory used in the calculations, especially when compared to the theory available today.

In this work, we aim to update the understanding of how impurity or promoter metals segregate on metal surfaces, particularly in the application of single-atom alloys for catalysis. Using density functional theory, we compare the surface energies of the idealized SAA with three other configurations. In the first configuration, we compare the SAA with an alloy where the single promoter metal is in the subsurface to determine if the promoter is more likely to dissolve into the bulk. Second, we examine dimers in the surface, where two atoms of the same promoter species are adjacent in the surface; this comparison allows us to determine if the promoter atom is more likely to stay as a monomer within the surface or dimerize and form islands. Lastly, we explore single promoter adatoms that sit on top of the host surfaces rather than within the host surfaces. Using this data, we create a 28 × 28 database that indicates which configurations are most stable and suggests which combinations of metals could yield single-atom alloys for potential catalytic purposes. Lastly, we propose various machine learning models to understand what properties and factors affect the energies of these different surfaces and drive the formation of one surface feature over another.

6.2. Methods

6.2.1. DFT Methods

We consider 28 different metals in our model; the metals are tabulated, along with their crystal structure, lattice constant(s), semi-core electron considerations, and bulk energies per atom in Table 9. Our goal was to consider all of the 3*d*, 4*d*, and 5*d* elements,

but three were removed from consideration, while two elements outside of the *d*-block were added. Manganese (Mn) was removed from consideration due to its uncommon cubic crystal structure, where it has an $I\bar{4}3m$ Hermann-Mauguin space group with 58 atoms per unit cell.[254,255] Technetium (Tc) was removed because it is a synthetic metal and is radioactive, while mercury (Hg) was removed due to its existence as a liquid at standard temperature and pressure. On the other hand, we included aluminum and lead due to their catalytic performances as antifouling or anti-coking agents.[256–258]

We began by calculating the lattice constants for all 28 metals. The calculated lattice constants were compared to experimental results and found to be in good agreement. These calculated lattice constants were used to simulate the surfaces of the facets with the highest planar densities; these were the (111), (0001), and (110) facets for the fcc, hcp, and bcc systems, respectively. All pure surfaces were 4×4×4 atoms in dimension, with a vacuum space of 20 Å that separates the periodically repeated images of the surface along its normal direction.

To create our 28×28 database, we tested four different alloy analogs of our pure surface, where every combination of promoter and host is examined. These four surface configurations are depicted in Figure 45(a-d). First, our "monomer" surfaces (Figure 45a) represent SAA surfaces, where one promoter atom replaces a surface host atom. Second, our "subsurface" models (Figure 45b) probe surface segregation, where one promoter atom replaces a host atom located in the first sublayer. If the subsurface configurations are more stable than the respective monomer configurations, then surface segregation does not occur under inert environments and the promoter metal would remain in the bulk. Third, our "dimer" models (Figure 45c) investigate phase separation and island formation in the

surface by replacing two adjacent surface host atoms with two promoter atoms. In all bcc(110) surfaces, two neighboring atoms separated by a short bridge were selected and replaced; this led in all cases to a lower dimer surface energy compared to promoter atoms separated by a long bridge. By comparing the relative stabilities of the dimer model with that of the monomer model, we can determine if the promoter prefers to stay isolated or if it would gather to form ensembles within the surface. Lastly, our "adatom" configurations (Figure 45d) consider potential adlayer or cluster growth. In this configuration, one promoter atom is adsorbed on top of the host surface, without replacement. The adatom is located on the fcc adsorption sites for the fcc(111) and hcp(0001) surfaces and on the 3-fold hollow site on the bcc(110) surfaces.

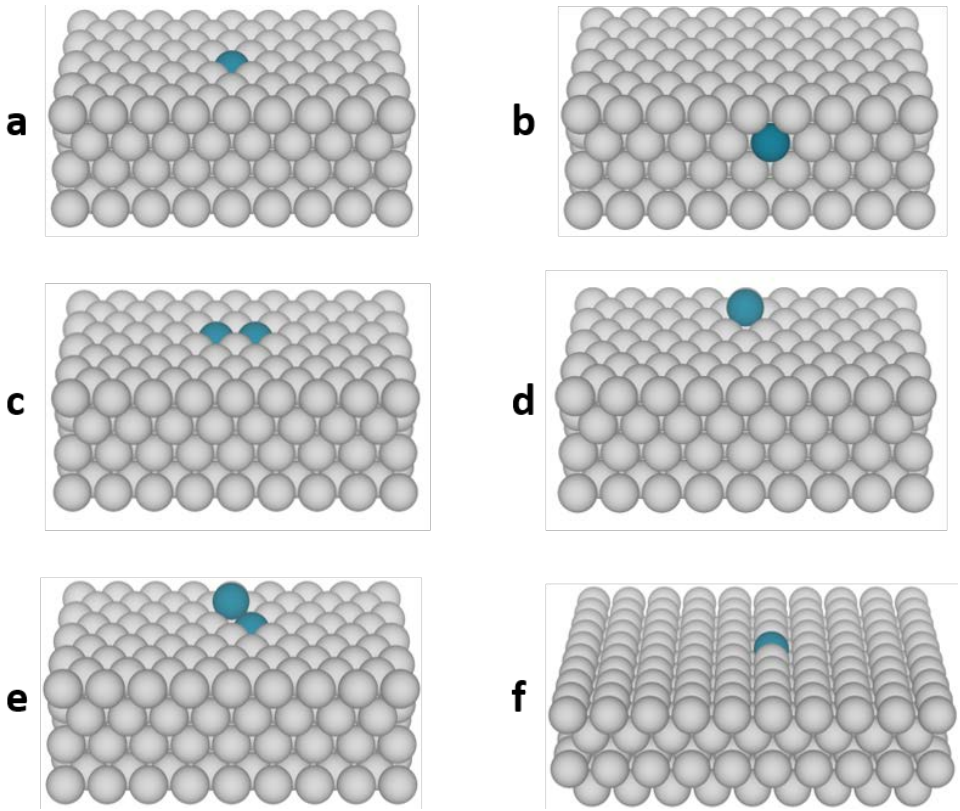

Figure 45. Model representations of **(a)** monomer, **(b)** subsurface, **(c)** dimer, **(d)** adatom, **(e)** adatom+monomer, and **(f)** fcc(100) monomer configurations.

After we created our predictive models, we selected a small subset of host and promoter atoms to test our models with new geometries. In our "adatom+monomer" geometry (Figure 45e), we combined the "monomer" and "adatom" geometries by adding a promoter adatom to an fcc or 3-fold adsorption site that contains a bordering monomeric, promoter atom. In our "fcc(100) monomer" geometry (Figure 45f), we used the (100) surface facet of various fcc host metals and replaced a host surface metal with a promoter metal. Although a comprehensive test of these geometries was not performed and we therefore cannot gather conclusive generalizations about these configurations, they do allow us to test the effectiveness of our predictive models.

In all calculations, the periodic density functional theory (DFT) calculations were performed using the Vienna ab initio Simulation Package (VASP) [93–96] interfaced with the Atomic Simulation Environment.[97] The exchange and correlation were described by the Perdew-Burke-Ernzenhof (PBE) functional.[72] The core and valence electrons are described by the projector augmented-wave (PAW) method;[98,99] many transition metals, particularly the early transition metals, require semi-core *s*- and *p*-states to be treated as valence electrons, so the pseudopotentials for those states are selected based on the recommendations by Kresse.[99] The special pseudopotentials are indicated in Table 9. Gaussian smearing [164] was used with Fermi temperatures of $k_bT = 0.1$ eV, and the electronic energies were extrapolated to 0 K. For the lattice constant calculations, an energy cutoff of 540 eV was used, and the Brillouin zone was sampled by an 11×11×11 Monkhorst-Pack *k*-point grid. Meanwhile, for the calculations of all surface configurations, an energy cutoff of 400 eV was used, and the Brillouin zone was sampled by a 4×4×1 Monkhorst-Pack *k*-point grid. All surface geometries were optimized until the forces were less than the

convergence criterion of 0.02 eV/Å, whereas the convergence criterion was $1.0e^{-5}$ eV/Å for the lattice constant calculations.

All machine learning (ML) methods were programmed using the scikit-learn python package.[259] Specifics regarding the implementation of the ML model are discussed in the Results section and in Chapter 6.2.3.

Table 9. The 28 metals and their crystal structures, calculated and experimental lattice parameters (obtained from Ashcroft and Mermin[260]), and their bulk energies per atom.

Atom	Crystal structure	a (Å), calculated	c (Å), calculated	a (Å), exp.	c (Å), exp.	Semi-core orbitals	Bulk Energy (eV/atom)
Al	fcc	4.041	-	4.05	-	none	-3.75
Sc	hcp	3.321	5.164	3.31	5.28	s	-6.33
Ti	hcp	2.94	4.649	2.95	4.68	s	-7.95
V	bcc	3.002	-	3.02	-	s	-9.12
Cr	bcc	2.852	-	2.88	-	p	-9.62
Fe	bcc	2.837	-	2.87	-	none	-8.31
Co	hcp	2.492	4.042	2.51	4.07	none	-7.11
Ni	fcc	3.522	-	3.52	-	none	-5.57
Cu	fcc	3.634	-	3.61	-	none	-3.72
Zn	hcp	2.745	4.589	2.66	4.94	none	-1.26
Y	hcp	3.66	5.673	3.65	5.73	s	-6.47
Zr	hcp	3.239	5.179	3.23	5.15	s	-8.55
Nb	bcc	3.315	-	3.30	-	s	-10.22
Mo	bcc	3.165	-	3.15	-	s	-10.91
Ru	hcp	2.735	4.305	2.70	4.28	p	-9.27
Rh	fcc	3.852	-	3.80	-	p	-7.34
Pd	fcc	3.956	-	3.89	-	none	-5.17
Ag	fcc	4.162	-	4.09	-	none	-2.83
Cd	hcp	3.131	5.373	2.98	5.62	none	-0.91
Hf	hcp	3.203	5.066	3.20	5.06	p	-9.96
Ta	bcc	3.318	-	3.31	-	p	-11.86
W	bcc	3.191	-	3.16	-	p	-12.94
Re	hcp	2.776	4.477	2.76	4.46	none	-12.42
Os	hcp	2.756	4.341	2.74	4.33	none	-11.25
Ir	fcc	3.879	-	3.84	-	none	-8.83
Pt	fcc	3.976	-	3.92	-	none	-6.06
Au	fcc	4.173	-	4.08	-	none	-3.28
Pb	fcc	5.036	-	4.95	-	d	-3.71

6.2.2. Energetic Evaluation of the Dilute Surface Alloys

We compare the relative stability of each of the four dilute surface alloy geometries in Figure 45 with respect to the basis of bulk-type reservoirs. In general, a host surface with *x* atoms gains *y* promoter atoms and loses *z* host atoms. The corresponding generalized reaction can be expressed as:

$$x\ Surface_{host} + y\ Bulk_{promoter} \rightarrow (x + y - z)Geometry + z\ Bulk_{host}. \quad (62)$$

For the particular geometries considered in this work, the relevant formation energies are calculated on a per promoter atoms basis as:

$$\Delta E^{SAA} = E_{SAA} + E_{Host-Bulk} - E_{Host-Surface} - E_{Promoter-Bulk}, \quad (63)$$

$$\Delta E^{Dimer} = \left(\frac{1}{2}\right)\left(E_{Dimer} + 2E_{Host-Bulk} - E_{Host-Surface} - 2E_{Promoter-Bulk}\right), \quad (64)$$

$$\Delta E^{Subsurface} = E_{Subsurface} + E_{Host-Bulk} - E_{Host-Surface} - E_{Promoter-Bulk}, \quad (65)$$

and

$$\Delta E^{Adatom} = E_{Adatom} - E_{Host-Surface} - E_{Promoter-Bulk}. \quad (66)$$

In these equations, ΔE represents the formation energy per promoter atom of the various conformations. The formation energies are divided by the number of promoter atoms to allow direct comparison between the dimer surfaces, which contain two promoter atoms, and other surfaces. The first term after the equal sign, $E_{geometry}$ (E_{SAA}, E_{Dimer}, $E_{Subsurface}$, and E_{Adatom}), is the DFT energy of the specified surface. The bulk energies of the host and promoter metals are $E_{Host\text{-}Bulk}$ and $E_{Promoter\text{-}Bulk}$ in the respective systems, and $E_{Host\text{-}Surface}$ is the surface energy of the pure host considered in the system. The most stable phase is defined as the geometry that has the most negative heat of formation per promoter atom with respect to Equations 63-66. In this work, the syntax for the combinations of hosts and promoters will be PromoterHost; for example, PdCu indicates a combination where Pd is

the promoter and Cu is the host. Sample calculations for all geometries of PdCu are provided in the Supplementary Material.

6.2.3. Evaluating Models

In this work we consider models of two forms: regression and classification. The regression models use the atomic species (configuration) and geometry as inputs, and outputs an energy (a continuous random variable) for that system. The accuracy of these models is evaluated using the classic Pearson correlation coefficient (R^2). The close the R^2 value is to 1, the better the model. To quantify the accuracy of classification models, whose outputs are a predicted geometry i.e. a discrete integer we consider the effective of true and false positive results. For binary classification, we compute the F_1 score which is defined as the harmonic mean of precision and recall (or sensitivity):

$$F_1 = \frac{2(precision * recall)}{precision + recall}, \tag{67}$$

where precision is the ratio of sum of true positives over sum of predicted conditional positives, and recall is the ratio of sum of true positives to sum of conditional positives. For both binary and multi class classification, the true and false positive rates for each class are considered, and the overall micro-average F_1 score is the average of the individual categorical F_1 scores weighted by the number of samples in that class. For multi class classification we at the area under the curve for the precision recall curve for each class and a micro-averaged area for the overall model performance.

6.3. Results and Discussion

6.3.1. Table of SAA Stability

The most stable surface alloy geometry for 28×28 combinations of promoter and host metals is color-coded in Figure 46. A dark blue square indicates that the SAA geometry is the most stable of the four geometries for that given combination of promoter and host, light blue represents the dimer geometry, light red the subsurface, and dark red indicates that the adatom configuration is most stable. The SAA and subsurface geometries are the most prevalent in the table, with 250 and 268 combinations, respectively. The dimer configuration is most stable in 183 compositions, while the adatom configuration is most stable only 55 times. In particular, the large number of SAA combinations is very promising, indicating that there may be many new SAA surfaces that have not received much attention but may have catalytic significance. One such SAA surface will be explored further in Chapter 7.

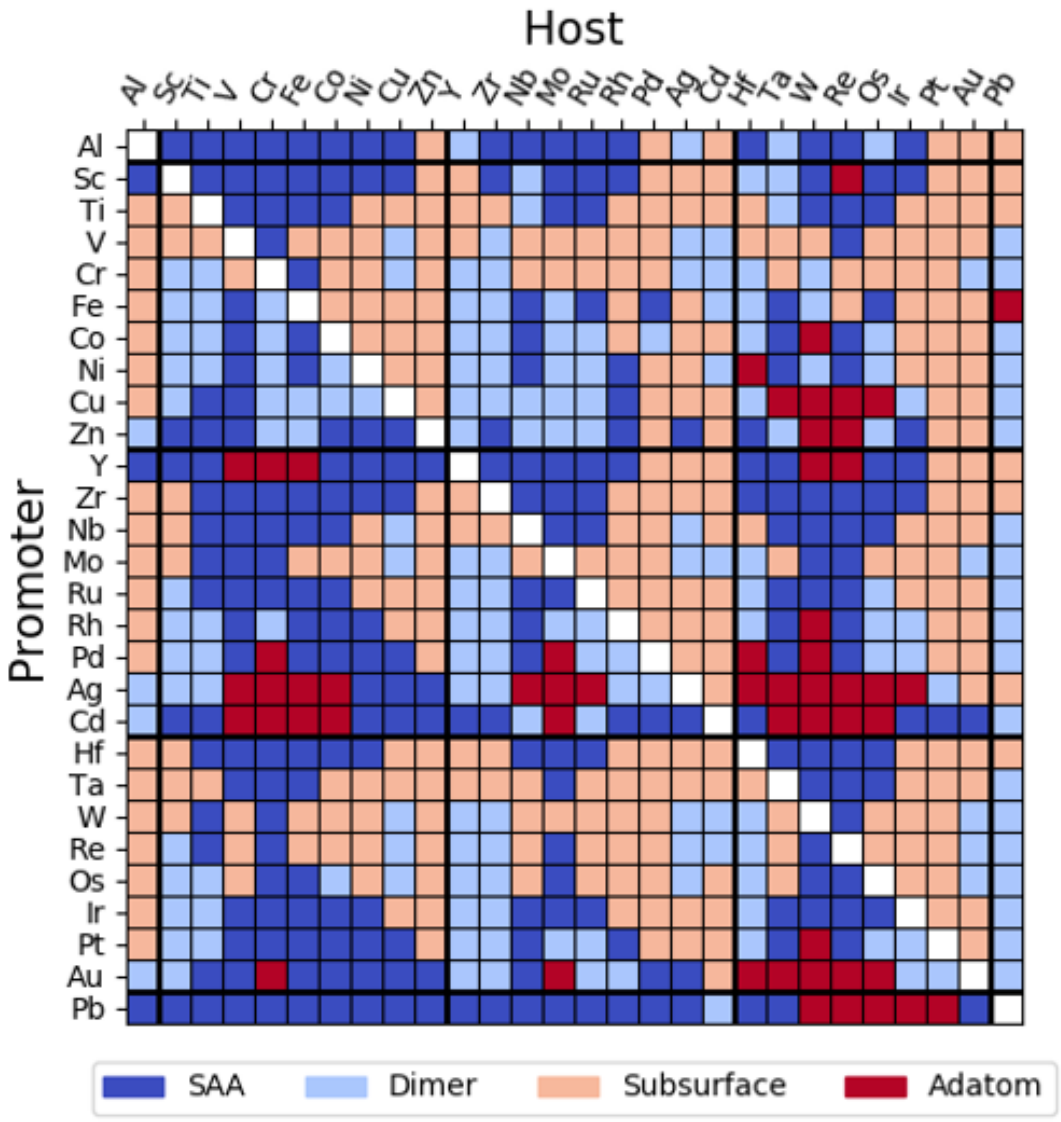

Figure 46. The most stable geometry for dilute binary surface alloys of different *d*-block promoters and hosts with DFT data.

From Figure 46, there seem to be a few patterns that repeat within the same groups in the periodic table. For instance, in all cases, when Group IV metals are promoters, they are most stable in the SAA configuration if Group VIII metals are the hosts. Likewise, when Group XI metals are promoters, the adatom configuration is always the most stable if Group VI metals are hosts. There also seem to be clusters of stability for the different

configurations, where adjacent groups are likely to behave similarly to each other. There does not appear to be any discernable trend, however, when moving across the d-block. In general, the prevalence of adatom and SAA geometries follows closely the segregation energy trends previously reported. [252,253,261]

From the catalysis literature regarding SAA surfaces, some of the best SAA surfaces are those that contain a host that binds intermediates weakly and a promoter that binds intermediates strongly.[45,144] Most experimental studies in the literature examine SAA catalysts containing a Group X promoter and a Group XI host.[46–48,92,144,158,262–271] Of the nine possible combinations of those promoters and hosts, only PdCu and PtCu have SAAs as the thermodynamically most stable geometry under idealized vacuum conditions. The experimental literature, [45,47,48,92,262–264,266,267,271] however, shows that other combinations of those possible nine can be synthesized and characterized as well, even though they are shown to have the subsurface geometry as the most stable configuration. This can be explained by the presence of adsorbates that induce segregation of isolated promoter atoms to the surface during synthesis or dynamically during catalysis. The meta-stable SAA geometries may then be preserved if the diffusion barriers for the promoter to enter the subsurface of the host are sufficiently large relative to the temperature of the reaction. From Figure 46, we believe there are many more combinations that may be promising for different catalytic purposes that have not yet been tested. We also report for which elemental combinations the SAA geometry is within 0.1, 0.2, and 0.5 eV of the most stable configuration in Figure 47 below to account for other possible experimental stabilizing effects or errors in the overall DFT methodology. Aside from the 250 combinations of stable SAAs, there are 119 combinations of SAAs that are within 0.0-0.1 eV of the most

stable configuration, 68 combinations that are within 0.1-0.2 eV of the most stable configuration, and 171 combinations that are within 0.2-0.5 eV of the most stable geometry.

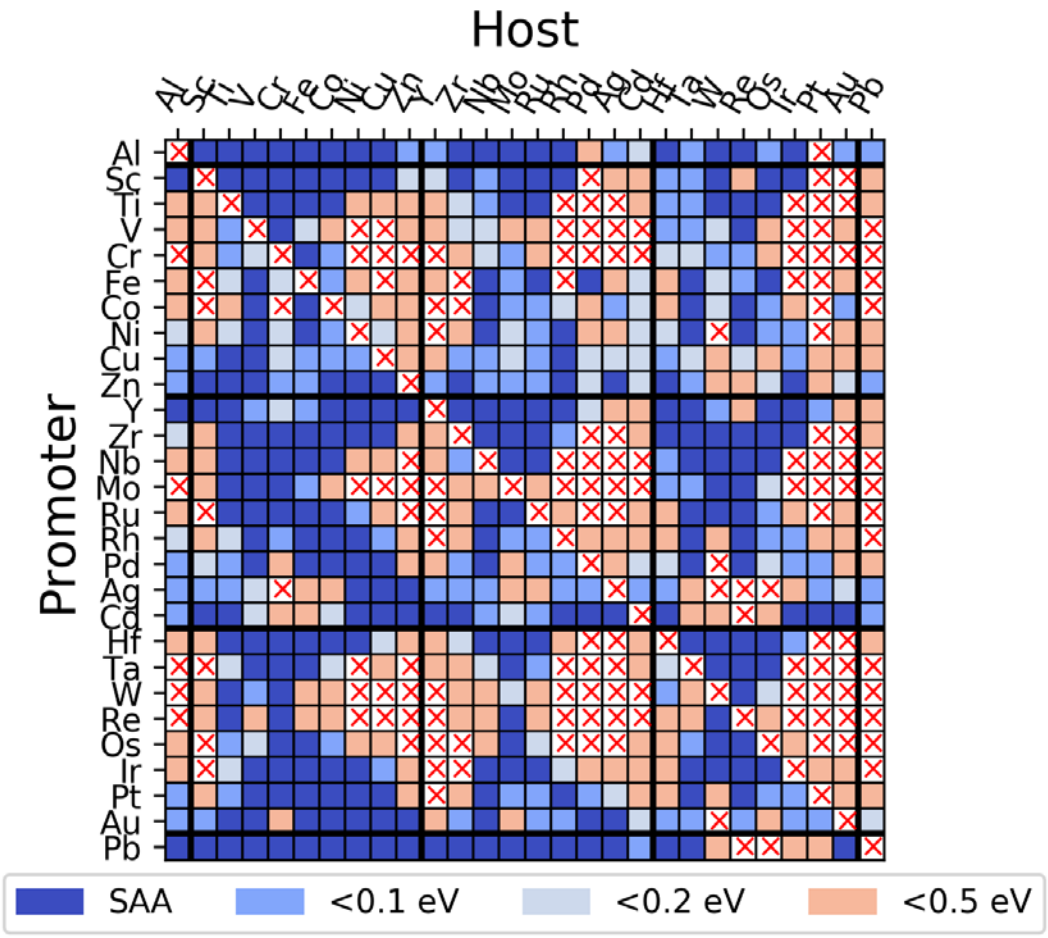

Figure 47. Differential plot of stability of SAAs for all configurations.

Although we present a rather extensive comparison of dilute surfaces, this list is by no means exhaustive. A model is necessary to extend such work to ternary or quaternary systems as complete DFT calculations would be infeasible because of the combinatorics involved with possible geometries. The data in this work presents two major opportunities from a modeling perspective: (1) it is rather exhaustive, having calculated energies for all

combinations for the four geometries, and (2) self-consistent, having been generated with same modeling parameters. Identifying physically relevant descriptors for inorganic materials from these data will also be necessary to understand how adsorbates and specific reaction conditions can induce or affect segregation. Models generated from these data is necessary to both better understand the trends in the data and predict new possible stable surfaces. We explore two specific models, one based on simple bond counting arguments, and a machine learning approach to identify physical properties to elucidate physically relevant processes between different stable geometries. By understanding why certain geometries are formed over others, we can begin to predict geometries or structures that have not yet been calculated and/or would be too computationally expensive to fully explore.

6.2.2. The Bond Counting Model

The ultimate determination of the most stable phase depends on the relative energy of each of the phases. In our calculation of the relative stability of the different geometries, the final energy per promoter atom is calculated with respect to the bulk and surface energy of each the host and promoter (Equations 63-66). Although the energies in Equations 63-66 are calculated from DFT, any model that estimates these energies can be used to predict the relative stability of the different geometries. By estimating the total energy of a system as a sum of bond energies (conceptually analogous to estimating a molecule's energy by summing its individual bond energies), we can also estimate the energy of a particular geometry as:

$$E = \sum n_i b_i, \tag{68}$$

where n_i is the number of i-type bonds, and b_i is the energy of the i-type bond. For pure, bulk systems, if we only consider bonds between nearest neighbors, the bulk energy can be calculated as:

$$H_{bulk} = n_{ii} b_{ii} = \frac{N * C_b}{2} * b_{ii}, \tag{69}$$

where b_{ii} therefore represents the bond energy in the bulk of element *i* and is equivalent to the cohesive energy rescaled to a per bond basis, *N* is the total number of atoms in the unit cell (for primitive cells, *N* = 1 for bcc/fcc metals and *N* = 2 for hcp metals), and C_b is the bulk coordination number (C_b = 12 for fcc and hcp metals and C_b = 8 for bcc metals).The factor of 2 is included because each bond connects two atoms. From the DFT calculated H_{bulk} energies we calculated the *i*-*i* bond energies explicitly and the agreement with experimentally measured cohesive energies is reasonable.

Similarly, from the slab energies, we can estimate the bond energy for each element to a fictitious vacuum atom:

$$E_{Surface} = n_{ii} b_{ii} + n_{iv} b_{iv}, \tag{70}$$

$$n_{ii} = N_{bulk} * \frac{C_b}{2} + N_{surface} * \left(\frac{C_b - C_v}{2}\right), \quad \text{and} \tag{71}$$

$$n_{iv} = N_{surface} * C_v, \tag{72}$$

where N_{bulk} is the total number of bulk-like atoms, $N_{surface}$ is the number of surface atoms, and C_v is the "vacuum coordination," which is the number of bonds that would be formed if a real atom were present (for fcc(111) and hcp(0001) surfaces C_v = 3, and for bcc(110) surface C_v = 2). Equation 70 assumes that all *i*-*i* bonds are of the same character, e.g. bonds within surface layers atoms are equivalent to bonds between layers, so the b_{iv} term physically represents the energy gained from surface relaxation. Although not explicitly

considered in this work, the b_{iv} terms can also physically represent the bond energy between a surface atom and an adsorbate. One advantage of this model description is the ease of extending it to cases where adsorbate-induced surface segregation is studied. Using the b_{ii} values calculated from Equation 70 and surface energies from DFT, we can explicitly calculate b_{iv} energies. We also note that the b_{iv} bond energies in this model are negative, and the difference between b_{iv} and b_{ii} is related to the conventional definition of surface energy.

Up to this point, the model perfectly replicates the DFT energies of monometallic bulk and surface geometries, which were used to fix the parameters b_{ii} and b_{iv} to known reference states using Equations 71 and 72. To estimate the energy of any other dilute binary surface alloy geometry of host *i* and promoter *j*, we can expand Equation 68 to include all possible pairwise interactions:

$$E_{geometry} = \boldsymbol{n} \cdot \boldsymbol{b} = \left[n_{ii}, n_{iv}, n_{jj}, n_{jv}, n_{ij}\right] * \left[b_{ii}, b_{iv}, b_{jj}, b_{jv} b_{jv}\right]^T. \quad (73)$$

The number of each type of bond can be counted explicitly in each geometry. Since the b_{ii} and b_{jj} terms are known from Equation 70 and b_{iv} and b_{jv} are calculated from Equation 72, the only unknown term is b_{ij}, which is the energy of the *i-j* bond. For our 28 element system, there are 378 distinct values of b_{ij}. We fit b_{ij} to the DFT energies of all four geometries (3024 data points) subject to the constraint that $b_{ij} = b_{ji}$.

Using the constrained values of b_{ii} and b_{iv} and the fitted values for b_{ij}, we can recalculate the relative stabilities of each of the geometries from Equation 68 to predict the most stable geometry. A comparison between the bond counting predictions shown in Figure 48 below with the raw DFT data suggests that the bond counting model systematically underestimates the prevalence of stable SAAs and dimers, and

overestimates the stabilities of adatoms and subsurface species. These errors may be attributed to false assumptions equating the bond strength in different geometries. For the dimer geometry, the assumption that the bond energy between atoms *j-j* are equal to the energy between bulk atom is inadequate because surface interactions are stronger than the bulk bonds leading to an undercount of the number of stable compositions. In the case of SAA, we neglect differences in b_{jv} associated with different atomic configurations. We would expect the energy associated with surface relation to be larger in the case when an atom *j* is surrounded by host atoms, *i*, rather than promoter atoms, *j*. The overestimation of the adatom configurations may result from the low coordination of the adatom to the surface which overestimates the stabilizing effect of the b_{jv} term. In the adatom geometry $n_{iv} = C_b - C_v$ which would overestimate the stability when compared to just C_v bonds in the relaxed surface. Finally, given the nature of the classification problem with finite categories, any model with systematic underestimations of Dimer and SAA configurations would lead to an overestimate of another category, in this case, Subsurface.

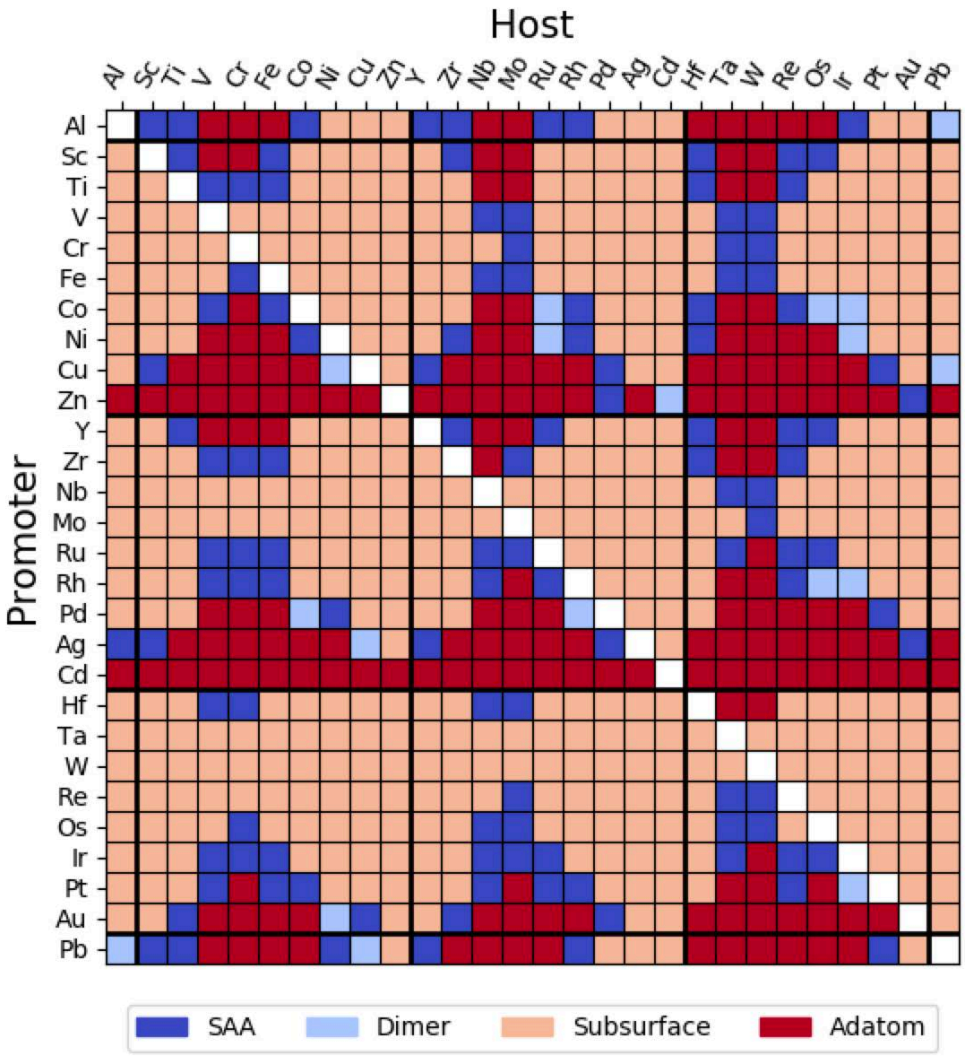

Figure 48. The table of stability based on the bond counting model.

Although the overall model performance of the bond counting model is accurate with respect to energies, (R^2 = 0.997), its ability to classify is not very strong with a micro-average precision recall area of 0.39. This poor predictability despite high accuracy in energies is because a geometry is often the most stable by approximately 0.1eV, requiring very high precision in the model to accurately predict the most stable geometry. One possible source of error in the model is the constraint that $b_{ij} = b_{ji}$. The uncertainty in this

assumption was largest when the promoter and host have different bulk coordination numbers, shown below in Figure 49. Relaxing the constraint and allowing $b_{ij} \neq b_{ji}$ when the bulk coordination numbers of the host and promoter are different did improve the overall energy calculation accuracy (R^2 = 0.9998) but did not improve the geometry predictability of the model (micro-average precision-recall area = 0.37).

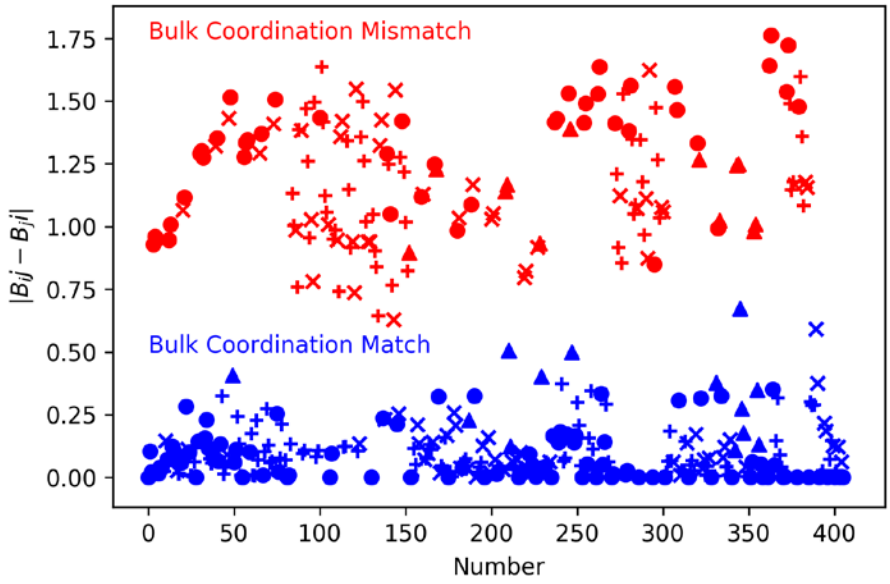

Figure 49. Mismatch in b_{ij} and b_{ji} due to differing bulk coordinations of the constituent metals.

6.3.3. Comparing SAAs and Other Geometries

We can use Equation 70 to calculate the energies required to determine the stability of various geometries (Equations 63-66). If we consider a pairwise comparison of the stability between SAA and the other geometries, the difference in formation energies can be simplified to:

$$\Delta E^{SAA} - \Delta E^{Dimer} = -b_{jj} + b_{ij}, \tag{74}$$

$$\Delta E^{SAA} - \Delta E^{Subsurface} = b_{ii} - b_{iv} + b_{jv} - b_{ij}, \tag{75}$$

and

$$\Delta E^{SAA} - \Delta E^{Adatom} = (2C_v - C_b)\left(\frac{b_{ii}}{2} + b_{jv} - b_{ij}\right). \quad (76)$$

Most synthesis methods for SAAs comprise the fabrication of the host nanocrystal and then a subsequent deposition of highly dilute amounts of promoter metal.[144,158] If a single promoter metal atom contacts the host surface, it can remain on top of the host surface as an adatom or enter the surface layer of the host as an SAA. Generally, when SAA catalysts are synthesized, the promoter metal is scarce such that there is a large distance between two promoter atoms. If there are two promoter metals that are nearby, however, the comparison between the stabilities of the SAA and dimer configurations can predict whether or not the promoter atoms would aggregate within the surface layer. From our DFT calculations, when only comparing SAA and Dimer, there are 422 combinations where the SAA is more stable than the dimer configuration and 334 combinations where the dimer is more stable, as depicted in Figure 50 below. Within Figure 50, there are distinct regions of SAA or dimer stability that appear to be repeatable across the periods of the table, particularly when the host metal is further to the right of the *d*-block. The stability criterion derived from the bond counting model (Equation 74) for the dimer geometry is simply $b_{ij} < b_{jj}$. If the bond between an *i* and *j* atom is stronger, i.e. more negative, than the energy of the *j*-*j* bond (promoter-promoter interaction), then a SAA is more likely to form than the dimer and vice versa and is shown in Figure 51. The bond counting model predicts 454 stable SAA configurations (332 true positive), and 302 Dimer geometries (189 true positives) with a micro averaged $F_1 = 0.70$.

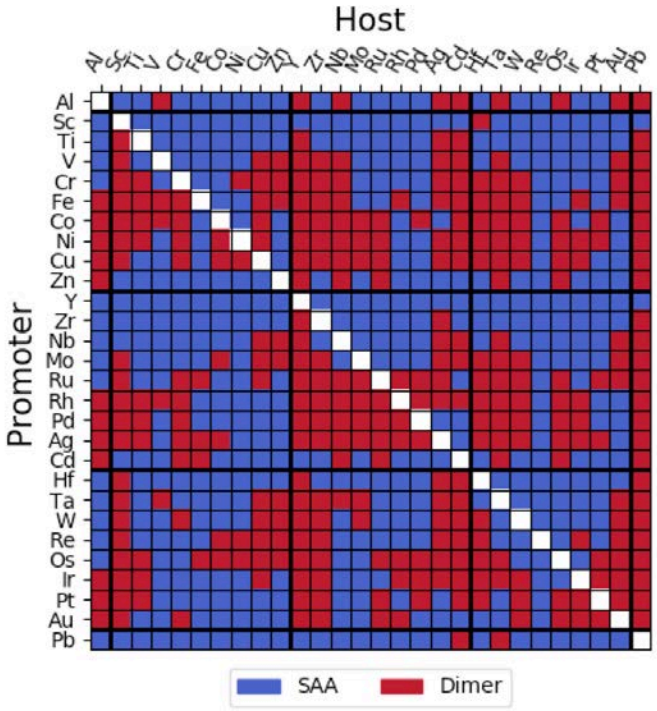

Figure 50. A binary comparison of the stability of SAAs and dimer configurations, calculated through DFT.

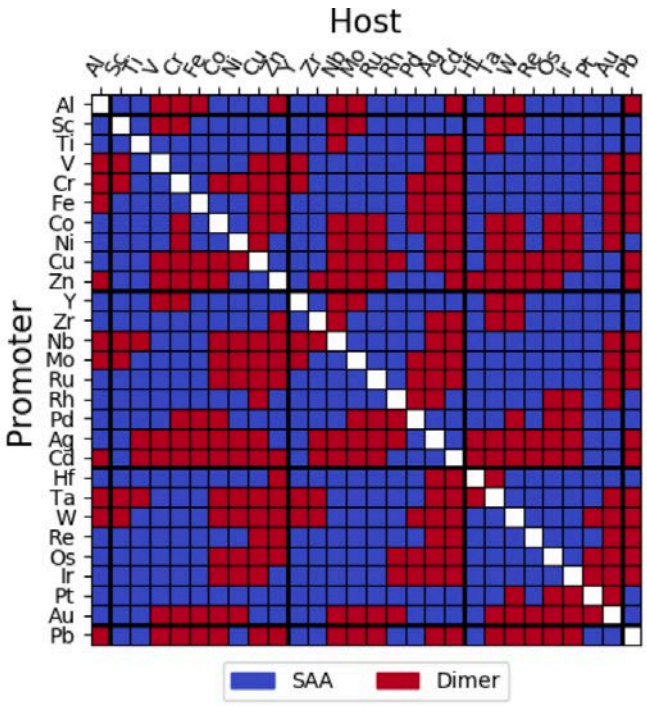

Figure 51. A binary comparison of the stability of SAAs and dimer configurations, calculated through the bond counting model.

One limitation of this bond counting approach is that if a dimer is more stable than a SAA, the model predicts trimer geometries are more stable than dimers, and surface clusters are more stable with more atoms. If $b_{ij} < b_{jj}$ then the model would extrapolate that including more and more j-j bonds (through larger and larger clusters) would be more favorable. Since dimer geometries have gained some theoretical interest as N_2 reduction catalysts,[82] this approach can not directly predict when dimers are more favorable than SAA and simultaneously more stable than trimers or larger cluster sized without modification. The dimer can be stabilized over the SAA and trimer geometries using the bond counting model if we introduce a fractional adsorbate bonding energy, i.e. an adsorbate binds only to a fraction of the possible promoter atoms. In this case where x fraction of the promotor sites are not free and not bound to the adsorbate ($0 \leq x \leq 1$) the rule of thumb for a dimer to be the most stable geometry between dimer and trimer is:

$$\frac{1}{2}\left(b_{ij} - b_{jj}\right) + x v_c \left(b_{jv}^{adsorbate} - b_{jv}\right) < 0. \tag{77}$$

If x = 0, (adsorbate binds to all promoter sites) we simplify to $b_{ij} - b_{jj} < 0$, which is in contradiction to the dimer vs. SAA stability rule and implies the dimer can never be both more stable than SAA and Trimer. If $x \neq 1$, where the adsorbate binds to a fraction of possible promoter sites, then a valid solution can be found for Equation 77. The first term in Equation 77 is guaranteed to be positive because we already assume dimer to be more stable than SAA, so this model shows that not only is it important to prevent the adsorbate from binding to all possible promoter sites (i.e. $0 \leq x$), but also that the adsorbate bind with sufficiently strength to compensate for the tendency of the promoters to cluster driven by the difference in b_{ij} and b_{jj} energies.

Once the single promoter atom has entered the surface layer of the host metal and if it does not dimerize, it can either remain in the surface layer or diffuse into the sublayer. By DFT, between only SAA and subsurface, we predict SAA in 356 configurations, and subsurface in 400 configurations, as shown in Figure 52 below. When comparing the stability of the SAA and subsurface in the bond counting model, $b_{ii} + b_{jv} < b_{ij} + b_{iv}$ must hold true for the SAA to be more stable. This criterion implies that combination of *i*-*j* and *i*-*v* bonds must be stronger than the *i*-*i* and *j*-*v* bonds. In the absence of adsorbates and surface relaxation effects, the vacuum bonds are weak and may be neglected. In this limiting case the stability criterion reduces to $b_{ii} < b_{ij}$, *i.e.*, the host atoms need to bind stronger to themselves than to the promoter atom. In the reaction relevant environment with a specific adsorbate present, the adsorbate may preferentially bind to a particular metal atom and significantly alter the strength of the b_{iv} and b_{jv} bonds which could also stabilize a particular promoter atom as compared to when exposed to a vacuum. In such cases a surface atom can be substantially stabilized and effectively prevented from diffusing into the bulk. This argument is consistent with the current models of surface segregation that are used to model near surface alloy or core-shell geometry stability versus subsurface.[37] Using this rule of thumb and fitted bond energies, we predict the stability of SAA versus subsurface rather well in Figure 53. In this comparison by the bond counting model, the SAA geometry is most stable 320 times (304 true positives) and the subsurface geometry is most stable 436 time (384 true positives) with a micro-averaged $F_1 = 0.79$.

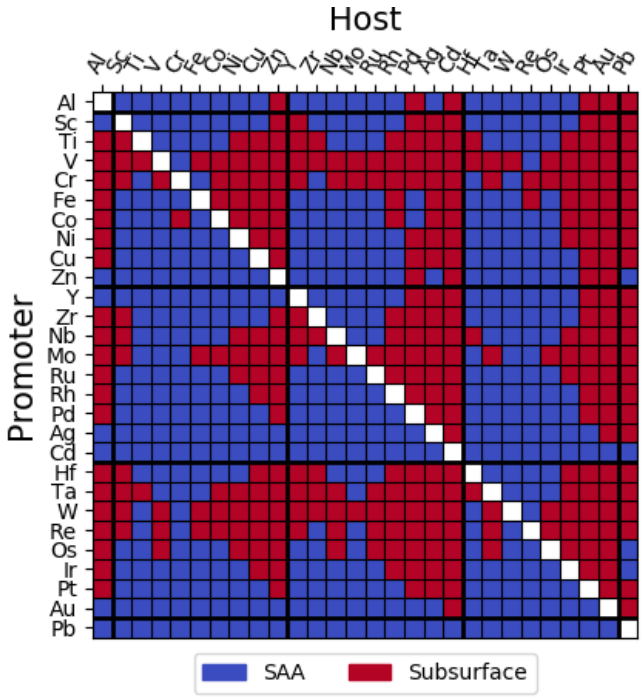

Figure 52. A binary comparison of the stability of SAAs and subsurface configurations, calculated through DFT.

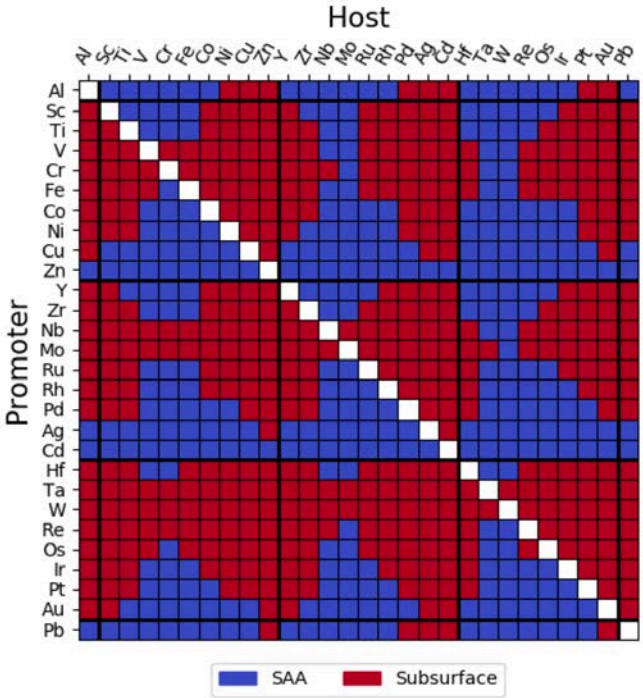

Figure 53. A binary comparison of the stability of SAAs and subsurface configurations, calculated through the bond counting model.

Finally, from our DFT calculations, the SAA geometry dominates over the adatom configuration and is the most stable configuration in 674 metal combinations, whereas the adatom geometry is most stable in only 82 configurations, as shown in Figure 54. The bond counting model in Figure 55 predicts 573 SAA configurations (548 are true positives), and 183 adatom geometries (57 are true positives) and a micro-averaged F_1 score of 0.81. By the bond counting model, the SAA is more stable than the adatom geometry, i.e., $\Delta E^{SAA} - \Delta E^{Adatom} < 0$. Because $(2C_v - C_b)$ is always negative, the criteria simplifies to $\frac{1}{2}b_{ii} + b_{jv} > b_{ij}$. In other words, the strength of the *i*-*j* bond creation must be more than the strength of half a host bulk bond and one host 'vacuum' bond. Given the bond values calculated from these geometries, this criterion explains why the adatom is relatively rare compared to the SAA. Physically, the dominance of the SAA geometry may be due to the greater coordination number for the promoter atom in the SAA geometry compared to the adatom geometry. Interestingly, in 37 of the 82 combinations (45.1%) where the adatom geometry is more stable, a BCC metal is the host, even though BCC metals only make up seven out of the 28 metals (25%) considered in this study. This may be due to a lower planar density on bcc(110) surfaces compared to the fcc(111) and hcp(0001) surfaces.

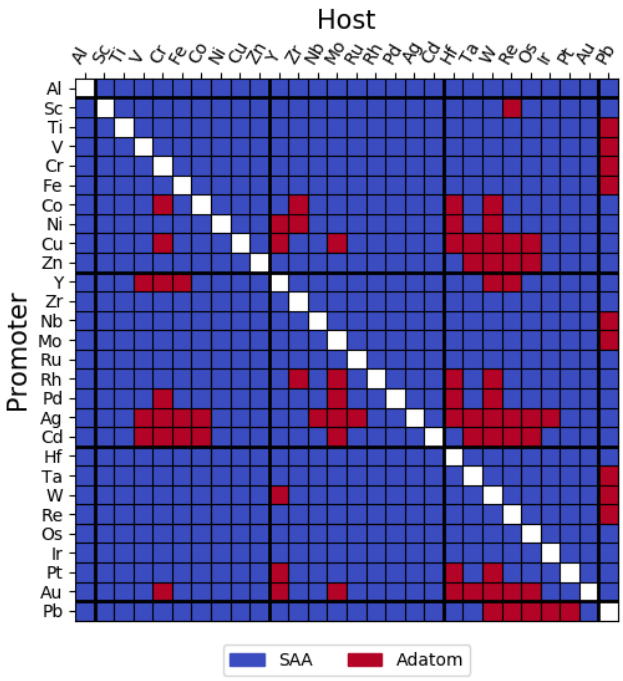

Figure 54. A binary comparison of the stability of SAAs and adatom configurations, calculated through DFT.

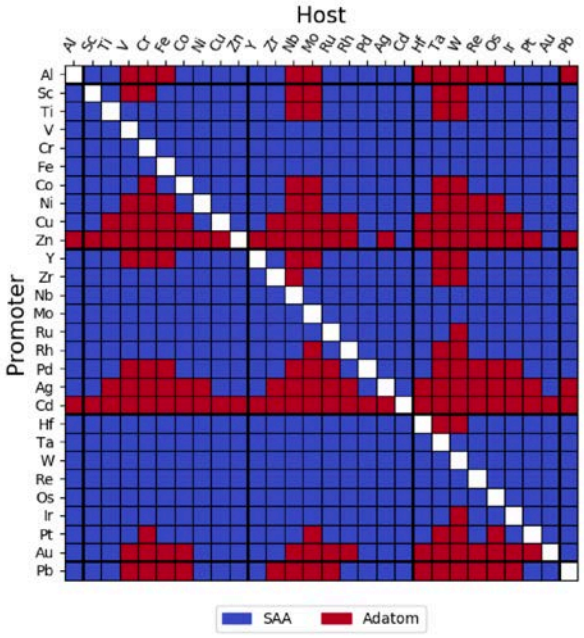

Figure 55. A binary comparison of the stability of SAAs and adatom configurations, calculated through the bond counting model.

While the bond counting model provides some physical insights in each of the 3 geometries, the overall predictive power of the model on the final stable geometry, when considering all 4 classes, is low with areas for the precision-recall curves of 0.33, 0.04, 0.76, and 0.41 for SAA, Dimer, Subsurface, and Adatom respectively, with an average of 0.39. To improve the accuracy of our models, we consider training different machine learning models to aid in predicting the stable geometry of a configuration.

6.3.4. Machine Learning Models

To address the systematic discrepancies in the bond counting model, we also analyze the data using machine learning. Given the rapid rise of machine learning and data science applied to material science we attempted to fit several machine learning models to classify a given binary combination of elements by their most stable predicted geometry. To analyze this classification problem, we considered three general and widely used models: support vector machines, decision trees, and neural networks. Such models estimate a general function *f* of the form

$$y = f(\boldsymbol{X}), \tag{78}$$

where $y \in [0,1,2,3]$ represents the geometry, and **X** is an input vector of properties of the constituent elements such as atomic radius, bond energy, cohesive energy, and other chemical properties. For our particular system of promoter and host atoms, X is a concatenation of the properties of the promotor and host atoms:

$$\boldsymbol{X} = \left[\boldsymbol{x_{promoter}} \| \boldsymbol{x_{host}}\right]; \boldsymbol{x_i} = \left[\, r_{atomic,i}, E_{Bond,i} E_{Cohesive,i} \ldots\right]. \tag{79}$$

We selected properties for the input vector which we expect to be correlated with the resulting geometry such as crystal structure, atomic radius, cohesive energy, and other

properties, some of which do not have an obvious relationship to the stability of isolated metal structures, such as electronegativity. Despite our input vector containing over 60 combinations of properties for both the promoter and host atoms, we were not able to fit any decision tree,[272] neural network,[273] or support vector machine[274] with an $F_1 > 0.3$ after cross validation. Given the poor fit, we show that these models operating in this paradigm do not perform well. Even if these models did capture the data effectively, such a classification model would also be extremely limited because they could not be easily extended to predict the relative stability of more classes without retraining the model with additional training data. Given the cost of generating more data, we instead take inspiration from the physical insight and simplicity of the previously discussed bond counting model to improve and guide the machine learning modeling algorithm and features to improve its accuracy.

6.3.5. Kernel Ridge Regression

Instead of a classification problem we now consider a simple regression model on the formation energies ($y_i \in \mathbb{R}$). By reformulating the problem as a regression, we are more reasonably able to expand the model to more system geometries. Under Equation 79, **X** only included chemical information because the geometries were fixed in the classification scheme. We additionally modify the input vector to include the number of each type of bond, and bond energies fitted from the bond counting model in addition to the chemical information in the equation

$$\boldsymbol{X} = \left[\boldsymbol{n} \| \boldsymbol{b} \| \boldsymbol{x}_{promoter} \| \boldsymbol{x}_{host}\right]. \tag{80}$$

Under the updated definition of Equation 80, the input vector **X** is expanded to include both geometric and chemical information. Additionally, including physically relevant physical properties such as the specific fitted bond energies as input parameters is important to not only increase the fitting, but also improve the physically interpretability of the model.

From the previously discussed bond counting model, we already know that products of the input variables would be physically relevant, so we expect products of the input features to correlate with the energies of the system. We solve for the function *f* of Equation 78 by using kernel ridge regression (KRR) with a polynomial kernel function of the second degree:

$$f(x) = \sum_{j=1}^{N} \alpha_j k(x, x_j); \;\; k(x_i, x_j) = \left(x_i^T x_j + 1\right)^2. \tag{81}$$

Using KRR with a second order polynomial kernel on the input data, we are performing regression not only on the parameters themselves, but also pairwise interactions between parameters. The weights are obtained through minimizing the cost function:

$$\sum_i \left(f(x_j) - f_j\right)^2 + \lambda \boldsymbol{\alpha}^T \boldsymbol{K} \boldsymbol{\alpha} \tag{82}$$

with a fixed positive regularization parameter λ (λ=150 by cross validation), which penalizes large components in $\boldsymbol{\alpha}$. These weights correspond with the coefficients in a weighted sum of pairwise interactions between components in **X**. This particular model then contains the bond counting model's predicted energy value and extends it to include more interaction terms such as the bond energies multiplied by physical parameters, and selects the appropriate weights to reduce the estimation error.

When using KRR, the energies are closer to the DFT results ($R^2 = 0.9999$), and the predicted geometries are more closely in alignment with the DFT data compared to just the bond counting model, as shown in Figure 56. Our KRR model predicts 222 stable SAA configurations (133 true positive). This new model also corrects for the overestimation of adatom geometries suggesting 54 stable configurations (25 true positive) from the bond counting model and suggests more dimer-based geometries (272 dimers predicted from KRR of which 106 are true positives, compared to 18 in bond counting with 9 true positives) and only predicts 54 stable adatom configurations compared (25 true positive) to the 58 from the DFT model and 182 from the bond counting model (52 true positive). The area under the precision-recall curve for each of the classes using KRR is greater than the bond counting model in all but the dimer case at 0.60, 0.38, 0.51, and 0.24 for SAA, dimer, subsurface, and adatom respectively. The area under the micro-averaged precision-recall curve is also greater than the bond counting model at 0.46 suggesting a better overall predictive model. The main source of error in the bond counting model was neglecting differences in bond energy in slightly different geometries. The KRR model addresses this issue and is able to estimate the error correction to this model by effectively including fitted error correction terms to adjust the bond energies based on both the geometric and chemical data included in the input vector **X**.

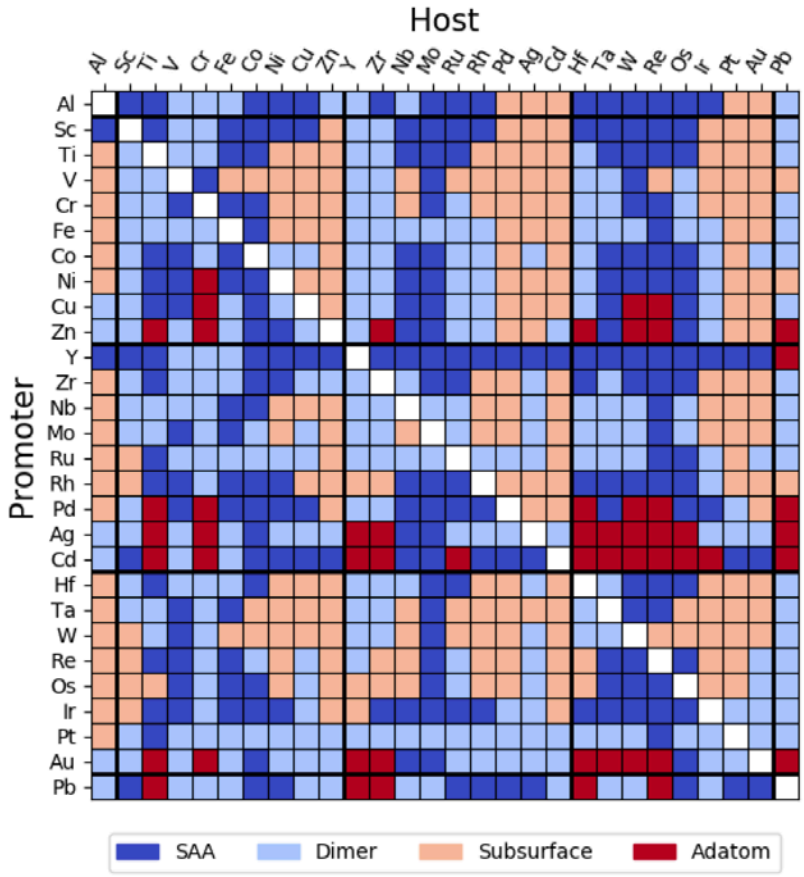

Figure 56. The most stable geometry for dilute binary surface alloys of different *d*-block promoters and hosts with kernel ridge regression.

The KRR model has a significant advantage over the brute force classification approach because its input vector **X** can be adjusted to estimate the energy of any geometry, not just those contained in the training data set. To test this transferability of our models we calculated the formation energy of an adatom adsorbed on top of a SAA site, modeled in Figure 45f and charted in Figure 57. In this small test, our bond energy model in Figure 57b is not accurate, only properly classifying 2/12 element combinations versus the DFT data in Figure 57a. This poor agreement is most likely a direct result of the assumptions mentioned earlier in the similar treatment of bond energies in all geometries. However, the

KRR model, while not entirely accurate either, manages to correctly predict 9/12 geometries in Figure 57c, compared to DFT data. As a wider variety of geometries are considered in the training set, we anticipate the model to increase in overall accuracy to predict the most stable geometry.

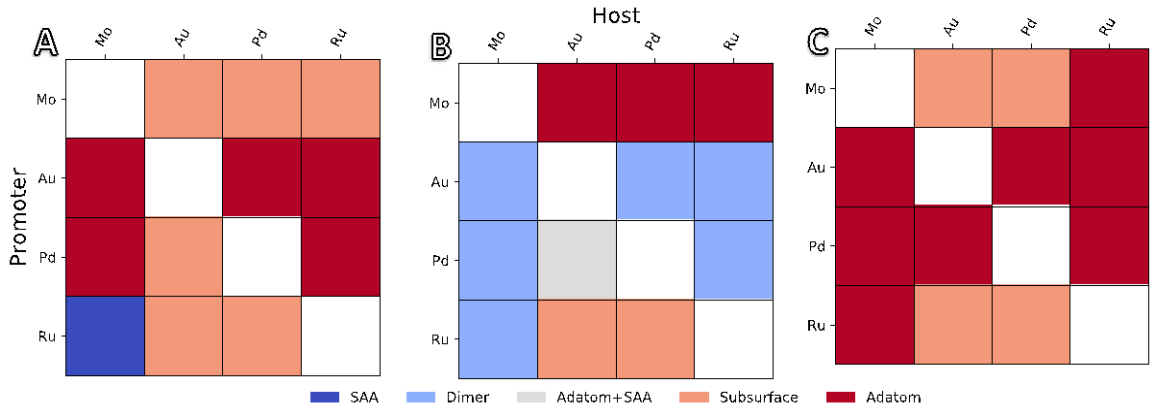

Figure 57. The most stable geometry predicted among five different geometries and the validation set considered using three methods: **(A)** DFT, **(B)** bond counting model, and **(C)** kernel ridge regression.

6.4. Conclusion

In this work, we use DFT to calculate the formation energies of four different configurations: SAA, Dimer, Subsurface, and Adatom. These calculations allow us to determine which configurations may form stable SAAs. We also show that despite having consistent data and an easy formulated classification problem, a brute force machine learning approach does not effectively capture trends in the data. Instead, we propose a simple and intuitive physical-based bond counting model to explain the observed trends. Although the bond counting model allows us to generalize rules of thumb for when each geometry is more stable compared to the SAA, the overall classification power of this model is poor. A more effective machine learning model was developed after incorporating insight from the bond counting model, highlighting the importance of including physically

relevant properties. The resulting model achieved the largest overall classification score and predicted a validation set with much higher accuracy than just the bond counting model. We expect the kernel ridge regression model can be expanded to include more geometries than the four considered here to get a better understanding of what dilute surface alloys may form to improve both the accuracy and classification score of the model.

Chapter 7. Pd- and Zn-Promoted Single-Atom Alloys for Methanol Dehydrogenation

In Chapter 5, we introduced our design paradigm for the prediction of optimal catalyst nanoparticles. By implementing first-principles density functional theory calculations from Chapter 4 into a terrace model in a kinetic Monte Carlo simulation in Chapter 5, we determined that our catalyst nanoparticle should be cubic in shape, and the first two steps of our design strategy illustrated in Figure 38 were fulfilled. To fulfill the final step in our design strategy, we would need to examine promoter atoms to improve catalytic activity on our designed nanoparticles. In Chapters 2 and 3, we found that single-atom alloy surface configurations can greatly promote even the most difficult reactions. Thus, for the final step in our design strategy, we intend to examine single-atom alloys for the catalytic dehydrogenation of methanol. Uncertain of which combinations of metals were stable as single-atom alloys, we performed a full test of 28×28 metal alloys and compared dilute promoter surfaces in Chapter 6. With the stability information provided in Figure 46 in Chapter 6, we are able to select single-atom alloy surfaces that can cater to our process needs. In this chapter, we examine two different promoter metals for the two terrace facets of silver nanocrystals. Exploratory DFT work on different SAA systems was performed by Cindy Mai, who was previously a high school mentee and eventually became an undergraduate researcher.

7.1. Introduction

In the industrial process of methanol decomposition to formaldehyde, various promoters have been added to silver catalyst surfaces to improve the yield of formaldehyde.

For instance, highly active metals such as Pd, Pt, Rh, Ru, and Ir have been found to improve the formaldehyde yield to over 90%.[192] On the other hand, Pb has been used to improve formaldehyde selectivity under incomplete conversions for the reaction.[192] In this study, we examine one of the highly active metals, Pd, as the promoter site. Pd-based catalysts have been examined for the dehydrogenation of methanol to formaldehyde,[205,275] and while these Pd catalysts are highly active and break the hydrogen bonds of methanol readily, they are also very unselective to the formation of formaldehyde and carbon monoxide is a primary product. As studied in Chapter 3 and in its publication,[276] by isolating Pd atoms in a weak-binding metal such as Au or Ag, the geometric ensemble effect is reduced, and while Pd will retain its dehydrogenation ability, it becomes less likely to fully dehydrogenate adsorbates due to the lack of a surrounding ensemble. Indeed, Pd-promoted SAAs have been heavily investigated in the literature; see Chapter 1.4 for a more comprehensive review of Pd-promoted SAAs for dehydrogenation reactions.

In addition to Pd, we also used the table of stability presented in Figure 46 of Chapter 6 to find another potential promoter. From that table, we find that Zn sits stably as an isolated promoter site within the close-packed Ag surface. Zinc metal has been well-studied as a catalyst for methanol dehydrogenation, both as an alloy and additive[223,277] and as a standalone catalyst,[278,279] and has been found to be very selective to formaldehyde in the target reaction.[279] Zinc has been found to bind oxygen strongly, which may be useful to bind methoxy stronger to the surface in the non-oxidative dehydrogenation of methanol.[278] In this chapter, both of these promoters are examined in the single-atom alloy configuration on the two terrace facets of Ag.

7.2. Density Functional Theory Methods

The periodic density functional theory (DFT) calculations were performed using the Vienna ab initio Simulation Package (VASP)[93–96] in the Atomic Simulation Environment.[97] The exchange-correlation effects were described by the Bayesian error estimation functional with van der Waals correction (BEEF-vdW)[74] using an energy cutoff of 400 eV. The core and valence electrons were represented with the projected augmented wave (PAW) method.[98,99] Gaussian smearing was used with Fermi temperatures of k_bT = 0.1 eV, and the electronic energies were subsequently extrapolated to 0 K. All geometries were optimized until the forces were less than the convergence criterion of 0.02 eV/Å.

The clean surfaces of Ag(100) and Ag(111), calculated in Chapter 4, are used in this chapter. To build the Pd- and Zn-promoted SAAs, one surface atom of each Ag surface was replaced by the promoters. The new SAA surfaces are depicted in Figure 58.

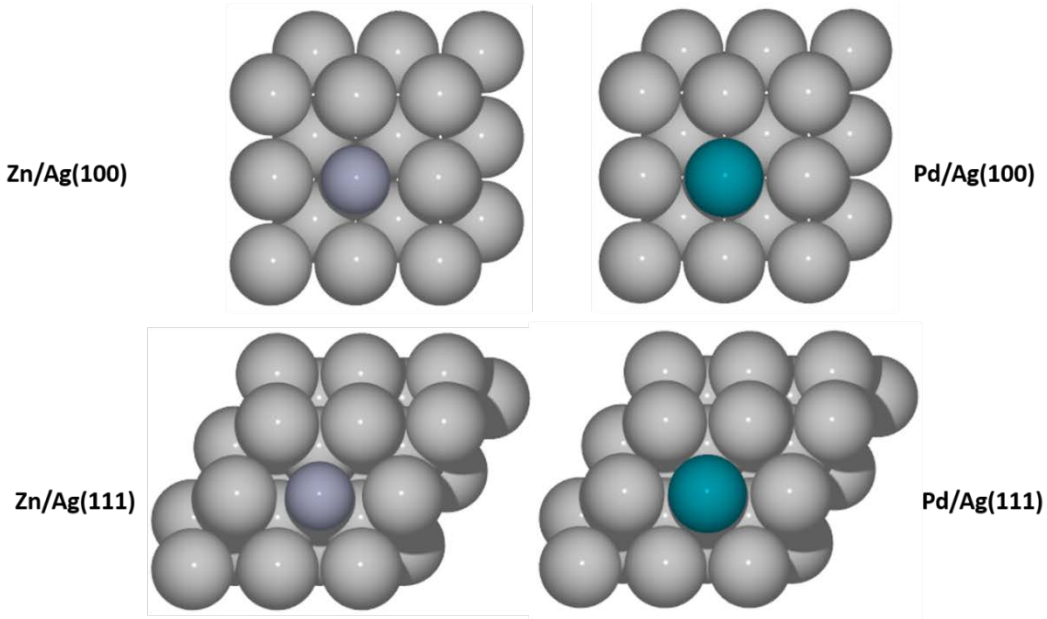

Figure 58. Top views of the Zn/Ag(100), Zn/Ag(111), Pd/Ag(100), and Pd/Ag(111) SAA surfaces.

Similarly to the work in Chapter 4, the following set of primary elementary dissociation reactions are examined:

Step 1: $CH_3OH^* + * \leftrightarrow CH_3O^* + H^*$, (83)

Step 2: $CH_3O^* + * \leftrightarrow CH_2O^* + H^*$, (84)

Step 3: $CH_2O^* + * \leftrightarrow CHO^* + H^*$, and (85)

Step 4: $CHO^* + * \leftrightarrow CO^* + H^*$. (86)

In addition, while multiple byproduct formation pathways were considered and calculated, only one is reported in this chapter, where the C-H bond of methanol is broken rather than the O-H bond:

Step 5: $CH_3OH^* + * \leftrightarrow CH_2OH^* + H^*$. (87)

Since there would be multiple H adatoms available on the surface, the recombination of hydrogen on the surface is given as

Step 6: $2H^* \leftrightarrow H_2^* + *$. (88)

Finally, the adsorption and desorption of physisorbed species is considered:

Step 7: $CH_3OH\ (g) + * \leftrightarrow CH_3OH^*$, (89)

Step 8: $CH_2O\ (g) + * \leftrightarrow CH_2O^*$, (90)

Step 9: $CO\ (g) + * \leftrightarrow CO^*$, and (91)

Step 10: $H_2\ (g) + * \leftrightarrow H_2^*$. (92)

The above reactions will be referred to by their Step number in this chapter. In addition, like in Chapter 5, the diffusion of H* and CH_3O^* are also considered. In this chapter, however, the diffusion of the adsorbates occur between a promoter metal binding site and a host metal binding site, as

Step 11: $CH_3O_p^* \leftrightarrow CH_3O_h^*$, (93)

and

Step 12: $H_p^* \leftrightarrow H_h^*$, (94)

where *p* indicates that the adsorbate is bound to a site adjacent to the promoter metal and *h* indicates that the adsorbate is bound to a site that is fully surrounded by host metal atoms. All binding energies are calculated with reference to the respective clean SAA surfaces and the gas-phase energies of methanol and hydrogen. The activation energy barriers were calculated using the climbing image nudged elastic band (CI-NEB) method[76] and the transition states were confirmed to be true saddle points using a vibrational analysis in the harmonic oscillator approximation, which showed one imaginary frequency along the reaction pathway.

As in Chapter 3, where methane could be activated through the Au or Pd Pathways, the reactions can occur either on the promoter atom or on the host metal atoms. Similarly to Chapters 2 and 3, the majority of the reactions that occur on the host metal atoms on the Pd- and Zn-promoted systems have nearly identical kinetics and thermodynamics as the pure Ag(100) and Ag(111) surfaces. In this chapter, for simplicity, it is assumed that the reaction energetics on the host sites of the SAAs are equivalent to the pure Ag surface analogs unless otherwise noted.

7.3. Results

7.3.1. Adsorption of Intermediates on the Pd- and Zn-promoted SAAs

First, the binding energies of all intermediates for the primary pathway of the deep, non-oxidative dehydrogenation of methanol to CO were calculated on the Ag(100) SAAs. The binding energies on the promoter sites, calculated with respect to gas-phase methanol

and hydrogen, alongside the binding energies on pure Ag(100), are provided below in Table 10.

Table 10. The binding energies (eV) of all methanol dehydrogenation intermediates on the promoter sites of the SAAs of Ag(100), calculated with respect to gas-phase methanol and hydrogen.

Adsorbate	**Ag(100)**	**Pd/Ag(100)**	**Zn/Ag(100)**
CH_3OH* (methanol)	-0.24	-0.27	-0.27
CH_3O* (methoxy)	0.10	0.24	-0.32
CH_2O* (formaldehyde)	0.87	0.71	0.86
CHO* (formyl)	1.68	1.07	1.27
CO* (carbon monoxide)	1.19	0.41	1.21
H_2* (dihydrogen)	-0.05	-0.03	-0.05
H* (hydrogen)	0.47	0.23	0.37
CH_2OH* (hydroxymethyl)	1.19	0.75	0.65

Going down Table 10, the first discrepancy comes at the binding of methoxy. On Pd/Ag(100), methoxy actually binds weaker on the promoter than on pure Ag(100) and on

the host metal sites, which maybe be promising for the second dehydrogenation step or even diffusion to the host sites. Meanwhile, on Zn/Ag(100), methoxy binds considerably stronger to the Zn site, possibly due to the affinity of Zn to oxygen.[280] Next, on Pd/Ag(100), formaldehyde physisorbs slightly stronger than on the pure Ag analog. Both Pd/ and Zn/Ag(100) bind formyl stronger than the pure Ag(100) surface. For carbon monoxide, Zn/Ag(100) physisorbs CO with a similar strength as the pure Ag surface, but Pd/Ag(100) chemisorbs it strongly through the carbon atom; other studies on Pd-promoted SAAs have shown that this may be a promising feature in other applications.[128,281–284] Hydrogen adatoms bind strongly to the bridge sites adjacent to the both promoter atoms; hydrogen adsorption has been well-studied on Pd-based SAAs.[92,268,283,285] Lastly, the hydroxymethyl (CH_2OH*) binds considerably stronger on the top site of both promoter atoms than on Ag(100).

Next, the adsorption of the intermediates on the Ag(111) SAAs is presented below in Table 11.

Table 11. The binding energies (eV) of all methanol dehydrogenation intermediates on the promoter sites of the SAAs of Ag(111), calculated with respect to gas-phase methanol and hydrogen.

Adsorbate	Ag(111)	Pd/Ag(111)	Zn/Ag(111)
CH_3OH* (methanol)	-0.21	-0.23	-0.21
CH_3O* (methoxy)	0.38	0.40	-0.08
CH_2O* (formaldehyde)	0.88	0.86	0.88
CHO* (formyl)	1.81	1.00	1.64
CO* (carbon monoxide)	1.25	0.40	1.36
H_2* (dihydrogen)	-0.05	-0.09	-0.05
H* (hydrogen)	0.42	0.11	0.46
CH_2OH* (hydroxymethyl)	1.24	0.67	1.01

As in Table 10, we can examine Table 11 for discrepancies in the binding energies of any of the adsorbates. First, similarly to its (100) counterpart, methoxy binds considerably stronger to Zn/Ag(111) than Ag(111). Methoxy binds very slightly weaker on the Pd promoter, but the difference is nearly indistinguishable on the (111) surface.

Formyl binds much stronger to the Pd/Ag(111) surface and slightly stronger to the Zn/Ag(111) than on the pure surface. Like on (100), CO binds strongly to the Pd site, but interestingly, the physisorption of CO on the Zn site is weaker than on the pure surface. Hydrogen adatoms bind stronger to the Pd site and bind at an indistinguishable energy to the Zn site. Lastly, the hydroxymethyl binds considerably stronger to Pd/Ag(111) and mildly stronger to the Zn/Ag(111) than the precursor Ag(111) surface.

7.3.2. Activation Energy Barriers for the Methanol Dehydrogenation on (100) SAAs

The activation energy barriers were calculated through the NEB method for each of the reactions in Chapter 7.2. Table 12 below shows the activation energy barriers for Steps 1-6 on the Ag(100) surface, as well as its two promoted surfaces. The values reported for the SAA surfaces correspond to the elementary step occurring on the promoter site.

Table 12. The activation energy barriers of Steps 1-6 over the Ag(100) SAA surfaces, in eV.

	Ag(100)	**Pd/Ag(100)**	**Zn/Ag(100)**
Step 1	1.40	1.12	1.32
Step 2	1.19	0.88	1.54
Step 3	1.56	0.77	1.15
Step 4	0.28	0.54	0.79
Step 5	2.25	1.53	2.23
Step 6	0.60	0.18	0.87

For all the steps above, all possible pathways were attempted; for instance, in the dissociation of methanol, a pathway where the resultant methoxy stabilized on a host site

while the hydrogen adatom bound to the promoter site was also tested. When comparing Pd/Ag(100), all barriers are considerably lowered except for Step 4, the dehydrogenation of formyl to CO. Since Step 1 was determined to be the rate-determining step in Chapter 4, a barrier improvement of 0.28 eV is promising. At the same time, however, the undesired dehydrogenation of formaldehyde to formyl in Step 3 was also made easier, with a 0.79 eV decrease in that barrier. With the lower barrier to deeper dehydrogenation, kinetic studies must be performed on Pd/Ag(100) to ensure that the deep dehydrogenation does not begin to dominate. As an alternative to Step 1, methanol can possibly dissociate at the C-H bond, but the kinetics and thermodynamics of Step 5 remain unfavorable. With the very low barrier for H_2 recombination in Step 6, it is possible that any H_2 recombination and desorption could occur on the promoter site, which has been examined and prevented in other literature.[283,284]

On Zn/Ag(100), the barrier for Step 1 was also mildly lowered. Interestingly, however, the barrier for Step 2 greatly increased, most likely due to the very strong binding of methoxy to the promoter site. If the dehydrogenation of methanol was to solely occur on the promoter site of Zn/Ag(100), Step 2 may become the rate-determining step. Meanwhile, the dehydrogenation of formaldehyde to formyl is also made easier on Zn/Ag(100), but not to the extent of Pd/Ag(100). Also like Pd/Ag(100), Step 4 is made harder. Lastly, in the H_2 recombination in Step 6 becomes more difficult, but this likely matters little because the Ag host sites are most prevalent anyways.

On Zn/Ag(100), it is possible for the methoxy adsorbate to diffuse away from the promoter site and onto the Ag(100) site, where the dehydrogenation of methoxy to formaldehyde becomes easier. The diffusion barriers of methoxy and hydrogen adatoms

away from the promoter site on Pd/Ag(100) and Zn/Ag(100) are given in Table 13 below, along with the diffusion barriers on Ag(100) in simple 4-fold-site hopping.

Table 13. The diffusion barriers, in eV, of methoxy and hydrogen adsorbates (Steps 11 and 12) on Ag(100), Pd/Ag(100), and Zn/Ag(100).

	Ag(100)	**Pd/Ag(100)**	**Zn/Ag(100)**
Step 11	0.26	0.17	0.63
Step 12	0.10	0.33	0.26

In the diffusion barriers, it is important to note that the diffusion of methoxy away from the Pd promoter site is exothermic, so the diffusion barrier away from Ag sites and to the Pd site can be calculated through microscopic reversibility as 0.31 eV, assuming that the binding energy at the Ag site is equivalent to that of a pure Ag(100) surface. The low barrier for methyl diffusion away from the Pd promoter is likely due to its preference for the Ag site, while the high barrier for H diffusion away from the Pd site is likely due to its preference for the Pd site. Meanwhile, there is a high diffusion barrier for methoxy away from the Zn site of Zn/Ag. By examining the transition state energies and assuming that the diffusion of adsorbates from the promoter site is solely dictated by kinetics, it still remains kinetically more favorable to dissociate the methoxy adsorbate on the Zn promoter site. On the other hand, at higher temperatures and considering the statistical mechanical equilibrium effect discussed in Chapter 1.5, diffusion away from the Zn promoter site may become more favorable and lead to the Ag sites dominating Step 2. In Figure 59 below, a potential energy diagram comparing the three surfaces is presented. It is assumed that all reactions on the SAAs occur on the promoter site, and that the hydrogen adatoms do not

recombine and desorb, as to show the effects of the highly different binding energies of hydrogen on the different surfaces.

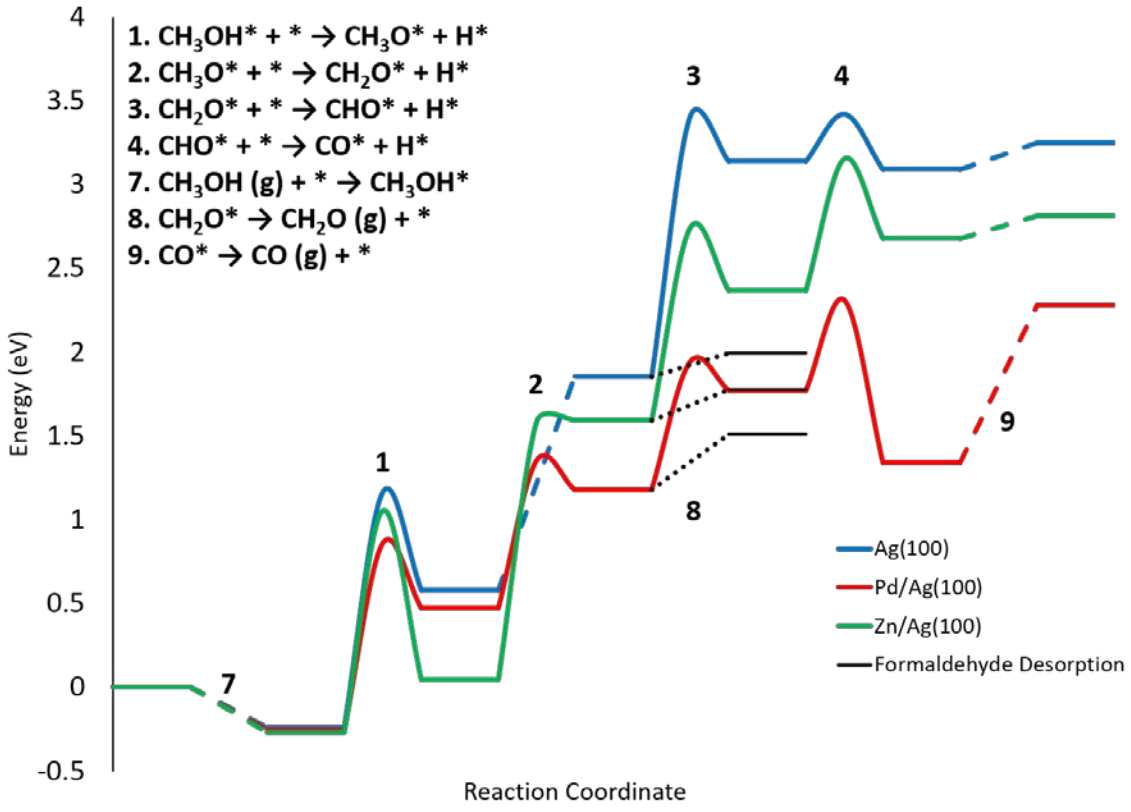

Figure 59. The potential energy diagram for the dehydrogenation of methanol over Ag(100), Pd/Ag(100), and Zn/Ag(100) and assuming that hydrogen does not recombine and desorb.

From Figure 59, it is seen that the addition of a single promoter atom on the surfaces can greatly improve the kinetics and thermodynamics of the methanol to formaldehyde reaction on Ag(100), which was established in Chapters 4 and 5 as the best surface for the reaction. In particular, Pd/Ag(100) substantially lowers all barriers and reaction energies. It remains difficult to elucidate the differences between the Ag(100) and Zn/Ag(100) due to the differences in hydrogen binding energies, so in Figure 60 below, all hydrogen adatoms are assumed to recombine and desorb in the gas-phase.

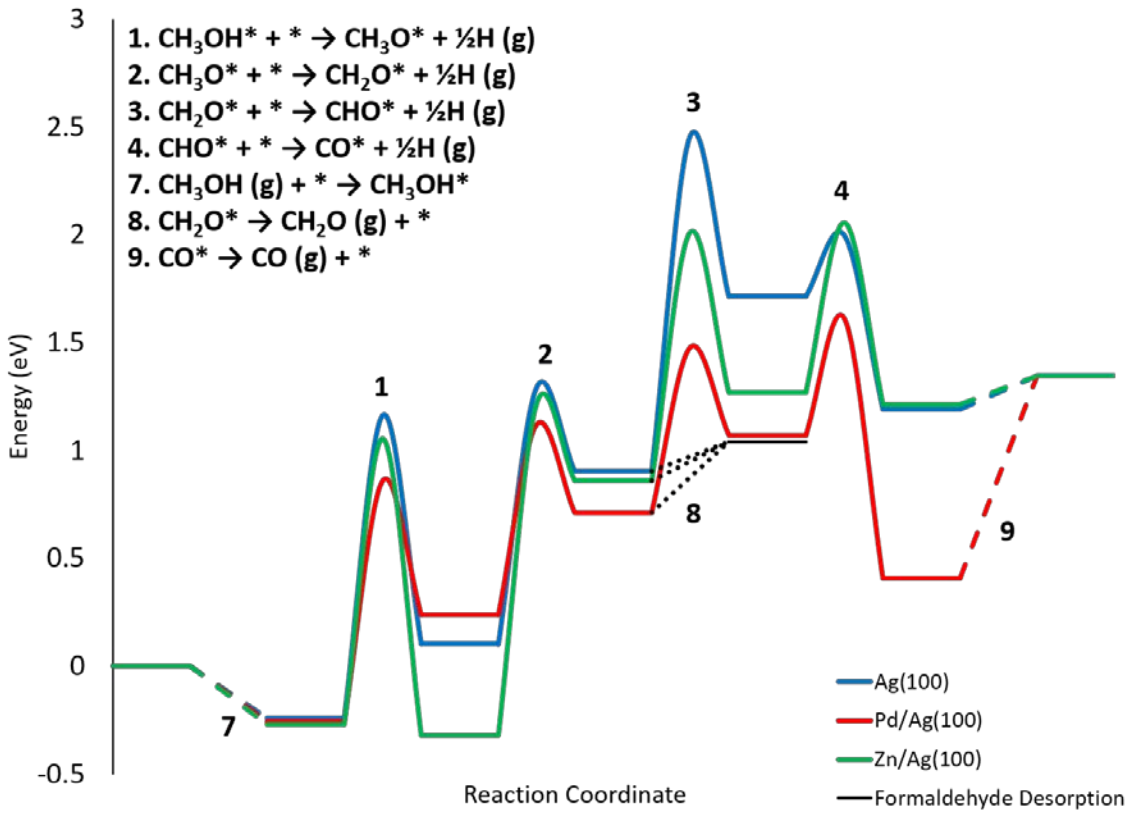

Figure 60. The potential energy diagram for the dehydrogenation of methanol over Ag(100), Pd/Ag(100), and Zn/Ag(100) and assuming that hydrogen recombines and desorbs.

After removing hydrogen in Figure 60, it becomes clearer that the Pd promoter should greatly improve the rate of dehydrogenation over Ag(100). Meanwhile, the Zn promoter provides only a visibly slight advantage over the pure Ag(100) surface. It is important to note, however, that since the Pd/Ag(100) "catalyst" is on the same surface as Ag(100) and the Zn/Ag(100) is also fully surrounded by Ag(100) sites, hopping can easily occur via entropically-driven diffusion between the red and blue curves, as well as the green and blue curves, of the potential energy diagram in Figure 60. For instance, when considering the Pd/Ag(100) curve, even though the undesired dehydrogenation of formaldehyde to formyl is easier on the promoter than on the pure Ag(100) sites, the

diffusion of formaldehyde far away from the promoter site to pure Ag(100) sites remains a kinetically simpler step, and those sites heavily favor the desorption of physisorbed formaldehyde over the deeper dehydrogenation. Likewise, on Zn/Ag(100), as discussed above, although the methoxy binds strongly to the promoter site and the dehydrogenation of methoxy is difficult on the promoter site, it can diffuse away to the pure Ag(100) sites and dissociate there.

7.3.3. Microkinetic Modeling of the Ag(100) SAAs

Microkinetic models were implemented to gain greater understandings into the kinetics of the reaction on the SAAs. Steps 1-12 in Chapter 7.2 were included in the microkinetic model, and the model was run for temperatures from 600-1000 K and pressures of 1-9 bar. The surface was assumed to be comprised of 90% host sites and 10% promoter sites. The inlet gas concentrations were varied, but the highest activity was obtained when the feed was pure methanol. The frequencies used in the model were obtained through vibrational frequency calculations on the adsorbates and the transition states of the dehydrogenation steps. Entropy corrections were applied in the model using the Shomate equation for the gas-phase molecules and the harmonic approximation for the adsorbates and transition states.[97] Table 14 below displays the production rates, in units of s^{-1}, of formaldehyde and CO on Ag(100), Pd/Ag(100), and Zn/Ag(100), respectively, at temperatures between 800 and 900 K and at 1 bar, which are the typical operating conditions of the reaction.

Table 14. The production rates in s^{-1} of formaldehyde and CO at 1 bar and varying temperatures for the Ag(100) SAAs.

	Ag(100)		**Pd/Ag(100)**		**Zn/Ag(100)**	
Temperature	**CH_2O**	**CO**	**CH_2O**	**CO**	**CH_2O**	**CO**
800 K	4.9e-2	3.3e-14	1.0e-1	2.4e-6	4.8e-2	8.6e-14
850 K	1.3e-1	2.7e-13	2.3e-1	7.2e-6	1.3e-1	5.0e-13
900 K	3.2e-1	1.8e-12	5.0e-1	2.0e-5	3.0e-1	2.5e-12

From the values in Table 14, the Pd/Ag(100) SAA approximately doubles the production of formaldehyde. The SAA does also greatly increase the production of CO, but the amount of formaldehyde produced in comparison to CO remains greater by an order of magnitude of four or five. Meanwhile, on the Zn/Ag(100) SAA, the production rates of formaldehyde slightly decrease, while the production rates of CO slightly increase. On all sites on all surfaces, the surface coverages remained zero. On all surfaces, from the examination of the degree of rate-control,[199–201] Step 1 remained the rate-determining step.

7.3.4. Activation Energy Barriers for the Methanol Dehydrogenation on (111) SAAs

The activation energy barriers were calculated through the NEB method for each of the reactions in Chapter 7.2. Table 15 below shows the activation energy barriers for Steps 1-6 on the Ag(111) surface, as well as its two promoted surfaces. The values reported for the SAA surfaces correspond to the elementary step occurring on the promoter site.

Table 15. The activation energy barriers of Steps 1-6 over the Ag(111) SAA surfaces, in eV.

	Ag(111)	**Pd/Ag(111)**	**Zn/Ag(111)**
Step 1	1.51	1.45	1.37
Step 2	1.32	0.99	1.60
Step 3	1.67	0.68	1.53
Step 4	0.56	0.66	0.50
Step 5	2.32	1.36	2.43
Step 6	0.80	0.67	0.77

Beginning with Zn/Ag(111), the kinetics of the rate-determining Step 1 are slightly improved. Just as the Zn promoter caused an increase in the kinetic barrier of Step 2 in Zn/Ag(100), the Zn promoter leads to a higher barrier on the Ag(111) surface, and the same considerations must be made regarding the diffusion of methoxy and hydrogen adatoms. The diffusion barrier away from the Zn promoter site for the methoxy adsorbate on the Zn/Ag(111) surface is 0.63 eV, which is equivalent to the corresponding barrier on the Zn/Ag(100) surface. Analogously to the (100) SAA, the kinetics and the entropic push of the diffusion of methoxy on the Zn/Ag(111) surface must be delved into further to fully clarify where reactions occur on the promoted surface.

From Table 15, Pd/Ag(111) very slightly improves the O-H bond scission step of methanol in Step 1, but not to the extent that the Pd promoter does on the Ag(100) surface. Similarly to the Pd promoter on Pd/Ag(100), Pd/Ag(111) considerably lowers the barrier for Step 3, opening the possibility of deep dehydrogenation to CO. The most notable value in Table 15, however, is the low barrier in Step 5. Step 5, which entails the scission of the

C-H bond of methanol rather than the O-H bond, competes with Step 1 and has a lower activation energy barrier. This is not necessarily surprising; the C-H bond scission is reported to occur first on Pd catalysts for the dehydrogenation of methanol.[194,205,275,286,287] In this work, however, the first few steps of the dehydrogenation of methanol through some species with a chemical formula of CH_3O to a species with a chemical formula of CH_2O is investigated on the Pd/Ag(111) SAA. The results of the study of the mechanisms over the Pd promoter is shown in the potential energy diagram below in Figure 61.

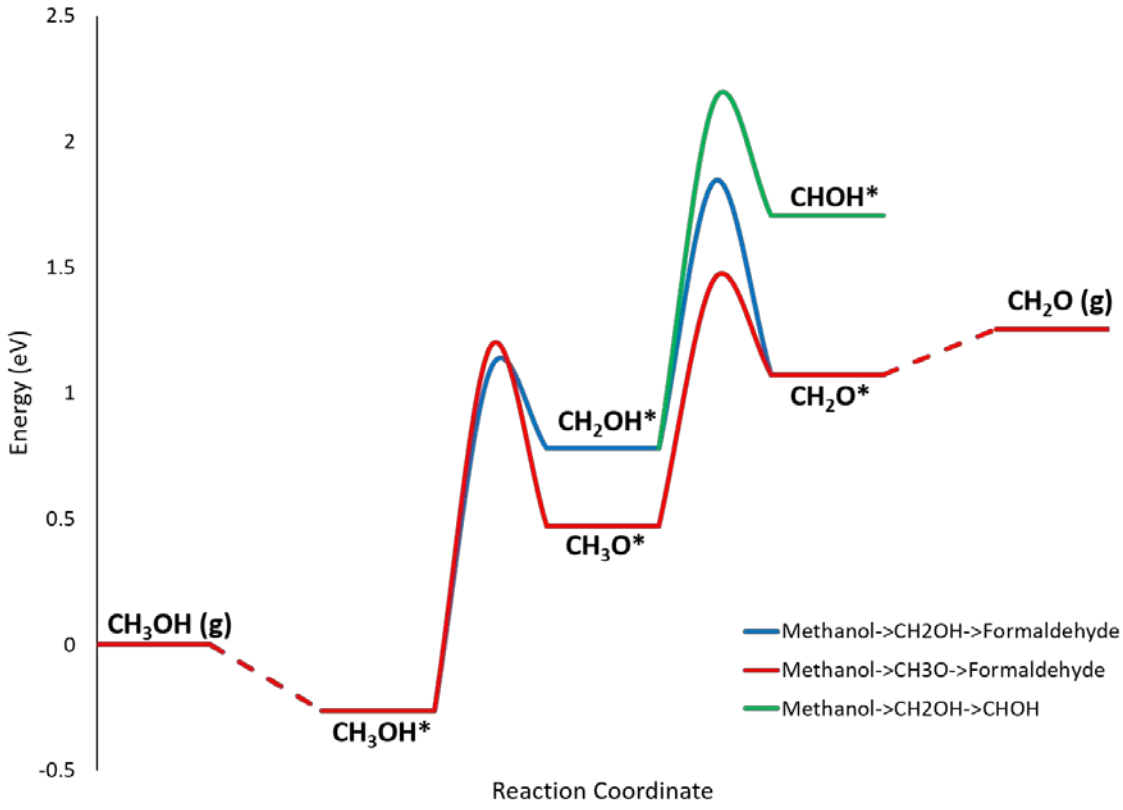

Figure 61. The potential energy diagram for the possible mechanisms of the removal of two hydrogen atoms on the promoter site of Pd/Ag(111).

From Figure 61 above, there are three major pathways that the removal of two hydrogen atoms can follow. In the red pathway, the dehydrogenation of methanol to formaldehyde follows the standard O-H scission, followed by a C-H scission. In the blue

pathway, the first bond cleavage is the C-H bond, followed by the O-H bond to still produce formaldehyde. The blue pathway gives a lower barrier for the first dehydrogenation step, but has a higher reaction energy, and the second step is even more kinetically unfavorable. Regardless, if the reaction follows either the red or blue pathway, formaldehyde will still be the product. Finally, in the green pathway, a C-H bond in methanol is broken first, followed by a second C-H bond. In this pathway, it is impossible to form formaldehyde without a hydrogenation step, so this pathway is undesired. The second step in this pathway is highly unfavorable though, indicating that the occurrence of this pathway is unlikely.

With the first dehydrogenation pathways now clarified on the Pd/Ag(111) catalyst, a potential energy diagram can be drawn comparing the three (111) surfaces in Figure 62. For the ease of readability, only the red pathway of Figure 62 is followed, but the reasonable possibility of a second and maybe third pathway must be acknowledged. In Figure 62 below, it is assumed that all reactions on the SAAs occur on the promoter site, and that the hydrogen adatoms do not recombine and desorb, as to show the effects of the highly different binding energies of hydrogen on the different surfaces.

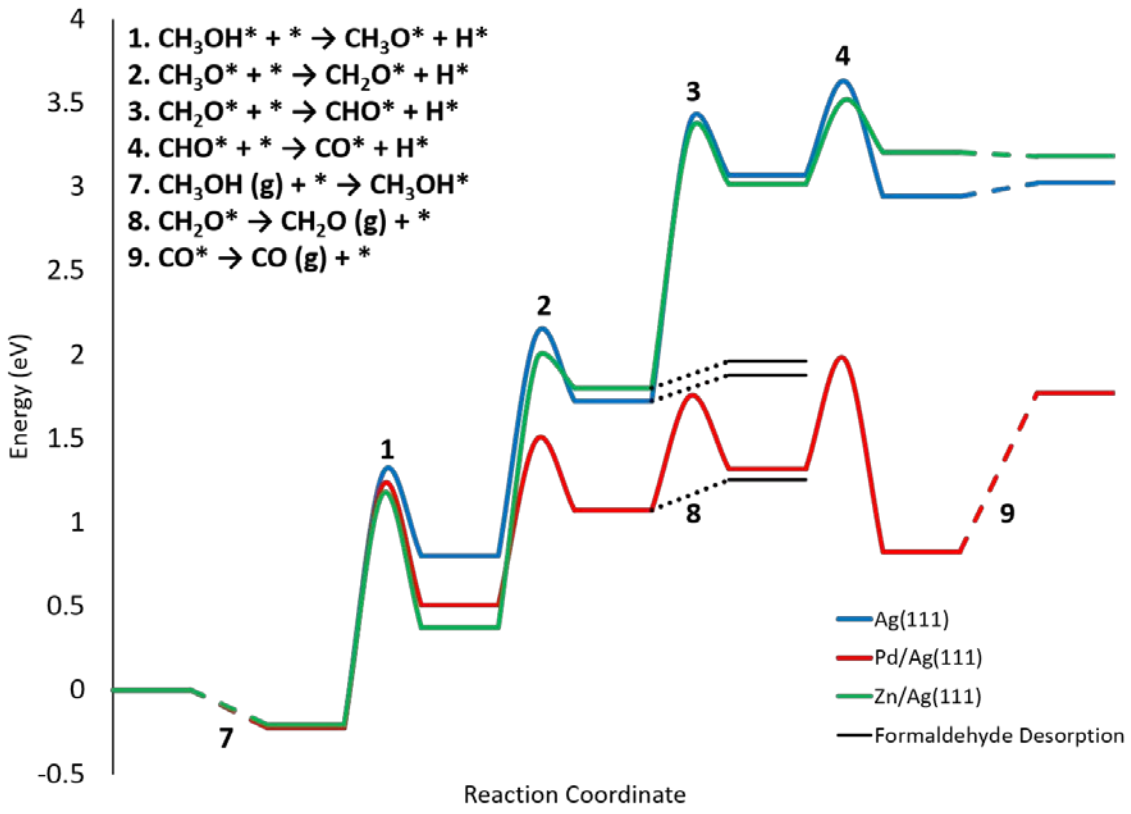

Figure 62. The potential energy diagram for the dehydrogenation of methanol over Ag(111), Pd/Ag(111), and Zn/Ag(111) and assuming that hydrogen does not recombine and desorb.

In Figure 62, the Pd/Ag(111) shows the most promising reaction pathway for the dehydrogenation of methanol to formaldehyde, but is not clearly better than the other pathways. A considerable concern, however, is that the barrier for the dehydrogenation of formaldehyde to formyl is too low and the deep dehydrogenation is too facile; this will be confirmed in kinetic modeling. Meanwhile, there is little distinction between the pure Ag(111) surface and the Zn/Ag(111) SAA outside of the strong methoxy binding near the Zn promoter. To discern between the two pathways, the effects of hydrogen are removed in Figure 63 below, as hydrogen adatoms are forced to recombine and desorb without barrier.

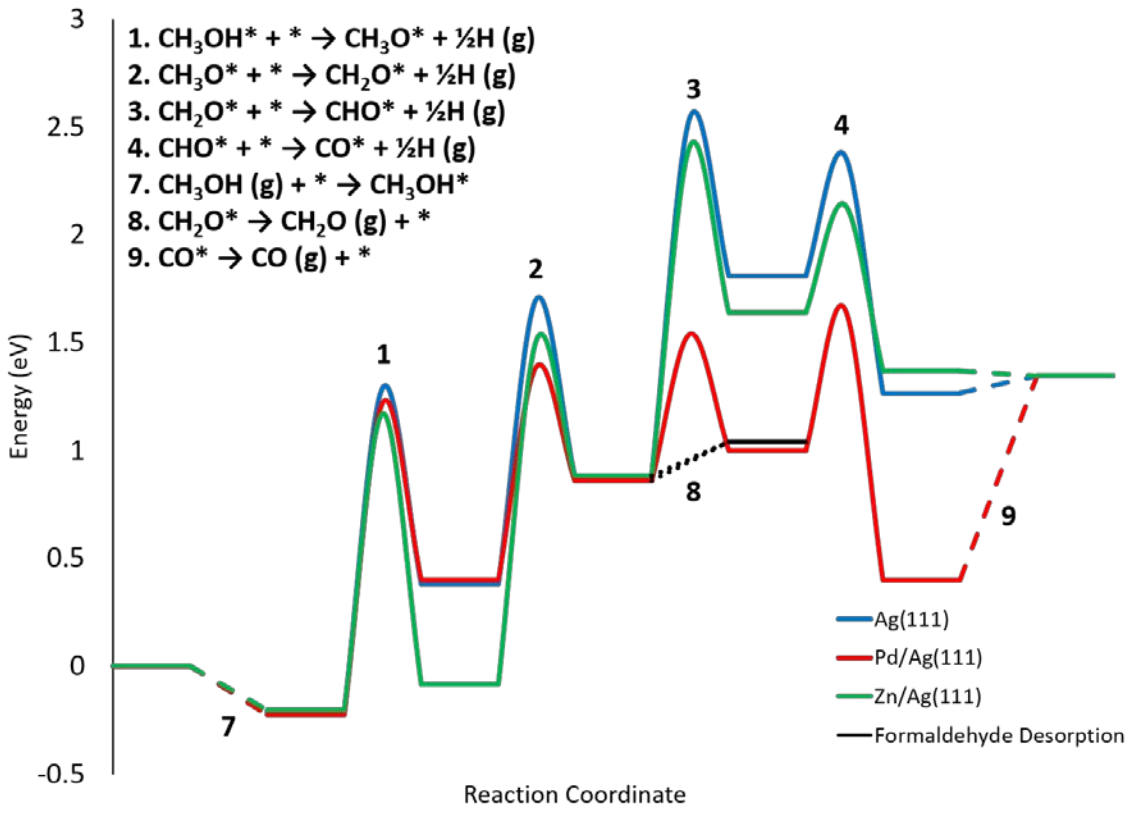

Figure 63. The potential energy diagram for the dehydrogenation of methanol over Ag(111), Pd/Ag(111), and Zn/Ag(111) and assuming that hydrogen recombines and desorbs.

From Figure 63 above, only two things seem to be clear in distinguishing between the three pathways. First, methoxy binds very strongly on the Zn site on Zn/Ag(111), which leads to a large barrier for the dissociation of methoxy to formaldehyde in Step 2. As discussed in Chapter 7.3.3, however, the adsorbates can spill over to the Ag(111) sites and follow the pathway for Ag(111), where the barrier in Step 2 is not so large. Second, the dehydrogenation of formaldehyde to CO* is much easier on Pd/Ag(111), which would hurt the selectivity of the reaction. If there is no clear kinetic advantage for the Pd promoter in Step 1, the rate-determining step, then the loss in selectivity upon usage of the Pd promoter on the Ag(111) surface may cause Pd to be a poor promoter on this surface. Interestingly,

at the end of the reaction on the Zn/Ag(111) SAA, CO binds so unfavorably to the Zn promoter that the desorption of CO is downhill in energy. This may have some relation to literature studies that show that Zn is an excellent anti-fouling additive.[11,288,289]

7.3.5. Microkinetic Modeling of the Ag(111) SAAs

Microkinetic models were implemented to gain greater understandings into the kinetics of the reaction on the SAAs. Steps 1-12 in Chapter 7.2 were included in the microkinetic model, and the model was run for temperatures from 600-1000 K and pressures of 1-9 bar. The surface was assumed to be comprised of 90% host sites and 10% promoter sites. The inlet gas concentrations were varied, but the highest activity was obtained when the feed was pure methanol. The frequencies used in the model were obtained through vibrational frequency calculations on the adsorbates and the transition states of the dehydrogenation steps. Entropy corrections were applied in the model using the Shomate equation for the gas-phase molecules and the harmonic approximation for the adsorbates and transition states.[97] Table 16 below displays the production rates, in units of s^{-1}, of formaldehyde and CO on Ag(111) and Pd/Ag(111), respectively, at temperatures between 800 and 900 K and at 1 bar, which are the typical operating conditions of the reaction. The Zn/Ag(111) surface was omitted in this study due to computational issues.

Table 16. The production rates in s^{-1} of formaldehyde and CO at 1 bar and varying temperatures for Ag(111) and Pd/Ag(111).

	Ag(111)		**Pd/Ag(111)**	
Temperature	**CH_2O**	**CO**	**CH_2O**	**CO**
800 K	1.0e-2	1.6e-13	8.7e-3	6.1e-10
850 K	3.1e-2	1.7e-12	2.6e-2	2.4e-9
900 K	8.2e-2	1.4e-11	6.9e-2	8.0e-9

From Table 16 above, the Pd promoter both lowers the production rate of formaldehyde and raises the production rate of the undesired CO. Although this study would need to be performed in a spatial model where diffusion is better understood and lateral interactions can be considered, the results in the MKM indicate that Pd is not a promising promoter for the non-oxidative methanol dehydrogenation on Ag(111), as all reaction steps would simply occur on the Ag sites.

7.3.6. Kinetic Monte Carlo Simulations on Pd/Ag(100)

From the DFT calculations and MKM simulations performed on the Ag(100) and Ag(111) SAAs, Pd/Ag(100) was seen to be the most promising one, as it offered lower activation barriers for methanol activation and gave the highest turnover frequencies. As mentioned previously, MKM simulations cannot fully encapsulate the effect of diffusion on the SAA catalysts, so KMC simulations were performed on the Pd/Ag(100) surface to examine diffusion and lateral interactions on the SAA surface.

The first challenge in modeling SAAs in KMC is to correctly define the lattice sites. In graph theoretical KMC, the pre-defined lattice sites are often assumed to be top sites of

catalyst surface. If a 3×3 Pd/Ag(100) surface layer were to be modeled in KMC such that it would mirror the image given in Figure 58, then intuitively, the center of the 3×3 box would be given energetic parameters of the Pd promoter site calculated in DFT. Unfortunately, if the surface were modeled in this way, two related issues would arise. First, adsorbates such as methoxy or H* would bind in the 4-fold sites rather than the top sites. While there is only one top site that is affiliated with the Pd promoter, there are four 4-fold sites that border that promoter site, so the intuitive top-site surface model in KMC would underestimate the true number of promoter binding sites that are available on the SAA surface. Second, if methanol were to dissociate into methoxy and H* on the intuitive top-site surface model, one of either the resulting methoxy or H* must reside on a Ag top site, since only one adsorbate can occupy a site at a given time. In the first-principles DFT calculations, however, when methanol dissociates over the Pd top site, the two resulting adsorbates occupy two of the four 4-fold sites that are adjacent to the Pd top site, indicating that the multiplicity of the intuitive top-site surface model would prove to be problematic.

To remedy these issues, the same lattices can be used, but shifted so that each lattice site is no longer a top site, but rather a 4-fold site. In Figure 64 below, the lattices used for a 3×3 surface and a 9×9 surface are depicted, where the squares represent 4-fold sites, and promoter binding sites are colored in purple, while the Ag binding sites are white. The intersections of gridlines in Figure 64 would represent surface top sites. For easier spatial visualization, the location where the promoter atom would reside is designated by the red dot, which is in the center of the cluster of promoter binding sites. Notably, in the 3×3 model, four of the nine available lattice sites (44.4%) are promoter sites, whereas in the 9×9 model, only four of the 81 available lattice sites (4.9%) are promoter sites.

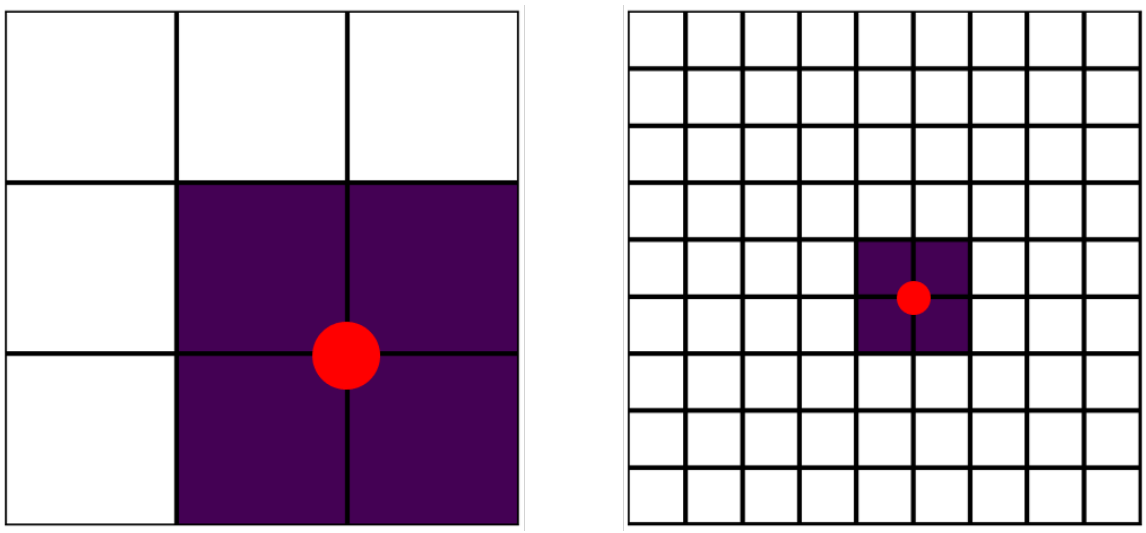

Figure 64. The lattice representations of the 3×3 and 9×9 SAA models of Pd/Ag(100) in KMC. The purple squares represent Pd 4-fold sites, the white squares represent Ag 4-fold sites, and the red dots indicate where the Pd promoter would reside.

The kinetic parameters of the SAA model in KMC are not straightforward, either. It is assumed that any dissociation or recombination reactions can only occur on two adjacent and similar sites. For instance, two H* adatoms can only recombine if they reside in adjacent Ag sites or adjacent Pd sites, but they cannot recombine if they sit in both Ag and Pd sites, even if they are adjacent. Likewise, an adsorbate can only dissociate into two similar sites; for example, when methanol dissociates, both resultant methoxy and H* must reside in Pd sites if it dissociates on a Pd site.

Diffusion is treated similarly to the studies in Chapter 6, where the barriers were artificially increased to reduce computational expense. In these studies, the diffusion barriers for methoxy and H* diffusion between similar sites was set at 0.75 eV. In DFT, the barrier for the diffusion of a methoxy adsorbate from a Pd site to a Ag site was calculated to be approximately 0.1 eV lower than diffusing from a pure Ag site to another pure Ag site on Pd/Ag(100). Thus, in KMC, the diffusion of methoxy from a Pd site to a

Ag site was artificially set at 0.65 eV to indicate that this diffusion step is easier than similar-site diffusion. Likewise, the diffusion of H* from a Pd site to a Ag site was calculated to be approximately 0.25 eV more difficult than from an Ag site to another Ag site, so in KMC, this diffusion barrier was set at 1.00 eV.

The adsorption parameters on the Pd sites were set to be the same as on the Ag sites. To decrease the over-occurrence of methanol adsorption and desorption, methanol adsorption was modeled to be dissociative and the pre-factor was set eight orders of magnitude lower. Lateral interactions between any two adsorbates were considered to be equal to the lateral interactions modeled on Ag(100); the lateral interaction between two methanol adsorbates on adjacent Pd sites, for instance, was equivalent to the lateral interaction between two methanol adsorbates on adjacent Ag sites.

To compare the pure Ag surface with that of the Pd-promoted surface, a 9×9 pure Ag(100) surface was compared to a 9×9 Pd/Ag(100) surface. The turnover frequency per site of the pure surface was calculated to be $1.34\pm0.01\ s^{-1}$, whereas the turnover frequency of the SAA surface was calculated to be $3.21\pm0.09\ s^{-1}$. This suggested that the presence of single Pd sites would greatly improve the activity of the Ag(100) surface. To elucidate the effects of dilution on the SAAs, 3×3, 5×5, 7×7, and 9×9 models were compared, each having only one Pd top site and therefore having four 4-fold sites. The results of these simulations are shown in Figure 65.

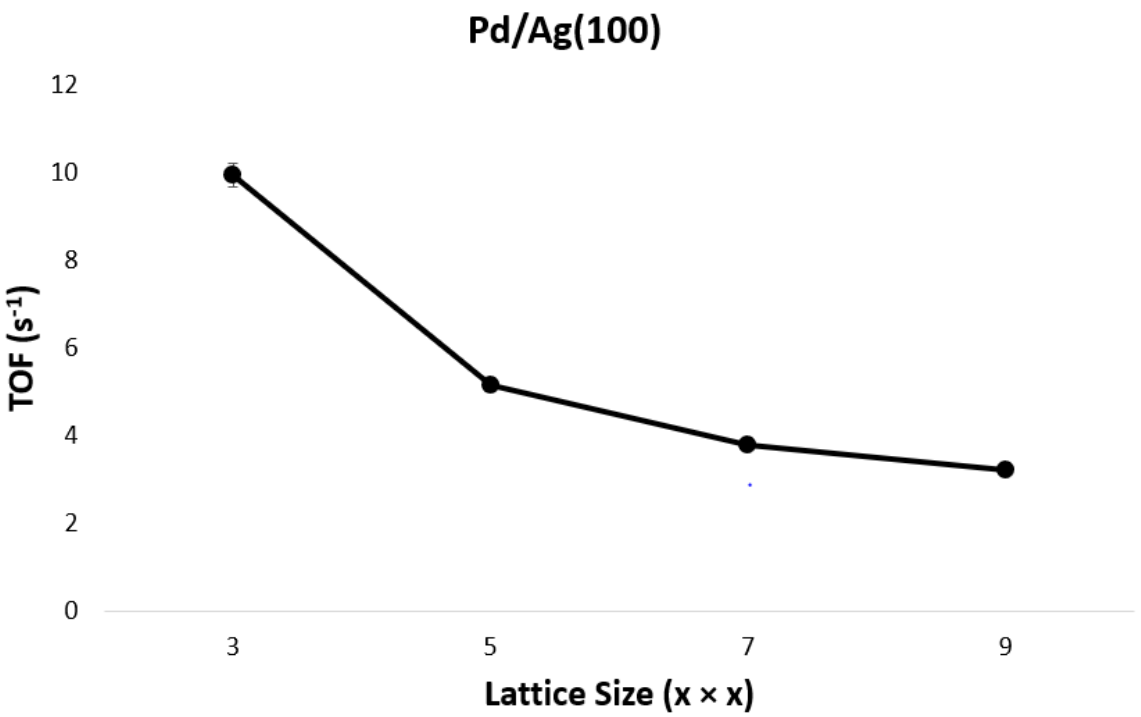

Figure 65. The effect of dilution of Pd sites on Pd/Ag(100) SAAs. A 3×3 lattice would have a higher dilution of Pd sites.

Figure 65 above suggests that higher concentrations of isolated Pd would yield higher turnover frequencies. In the 3×3 lattice, only 55.6% of the available sites are pure Ag(100) sites, in comparison to 95.1% on the 9×9 lattice. Since the Pd site is much more active for the dehydrogenation reaction than the Ag site, the number of isolated Pd sites should be maximized to increase the TOF. To confirm this, the reaction event frequencies were examined, and it was found that almost 98% of the resultant formaldehyde was formed on the Pd sites on the 3×3 lattice, while only 64% of the formaldehyde was formed on the Pd sites on the 9×9 lattice.

These studies also suggest that the true role of the Pd promoter in the SAAs for methanol dehydrogenation is to simply lower the barriers of dehydrogenation on otherwise less-reactive Ag surfaces. Unlike our studies on N_2 dissociation and CH_4 activation in

Chapters 2 and 3, spillover of adsorbates from the promoter sites to the host sites does not play a crucial role in this reaction. Indeed, even though methoxy binds weaker to the Pd site than the Ag site, more diffusion occurs from Ag sites to Pd sites than in the reverse direction because methoxy dissociates easier to formaldehyde on the Pd sites than on the Ag sites. It is crucial, however, that Pd remains isolated in the surface to prevent the deep dehydrogenation to CO. In these studies, no CO was formed. In the DFT calculations, the presence of adjacent Ag atoms weakened the binding of adsorbates enough such the dehydrogenation of formaldehyde to formyl on the Pd site remained difficult enough that selectivity would be retained. When Pd sites aggregate and form ensembles, however, the deep dehydrogenation of methanol would become preferred.[205,275] Thus, although higher concentrations of isolated Pd sites would be optimal for this reaction, extra care must be taken to ensure that Pd atoms are not too geometrically close to each other such that they would aggregate easily.

7.4. Conclusion

In this chapter, we examined two different promoters, palladium and zinc, on the Ag(100) and Ag(111) surfaces as single-atom alloys. The Pd-promoted Ag(100) and Ag(111) surfaces lowered dehydrogenation rates, allowing lower barriers to form formaldehyde from methanol, but also lowered the barriers towards deep dehydrogenation. Meanwhile, the Zn-promoted surfaces bound methoxy very strongly, and if adsorbate spillover from the Zn promoter site to the host sites occurred, then the Zn-promoted surfaces would be promising SAAs as well. The obtained energetic data from density functional theory was input into microkinetic modeling simulations, and while these

simulations have limitations due to their lack of spatial features, they do predict that the Pd/Ag(100) SAA would heavily promote the non-oxidative formation of formaldehyde from methanol. The Pd/Ag(100) SAA was then examined using KMC, and the presence of isolated Pd sites did improve the activity of pure Ag(100). We determined that the role of Pd sites in SAAs for methanol dehydrogenation was simply to improve activity, as spillover did not play a considerable role in the mechanism and selectivity was already high. We also found that higher concentrations of isolated Pd sites would improve activity. The studies in this chapter lay the groundwork and offer an example on how promoter metals can be theoretically examined to provide greater activity on rationally designed catalysts.

Chapter 8. Concluding Remarks

8.1. Final Conclusions

In this doctoral study, we sought to develop new catalyst strategies and insights to impact the field of catalytic dehydrogenation. Much of catalytic dehydrogenation is defined by rules, laws, or trendlines, and we investigated different methods to break those rules, laws, and trendlines and lay the groundwork for a rational design paradigm that could bridge the gap between theoretical and experimental catalysis.

We began by investigating single-atom alloys (SAAs). SAAs consist of a highly-reactive, isolated promoter metal that sits within a host of less-reactive metal atoms. A reactant molecule would dissociate over the promoter metal and the resulting adsorbates would spillover or disperse away from the promoter metal to the host metal, where they would bind weakly and be available for further reaction. These SAAs boast low activation energies due to the reactive promoter metal, yet do not have highly exothermic reaction energies because the adsorbates spill over to the weak-binding host sites of the catalyst surface. These two properties come together to break traditional scaling relations, which state that catalysts that have low activation energies tend to have very exothermic reaction energies as well. The ability of the SAAs to break these scaling relations was tested for the Haber-Bosch reaction, where the single atom must be able to break the strong triple bond of N_2. We found that our SAAs did indeed circumvent the established trendlines by lowering activation energy barriers yet binding the resultant nitrogen adatoms weakly, allowing for easier hydrogenation to form ammonia. In particular, we found that Mo-promoted Co(0001) and Fe-promoted Co(0001) were promising SAAs for this reaction.

With the understanding that isolated reactive atoms were promising tools in catalysis, we took aim at the base case of hydrocarbon dehydrogenation: the activation of methane. Methane is a notoriously difficult molecule to successfully activate; its C-H bonds are very strong, requiring a catalyst that exhibits excellent activity, yet once one of the C-H bonds is broken, it is likely that all of the C-H bonds will break, requiring a catalyst that is selective. We examined the $Au_3Pd(111)$ surface, which contains a single Pd atom that is fully surrounded by Au atoms, reminiscent of the surface geometry of SAAs. In the non-oxidative activation of methane on $Au_3Pd(111)$, the second dehydrogenation step of methane is more difficult than the first one, suggesting that there may be a temperature in which methane is dehydrogenated to methyl, which can sit on the Pd site for further chemistry. The oxidative activation of methane is also promising on this catalyst, as the isolated Pd atom draws oxygen to the otherwise inert Au surface, and the surface oxygenates readily abstract hydrogen from the methane molecule. From this work, we found that isolated metal atoms can combine activity and selectivity into one catalyst for both non-oxidative and oxidative reaction schemes.

From here, we wanted to create a new design paradigm for the prediction of an optimal catalyst for any reaction performed on a metal surface. By probing reactions on multiple surface facets of a catalyst and inputting the obtained energetic parameters into a kinetic Monte Carlo (KMC) simulation, reaction rates and turnover frequencies can be obtained from the first-principles density functional theory calculations. For our KMC simulations, we developed a terrace model that simulated the different terrace facets of a crystal, separated by a step site. Since each terrace represented a different surface facet, by increasing and decreasing the terrace lengths in our terrace model, we can find an optimal

size and shape for a nanoparticle for that particular reaction. By examining the non-oxidative dehydrogenation of methanol to formaldehyde on silver nanoparticles as a case study, we found that small, cube-like nanoparticles would be most active for the reaction.

We wanted to wield our knowledge of single-atom alloys to add promoters to the catalyst nanoparticles that were predicted in our terrace model in KMC, but first, we needed to understand the stability of the SAA surfaces. The dilute promoter atom on a SAA surface can go multiple places; it can diffuse into the subsurface of the catalyst, it can dimerize and aggregate with other promoter atoms within the surface layer of the catalyst, or it can sit on top of the surface layer as an adatom. We calculated and compared the stability of each case for all combinations of the *d*-block metals and developed a chart with nearly 30×30 elements. This chart presents information on what the most stable surface configuration is for that combination of elements and allows for the discovery of new SAA catalysts in reactions that may have never been tested before.

Using our developed chart of SAA stability, we returned to the dehydrogenation of methanol and examined Pd and Zn promoters for the reaction on different Ag facets. In a combined density functional theory and microkinetic modeling study, we find that Pd promoters aid in the dehydrogenation kinetics, while Zn promoters allow for the stronger binding of certain intermediates. We conclude that the rational selection of promoter metals for catalytic dehydrogenation reactions and other reactions in heterogeneous reactions could significantly improve the activity of the catalyst.

From this doctoral work, we have developed a research paradigm that combines first-principles density functional theory calculations with kinetic Monte Carlo simulations and allows for the determination of the optimal size, shape, and promoters for a catalyst

nanoparticle. While the chasm between theoretical and experimental catalysis is large, we hope that our efforts have laid the groundwork for the first bridges to span the computational and laboratory worlds.

8.2. Future Work

Since a large bevy of topics were covered in this doctoral work, there are many different research questions and directions that could be followed. There are two directions, however, that I believe could be most lucrative in research.

First, I believe that a continuation of the kinetic Monte Carlo simulations discussed in this work would be promising. There remain multiple tasks to accomplish within those simulations, including the implementation of the single-atom alloys. There is little literature involving KMC on SAAs, so this could potentially be a source of multiple publications in understanding the diffusion rates of adsorbates on SAAs.

Second, and more importantly, I believe that there is a route for future exploration on selective oxidation on SAAs, similar to the study that was performed in Chapter 3. To finish the methanol dehydrogenation work, the introduction of oxygen to the system would add new and more impactful insights than what has been reported in Chapters 4, 5, and 7. There is little to no literature on selective oxidation on SAAs, and the Formox process is not the only reaction that could be promising. Selective oxidation on SAAs could be studied for ethylene epoxidation, isopropyl alcohol to acetone, or propene to acrolein. SAAs can also be used to draw water to the surface for hydration reactions.

References

(1) On Purpose – What's Driving New Propane Dehydrogenation Projects in North America? | Nexant https://www.nexant.com/resources/purpose-what-s-driving-new-propane-dehydrogenation-projects-north-america (accessed Nov 3, 2019).

(2) Khodakov, A.; Yang, J.; Su, S.; Iglesia, E.; Bell, A. T. *J. Catal.* **1998**, *177* (2), 343–351.

(3) Siahvashi, A.; Chesterfield, D.; Adesina, A. A. *Ind. Eng. Chem. Res.* **2013**, *52* (11), 4017–4026.

(4) Grant, J. T.; Carrero, C. A.; Goeltl, F.; Venegas, J.; Mueller, P.; Burt, S. P.; Specht, S. E.; McDermott, W. P.; Chieregato, A.; Hermans, I. *Science (80-.).* **2016**, *354* (6319), 1570–1573.

(5) Chen, K.; Bell, A. T.; Iglesia, E. *J. Phys. Chem. B* **2000**, *104* (6), 1292–1299.

(6) Sattler, J. J. H. B.; Ruiz-Martinez, J.; Santillan-Jimenez, E.; Weckhuysen, B. M. *Chem. Rev.* **2014**, *114* (20), 10613–10653.

(7) Wang, H.; Cong, Y.; Yang, W. *Chem. Commun.* **2002**, *2* (14), 1468–1469.

(8) Ruscic, B. *J. Phys. Chem. A* **2015**, *119* (28), 7810–7837.

(9) Wang, S.; Temel, B.; Shen, J.; Jones, G.; Grabow, L. C.; Studt, F.; Bligaard, T.; Abild-Pedersen, F.; Christensen, C. H.; Nørskov, J. K. *Catal. Letters* **2011**, *141* (3), 370–373.

(10) Latimer, A. A.; Kulkarni, A. R.; Aljama, H.; Montoya, J. H.; Yoo, J. S.; Tsai, C.; Abild-Pedersen, F.; Studt, F.; Nørskov, J. K. *Nat. Mater.* **2017**, *16* (2), 225–229.

(11) Studt, F.; Abild-Pedersen, F.; Bligaard, T.; Sørensen, R. Z.; Christensen, C. H.; Nørskov, J. K. *Science* **2008**, *320* (5881), 1320–1322.

(12) Andersen, M.; Medford, A. J.; Nørskov, J. K.; Reuter, K. *ACS Catal.* **2017**, *7* (6), 3960–3967.

(13) Vojvodic, A.; Nørskov, J. K. *Natl. Sci. Rev.* **2015**, *2* (2), 140–149.

(14) Medford, A. J.; Vojvodic, A.; Hummelshøj, J. S.; Voss, J.; Abild-Pedersen, F.; Studt, F.; Bligaard, T.; Nilsson, A.; Nørskov, J. K. *J. Catal.* **2015**, *328*, 36–42.

(15) Nørskov, J. K.; Abild-Pedersen, F.; Studt, F.; Bligaard, T. *Proc. Natl. Acad. Sci. U. S. A.* **2011**, *108* (3), 937–943.

(16) Wang, S.; Petzold, V.; Tripkovic, V.; Kleis, J.; Howalt, J. G.; Skúlason, E.; Fernández, E. M.; Hvolbæk, B.; Jones, G.; Toftelund, A.; Falsig, H.; Björketun, M.; Studt, F.; Abild-Pedersen, F.; Rossmeisl, J.; Nørskov, J. K.; Bligaard, T. *Phys. Chem. Chem. Phys.* **2011**, *13* (46), 20760–20765.

(17) Grabow, L. C.; Studt, F.; Abild-Pedersen, F.; Petzold, V.; Kleis, J.; Bligaard, T.; Nørskov, J. K. *Angew. Chem. Int. Ed. Engl.* **2011**, *50* (20), 4601–4605.

(18) Vojvodic, A.; Medford, A. J.; Studt, F.; Abild-Pedersen, F.; Khan, T. S.; Bligaard, T.; Nørskov, J. K. *Chem. Phys. Lett.* **2014**, *598*, 108–112.

(19) Bronsted, J. N. *Chem. Rev.* **1928**, *5* (3), 231–338.

(20) Evans, M. G.; Polanyi, M. *Trans. Faraday Soc.* **1938**, *34*, 11–24.

(21) Logadottir, A.; Rod, T. .; Nørskov, J. .; Hammer, B.; Dahl, S.; Jacobsen, C. J. . *J. Catal.* **2001**, *197* (2), 229–231.

(22) Sabatier, P. *Berichte der Dtsch. Chem. Gesellschaft* **1911**, *44* (3), 1984–2001.

(23) Laursen, A. B.; Man, I. C.; Trinhammer, O. L.; Rossmeisl, J.; Dahl, S. *J. Chem. Educ.* **2011**, *88* (12), 1711–1715.

(24) Laursen, A. B.; Varela, A. S.; Dionigi, F.; Fanchiu, H.; Miller, C.; Trinhammer, O.

L.; Rossmeisl, J.; Dahl, S. *J. Chem. Educ.* **2012**, *89* (12), 1595–1599.

(25) Busch, M.; Wodrich, M. D.; Corminboeuf, C. *Chem. Sci.* **2015**, *6* (12), 6754–6761.

(26) Jacobsen, C. J. H.; Dahl, S.; Clausen, B. G. S.; Bahn, S.; Logadottir, A.; Nørskov, J. K. *Journal of the American Chemical Society*. 2001, pp 8404–8405.

(27) Andersson, M. P.; Bligaard, T.; Kustov, A.; Larsen, K. E.; Greeley, J.; Johannessen, T.; Christensen, C. H.; Nørskov, J. K. *J. Catal.* **2006**, *239* (2), 501–506.

(28) Greeley, J.; Jaramillo, T. F.; Bonde, J.; Chorkendorff, I.; Nørskov, J. K. *Nat. Mater.* **2006**, *5* (11), 909–913.

(29) Nørskov, J. K.; Bligaard, T.; Rossmeisl, J.; Christensen, C. H. *Nature Chemistry*. Nature Publishing Group April 1, 2009, pp 37–46.

(30) Hansen, H. A.; Varley, J. B.; Peterson, A. A.; Nørskov, J. K. *J. Phys. Chem. Lett.* **2013**, *4* (3), 388–392.

(31) Rodriguez, J. *Surf. Sci. Rep.* **1996**, *24* (7–8), 223–287.

(32) Liu, P.; Nørskov, J. K. *Phys. Chem. Chem. Phys.* **2001**, *3* (17), 3814–3818.

(33) Pleth Nielsen, L.; Besenbacher, F.; Stensgaard, I.; Laegsgaard, E.; Engdahl, C.; Stoltze, P.; Jacobsen, K. W.; Nørskov, J. K. *Phys. Rev. Lett.* **1993**, *71* (5), 754–757.

(34) Schlapka, A.; Lischka, M.; Groß, A.; Käsberger, U.; Jakob, P. *Phys. Rev. Lett.* **2003**, *91* (1), 016101/1-016101/4.

(35) Hwu, H. H.; Eng, J.; Chen, J. G. *J. Am. Chem. Soc.* **2002**, *124* (4), 702–709.

(36) Klötzer, B.; Unterberger, W.; Hayek, K. In *Surface Science*; 2003; Vol. 532–535, pp 142–147.

(37) Greeley, J.; Mavrikakis, M. *Nat. Mater.* **2004**, *3* (11), 810–815.

(38) Greeley, J.; Mavrikakis, M. *Catal. Today* **2006**, *111* (1–2), 52–58.

(39) Tierney, H. L.; Baber, A. E.; Sykes, E. C. H. *J. Phys. Chem. C* **2009**, *113* (17), 7246–7250.

(40) Zhang, X.; Yu, S.; Zheng, W.; Liu, P. *Phys. Chem. Chem. Phys.* **2014**, *16* (31), 16615–16622.

(41) Yang, X.-F.; Wang, A.; Qiao, B.; Li, J.; Liu, J.; Zhang, T. *Acc. Chem. Res.* **2013**, *46* (8), 1740–1748.

(42) Liang, S.; Hao, C.; Shi, Y. *ChemCatChem* **2015**, *7* (17), 2559–2567.

(43) Wang, A.; Li, J.; Zhang, T. *Nature Reviews Chemistry*. Nature Publishing Group June 1, 2018, pp 65–81.

(44) Zhang, H.; Liu, G.; Shi, L.; Ye, J. *Adv. Energy Mater.* **2018**, *8* (1), 1701343.

(45) Darby, M. T.; Stamatakis, M.; Michaelides, A.; Sykes, E. C. H. *J. Phys. Chem. Lett.* **2018**, *9* (18), 5636–5646.

(46) Lucci, F. R.; Liu, J.; Marcinkowski, M. D.; Yang, M.; Allard, L. F.; Flytzani-Stephanopoulos, M.; Sykes, E. C. H. *Nat. Commun.* **2015**, *6*, 8550.

(47) Pei, G. X.; Liu, X. Y.; Wang, A.; Lee, A. F.; Isaacs, M. A.; Li, L.; Pan, X.; Yang, X.; Wang, X.; Tai, Z.; Wilson, K.; Zhang, T. *ACS Catal.* **2015**, *5* (6), 3717–3725.

(48) Aich, P.; Wei, H.; Basan, B.; Kropf, A. J.; Schweitzer, N. M.; Marshall, C. L.; Miller, J. T.; Meyer, R. *J. Phys. Chem. C* **2015**, *119* (32), 18140–18148.

(49) Thirumalai, H.; Kitchin, J. R. *Top. Catal.* **2018**, 1–13.

(50) Kyriakou, G.; Boucher, M. B.; Jewell, A. D.; Lewis, E. A.; Lawton, T. J.; Baber, A. E.; Tierney, H. L.; Flytzani-Stephanopoulos, M.; Sykes, E. C. H. *Science (80-.*

). **2012**, *335* (6073), 1209–1212.

(51) Shan, J.; Lucci, F. R.; Liu, J.; El-Soda, M.; Marcinkowski, M. D.; Allard, L. F.; Sykes, E. C. H.; Flytzani-Stephanopoulos, M. *Surf. Sci.* **2016**, *650*, 121–129.

(52) Han, Z.; Li, S.; Jiang, F.; Wang, T.; Ma, X.; Gong, J. *Nanoscale* **2014**, *6* (17), 10000–10008.

(53) Sun, S.; Zhang, G.; Gauquelin, N.; Chen, N.; Zhou, J.; Yang, S.; Chen, W.; Meng, X.; Geng, D.; Banis, M. N.; Li, R.; Ye, S.; Knights, S.; Botton, G. A.; Sham, T. K.; Sun, X. *Sci. Rep.* **2013**, *3* (1), 1775.

(54) Qiao, B.; Liu, J.; Wang, Y.-G.; Lin, Q.; Liu, X.; Wang, A.; Li, J.; Zhang, T.; Liu, J. (Jimmy). *ACS Catal.* **2015**, *5* (11), 6249–6254.

(55) Cheng, M.-J.; Clark, E. L.; Pham, H. H.; Bell, A. T.; Head-Gordon, M. *ACS Catal.* **2016**, *6* (11), 7769–7777.

(56) Jirkovský, J. S.; Panas, I.; Ahlberg, E.; Halasa, M.; Romani, S.; Schiffrin, D. J. *J. Am. Chem. Soc.* **2011**, *133* (48), 19432–19441.

(57) Grabow, L. C. *ChemCatChem*. John Wiley & Sons, Ltd December 1, 2012, pp 1887–1888.

(58) Jones, R. O. *Rev. Mod. Phys.* **2015**, *87* (3), 897–923.

(59) Becke, A. D. *J. Chem. Phys.* **2014**, *140* (18), 18A301.

(60) Sholl, D.; Steckel, J. A. *Density Functional Theory: A Practical Introduction*; John Wiley & Sons, 2011.

(61) Dreizler, R. M.; Gross, E. K. U. *Density Functional Theory: An Approach to the Quantum Many-Body Problem*; Springer Science & Business Media, 2012.

(62) Thomas, L. H. *Math. Proc. Cambridge Philos. Soc.* **1927**, *23* (05), 542.

(63) Fermi, E. Statistical method to determine some properties of atoms.

(64) Dirac, P. A. M. *Math. Proc. Cambridge Philos. Soc.* **1930**, *26* (03), 376.

(65) Slater, J. C. *Phys. Rev.* **1951**, *81* (3), 385–390.

(66) Hohenberg, P. *Phys. Rev.* **1964**, *136* (3B), B864–B871.

(67) Kohn, W.; Sham, L. J. *Phys. Rev.* **1965**, *140* (4A), A1133–A1138.

(68) Perdew, J. P. In *AIP Conference Proceedings*; AIP, 2001; Vol. 577, pp 1–20.

(69) Physik, T. U. D. I. für T.; Society, E. P. *Electronic structure of solids '91: proceedings of the 75. WE-Heraeus-Seminar and 21st Annual International Symposium on Electronic Structure of Solids held in Gaussig (Germany), March 11-15, 1991*; Akademie Verlag, 1991.

(70) Perdew, J. P.; Wang, Y. *Phys. Rev. B* **1992**, *46* (20), 12947–12954.

(71) Tsuzuki, S.; Lüthi, H. P. *J. Chem. Phys.* **2001**, *114* (9), 3949.

(72) Perdew, J. P.; Burke, K.; Ernzerhof, M. *Phys. Rev. Lett.* **1996**, *77* (18), 3865–3868.

(73) Hammer, B.; Hansen, L. B.; Nørskov, J. K. *Phys. Rev. B* **1999**, *59* (11), 7413–7421.

(74) Wellendorff, J.; Lundgaard, K. T.; Møgelhøj, A.; Petzold, V.; Landis, D. D.; Nørskov, J. K.; Bligaard, T.; Jacobsen, K. W. *Phys. Rev. B* **2012**, *85* (23), 235149.

(75) Brogaard, R. Y.; Moses, P. G.; Nørskov, J. K. *Catal. Letters* **2012**, *142* (9), 1057–1060.

(76) Henkelman, G.; Uberuaga, B. P.; Jónsson, H. *J. Chem. Phys.* **2000**, *113* (22), 9901.

(77) Henkelman, G.; Jónsson, H. *J. Chem. Phys.* **2000**, *113* (22), 9978.

(78) Henkelman, G.; Jónsson, H. *J. Chem. Phys.* **1999**, *111* (15), 7010–7022.

(79) Kammler, T.; Küppers, J. *J. Chem. Phys.* **1999**, *111* (17), 8115–8123.

(80) Erisman, J. W.; Sutton, M. A.; Galloway, J.; Klimont, Z.; Winiwarter, W. *Nat. Geosci.* **2008**, *1* (10), 636–639.

(81) Smil, V. *Nature* **1999**, *400* (6743), 415–415.

(82) Singh, A. R.; Montoya, J. H.; Rohr, B. A.; Tsai, C.; Vojvodic, A.; Nørskov, J. K. *ACS Catal.* **2018**, *8* (5), 4017–4024.

(83) Singh, A. R.; Rohr, B. A.; Schwalbe, J. A.; Cargnello, M.; Chan, K.; Jaramillo, T. F.; Chorkendorff, I.; Nørskov, J. K. *ACS Catal.* **2017**, *7* (1), 706–709.

(84) Chorkendorff, I.; Niemantsverdriet, J. W. *Concepts of Modern Catalysis and Kinetics*, 2nd ed.; Wiley-VCH Verlag GmbH & Co. KGaA, 2007.

(85) *Ullmann's Encyclopedia of Industrial Chemistry*; Wiley-VCH Verlag GmbH & Co. KGaA: Weinheim, Germany, 2000.

(86) Ertl, G.; Huber, M.; Thiele, N. *Zeitschrift für Naturforsch. A* **1979**, *34* (1), 30–39.

(87) Honkala, K.; Hellman, A.; Remediakis, I. N.; Logadottir, A.; Carlsson, A.; Dahl, S.; Christensen, C. H.; Nørskov, J. K. *Science (80-.).* **2005**, *307* (5709).

(88) Aika, K. ichi; Hori, H.; Ozaki, A. *J. Catal.* **1972**, *27* (3), 424–431.

(89) Andersen, M.; Medford, A. J.; Nørskov, J. K.; Reuter, K. *Angew. Chemie Int. Ed.* **2016**, *55* (17), 5210–5214.

(90) Andersen, M.; Medford, A. J.; Nørskov, J. K.; Reuter, K. *ACS Catal.* **2017**, *7* (6), 3960–3967.

(91) Lucci, F. R.; Marcinkowski, M. D.; Lawton, T. J.; Sykes, E. C. H. *J. Phys. Chem. C* **2015**, *119* (43), 24351–24357.

(92) Lucci, F. R.; Darby, M. T.; Mattera, M. F. G.; Ivimey, C. J.; Therrien, A. J.; Michaelides, A.; Stamatakis, M.; Sykes, E. C. H. *J. Phys. Chem. Lett.* **2016**, *7* (3),

480–485.

(93) Kresse, G.; Hafner, J. *Phys. Rev. B* **1993**, *47* (1), 558–561.

(94) Kresse, G.; Hafner, J. *Phys. Rev. B* **1994**, *49* (20), 14251–14269.

(95) Kresse, G.; Furthmüller, J. *Phys. Rev. B* **1996**, *54* (16), 11169–11186.

(96) Kresse, G.; Furthmüller, J. *Comput. Mater. Sci.* **1996**, *6* (1), 15–50.

(97) Bahn, S. R.; Jacobsen, K. W. *Comput. Sci. Eng.* **2002**, *4* (3), 56–66.

(98) Blöchl, P. E. *Phys. Rev. B* **1994**, *50* (24), 17953–17979.

(99) Kresse, G. *Phys. Rev. B* **1999**, *59* (3), 1758–1775.

(100) Hull, A. W. *Phys. Rev.* **1921**, *17* (5), 571–588.

(101) Jette, E. R.; Foote, F. *J. Chem. Phys.* **1935**, *3* (10), 605–616.

(102) Monkhorst, H. J.; Pack, J. D. *Phys. Rev. B* **1976**, *13* (12), 5188–5192.

(103) Medford, A. J.; Shi, C.; Hoffmann, M. J.; Lausche, A. C.; Fitzgibbon, S. R.; Bligaard, T.; Nørskov, J. K. *Catal. Letters* **2015**, *145* (3), 794–807.

(104) Falsig, H.; Shen, J.; Khan, T. S.; Guo, W.; Jones, G.; Dahl, S.; Bligaard, T. *Top. Catal.* **2014**, *57* (1–4), 80–88.

(105) Hammer, B.; Nørskov, J. K. *Surf. Sci.* **1995**, *343* (3), 211–220.

(106) Cordero, B.; Gómez, V.; Platero-Prats, A. E.; Revés, M.; Echeverría, J.; Cremades, E.; Barragán, F.; Alvarez, S. *J. Chem. Soc. Dalt. Trans.* **2008**, No. 21, 2832–2838.

(107) Medford, A. J.; Vojvodic, A.; Hummelshøj, J. S.; Voss, J.; Abild-Pedersen, F.; Studt, F.; Bligaard, T.; Nilsson, A.; Nørskov, J. K. *J. Catal.* **2015**, *328*, 36–42.

(108) Logadóttir, Á.; Nørskov, J. K. *J. Catal.* **2003**, *220* (2), 273–279.

(109) Jacobsen, C. J. H. *Chem. Commun.* **2000**, No. 12, 1057–1058.

(110) Kojima, R.; Aika, K. I. *Appl. Catal. A Gen.* **2001**, *219* (1–2), 157–170.

(111) Kojima, R.; Aika, K. I. *Appl. Catal. A Gen.* **2001**, *218* (1–2), 121–128.

(112) Kojima, R.; Aika, K. I. *Appl. Catal. A Gen.* **2001**, *215* (1–2), 149–160.

(113) Adamski, P.; Moszyński, D.; Nadziejko, M.; Komorowska, A.; Sarnecki, A.; Albrecht, A. *Chem. Pap.* **2019**, *73* (4), 851–859.

(114) Hargreaves, J. S. J.; Mckay, D. *J. Mol. Catal. A Chem.* **2009**, *305* (1–2), 125–129.

(115) Bion, N.; Can, F.; Cook, J.; Hargreaves, J. S. J.; Hector, A. L.; Levason, W.; McFarlane, A. R.; Richard, M.; Sardar, K. *Appl. Catal. A Gen.* **2015**, *504*, 44–50.

(116) McAulay, K.; Hargreaves, J. S. J.; McFarlane, A. R.; Price, D. J.; Spencer, N. A.; Bion, N.; Can, F.; Richard, M.; Greer, H. F.; Zhou, W. Z. *Catal. Commun.* **2015**, *68*, 53–57.

(117) Kojima, R.; Aika, K. I. *Appl. Catal. A Gen.* **2001**, *209* (1–2), 317–325.

(118) Kaleńczuk, R. J. *J. Chem. Technol. Biotechnol.* **1994**, *59* (1), 73–81.

(119) Kaleńczuk, R. J. *Int. J. Inorg. Mater.* **2000**, *2* (2–3), 233–239.

(120) Hagen, S.; Barfod, R.; Fehrmann, R.; Jacobsen, C. J. H.; Teunissen, H. T.; Chorkendorff, I. *J. Catal.* **2003**, *214* (2), 327–335.

(121) Smith, P. J.; Taylor, D. W.; Dowden, D. A.; Kemball, C.; Taylor, D. *Appl. Catal.* **1982**, *3* (4), 303–314.

(122) Nørskov, J. K.; Bligaard, T.; Logadottir, A.; Bahn, S.; Hansen, L. B.; Bollinger, M.; Bengaard, H.; Hammer, B.; Sljivancanin, Z.; Mavrikakis, M.; Xu, Y.; Dahl, S.; Jacobsen, C. J. H. *J. Catal.* **2002**, *209* (2), 275–278.

(123) Tierney, H.; Baber, A.; Kitchin, J.; Sykes, C. In *ACS National Meeting Book of Abstracts*; 2010.

(124) Kozuch, S.; Shaik, S. *Acc. Chem. Res.* **2011**, *44* (2), 101–110.

(125) Chatterjee, A.; Vlachos, D. G. *J. Comput. Mater. Des.* **2007**, *14* (2), 253–308.

(126) Stamatakis, M.; Vlachos, D. G. *J. Chem. Phys.* **2011**, *134* (21).

(127) Stamatakis, M.; Vlachos, D. G. *ACS Catalysis*. December 7, 2012, pp 2648–2663.

(128) Papanikolaou, K. G.; Darby, M. T.; Stamatakis, M. *J. Phys. Chem. C* **2019**, *123* (14), 9128–9138.

(129) BP. Natural Gas section - Statistical Review of World Energy http://www.bp.com/content/dam/bp/pdf/energy-economics/statistical-review-2015/bp-statistical-review-of-world-energy-2015-natural-gas-section.pdf (accessed Mar 18, 2016).

(130) Makogon, Y. F.; Holditch, S. A.; Makogon, T. Y. *J. Pet. Sci. Eng.* **2007**, *56* (1–3), 14–31.

(131) Dawe, R. A.; Thomas, S. *Energy Sources, Part A* **2007**.

(132) Wang, Q.; Chen, X.; Jha, A. N.; Rogers, H. *Renew. Sustain. Energy Rev.* **2014**, *30*, 1–28.

(133) Bousquet, P.; Ciais, P.; Miller, J. B.; Dlugokencky, E. J.; Hauglustaine, D. A.; Prigent, C.; Van der Werf, G. R.; Peylin, P.; Brunke, E.-G.; Carouge, C.; Langenfelds, R. L.; Lathière, J.; Papa, F.; Ramonet, M.; Schmidt, M.; Steele, L. P.; Tyler, S. C.; White, J. *Nature* **2006**, *443* (7110), 439–443.

(134) Weiland, P. *Appl. Microbiol. Biotechnol.* **2010**, *85* (4), 849–860.

(135) Horn, R.; Schlögl, R. *Catal. Letters* **2014**, *145* (1), 23–39.

(136) Rostrup-Nielsen, J. R.; Sehested, J.; Nørskov, J. K. *Adv. Catal.* **2002**, *47*, 65–139.

(137) Tsang, S. C.; Claridge, J. B.; Green, M. L. H. *Catal. Today* **1995**, *23* (1), 3–15.

(138) Aasberg-Petersen, K.; Dybkjær, I.; Ovesen, C. V.; Schjødt, N. C.; Sehested, J.;

Thomsen, S. G. *J. Nat. Gas Sci. Eng.* **2011**, *3* (2), 423–459.

(139) *Hydrogen and Syngas Production and Purification Technologies*; Liu, K., Song, C., Subramani, V., Eds.; John Wiley & Sons, Inc.: Hoboken, NJ, USA, 2009.

(140) Rostrup-Nielsen, J.; Christiansen, L. J. *Concepts in Syngas Manufacture*; World Scientific, 2011.

(141) German, E. D.; Sheintuch, M. *J. Phys. Chem. C* **2013**, *117* (44), 22811–22826.

(142) Schwach, P.; Pan, X.; Bao, X. *Chem. Rev.* **2017**, *117* (13), 8497–8520.

(143) Liu, J. *ACS Catal.* **2017**, *7* (1), 34–59.

(144) Kyriakou, G.; Boucher, M. B.; Jewell, A. D.; Lewis, E. A.; Lawton, T. J.; Baber, A. E.; Tierney, H. L.; Flytzani-Stephanopoulos, M.; Sykes, E. C. H. *Science (80-.).* **2012**, *335* (6073).

(145) Chen, M.; Kumar, D.; Yi, C.-W.; Goodman, D. W.; Carley, A. F.; Herzing, A. A.; Watanabe, M.; Kiely, C. J.; Knight, D. W.; Hutchings, G. J. *Science (80-.).* **2005**, *310* (5746), 291–293.

(146) Ham, H. C.; Hwang, G. S.; Han, J.; Nam, S. W.; Lim, T. H. *J. Phys. Chem. C* **2009**, *113* (30), 12943–12945.

(147) Baddeley, C. J.; Tikhov, M.; Hardacre, C.; Lomas, J. R.; Lambert, R. M. *J. Phys. Chem.* **1996**, *100* (6), 2189–2194.

(148) Wu, Z.; Deng, J.; Liu, Y.; Xie, S.; Jiang, Y.; Zhao, X.; Yang, J.; Arandiyan, H.; Guo, G.; Dai, H. *J. Catal.* **2015**, *332*, 13–24.

(149) Ab Rahim, M. H.; Forde, M. M.; Jenkins, R. L.; Hammond, C.; He, Q.; Dimitratos, N.; Lopez-Sanchez, J. A.; Carley, A. F.; Taylor, S. H.; Willock, D. J.; Murphy, D. M.; Kiely, C. J.; Hutchings, G. J. *Angew. Chemie - Int. Ed.* **2013**, *52* (4), 1280–

1284.

(150) Agarwal, N.; Freakley, S. J.; McVicker, R. U.; Althahban, S. M.; Dimitratos, N.; He, Q.; Morgan, D. J.; Jenkins, R. L.; Willock, D. J.; Taylor, S. H.; Kiely, C. J.; Hutchings, G. J. *Science (80-.).* **2017**, *358* (6360), 223–227.

(151) Luo, Z.; Kriz, D. A.; Miao, R.; Kuo, C. H.; Zhong, W.; Guild, C.; He, J.; Willis, B.; Dang, Y.; Suib, S. L.; Nandi, P. *Appl. Catal. A Gen.* **2018**, *554*, 54–63.

(152) Gao, F.; Wang, Y.; Goodman, D. W. *J. Am. Chem. Soc.* **2009**, *131* (16), 5734–5735.

(153) Han, S.; Mullins, C. B. *ACS Catal.* **2018**, *8* (4), 3641–3649.

(154) Hughes, M. D.; Xu, Y. J.; Jenkins, P.; McMorn, P.; Landon, P.; Enache, D. I.; Carley, A. F.; Attard, G. A.; Hutchings, G. J.; King, F.; Stitt, E. H.; Johnston, P.; Griffin, K.; Kiely, C. J. *Nature* **2005**, *437* (7062), 1132–1135.

(155) Hayashi, T.; Tanaka, K.; Haruta, M. *J. Catal.* **1998**, *178* (2), 566–575.

(156) Haruta, M.; Kobayashi, T.; Sano, H.; Yamada, N. *Chem. Lett.* **1987**, *16* (2), 405–408.

(157) Saavedra, J.; Doan, H. A.; Pursell, C. J.; Grabow, L. C.; Chandler, B. D. *Science* **2014**, *345* (6204), 1599–1602.

(158) Wrasman, C. J.; Boubnov, A.; Riscoe, A. R.; Hoffman, A. S.; Bare, S. R.; Cargnello, M. *J. Am. Chem. Soc.* **2018**, *140* (40), 12930–12939.

(159) Cao, X.; Ji, Y.; Luo, Y. *J. Phys. Chem. C* **2015**, *119* (2), 1016–1023.

(160) Kresse, G.; Hafner, J. *Phys. Rev. B* **1993**, *47* (1), 558–561.

(161) Kresse, G.; Furthmüller, J. *Comput. Mater. Sci.* **1996**, *6* (1), 15–50.

(162) Bahn, S. R.; Jacobsen, K. W. *Comput. Sci. Eng.* **2002**, *4* (3), 56–66.

(163) Perdew, J. P.; Chevary, J. A.; Vosko, S. H.; Jackson, K. A.; Pederson, M. R.; Singh, D. J.; Fiolhais, C. *Phys. Rev. B* **1992**, *46* (11), 6671–6687.

(164) Stevens, E. D.; Rys, J.; Coppens, P. *J. Am. Chem. Soc.* **1978**, *100* (8), 2324–2328.

(165) Yan, X.; Lin, P.; Qi, X.; Yang, L. *Int. J. Mater. Res.* **2011**, *102* (4), 381–388.

(166) Gillan, M. J. *J. Phys. Condens. Matter* **1989**, *1* (4), 689–711.

(167) Mowbray, D. J.; Martinez, J. I.; García Lastra, J. M.; Thygesen, K. S.; Jacobsen, K. W. *J. Phys. Chem. C* **2009**, *113* (28), 12301–12308.

(168) Mowbray, D. J.; Migani, A.; Walther, G.; Cardamone, D. M.; Rubio, A. *J. Phys. Chem. Lett.* **2013**, *4* (17), 3006–3012.

(169) Hammer, B.; Nørskov, J. K. *Adv. Catal.* **2000**, *45*, 71–129.

(170) Tang, W.; Sanville, E.; Henkelman, G. *J. Phys. Condens. Matter* **2009**, *21* (8), 084204.

(171) Hibbitts, D.; Neurock, M. *Surf. Sci.* **2016**, *650*, 210–220.

(172) Tsai, C.; Latimer, A. A.; Yoo, J. S.; Studt, F.; Abild-Pedersen, F. *J. Phys. Chem. Lett.* **2015**, *6* (18), 3670–3674.

(173) Yoo, J. S.; Khan, T. S.; Abild-Pedersen, F.; Nørskov, J. K.; Studt, F. *Chem. Commun.* **2015**, *51* (13), 2621–2624.

(174) Chin, Y.-H. H.; Iglesia, E. *J. Phys. Chem. C* **2011**, *115* (36), 17845–17855.

(175) Chin, Y. H.; Buda, C.; Neurock, M.; Iglesia, E. *J. Am. Chem. Soc.* **2011**, *133* (40), 15958–15978.

(176) Meng-Sheng Liao; Chak-Tong Au; Ching-Fai Ng. *Chem. Phys. Lett.* **2003**, *272* (5–6), 445–452.

(177) Au, C.-T.; Ng, C.-F.; Liao, M.-S. *J. Catal.* **1999**, *185*, 12–22.

(178) Chase, M. W.; Curnutt, J. L.; Prophet, H.; McDonald, R. A.; Syverud, A. N. *J. Phys. Chem. Ref. Data* **1975**, *4* (1), 1.

(179) Xing, B.; Wang, G.-C. *Phys. Chem. Chem. Phys.* **2014**, *16* (6), 2621.

(180) Parker, D. H.; Koel, B. E. *J. Vac. Sci. Technol. A Vacuum, Surfaces, Film.* **1990**, *8* (3), 2585–2590.

(181) Saliba, N.; Parker, D. .; Koel, B. . *Surf. Sci.* **1998**, *410* (2–3), 270–282.

(182) Pireaux, J. J.; Chtaïb, M.; Delrue, J. P.; Thiry, P. A.; Liehr, M.; Caudano, R. *Surf. Sci.* **1984**, *141* (1), 211–220.

(183) Chin, Y.-H. H.; Buda, C.; Neurock, M.; Iglesia, E. *J. Am. Chem. Soc.* **2013**, *135* (41), 15425–15442.

(184) Mills, G.; Gordon, M. S.; Metiu, H. *J. Chem. Phys.* **2003**, *118* (9), 4198–4205.

(185) Shi, H.; Stampfl, C. *Phys. Rev. B* **2007**, *76* (7), 075327.

(186) Latimer, A. A.; Aljama, H.; Kakekhani, A.; Yoo, J. S.; Kulkarni, A.; Tsai, C.; Garcia-Melchor, M.; Abild-Pedersen, F.; Nørskov, J. K. *Phys. Chem. Chem. Phys.* **2017**, *19* (5), 3575–3581.

(187) *Formaldehyde Producers Boost U.S. Economy*; 2014.

(188) Kowatsch, S. In *Phenolic Resins: A Century of Progress*; Springer Berlin Heidelberg: Berlin, Heidelberg, 2010; pp 25–40.

(189) Kent, J. A. *Handbook of industrial chemistry and biotechnology : volume 1 and 2*; Springer, 2012.

(190) Cornils, B.; Herrmann, W. A. (Wolfgang A. .; Zanthoff, H.-W. *Catalysis from A to Z.*

(191) Wittcoff, H.; Reuben, B. G.; Plotkin, J. S. *Industrial organic chemicals*; Wiley,

2013.

(192) Millar, G. J.; Collins, M. *Industrial and Engineering Chemistry Research*. American Chemical Society August 23, 2017, pp 9247–9265.

(193) Spreadborough, J.; Christian, J. W. *J. Sci. Instrum.* **1959**, *36* (3), 116–118.

(194) Takezawa, N.; Iwasa, N. *Catal. Today* **1997**, *36* (1), 45–56.

(195) Kandoi, S.; Greeley, J.; Sanchez-Castillo, M. A.; Evans, S. T.; Gokhale, A. A.; Dumesic, J. A.; Mavrikakis, M. *Top. Catal.* **2006**, *37* (1), 17–27.

(196) Vojvodic, A.; Nørskov, J. K. *Natl. Sci. Rev.* **2015**, *2* (2), 140–149.

(197) Abild-Pedersen, F.; Greeley, J.; Studt, F.; Rossmeisl, J.; Munter, T. R.; Moses, P. G.; Skúlason, E.; Bligaard, T.; Nørskov, J. K. *Phys. Rev. Lett.* **2007**, *99* (1).

(198) Kourouklis, H. N.; Nix, R. M. *J. Chem. Soc. Faraday Trans.* **1995**, *91* (21), 3963–3968.

(199) Campbell, C. T. *Journal of Catalysis*. Academic Press Inc. 2001, pp 520–524.

(200) Stegelmann, C.; Andreasen, A.; Campbell, C. T. *J. Am. Chem. Soc.* **2009**, *131* (23), 8077–8082.

(201) Wolcott, C. A.; Medford, A. J.; Studt, F.; Campbell, C. T. *J. Catal.* **2015**, *330*, 197–207.

(202) Gokhale, A. A.; Kandoi, S.; Greeley, J. P.; Mavrikakis, M.; Dumesic, J. A. In *Chemical Engineering Science*; Elsevier Ltd, 2004; Vol. 59, pp 4679–4691.

(203) Greeley, J.; Mavrikakis, M. *J. Am. Chem. Soc.* **2004**, *126* (12), 3910–3919.

(204) Li, H. J.; Lausche, A. C.; Peterson, A. A.; Hansen, H. A.; Studt, F.; Bligaard, T. *Surf. Sci.* **2015**, *641*, 105–111.

(205) Jiang, R.; Guo, W.; Li, M.; Fu, D.; Shan, H. *J. Phys. Chem. C* **2009**, *113* (10),

4188–4197.

(206) Lausche, A. C.; Abild-Pedersen, F.; Madix, R. J.; Nørskov, J. K.; Studt, F. *Surf. Sci.* **2013**, *613*, 58–62.

(207) Andreasen, A.; Lynggaard, H.; Stegelmann, C.; Stoltze, P. *Surf. Sci.* **2003**, *544* (1), 5–23.

(208) Andreasen, A.; Lynggaard, H.; Stegelmann, C.; Stoltze, P. *Appl. Catal. A Gen.* **2005**, *289* (2), 267–273.

(209) Wachs, I. E. *Surface Science*. 2003, pp 1–4.

(210) Jørgensen, M.; Grönbeck, H. *ACS Catal.* **2016**, *6* (10), 6730–6738.

(211) Wang, H.; He, C. Z.; Huai, L. Y.; Liu, J. Y. *J. Phys. Chem. C* **2013**, *117* (9), 4574–4584.

(212) Lu, X.; Deng, Z.; Guo, C.; Wang, W.; Wei, S.; Ng, S. P.; Chen, X.; Ding, N.; Guo, W.; Wu, C. M. L. *ACS Appl. Mater. Interfaces* **2016**, *8* (19), 12194–12204.

(213) Choksi, T.; Greeley, J. *ACS Catal.* **2016**, *6* (11), 7260–7277.

(214) Pineda, M.; Stamatakis, M. *J. Chem. Phys.* **2017**, *147* (2).

(215) Andersen, M.; Plaisance, C. P.; Reuter, K. *J. Chem. Phys.* **2017**, *147* (15).

(216) Bortz, A. B.; Kalos, M. H.; Lebowitz, J. L. *J. Comput. Phys.* **1975**, *17* (1), 10–18.

(217) Stamatakis, M.; Vlachos, D. G. *Comput. Chem. Eng.* **2011**, *35* (12), 2602–2610.

(218) Gillespie, D. T. *J. Comput. Phys.* **1976**, *22* (4), 403–434.

(219) Xu, L.; Mei, D.; Henkelman, G. *J. Chem. Phys.* **2009**, *131* (24).

(220) Lin, S.; Ma, J.; Zhou, L.; Huang, C.; Xie, D.; Guo, H. *J. Phys. Chem. C* **2013**, *117* (1), 451–459.

(221) Sakong, S.; Sendner, C.; Groß, A. *J. Mol. Struct. THEOCHEM* **2006**, *771* (1–3),

117–122.

(222) Sendner, C.; Sakong, S.; Groß, A. *Surf. Sci.* **2006**, *600* (16), 3258–3265.

(223) Zuo, Z.-J.; Gao, X.-Y.; Han, P.-D.; Liu, S.-Z.; Huang, W. *J. Phys. Chem. C* **2016**, *120* (48), 27500–27508.

(224) Nielsen, J.; D'Avezac, M.; Hetherington, J.; Stamatakis, M. *J. Chem. Phys.* **2013**, *139* (22).

(225) Campbell, C. T.; Sellers, J. R. V. *J. Am. Chem. Soc.* **2012**, *134* (43), 18109–18115.

(226) Mei, D.; Sheth, P. A.; Neurock, M.; Smith, C. M. *J. Catal.* **2006**, *242* (1), 1–15.

(227) Choi, Y.; Liu, P. In *Catalysis Today*; 2011; Vol. 165, pp 64–70.

(228) Weber, R. S.; Olarte, M. V.; Wang, H. *Energy and Fuels* **2015**, *29* (1), 273–277.

(229) Nørskov, J. K.; Bligaard, T.; Rossmeisl, J.; Christensen, C. H. *Nat. Chem.* **2009**, *1* (1), 37–46.

(230) Wang, S.; Temel, B.; Shen, J.; Jones, G.; Grabow, L. C.; Studt, F.; Bligaard, T.; Abild-Pedersen, F.; Christensen, C. H.; Nørskov, J. K. *Catal. Letters* **2011**, *141* (3), 370–373.

(231) van Santen, R. A.; Neurock, M.; Shetty, S. G. *Chem. Rev.* **2010**, *110* (4), 2005–2048.

(232) Cheng, J.; Hu, P.; Ellis, P.; French, S.; Kelly, G.; Lok, C. M. *J. Phys. Chem. C* **2008**, *112* (5), 1308–1311.

(233) Bligaard, T.; Nørskov, J. K.; Dahl, S.; Matthiesen, J.; Christensen, C. H.; Sehested, J. *J. Catal.* **2004**, *224* (1), 206–217.

(234) Nilekar, A. U.; Xu, Y.; Zhang, J.; Vukmirovic, M. B.; Sasaki, K.; Adzic, R. R.; Mavrikakis, M. *Top. Catal.* **2007**, *46* (3–4), 276–284.

(235) Groß, A. *Top. Catal.* **2006**, *37* (1), 29–39.

(236) Ruff, M.; Takehiro, N.; Liu, P.; Nørskov, J. K.; Behm, R. J. *ChemPhysChem* **2007**, *8* (14), 2068–2071.

(237) Li, Y.; Sun, Q. *Adv. Energy Mater.* **2016**, *6* (17), 1600463.

(238) Calle-Vallejo, F.; Krabbe, A.; García-Lastra, J. M. *Chem. Sci.* **2016**, *8* (1), 124–130.

(239) Wang, P.; Chang, F.; Gao, W.; Guo, J.; Wu, G.; He, T.; Chen, P. *Nat. Chem.* **2017**, *9* (1), 64–70.

(240) Greeley, J.; Mavrikakis, M. *J. Phys. Chem. B* **2005**, *109* (8), 3460–3471.

(241) Rameshan, C.; Stadlmayr, W.; Weilach, C.; Penner, S.; Lorenz, H.; Hävecker, M.; Blume, R.; Rocha, T.; Teschner, D.; Knop-Gericke, A.; Schlögl, R.; Memmel, N.; Zemlyanov, D.; Rupprechter, G.; Klötzer, B. *Angew. Chemie - Int. Ed.* **2010**, *49* (18), 3224–3227.

(242) Knudsen, J.; Nilekar, A. U.; Vang, R. T.; Schnadt, J.; Kunkes, E. L.; Dumesic, J. A.; Mavrikakis, M.; Besenbacher, F. *J. Am. Chem. Soc.* **2007**, *129* (20), 6485–6490.

(243) Hong, X.; Chan, K.; Tsai, C.; Nørskov, J. K. *ACS Catal.* **2016**, *6* (7), 4428–4437.

(244) Zandkarimi, B.; Alexandrova, A. N. *J. Phys. Chem. Lett.* **2019**, *10* (3), 460–467.

(245) Jansonius, R. P.; Reid, L. M.; Virca, C. N.; Berlinguette, C. P. *ACS Energy Lett.* **2019**, *4* (4), 980–986.

(246) Khorshidi, A.; Violet, J.; Hashemi, J.; Peterson, A. A. *Nat. Catal.* **2018**, *1* (4), 263–268.

(247) Lambin, P.; Gaspard, J. P. *J. Phys. F Met. Phys.* **1980**, *10* (11), 2413–2428.

(248) Chelikowsky, J. R. *Surf. Sci.* **1984**, *139* (2–3), L197–L203.

(249) Mukherjee, S.; Morán-López, J. L. *Surf. Sci. Lett.* **1987**, *188* (3), L742–L748.

(250) Miedema, A. R.; de Boer, F. R.; Boom, R. *Calphad* **1977**, *1* (4), 341–359.

(251) Christensen, A.; Ruban, A. V.; Stoltze, P.; Jacobsen, K. W.; Skriver, H. L.; Nørskov, J. K.; Besenbacher, F. *Phys. Rev. B* **1997**, *56* (10), 5822–5834.

(252) Ruban, A. V.; Skriver, H. L.; Nørskov, J. K. *Phys. Rev. B* **1999**, *59* (24), 15990–16000.

(253) Ruban, A. V.; Skriver, H. L. *Comput. Mater. Sci.* **1999**, *15* (2), 119–143.

(254) Bradley, A. J.; Thewlis, J. *Proc. R. Soc. A Math. Phys. Eng. Sci.* **2006**, *115* (771), 456–471.

(255) Oberteuffer, J. A.; Ibers, J. A. *Acta Crystallogr. Sect. B Struct. Crystallogr. Cryst. Chem.* **1970**, *26* (10), 1499–1504.

(256) L.E. Reed, R.A. Porter, F.E. Farha, Guillory, J. P. September 30, 1985.

(257) Cayton, R. **1993**, 1–4.

(258) Heyse, J. V.; Johnson, P. G.; Mulaskey, B. F. Dehydrogenation processes, equipment and catalyst loads therefor, December 12, 1998.

(259) Pedregosa, F.; Varoquaux, G.; Gramfort, A.; Michel, V.; Thirion, B.; Grisel, O.; Blondel, M.; Prettenhofer, P.; Weiss, R.; Dubourg, V.; Vanderplas, J.; Passos, A.; Cournapeau, D.; Brucher, M.; Perrot, M.; Duchesnay, É. *J. Mach. Learn. Res.* **2011**, *12* (Oct), 2825–2830.

(260) Ashcroft, N. W.; Mermin, N. D. *Solid state physics*; Holt, Rinehart and Winston, 1976.

(261) Christensen, A.; Ruban, A. V.; Stoltze, P.; Jacobsen, K. W.; Skriver, H. L.;

Nørskov, J. K.; Besenbacher, F. *Phys. Rev. B* **1997**, *56* (10), 5822–5834.

(262) Miura, H.; Endo, K.; Ogawa, R.; Shishido, T. *ACS Catal.* **2017**, *7* (3), 1543–1553.

(263) Zhang, L.; Wang, A.; Miller, J. T.; Liu, X.; Yang, X.; Wang, W.; Li, L.; Huang, Y.; Mou, C. Y.; Zhang, T. *ACS Catal.* **2014**, *4* (5), 1546–1553.

(264) Giannakakis, G.; Trimpalis, A.; Shan, J.; Qi, Z.; Cao, S.; Liu, J.; Ye, J.; Biener, J.; Flytzani-Stephanopoulos, M. *Top. Catal.* **2018**, *61* (5–6), 475–486.

(265) Pei, G. X.; Liu, X. Y.; Yang, X.; Zhang, L.; Wang, A.; Li, L.; Wang, H.; Wang, X.; Zhang, T. *ACS Catal.* **2017**, *7* (2), 1491–1500.

(266) Liu, J.; Shan, J.; Lucci, F. R.; Cao, S.; Sykes, E. C. H.; Flytzani-Stephanopoulos, M. *Catal. Sci. Technol.* **2017**, *7* (19), 4276–4284.

(267) Shan, J.; Liu, J.; Li, M.; Lustig, S.; Lee, S.; Flytzani-Stephanopoulos, M. *Appl. Catal. B Environ.* **2018**, *226*, 534–543.

(268) Boucher, M. B.; Zugic, B.; Cladaras, G.; Kammert, J.; Marcinkowski, M. D.; Lawton, T. J.; Sykes, E. C. H.; Flytzani-Stephanopoulos, M. *Phys. Chem. Chem. Phys.* **2013**, *15* (29), 12187–12196.

(269) Marcinkowski, M. D.; Liu, J.; Murphy, C. J.; Liriano, M. L.; Wasio, N. A.; Lucci, F. R.; Flytzani-Stephanopoulos, M.; Sykes, E. C. H. *ACS Catal.* **2017**, *7* (1), 413–420.

(270) Wang, Z. T.; Darby, M. T.; Therrien, A. J.; El-Soda, M.; Michaelides, A.; Stamatakis, M.; Sykes, E. C. H. *J. Phys. Chem. C* **2016**, *120* (25), 13574–13580.

(271) Serna, P.; Concepción, P.; Corma, A. *J. Catal.* **2009**, *265* (1), 19–25.

(272) Hastie, T.; Tibshirani, R.; Friedman, J. In *Encyclopedia of Neuroscience*; 2008; pp 4154–4154.

(273) Glorot, X.; Bengio, Y. In *Journal of Machine Learning Research*; 2010; Vol. 9, pp 249–256.

(274) Platt, J. C. In *Advances in Large Margin Classifiers*; 2000; Vol. 10, pp 61–74.

(275) Iwasa, N.; Takezawa, N. *Top. Catal.* **2003**, *22* (3–4), 215–224.

(276) Do, Q. K.; Tran, H.-V.; Wang, S.; Grabow, L. C. *Energy Technol.* **2019**, 1900732.

(277) Imai, H.; Tagawa, T.; Nakamura, K. *React. Kinet. Catal. Lett.* **1991**, *43* (2), 355–359.

(278) Su, S.; Zaza, P.; Renken, A. *Chem. Eng. Technol.* **1994**, *17* (1), 34–40.

(279) Saito, Y.; Hiramatsu, N.; Kawanami, N.; Ogino, Y. *Bull. Japan Pet. Inst.* **1972**, *14* (2), 169–173.

(280) Xiao, X.; Bergstrom, H.; Saenger, R.; Johnson, B.; Sun, R.; Peterson, A. *Catal. Sci. Technol.* **2018**, *8* (7), 1819–1827.

(281) Darby, M. T.; Sykes, E. C. H.; Michaelides, A.; Stamatakis, M. *Top. Catal.* **2018**, *61* (5–6), 428–438.

(282) Simonovis, J. P.; Hunt, A.; Palomino, R. M.; Senanayake, S. D.; Waluyo, I. *J. Phys. Chem. C* **2018**, *122* (8), 4488–4495.

(283) Marcinkowski, M. D.; Jewell, A. D.; Stamatakis, M.; Boucher, M. B.; Lewis, E. A.; Murphy, C. J.; Kyriakou, G.; Sykes, E. C. H. *Nat. Mater.* **2013**, *12* (6), 523–528.

(284) Darby, M. T.; Lucci, F. R.; Marcinkowski, M. D.; Therrien, A. J.; Michaelides, A.; Stamatakis, M.; Sykes, E. C. H. *J. Phys. Chem. C* **2019**, *123* (16), 10419–10428.

(285) McCue, A. J.; McRitchie, C. J.; Shepherd, A. M.; Anderson, J. A. *J. Catal.* **2014**, *319*, 127–135.

(286) Morkel, M.; Kaichev, V. V.; Rupprechter, G.; Freund, H. J.; Prosvirin, I. P.; Bukhtiyarov, V. I. *J. Phys. Chem. B* **2004**, *108* (34), 12955–12961.

(287) Huang, Y.; Chen, Z. X. *Langmuir* **2010**, *26* (13), 10796–10802.

(288) Velichkina, L. M.; Pestryakov, A. N.; Vosmerikov, A. V.; Tuzovskaya, I. V.; Bogdanchikova, N. E.; Avalos, M.; Farias, M.; Tiznado, H. *Pet. Chem.* **2008**, *48* (5), 355–359.

(289) Yu, C.; Xu, H.; Ge, Q.; Li, W. *J. Mol. Catal. A Chem.* **2007**, *266* (1–2), 80–87.